

Enhancing the Hydrogen Evolution Reaction on Nanostructured Metal/Silicon Electrodes by a Bifunctional Mechanism

Thomas Lorenz Maier

Vollständiger Abdruck der von der TUM School of Natural Sciences der Technischen Universität München zur Erlangung eines

Doktors der Naturwissenschaften (Dr. rer. nat.)

genehmigten Dissertation.

Vorsitz: Prof. Dr. David Egger

Prüfer*innen der Dissertation:

1. Prof. Dr. Katharina Krischer
2. Prof. Dr. Ian Sharp

Die Dissertation wurde am 22.12.2022 bei der Technischen Universität München eingereicht und durch die TUM School of Natural Sciences am 09.03.2023 angenommen.

The whole can be greater than the sum of its parts.

Aristotle

Abstract

In this work, we investigate silicon-based (photo-)electrodes patterned with a well-defined array of metal nanostructures regarding their electrocatalytic activity for hydrogen evolution reaction (HER). We show that the patterned electrodes exhibit an increased catalytic activity for HER compared to bare metal surfaces. By varying the geometry of the patterning and performing local current measurements, we can conclude that the increased activity is due to a higher HER rate at the metal/insulator interface, which is intrinsically present on the nanopatterned electrode surface. Based on the results of comprehensive studies varying several system parameters, such as the catalyst material (Au, Cu, Pt), the 'support' material (silicon oxide, silicon nitride), and several parameters of the electrolyte (pH value, concentration of ions, cationic species), we finally propose a bifunctional mechanism, in which the support material works as an additional proton source for HER. The bifunctional mechanism is able to explain the selective enhancement of HER at the metal/insulator interface and is in accordance with all results and conclusions obtained in this work. The findings in this work can have major relevance for the understanding of heterogeneous metal/insulator interfaces and their applications in the future.

Contents

1	Introduction	1
2	Theoretical background	5
2.1	Interfaces of metal/silicon electrodes	5
2.1.1	Metal/insulator/semiconductor interface	5
2.1.2	Electrolyte/MIS interface	9
2.1.3	Surface chemistry of the silicon oxide and silicon nitride	10
2.2	Electrochemical equilibrium	14
2.2.1	Electrochemical double layer	14
2.2.2	Nernst equation	15
2.3	Reaction kinetics	16
2.3.1	Multistep reactions	16
2.3.2	Tafelslope change in multistep reactions	18
2.4	Electrocatalysis of the Hydrogen Evolution Reaction	21
2.4.1	Mechanisms of the Hydrogen Evolution Reaction	21
2.4.2	Hydrogen adsorption kinetics	21
3	Experimental details	27
3.1	Fabrication and characterization of nanostructured electrodes	27
3.1.1	Design and composition of the nanostructured electrodes	27
3.1.2	Electrode fabrication: Lift-Off Nanoimprint Lithography	29
3.1.3	Dry electrode characterization	33
3.2	Electrochemical investigation	39
3.2.1	Three-electrode setup and IR-correction	39
3.2.2	Electrolytes	40
3.2.3	Measurement equipment and measurement techniques	40
3.2.4	Photoelectrochemical measurements	41
3.2.5	Recessed Rotating Disk Electrode setup (ReRDE) - Introduction and characterization	43
3.2.6	Local current mapping - SECCM and SICM measurements	48
3.2.7	Area determination	51
4	Electrochemical behavior of nanostructured metal/p-Si photoelectrodes	55
4.1	General behavior of Au/p-Si photoelectrodes	55
4.2	Simulating the overpotential-distribution in the combined junction	59
4.3	Increasing HER activity with decreasing structure size	63
4.4	Investigation of Pt-based structures	65
4.5	Summary	69

5	Enhanced HER kinetics at the gold/silicon oxide interface	71
5.1	Increased HER activity of laterally patterned Au-SiO _x /n-Si electrodes . . .	73
5.1.1	Tafel analysis in alkaline electrolyte - Enhanced border activity . . .	74
5.1.2	Tafel analysis in acidic electrolyte - Change of reaction mechanism .	77
5.2	Local current mapping	82
5.2.1	Acidic medium - SECCM measurement	82
5.2.2	Neutral medium - SICM measurement	86
5.3	Influence of particle transport	91
5.3.1	Primary current distribution	91
5.3.2	Macroscopic diffusion - ReRDE measurement	92
5.3.3	Microscopic diffusion - Diffusion in microelectrode arrays	94
5.4	Summary	98
6	Influence of various system parameters on the HER enhancement	99
6.1	Electrocatalytic surface and catalyst material	99
6.1.1	Au surface topography of nanostructured electrodes	100
6.1.2	SiO _x nanostructures on Au(pc) electrode	102
6.1.3	Pt-based structured electrode	105
6.1.4	Cu-based structured electrode	107
6.2	Passivation layer	112
6.2.1	Covering the silicon oxide surface	112
6.2.2	Nanostructured electrodes with silicon nitride as passivation layer .	114
6.3	Electrochemical environment	120
6.3.1	pH value of the electrolyte	120
6.3.2	Cation concentration	125
6.3.3	Cationic species	127
6.4	Summary	132
7	Increasing the double layer capacitance by electrode nanostructuring	135
7.1	Differential capacitance determined via cyclic voltammetry	135
7.1.1	Comparison of protruding and embedded structures	136
7.1.2	Dependence of the differential capacitance on the size of the nanos- tructures	138
7.2	Capacitance determined via impedance spectroscopy	142
7.2.1	Capacitive behavior of the silicon/oxide/electrolyte interface	142
7.2.2	Capacitive behavior of the continuous Au layer electrode	145
7.2.3	Simulation of the capacitive behavior by the modified Poisson-Boltzmann equation in 1D	147
7.2.4	Increased capacitance of nanostructured electrodes	152
7.3	Summary	156
8	Bifunctional mechanism at the metal/insulator interface	157
8.1	Bifunctional mechanism	157
8.2	Discussion of the experimental results on the basis of the proposed bifunc- tional mechanism	159
8.2.1	Smaller HER enhancement in acidic medium	159
8.2.2	Dependence on the electrocatalytic active surface material and struc- ture	160
8.2.3	Dependence on the nature of cations, concentration and pH	161
8.2.4	Higher capacitance as the reason for enhanced HER rate?	163

8.3	Implications of the proposed mechanism	163
8.3.1	No enhancement of other electrocatalytic reactions?	163
8.3.2	Enhancement of OER?	166
9	Conclusion and Outlook	169
A	Supplementary Information	187
A.1	Etching of borosilicate glass in alkaline electrolyte	187
A.2	Transfer coefficients for various HER/HOR reaction pathways	187
A.3	HER reaction network on Au(pc) in acidic medium	188
A.4	Metal nanostructure array on glassy carbon substrate	189
A.5	Presence of protruding edges on metal nanostructures	190
A.6	List of chemicals used	191
A.7	Theoretical curve of HOR in an RDE setup	192
A.8	Time dependence of the electrode current with variable electrode potential .	192
A.9	Tafel analysis of acidic HER at a lower potential scan rate	193
A.10	CVs of Pt-based nanostructured electrodes in acidic medium	194
A.11	XPS spectra of a silicon nitride film at various angles	194
A.12	Tafel plot of LSV curves in neutral electrolyte	196
A.13	Comparison of fitting models of impedance data	196

Chapter 1

Introduction

Ecologically produced hydrogen gas ('green hydrogen') will be one of the main energy carriers of the clean and sustainable energy economy in the future [BW10]. Apart from electrolyzers utilizing electricity of any renewable energy source [Gah13], the direct production of hydrogen from solar light and water in solar-driven water splitting devices is regarded as one of the key emerging techniques [OW89; Now+05]. Thus, research in this field has gained much attention in recent years. Devices based on silicon photoelectrodes are, among others, such as metal oxides [Par+11; Abd+13] or III-V semiconductors [KT98; DKT06], very promising candidates for solar-to-hydrogen devices due to the abundance of silicon and its suitable material properties for solar light harvesting [McK+11; Boe+11; Urb+14].

To make a silicon-based light absorber effective for a specific (photo-)electrochemical reaction, its surface needs to be modified. On the one hand, the absorber surface in contact with the electrolyte needs to be stabilized against corrosion to assure a long-term operation of the device [Sch+99]. On the other hand, the surface needs to be partly modified by a suitable catalyst driving the desired electrochemical reaction. This can be achieved e.g. by metal particles or islands [Hin+98; Esp+13; Che+15]. However, it is important to cover only part of the absorber surface by metal structures (i.e. patterning) to assure a good light transmittance of the surface, as metals usually exhibit a rather high reflectivity of light in the visible range. A scheme of such a potential solar-to-hydrogen device is shown in Figure 1.1.

To make the operation of such a device economically feasible, a high efficiency of the device needs to be ensured. Besides the absorption properties mentioned above, also the kinetics of the involved reactions, namely the Hydrogen Evolution Reaction (HER) and the Oxygen Evolution Reaction (OER), and the stability of the respective catalysts are crucial parameters for optimization [Coo+10; Wal+10; McC+15]. Although the electrocatalytic behavior of the catalysts is largely determined by fundamental material properties, the actual implementation of the catalysts in the final device, i.e. the device architecture, can further alter the catalytic behavior significantly, since a variety of possible effects can appear at the complex interfaces of photo-electrochemical devices at operation conditions [ML14]. For example, the diffusion length of photoexcited charge carriers depends significantly on the used absorber material [Jia+17], which further determines the needed amounts and 'positions' of the catalysts. However, the catalytic activity of metal nanoparticles depends strongly on their size/shape [PY09] and surface loading [Kem+15].

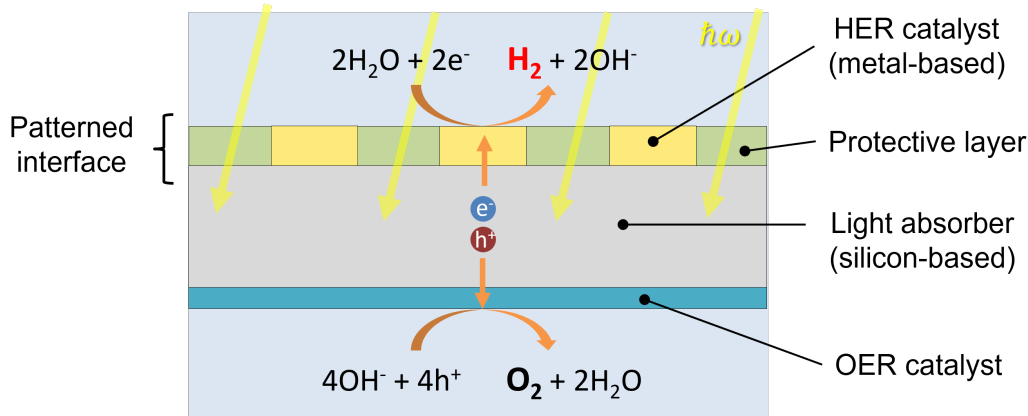


Figure 1.1: Scheme of a potential solar-to-hydrogen device. The incoming solar light (light yellow) is absorbed in the silicon-based light absorber (gray). The photoexcited charge carriers approach either the metal-based HER catalyst (yellow) or the OER catalyst (blue), where the respective electrochemical reaction can proceed. In order to achieve a high transmittance of light into the absorber, the light-facing interface needs to be patterned. In addition, the absorber surface exposed to the electrolyte (light blue) needs to be stabilized against corrosion by a protective layer (green).

Since many system parameters in combined devices can partly affect each other, it becomes clear that the attribution of an observed catalytic behavior of an incorporated catalyst to a certain fundamental mechanism can be very challenging. This becomes very present when considering HER in several model systems: For example, Hinogami et al. [Hin+98] noticed that silicon-based photoelectrodes consisting of particulate metal (Cu, Au, and Ag particles) exhibit a much more positive onset potential for the HER than the corresponding bare metal electrodes. Although the authors explained that the difference stems from a huge photovoltage induced in the system, their results suggest that the difference can not only be explained by the appearing photoeffect. Esposito et al. [Esp+13] investigated HER on well-defined Pt cylinders on silicon-based photoelectrodes. They showed that the presence of the silicon(-oxide) surface close to metal islands enhances the HER locally compared to the metal bulk. The authors explained the observed behavior by an inversion channel for photoexcited charge carriers, which enables a lateral hydrogen spillover of adsorbed hydrogen from the metal to the silicon oxide leading to the enhanced rate. However, the question remains, if these mechanisms are the only effects present in the particular systems appearing at the metal/silicon interface, as there is evidence that already the presence of mesoscopic metal structures on silicon surfaces can lead to an increased HER activity of the electrodes compared to the activity of bare metal surfaces [Fil+18; Mai+20].

The observed increase of HER reactivity in the metal/silicon photosystems may be complemented by other fundamental effects enhancing HER at heterogeneous interfaces. There are multiple examples in the literature showing that HER kinetics can be altered significantly on non-homogeneous interfaces [Str+16; Wu+21]. For example, Danilovic et al. [Dan+12] showed that the coverage of various metal surfaces by metal-oxide particles (in particular $\text{Ni}(\text{OH})_2$ nanoparticles) can enhance the HER kinetics significantly. Due to the surface modification, the activity of the metal surfaces in alkaline medium approaches their activity in acidic medium (cf. Figure 1.2). The authors explained the enhancement by the appearance of a bifunctional mechanism at the metal/particle interface promoting the water dissociation step. However, the actual mechanistic reason responsible for

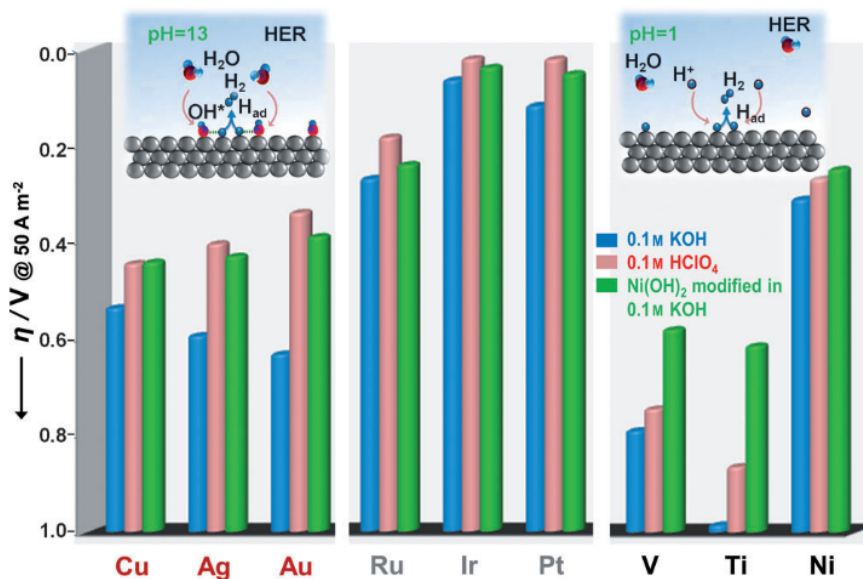


Figure 1.2: Comparison between activities for the HER, expressed in overpotential (η) required for a current density of 5 mA cm^{-2} for various metal surfaces. Blue: Bare metal surface in alkaline electrolyte. Green: Metal surfaces decorated by Ni(OH)_2 particles in alkaline electrolyte. Red: Bare metal surfaces in acidic electrolyte. Original Figure from Danilovic et al. [Dan+12].

the observed enhancement is still under discussion [Sub+11; Dan+12; Led+17; Sar+18; Reb+18].

This work provides a fundamental study of HER kinetics in model systems relevant for future photo-electrochemical applications. It elucidates how the heterogeneous surface of silicon-based (photo-)electrodes, which stems from its patterning with metal meso- and nanostructures, influences their electrocatalytic activity regarding HER. The unique feature of this work is the design of the investigated electrodes. They consist of silicon-based substrates, which surfaces are modified on large scale with well-defined arrays of metal nanostructures working as the HER catalysts. The residual silicon surface is covered by a protective layer based on either silicon oxide or silicon nitride to minimize chemical corrosion while maintaining good light transmittance. The surface patterning on large scale with a very homogeneous metal nanostructure array is achieved by the technique Lift-Off Nanoimprint Lithography [Nag18].

In this thesis, we show that metal nanostructured photo-active electrodes based on silicon (cf. chapter 4) as well as photo-inactive electrodes of similar composition (cf. chapter 5) exhibit an enhanced catalytic activity for HER. By changing the geometry of the metal patterning and performing local current measurements we show that the metal/insulator interface, where the metal catalyst is in close contact with the silicon-based protective material (insulator), exhibits a strongly enhanced HER rate compared to a bare metal surface. Based on the results obtained when changing several parameters of the system, such as the material combinations and properties of the electrolyte (cf. chapter 6), we propose a bifunctional mechanism (cf. chapter 8) occurring at the metal/insulator interface, which explains the observed behavior and is in accordance with all results and dependencies obtained in this work.

Chapter 2

Theoretical background

This chapter provides the theoretical background necessary for following the argumentation in this work and it introduces relevant quantities, which are important within the scope of this work. More explicitly, this chapter introduces the electrical and chemical properties of the relevant interfaces present in the nanostructured electrodes (section 2.1), concepts regarding reaction kinetics of multistep reactions (section 2.3), and theoretical fundamentals regarding electrocatalysis of the Hydrogen Evolution Reaction (section 2.4), which is the main electrochemical reaction investigated in this work.

2.1 Interfaces of metal/silicon electrodes

2.1.1 Metal/insulator/semiconductor interface

The nanostructured electrodes investigated in this work exhibit metal/insulator/semiconductor (MIS) interfaces. Refer to section 3.1 for a detailed description of the design of the electrodes, the fabrication procedure and the materials used. At this point, we give a short introduction to the electrical response of MIS interfaces, as it is typically observed for the electrodes investigated in this work.

In the MIS interface, always silicon (Si) with either n- or p-doping, depending on the 'type' of the electrode (photo-inactive electrode or photoelectrode, see below) is used as the semiconductor material. The silicon surface is usually intrinsically covered by a thin (< 2 nm) layer of silicon oxide (insulator). Although silicon oxide is labeled as 'insulator', electrons and holes are able to tunnel through this layer due to its low thickness. The silicon oxide layer is in contact with a titanium layer (Ti) with a thickness of approx. 3 nm. The titanium promotes the adhesion between the silicon oxide/silicon substrate and the metal catalyst, which is deposited on top. In this work, either gold (Au) or platinum (Pt) is used as the catalyst material. Although the metal side is a stack of two metals with very different work functions ($\Phi_{\text{Ti}} \approx 4.3$ eV, $\Phi_{\text{Au}} \approx 5.1$ eV, $\Phi_{\text{Pt}} \approx 5.6$ eV [Sze07]), we will see below that the electrical behavior of the MIS interfaces investigated here is predominately determined by Ti.

If two phases α and β are brought in contact and a common charged species i can cross the interface, the electrochemical potentials $\tilde{\mu}_i^\alpha$ and $\tilde{\mu}_i^\beta$ of the species align in equilibrium. This alignment leads to an accumulation of charge carriers at the interface and consequently to a drop of the electrostatic potential at the interface. In case of a metal and a semiconducting

phase, the main part of the potential drop occurs on the semiconductor side, which results in the formation of a space charge layer and band bending. Depending on the actual material and fabrication properties, the electrical response of the formed interface exhibits either a diodic- or an ohmic-like behavior.

Schottky contacts of p-doped silicon based junctions

The photo-active electrodes (photoelectrodes) investigated in this work utilize moderately p-doped silicon as the semiconducting material. It will be shown later (cf. section 3.1.3) that the dry electrical response of the Ti/SiO₂/p-Si based MIS interface behaves like a Schottky contact. The cause for its diodic electrical response with and without illumination is shortly described here.

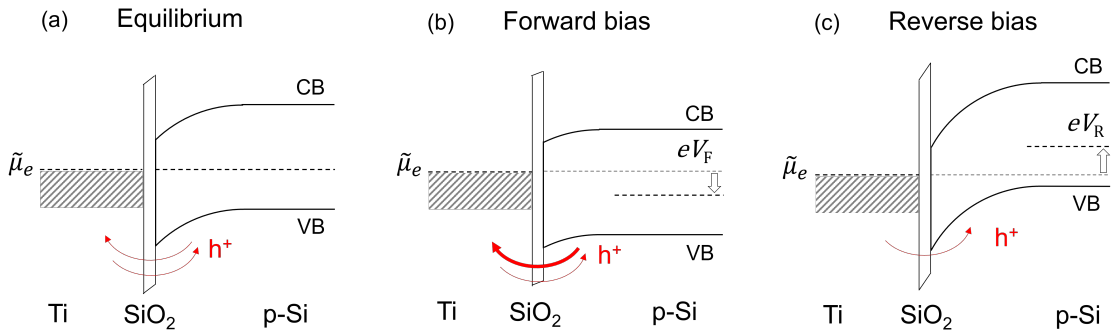


Figure 2.1: Schematic band diagram of an ideal Ti/SiO₂/p-Si interface for different biasing conditions: (a) Equilibrium, (b) Forward bias, (c) Reverse bias. The red arrows symbolize the hole current flow across the interface. In equilibrium, the electrochemical potential of electrons is constant across the interface. No net flow of holes occurs. If the system is forward biased, the energetic barrier for holes in the VB of p-Si is lowered, resulting in a net hole flow from p-Si towards the metal side, depending on the magnitude of the forward bias V_F . If the system is reverse biased, the hole flow from p-Si to the metal decreases, but the energetic barrier height seen by the holes in Ti remains constant. This results in a net current flow from the metal towards p-Si, independent of the magnitude of the reverse bias V_R . The interface behaves as a Schottky contact (diode).

A schematic band diagram of an ideal Ti/SiO₂/p-Si interface for different biasing conditions is shown in Figure 2.1. In equilibrium, the electrochemical potential of electrons $\tilde{\mu}_e$ is constant across the interface. In this case the conduction band (CB) and the valence band (VB) of the semiconductor at the metal/silicon junction bend downwards, forming an energetic barrier for the excess holes (majority charge carriers) in the VB of p-Si. No net hole current flows across the interface in equilibrium. If a forward bias V_F is applied to the system, the electrochemical potential of VB holes in the p-Si bulk is energetically decreased compared to the electrochemical potential in the metal. The barrier height seen by holes in the VB of p-Si is decreased, whereas the barrier height seen by holes in Ti is not affected. This results in a net flow of holes (thermoionic emission) from p-Si through the interface towards Ti and, consequently, in an electrical current. As the density of minority charge carriers (here electrons) is negligible compared to the density of the majority charge carriers (here holes), all currents conducted by them can be neglected. The junction is operated in 'forward direction'. If a reverse bias V_R is applied to the system, the electrochemical potential of VB holes in the silicon bulk is energetically increased compared to the electrochemical potential in Ti. The barrier height seen by holes in the VB of p-Si is increased, consequently the current of holes from p-Si towards Ti is decreased.

The barrier height seen by holes in Ti is, again, not affected. This results in a net flow of holes from Ti towards p-Si, which is independent of the magnitude of V_R . The junction is operated in 'reverse direction'.

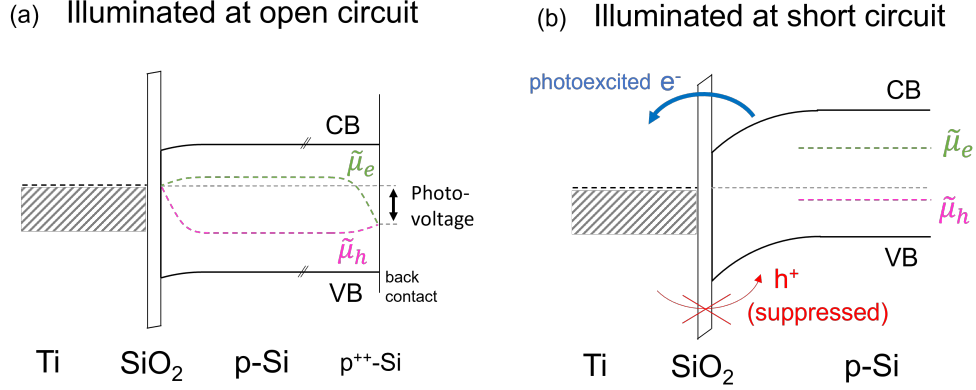


Figure 2.2: Schematic band diagram of an illuminated ideal Ti/SiO₂/p-Si interface combined with a suitable back contact (i.e. photodiode): (a) At open circuit condition, (b) at short circuit condition. The green and purple dashed lines indicate the quasi-electrochemical potentials of electrons in the CB $\tilde{\mu}_e$ and of holes in the VB $\tilde{\mu}_h$, respectively. At open circuit condition, the excited excess charge carriers, which are present due to the continuous absorption of photons with an energy larger than the bandgap, recombine within the absorbing material. No net current flows across the interfaces. If load is connected to the device or the circuit is shorted, a net current flow of electrons from p-Si towards the metal side is established.

Combining the mentioned ideal Ti/SiO₂/p-Si interface with a suitable (hole selective) back contact creates a photodiode. Photons with an energy larger than the band gap of silicon ($E_{g,\text{Si}} \approx 1.12$ eV at room temperature [Sze07]) can be absorbed, which results in an excess density of electrons in the conduction band (CB) and holes in the valence band (VB) compared to the case without illumination. The energetic distributions of the excess electrons in the CB and holes in the VB need to be considered individually, which necessitates the definition of individual quasi-electrochemical potentials of electrons in the CB $\tilde{\mu}_e$ and of holes in the VB $\tilde{\mu}_h$. Figure 2.2(a) shows a schematic band diagram of the photodiode under illumination at open circuit condition. The excited excess charge carriers recombine within the absorber material or at the interfaces and no net current flows across the interfaces. The electrodes we consider in this work have two different materials as contacts: The front contact is made of Ti, the back contact is made of Al. Due to an annealing process after evaporation of the Al layer, a p⁺⁺ doped region is formed at the back side of the sample (cf. section 3.1.2 for details on the fabrication process) giving the selective contact. As a consequence, photovoltage can build up and the photo-excited electrons can be extracted at a higher energetic level at the front side than they are inserted at the (ohmic) back contact of the device (a more detailed explanation is given e.g. by Krischer and Schönleber [KS15]). If load is connected to the illuminated diode or it is short-circuited, a net flow of photoexcited electrons from the CB of p-Si towards Ti and, consequently, a net electrical current across the interfaces is established. A schematic diagram of this situation at the MIS interface is shown in Figure 2.2(b). The flow of holes from Ti towards p-Si can be neglected at the same time.

Note that we only explained the ideal behavior of a the Ti/SiO₂/p-Si MIS interface here. The real situation is more complicated to describe theoretically due to various interfacial

effects, such as Fermi level pinning and trap states [Sze07]. However, typical p-Si based electrodes investigated in this work show a Schottky-contact-like, i.e. diodic, electrical response of the MIS junction, cf. Figure 3.7(a), as well as photovoltage. Consequently, these types of electrodes based on p-doped silicon substrate are labeled as 'photoelectrodes' in the following.

(Quasi-)Ohmic contacts of n-doped silicon based junctions

When varying the species of dopant atoms in silicon to electron donors, here we use a moderately n-doping of silicon, the behavior of the MIS interface changes significantly. Figure 2.3 shows a schematic band diagram of an idealized MIS interface with n-doped silicon, exemplary (a) for a metal with a high work function (e.g. Au or Pt) and (b) for a metal with a low work function (e.g. Ti). When using a metal with a comparatively high work function, a depletion layer forms at the n-Si side. The bands consequently bend upwards. Since the main contribution to the current stems from the majority charge carriers, here now electrons in the conduction band, the interface would behave like a Schottky diode. The behavior of this junction is very similar to the p-Si based system shown above. If the metal has a comparatively low work function, the electrons in n-Si would accumulate at the interface, resulting in a downwards bending of the bands. Consequently, the barrier height seen by the electrons is much smaller than it is in the case using a high metal work function. Although the interface still behaves like a Schottky contact, the equilibrium current density is much larger than in the other case (this is indicated by the thicker blue arrows in the Figure). As a consequence, the limiting current density in reverse direction is significantly higher. In the range of small current densities, the electric behavior can thus be approximated as linear (i.e. quasi-ohmic). Due to interfacial effects (e.g. energetic states inside the band gap and Fermi level pinning), the electron density at the interface may be so high that the junction exhibits a (quasi-)ohmic behavior even at comparatively large current densities.

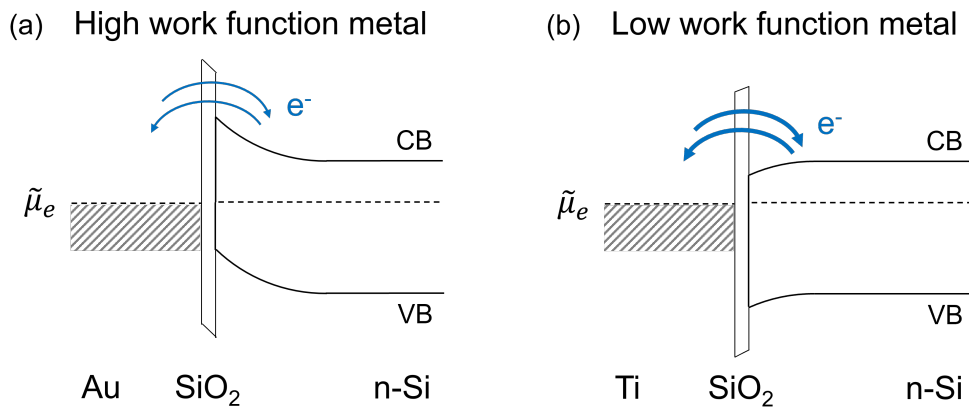


Figure 2.3: Schematic band diagram of an idealized metal/SiO₂/n-Si interface in equilibrium for two metals with different work functions: (a) high metal work function (e.g. Au or Pt), (b) low metal work function (e.g. Ti). In the case of a high work function metal, the MIS interface behaves (in an ideal case) like a Schottky contact (see above). In the case of a low work function metal, the barrier height appears to be much smaller. Consequently, the equilibrium current density is much higher (indicated by the thicker blue arrows) resulting in a quasi-linear (quasi-ohmic) electrical response for small current densities.

Experimental data of the electrical response n-Si based electrodes investigated in this work indicate a linear current-voltage characteristic, even at comparatively high current densities, cf. Figure 3.7(b). Thus, it appears reasonable that the electrical response of this system is determined predominately by the properties of Ti, although its actual layer thickness is just 3 nm. Since the electrical response of the produced electrodes using n-doped silicon as the substrate further appears to be rather insensitive for illumination, the electrodes are labeled as 'photo-inactive' electrodes in the following.

2.1.2 Electrolyte/MIS interface

When bringing an electrolyte and a MIS interface (electrode) in contact, the electrochemical potential of a transferable charged species, such as electrons for electron-transfer reactions, aligns over all phases. This alignment can further lead to an accumulation/depletion of charged species at each interface between the phases. However, when defining the Fermi level of electrons in the electrolyte, solid state physics models can also be applied for modeling electrode/electrolyte interfaces under non-equilibrium condition [Ger60]. If the electrolyte contains a dominating redox couple, this couple provides states which can be filled and emptied by electrons via charge transfer reactions. The states can be modeled by distribution functions W_{red} and W_{ox} of the reduced and oxidized species, respectively [Ger60; SS10]. The electrochemical potential of electrons on the electrolyte side is given by the intersect of the two distribution functions [SS10].

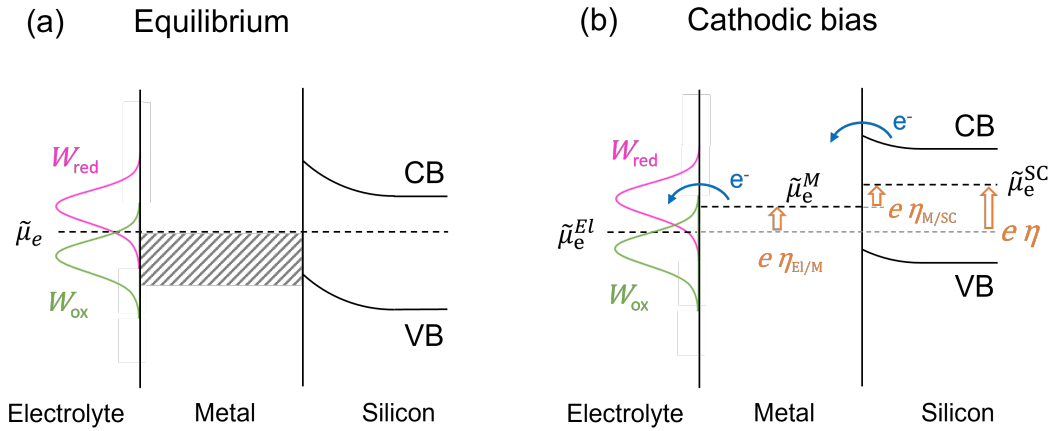


Figure 2.4: Schematic band diagram of an idealized electrolyte/MIS interface for different biasing conditions: (a) Equilibrium. The electrochemical potential $\tilde{\mu}$ of the transferable species (electrons) aligns over all interfaces. (b) Cathodic bias leads to charge transfer across the interfaces.

Figure 2.4(a) shows the energetic diagram of an idealized exemplary electrolyte/MIS interface in equilibrium. The electrochemical potential of electrons $\tilde{\mu}_e$ is constant over all phases. Applying an overpotential η to the electrolyte/MIS system, the electrochemical potential of electrons in the semiconductor bulk is changed with respect to the electrolyte bulk. Figure 2.4(b) shows the energetic diagram of the idealized electrolyte/MIS interface in the case of a cathodic bias. The total applied overpotential η can be separated into two contributions:

$$\eta = \eta_{\text{El/M}} + \eta_{\text{M/SC}} \quad (2.1)$$

Here, $\eta_{\text{El/M}}$ is the fraction of the applied overpotential that drops across the electrolyte/metal

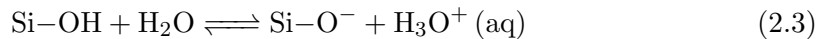
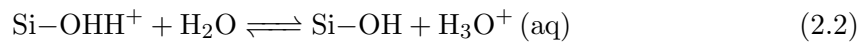
interface, and $\eta_{M/SC}$ is fraction of overpotential that drops across the metal/semiconductor interface. The electrical response of the system is now dependent on the properties of the electrolyte/metal and the metal/semiconductor interface and in general rather complex to describe theoretically. The actual electrochemical and 'electrical' properties of the combined electrolyte/MIS junction are investigated experimentally and further described theoretically in the results section in chapter 4.

2.1.3 Surface chemistry of the silicon oxide and silicon nitride

In this work, nanostructured electrodes are investigated. As already described above, due to the structuring a part of the silicon surface around the metal structures is exposed to the electrolyte. To minimize degradation or corrosion of the silicon material, especially in alkaline electrolyte, its exposed surface is covered by a protection/passivating layer based on either thermal silicon oxide or LPCVD silicon nitride (see section 3.1.1). The surface chemistry of these layers in contact with an aqueous electrolyte is introduced in this section.

Surface chemistry of silicon oxide

The chemical composition of the silicon oxide surface exposed to the electrolyte is dominated by the surface protonation/deprotonation reactions of the silicon hydroxy group:



For a given pH of the solution, the chemical composition of the silicon oxide surface is in equilibrium with the bulk of the solution. At low pH, the surface is terminated by protons (Si-OOH^+) and hydroxy groups (Si-OH). With increasing pH the surface becomes deprotonated and the protons are released to the bulk of the solution according to equation (2.2). At a certain pH, the surface is completely covered by hydroxy groups. At this point there is not net charge at the silicon oxide surface (point-of-zero-surface-charge, PZSC). The actual pH value of the PZSC depends on the nature of the silicon oxide and its surface treatment, but it is usually at pH values between 2 and 4 [Per+15]. With further increasing pH, the surface becomes negatively charged according to equation (2.3) as now, beside of the hydroxy group, Si-O^- forms progressively.

The charged silicon oxide surface is accompanied by a counter charge in the electrolyte forming an electrochemical double layer. For a positively charged surface the counter charge is made up of the anions present in solution. For negatively charged surface below pH 7, the counter charge is either protons or cations, depending on their respective bulk concentration, and above pH 7 it is made up exclusively from cations, since all alkaline electrolytes necessitate the presence of cations [Zha04a]. An overview of the approximate surface coverage of the different functional groups at selected pH values important in this work is given in Table 2.1.

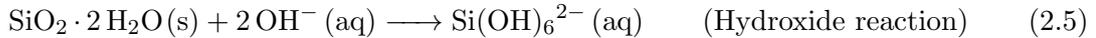
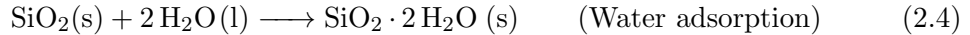
Note that, especially for strongly negatively polarized surfaces at high pH values, there can be partial adsorption of cations present at the surface. The grade of partial adsorption would depend on various parameters, such as the solvation energy of the respective cationic species [Zha04b].

	Fraction of surface coverage θ			Source
	Si-OHH ⁺	Si-OH	Si-O ⁻	
pH 1	< 0.1%	> 99.9%	-	[Zha04a]
PZSC (\approx pH 2.5)	-	100%	-	[Per+15]
pH 7	-	\approx 99.7%	\approx 0.3%	[Zha04a]
pH 13	-	\approx 70%	\approx 30%	[Zha04a]

Table 2.1: Fraction of surface coverage of the macroscopic silicon oxide/electrolyte interface for several selected pH values. At low solution pH, the surface is slightly positively charged, while it is negatively charged at high pH values. At the point-of-zero-surface-charge (PZSC) the surface is neither positively nor negatively charged, which appears to occur at a certain pH, depending on the nature of the silicon oxide and its surface treatment. At this pH, the surface is completely covered by hydroxy groups.

Dissolution of silicon oxide in alkaline solution

The chemical dissolution of silicon oxide in alkaline solution is closely related with its surface termination at high pH values. According to J. Hooley [Hoo61], the dissolution process consists of two consecutive steps: water adsorption at the surface and a reaction with hydroxide ions present in solution, which leads to the breaking of a Si-O bond and finally to the formation of a soluble product:



Depending on the concentration of hydroxide ions present in solution, either water adsorption or the hydroxide reaction is the rate determining step (RDS). At moderate hydroxide bulk concentration (approx. < 8 M for dissolved NaOH salt) the hydroxide reaction (2.5) appears to be the RDS [Hoo61]. Note that these reaction equations are just given for illustrating the dissolution process of one silicon atom. The assumed etching mechanism, i.e. the mechanism of breaking a single Si-O bond, is explained more in detail in the following:

In alkaline solution, the surface consists partly of negatively charged oxygen atoms as already mentioned above. These negative surface charges 'shield' the surface from the negatively charged hydroxide ions in solution and avoid a reaction between the hydroxide ion in solution and the first layer of silicon atoms carrying a positive partial charge. However, if water is used as the solvent, there exists a dipol-ion interaction between water molecules close to the surface and the negatively charged oxygen ions at the surface. This process is also referred as water adsorption. The close interaction between the hydrogen atom in the water molecule and the oxygen ion at the surface leads to a charge transfer. This suppresses the local electrostatic shielding of the surface and a hydroxide ion can react with the partially positively charged silicon atom. The reaction of the silicon atom with the hydroxide ion finally leads to a breaking of the bond to one of its adjacent oxygen atoms. A scheme of this mechanism is shown in Figure 2.5.

The repetition of these two consecutive steps finally forms a soluble silicon species and leads to the dissolution of silicon oxide in alkaline solutions. If the hydroxide reaction (2.5) is the RDS, increasing the concentration of hydroxide species in the bulk would also increase the etching rate, although the surface becomes more negatively charged.

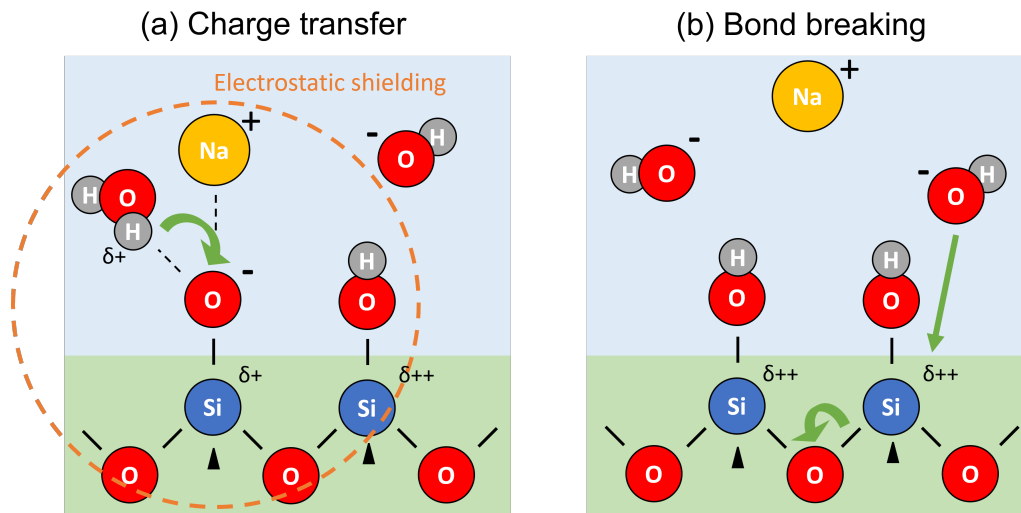


Figure 2.5: Illustration of the assumed etching mechanism of silicon oxide in alkaline media. The mechanism consists of two consecutive steps: (a) The charge/proton transfer between a water molecule in the first solvation layer and a negatively charged oxygen atom on the surface, and (b) the breaking of a Si-O bond due to the interaction of a polarized silicon atom with an hydroxide species in solution.

Consequently, the dissolution of silicon oxide comes from a strong interaction between the negatively charged hydroxide ion in solution and the silicon atom in the first layer of the oxide, carrying a large positive partial charge. The positive partial charge of the silicon atom stems from the huge difference in electronegativity between oxygen ($\chi_{\text{O}} \approx 3.4$) and silicon ($\chi_{\text{Si}} \approx 1.9$) and the stoichiometric composition of ideal silicon oxide (SiO_2). As a consequence the silicon atom is highly polarized in this configuration.

Parameters affecting the silicon oxide etching rate in alkaline medium

The actual macroscopic dissolution/etching rate of a silicon oxide surface in alkaline solution depends on a variety of parameters. A selection of relevant parameters is presented here. First, the actual nature of the silicon oxide influences the etching rate, cf. the comparison of etching rates of several types of silicon oxide in Table 2.2. The etching rate of the crystalline phase (quartz) is smaller compared to the one of the amorphous phase (fused silica), due to its different structure on the atomic level and its higher density [BP61]. In addition, the defect density of a non-pure silicon oxide composition influences its etching rate: Thermal silicon oxide is more stable against corrosion than silicon oxide produced by physical vapor deposition [Zha04b](p. 146) or anodic silicon oxide [Zha04b](p. 164). When not just considering 'pure' silicon oxide compounds, but different types of glass, which contain various additives beside of silicon oxide, the etching rate further varies. For example borosilicate glass ($\approx 80\% \text{SiO}_2$, 12-13% B_2O_3) is comparably stable against chemical corrosion in alkaline medium at moderate environmental conditions [SCH20].

In addition to properties of the silicon oxide composition, other system parameters affect the etching rate, of which the most important ones are: The cationic species present in the electrolyte [Hoo61][Zha04b](p. 144), the pH value of the electrolyte (which is proportional to the concentration of hydroxide ions present in the electrolyte) and the system temperature. The latter has a significant impact on the actual dissolution rate [SCH20]. To get an impression for the dependence of glass dissolution on these 'environmental' parameters,

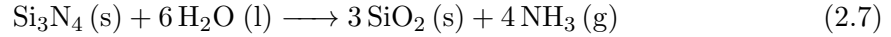
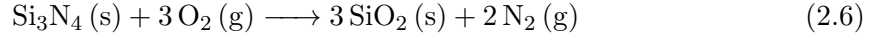
the etching rate of commercially available borosilicate glass is given as a function of the pH value and the temperature in the appendix A.1.

Material	Etchant	Conditions	Etching rate [nm/s]	Source
Quartz (particulate)	0.1 M NaOH	23 °C	$1.5 \cdot 10^{-5}$	[Zha04b], Ref. 444
Thermal SiO ₂	40wt% KOH	85 °C	$2 \cdot 10^{-2}$	[Zha04b], Ref. 918
	2 M KOH	room temp.	$2 \cdot 10^{-4}$	[Zha04b], Ref. 378
	1 M KOH	room temp.	$1.3 \cdot 10^{-4}$	this work
Anodic SiO ₂	2 M KOH	room temp.	$1 \cdot 10^{-3}$	[Zha04b], Ref. 378
Soda-lime glass	30wt% KOH	70 °C	$1.7 \cdot 10^{-2}$	[Sak+13]
Borosilicate glass ¹	1 M NaOH	45 °C	$2.7 \cdot 10^{-3}$	[SCH20], self-calculated

Table 2.2: Comparison of etching rates of various types of silicon oxides and glasses in alkaline media. ¹Commercial SCHOTT DURAN®.

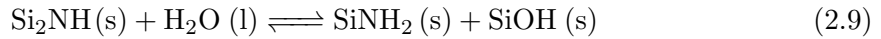
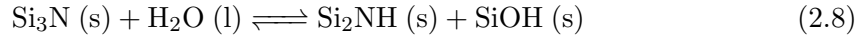
Silicon Nitride

It is well known that the etching rate of silicon nitride is orders of magnitude smaller in alkaline solution compared to silicon oxide, which makes silicon nitride an interesting material to utilize as the protection layer of silicon-based electrodes. However, when the silicon nitride surface is exposed to air or water, it is oxidized. The oxidation of (bulk) silicon nitride with oxygen present in air or with water is given by the following stoichiometric reaction equations:

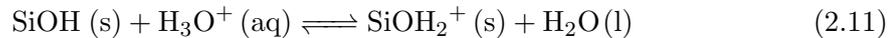
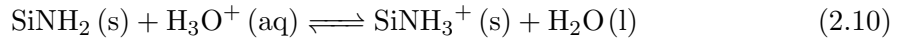


These reaction are thermodynamically favored. However, the kinetics of the reactions at room temperature appears to be very slow, which leads to the formation of only a thin layer (thickness < 2 nm) of oxidized nitride at the surface in finite time [Rai+76]. Furthermore, the composition of the emerging film is rather determined by silicon oxynitride in various stoichiometric composition, than by pure oxide [Rai+76].

When bringing a pure silicon nitride film in contact with water, its surface undergoes chemical reaction with water according to:



Since both reactions appear to be quite fast [Lai87], the emerging nitride/water interface accumulates SiNH₂ and SiOH sites [MB96]. Similar to the situation of the oxide/electrolyte interface, these surface species can also be protonated/deprotonated, depending on the actual pH value of the covering solution [MB96]:



It appears to be the case that silicon oxide as well as silicon nitride have similar surface compositions and chemical properties (i.e. proton ad-/desorption) when they are exposed to the same electrolyte, with silicon nitride being more resistant against bulk corrosion.

2.2 Electrochemical equilibrium

2.2.1 Electrochemical double layer

When an electrode is brought in contact with an electrolyte, the alignment of the electrochemical potentials of the transferable species in the two phases (e.g. electrons) results in a potential drop across and an accumulation of charged species at the interface. This charge separation across the interface is known as the electrochemical double layer (DL). If a metal is used as the electrode material, the charge present on the electrode side is located rather close to the actual interface. The distribution of the counter charge present on the electrolyte side is depending on the chemical properties of the electrolyte and the electrode surface. Specifically adsorbed ions on the metal surface form the inner Helmholtz plane (IHP). The outer Helmholtz plane (OHP) is formed by solvated ions, which are in close contact with the metal surface. In the Helmholtz planes, the electrostatic interaction of the ions with the charged electrode surface is the dominating contribution. The electrostatic potential can be assumed to drop almost linearly in this region [BF01]. Further away from the interface, the contribution of the thermal motion of the ions cannot longer be neglected. Thus, the ions present here form the diffuse or Gouy-Chapman (GC) layer. This layer can range from the OHP into the bulk of the solution. Its thickness depends on the ionic strength of the solution. For concentrations greater than 10 mM its thickness is less than 10 nm [BF01]. The spatial structure of the double layer and the potential distribution is shown in Figure 2.6.

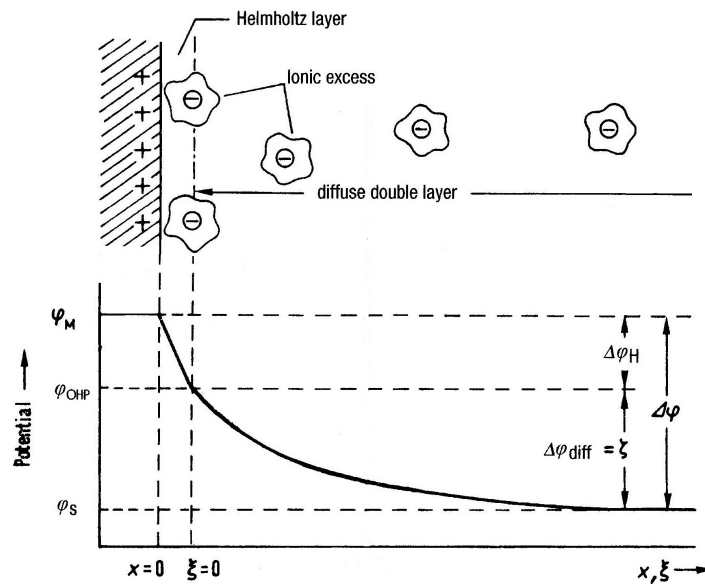


Figure 2.6: Illustration of the structure (top) and the potential distribution (bottom) in the electrochemical double layer. The total potential dropping at the electrochemical interface is labeled $\Delta\varphi$. Adapted with modifications from [HHV07], p. 119.

The capacitive behavior of the electrochemical double layer C_{DL} can be modeled by a series connection of the capacities of the individual capacitances:

$$\frac{1}{C_{DL}} = \frac{1}{C_H} + \frac{1}{C_{GC}} \quad (2.12)$$

where C_H is the capacitance of Helmholtz layer and C_{GC} is the capacitance of the diffuse/Gouy-Chapman layer. At large ion concentrations and at potentials sufficiently away from the point-of-zero-charge (PZC), the capacitance of the double layer can be approximated by the capacitance of the Helmholtz layer. The Helmholtz capacitance can be well modeled by a typical parallel plate capacitor [BF01]:

$$c_d = \frac{\partial \sigma^M}{\partial \phi} = \frac{\varepsilon_r \varepsilon_0}{d} \quad (2.13)$$

Here, c_d is the differential capacitance of the interface (change of the surface charge density σ^M with the electrode potential ϕ), d is the distance of the separated charges in the capacitor, ε_r is the relative permittivity of the medium (in the Helmholtz layer) and ε_0 is the dielectric constant.

2.2.2 Nernst equation

Let us consider an electrochemical reaction, such as the hydrogen oxidation/reduction reaction



which is supposed to be in equilibrium at an electrochemical interface. In equilibrium, the electrode potential E (half-cell potential) is given by the Nernst equation:

$$E = E_{\text{H}_2/\text{H}^+}^0 + \frac{RT}{2F} \ln \frac{a_{\text{H}^+}^2}{a_{\text{H}_2}} \quad (2.15)$$

where $E_{\text{H}_2/\text{H}^+}^0$ is the standard electrode potential of this reaction and a_{H^+} and a_{H_2} are the activities of the oxidized and reduced species, respectively, $F \approx 96\,485 \text{ C mol}^{-1}$ is the Faraday constant, $R \approx 8.3145 \text{ J mol}^{-1} \text{ K}^{-1}$ is the gas constant, and T is the temperature. According to the common convention in electrochemistry, the standard electrode potential of the hydrogen reaction is set to zero: $E_{\text{H}_2/\text{H}^+}^0 = 0 \text{ V}$ and defines the reference scale of the standard hydrogen electrode (SHE). The electrode potential given by the Nernst equation, at which the electrochemical reaction is in equilibrium, is often referred to as the equilibrium potential E_{eq} . In the case of the hydrogen reaction the Nernst equation can be expressed in terms of the pH value, which is defined as:

$$\text{pH} = -\log_{10} a_{\text{H}^+}, \quad (2.16)$$

and becomes:

$$E_{\text{eq}} = E_{\text{H}_2/\text{H}^+}^0 - \underbrace{\frac{2.303RT}{F}}_{\approx 59 \text{ mV}} \text{pH} - \frac{RT}{2F} \ln a_{\text{H}_2} \quad (2.17)$$

The factor ahead the pH value is approximately 59 mV at $T = 25^\circ \text{C}$. The equilibrium potential of the hydrogen reaction consequently scales by this factor with the pH value of the electrolyte. In addition, a practical assumption is $a_{\text{H}_2} = 1$, since the pressure of hydrogen gas in solution is usually 1 atm.

2.3 Reaction kinetics

According to the standard model of outer-sphere single electron transfer reactions derived by R. Marcus [Mar56], the reaction rate depends exponentially on the activation barrier. This dependence is also known as the Arrhenius law. By changing the electrode potential, the energetic difference of the states as well as the respective barrier height of the forward and reverse reaction are altered. The resulting correlation between the reaction rate and the applied electrode potential is given by the famous Butler-Volmer equation:

$$j(\eta) = j_a + j_c \quad (2.18)$$

$$= j_0 \left[e^{\beta F\eta/RT} - e^{-(1-\beta)F\eta/RT} \right] \quad (2.19)$$

Here, j is the (net) current density, j_a/j_c is the current density in anodic/cathodic direction, respectively, $j_0 > 0$ is the exchange current density, β is the symmetry coefficient of the reaction, and η is the overpotential. The overpotential is defined as the difference between the actual electrode potential E and the equilibrium potential of the respective reaction E_{eq} :

$$\eta = E - E_{\text{eq}} \quad (2.20)$$

In case of the hydrogen reaction, the equilibrium potential is given by equation (2.17).

2.3.1 Multistep reactions

The Butler-Volmer equation describing the kinetics of a multistep reaction is given by [KS08]:

$$j(\eta) = j_0 \left[e^{\alpha_a F\eta/RT} - e^{-\alpha_c F\eta/RT} \right] \quad (2.21)$$

Here, α_a is the anodic transfer coefficient and α_c the cathodic transfer coefficient. It appears that this equation has a very similar form as the one for a single electron transfer.

Exchange current density

Within the sequence of multiple steps there is often one step which proceeds much slower than the others. This step is known as the rate determining step (RDS) and determines the kinetics of the total reaction [KS08]:

$$j_0 \propto k_{0,\text{RDS}} \quad (2.22)$$

Here, $k_{0,\text{RDS}}$ is the standard rate constant of the RDS. The exchange current density in multistep reactions depends on multiple parameters, such as the equilibrium constants of the steps in equilibrium (virtually all other steps), the bulk concentrations of reduced and oxidized species, its transfer coefficient and the number of electrons transferred in the steps preceding the RDS [KS08]. An explicit formulation of the exchange current density based on the mentioned parameters is not given at this point, it can be derived by the quasi-equilibrium method and found, for example, in [BGR02].

Tafel analysis

In order to investigate the kinetics and the identity of the RDS, one can conduct a Tafel analysis. For potentials sufficiently far away from the equilibrium potential, here exemplarily given for negative overpotentials, the Butler-Volmer equation can be written as:

$$j(\eta) \approx j_c(\eta) = -j_0 \exp\left(-\frac{\alpha_c F}{RT} \eta\right) \quad \text{with } \eta < 0 \quad (2.23)$$

After applying the logarithm one gets the famous Tafel equation:

$$\log_{10}(|j_c|) = \log_{10}(j_0) - \frac{\alpha_c F}{2.303RT} \eta \quad (2.24)$$

Consequently, the analysis of the linear potential dependence of the logarithmized current density yields information about the kinetics and the identity of the RDS. The actual exchange current density can be determined from the intercept of the linear fit with the y -axis (at zero overpotential), while the slope of the fitting gives information about the transfer coefficient, i.e. the mechanism (see below). The inverted slope is often referred as the Tafel slope TS (with units of mV dec^{-1}) and is defined as follows:

$$\frac{\partial \log_{10}(|j_c|)}{\partial E} = -\frac{\alpha_c F}{2.303RT} \approx -\alpha_c \cdot 17 \text{ V}^{-1} \quad (\text{at } T = 20^\circ\text{C}) \quad (2.25)$$

$$TS = \left(\frac{\partial \log_{10}(|j_c|)}{\partial E}\right)^{-1} \approx -\frac{60 \text{ mV dec}^{-1}}{\alpha_c} \quad (\text{at } T = 20^\circ\text{C}) \quad (2.26)$$

Transfer coefficients

According to IUPAC recommendation [Gui+14], the transfer coefficients α_c and α_a are defined as:

$$\alpha_c = -\frac{RT}{F} \frac{d \ln(|j_c|)}{dE}; \quad \alpha_a = \frac{RT}{F} \frac{d \ln(j_a)}{dE} \quad (2.27)$$

This formulation is similar to the definition given above. For a multistep reaction, in which there is one rate determining step, which is at least 100 times slower than all the other steps, which is similar in the forward and the backward direction of the reaction, and which occurs just once in the sequence of steps, the sum of the anodic and cathodic transfer coefficient can be written as the total number of transferred electrons n :

$$\alpha_c + \alpha_a = n \quad (2.28)$$

In addition, the total number of electrons transferred is given by the sum

$$n = n_f + n_r + n_b \quad (2.29)$$

Here, n_f is the number of electrons transferred before the RDS (in cathodic direction), n_b is the number of electrons transferred after the RDS (in cathodic direction) and n_r is the number of electrons transferred during the RDS. n_r depends on the nature of the RDS. If this step is a chemical step, i.e. without electron transfer, its value is zero. If the RDS is an electrochemical step, it is very likely of being unity, as the simultaneous transfer of more than one electron is highly unlikely [Gui+14]. The individual transfer coefficients of the cathodic and the anodic reaction are then given by:

$$\alpha_c = n_f + n_r \beta \quad (2.30)$$

$$\alpha_a = n_b + n_r (1 - \beta) \quad (2.31)$$

Here, β is the symmetry factor of the electrochemical RDS, which often has values around 0.5. A derivation of the equation for the cathodic transfer coefficient based on the quasi-equilibrium method can be found, for example, in [BGR02].

If the RDS is of electrochemical nature, but occurs multiple times in the reaction as written (exemplary for the Hydrogen Evolution Reaction with the Volmer(RDS)-Tafel mechanism), the equations need to be slightly modified:

$$\alpha_c + \alpha_a = \frac{n}{\nu} \quad (2.32)$$

Here ν the number of times the RDS occurs in the reaction. The total number of electrons transferred during the reaction is then:

$$n = n_f + \nu n_r + n_b \quad (2.33)$$

The individual transfer coefficients are then given by:

$$\alpha_c = \frac{n_f}{\nu} + n_r \beta \quad (2.34)$$

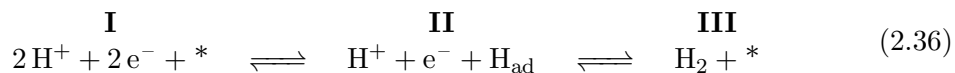
$$\alpha_a = \frac{n_b}{\nu} + n_r(1 - \beta) \quad (2.35)$$

Again, n_r is very likely being unity. In the appendix, one can find an overview of the calculated, predicted transfer coefficients for various reaction pathways of HER and HOR (cf. appendix A.2).

2.3.2 Tafel slope change in multistep reactions

The determination of RDS kinetics and the mechanism via the Tafel analysis necessitates a potential scan experiment. However, when changing the electrode potential, one also modifies the energetic landscape of the reaction. The variation of the landscape itself may change the RDS and the occurring mechanism. The following considerations are based on the work of Exner et al. [ESO18; Exn19]:

We consider a two electron transfer reaction, here exemplary the Hydrogen Evolution Reaction (HER). The initial and the final states are the product and the educt state, respectively. However, there is a (metastable) state in between, in which already one electron has been transferred (see also the HER mechanism in section 2.4.1). For HER this can be written as:



Here $*$ symbolizes a free adsorption site on the electrode surface. This sequence of states (I-III) and transitions is denoted as the 'catalytic cycle' of the reaction, since the final state is the initial state of a new reaction sequence. An exemplary energetic landscape of this cycle is shown in Figure 2.7(a). At the equilibrium potential ($\eta = 0$) the whole reaction is in equilibrium, i.e. the educt state I and the product state III are at the same energetic level. The step i exhibiting the highest energetic barrier G_i^\ddagger is the RDS.

If the electrode is polarized negatively $\eta < 0$, the energetic landscape changes, cf. Figure 2.7(b). The energetic level of electrons present in the electrode is lifted, which shifts the energetic level of states I and II with respect to state III according to the stoichiometric

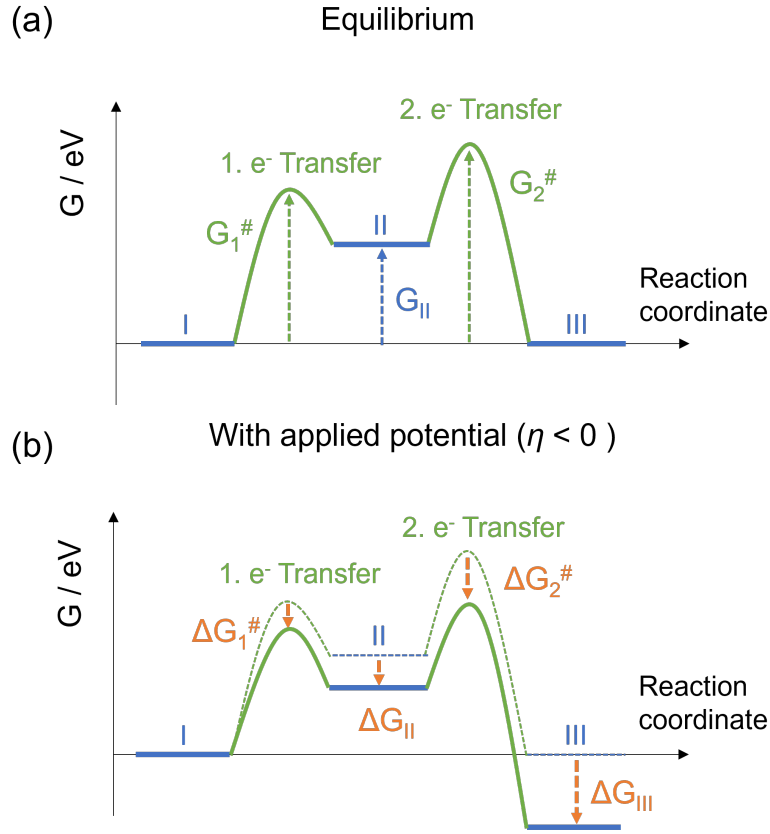


Figure 2.7: Exemplary energetic landscape of a two-electron-transfer reaction, such as HER given by reaction (2.36), (a) at equilibrium potential and (b) with an applied cathodic overpotential ($\eta < 0$). In equilibrium, the states I and III are at the same energetic level. The energetic levels of the states G_j as well as the barrier heights of the transition states $G_i^\#$ change when applying an overpotential.

number of electrons present in the respective state. This lifting is similar to a decrease of the energetic level of states II and III with respect to state I by:

$$\Delta G_{II} = e\eta, \quad \Delta G_{III} = 2e\eta \quad (2.37)$$

The energetic barriers of the transitions are also changed by applying a potential according to:

$$\Delta G_1^\# = e\beta_1\eta, \quad \Delta G_2^\# = e(1 + \beta_2)\eta \quad (2.38)$$

Here, β_i is the symmetry coefficient of the respective electrochemical reaction. Consequently, the application of an overpotential changes the energetic landscape of a multi-step reaction. Furthermore, the energetic levels of the transition states (energetic barriers) and the states scale differently with the applied potential, which may further lead to a non-linear change of the system.

As the determination of RDS kinetics and the mechanism via the Tafel analysis necessitates a potential scan, one may see a change of the Tafel slope when performing the potential scan experiment. The two main reasons for a Tafel slope change during a potential scan experiment are illustrated in the following:

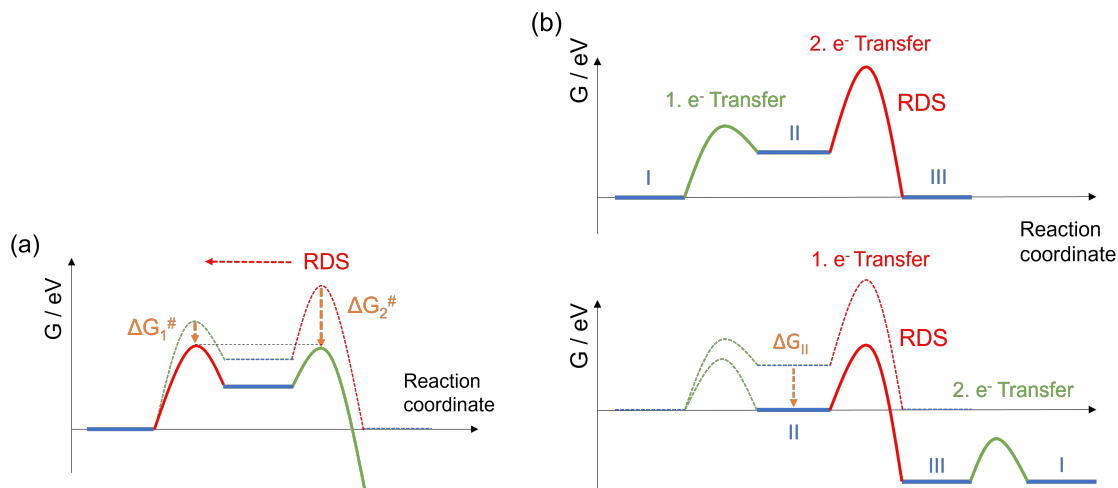


Figure 2.8: Change of an exemplary energetic-landscapes during a potential scan experiment. The dashed line depicts the situation for $\eta = 0$, the solid lines indicates the situation for a specific $\eta < 0$. (a) Change of the RDS in the catalytic cycle. During the scan, the barrier height of the second electron transfer becomes smaller than the barrier height of the first electron transfer. Thus, the first electron transfer becomes the RDS. (b) Change of the 'starting surface' in the catalytic cycle. State II becomes energetically lower than state I. Thus, state II becomes the new starting surface of the catalytic cycle, which necessitates a renumbering of the electron transfer steps.

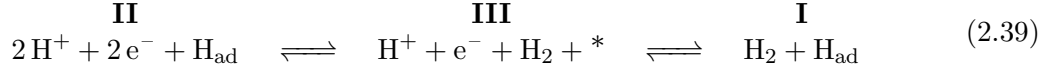
(a) Change of the RDS in the catalytic cycle

The symmetry coefficients of the individual electron transfer reactions are all in the same range of $0 < \beta_i < 1$. However, the absolute energetic shift increases with increasing number of electrons transferred. We consider the situation shown in Figure 2.7(a), i.e. the energetic barrier of the second electron transfer G_2^\ddagger is higher than the one of the first electron transfer G_1^\ddagger at $\eta = 0$. When applying a negative overpotential, the energetic barrier of the second electron transfer is decreased more than the one of the first electron transfer according to equation (2.38). Consequently, depending on the actual barrier height of the transition states, there may be a potential, at which the barrier height of the first electron transfer step becomes larger than the one of the second one (with respect to state I). This leads to a changing RDS of the catalytic cycle, which now appears to be the first electron transfer. This situation is illustrated in Figure 2.8(a). Considering a typical experimental situation: Below a certain negative overpotential, the determined Tafel-slope may change from a smaller to a larger value, i.e. the determined cathodic transfer coefficient α_c would decrease.

(b) Change of the 'starting surface' in the catalytic cycle

In addition, the energetic levels of the actual states change when applying a non-zero overpotential. Again, we consider the situation shown in Figure 2.7(a). At a certain overpotential, the energetic level of state II may be at the same energetic level as the starting state I. If the RDS is the step occurring after state II, there will be a change of the starting surface of the catalytic cycle. The starting surface of the new catalytic cycle is now state II. In the example of the HER, this would mean that the starting surface of the catalytic cycle is now not the 'blank' electrode surface anymore, but the surface covered by adsorbed hydrogen atoms. This means the catalytic cycle, previously given by

equation (2.36), now changes to:

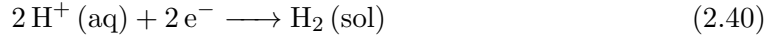


The change of the starting surface necessitates a renumbering of the electron transfers. The former second electron transfer now becomes the first electron transfer, and the former first one becomes the second one. This situation is illustrated in Figure 2.8(b). The appearance of this effect in a typical experimental situation is similar to the case presented above: Although the actual RDS mechanism stays the same, the Tafel-slope changes from a smaller to a larger value (i.e. the determined cathodic transfer coefficient α_c decreases) during an experimentally conducted potential scan.

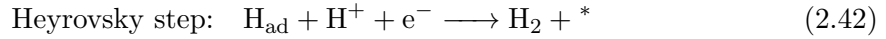
2.4 Electrocatalysis of the Hydrogen Evolution Reaction

2.4.1 Mechanisms of the Hydrogen Evolution Reaction

The Hydrogen Evolution Reaction (HER) is a two-electron transfer process. The reaction is given by



in acidic media. It is widely accepted in literature that HER can occur via three elemental steps, namely the Volmer, Heyrovsky and Tafel step. In acidic medium, HER occurs via the reduction of protons. Thus, the elementary steps are given by:



Here $*$ indicates a free adsorption site on the electrode surface. According to Kahyarian et al. [KBN17], considering poly-crystalline Au as the electrode material, the reaction network in acidic media needs to be complemented by an additional surface diffusion step of absorbed hydrogen. The resulting reaction network is shown in the appendix A.3.

In alkaline media the concentration of protons is negligible and, thus, HER can only occur via the reduction of water:



The elementary steps are now given by:



2.4.2 Hydrogen adsorption kinetics

Let us consider the adsorption reaction of a hydrogen atom given in equation (2.41), i.e. the Volmer step. If the hydrogen adsorption reaction is the RDS of the hydrogen evolution reaction, the kinetics of this step dictates the kinetics of the whole reaction.

It is experimentally observed that different metal species show very different kinetics for hydrogen evolution, although hydrogen adsorption is supposed to be the RDS in all cases. A good overview is given by S. Trasatti [Tra72]. According to the theoretical work by Nørskov et al. [HN95], Schmickler et al. [Qua+14; San+09] and others based on Density Functional Theory and quantum statistics, there are two main aspects determining the catalytic activity of a metal system for hydrogen adsorption:

1. The Free Energy of adsorption ΔG_{ad} should be close to zero at equilibrium potential (which is tantamount to the famous Sabatier's principle).
2. The metal d-band should comprise the Fermi level and there should be a strong and long-ranged interaction between the metal d-band and the hydrogen 1s-orbital.

As these aspects influence the activation energy of hydrogen adsorption and, hence, the kinetics, a difference in these aspects is supposed to be the reason for the experimentally observed significant difference in activity of different metal species regarding HER. Thus, the aspects are further explained in the following.

Free energy of adsorption

One of the main contributions of the hydrogen adsorption to the reaction kinetics is the energetic difference of the related states. Nørskov et al. [Nør+05] calculated the hydrogen adsorption (chemisorption) energy ΔE_{Had} from DFT according to:

$$\Delta E_{\text{Had}} = E(\text{surf} + \text{H}) - E(\text{surf}) - \frac{1}{2}E(\text{H}_2) \quad (2.48)$$

Here $E(\text{surf})$ is the energy of the pure surface, $E(\text{surf} + \text{H})$ is the energy of the system with the adsorbed hydrogen atom on the surface, and $E(\text{H}_2)$ is the energy of the hydrogen molecule. It needs to be mentioned that the actual chemisorption energy can depend strongly on other parameters, such as the surface configuration of the metal, i.e. the crystal surface plane or the distribution of adsorption sites [FK89], co-adsorbed species [Bir98], etc. The values shown here have been calculated by Nørskov et al. for the (111) plane and for a coverage of 0.25 monolayers of hydrogen for all metals considered.

According to their calculations, the adsorption energy can be further related to the Free Energy of adsorption ΔG_{Had} . At standard conditions, the correlation is given by:

$$\Delta G_{\text{Had}} = \Delta E_{\text{Had}} + 0.24 \text{ eV} \quad (2.49)$$

The calculated values of ΔG_{Had} for selected metals, which are important within the scope of this thesis, are shown in Table 2.3.

Metal	Pt	Ir	Cu	Au	Ag
$\Delta G_{\text{Had}} / \text{eV}$	-0.09	0.03	0.19	0.45	0.51

Table 2.3: Free Energy of adsorption of a hydrogen atom on different metal surfaces. The values were calculated from DFT for the (111) plane for a coverage of 0.25 ML. The values are taken from Nørskov et al. [Nør+05].

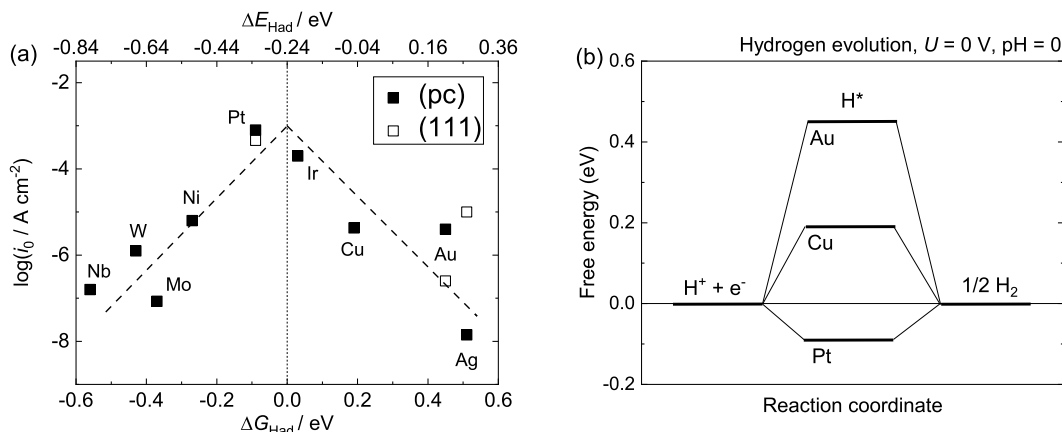


Figure 2.9: (a) Experimentally measured exchange current densities for HER at different metal surfaces plotted as a function of the calculated Free Energy of hydrogen adsorption per atom. Single crystal data ((111) surface) are indicated by open symbols, poly-crystalline data (pc) are indicated by filled symbols. (b) Free Energy diagram for hydrogen evolution on selected metals at equilibrium ($U = 0$ V) according to data given in Table 2.3. Both Figures are replotted from Nørskov et al. [Nør+05].

Nørskov et al. furthermore plotted the available experimental data of exchange current densities of the HER on the different metals versus the calculated Free Energy of adsorption and noticed the famous volcano-like behavior. This plot is shown in Figure 2.9(a). It needs to be mentioned that many of the metals in the ascending branch of the volcano plot are covered with an oxide film during hydrogen evolution, which usually reduces its activity by several orders of magnitude [Qua+14]. However, the plot clearly shows that the Free Energy of adsorption is one of the main descriptors for the kinetics of hydrogen evolution, if hydrogen adsorption is the RDS.

Figure 2.9(b) shows the Free Energy diagram for hydrogen evolution when the reaction is at equilibrium ($U = 0$ V at $\text{pH} = 0$) exemplary for Au, Cu, and Pt. It is visible that the energy difference between the initial state and the adsorbed state H^* is positive for Au and Cu, but negative for Pt. Consequently, the adsorbed state is the preferred state in equilibrium for Pt, while it is on a higher energetic level for Au or Cu. Consequently, Pt shows a much higher exchange current density for hydrogen evolution than Au.

Although the model explains the overall trend quite well, it is not sufficient to explain the experimentally observed difference of the 'coinage metals' (Cu, Au, Ag), i.e. why the exchange current density of Cu is similar to the one of Au, although the hydrogen adsorption energy is much closer to the optimum. In order to understand this, we need to consider the interaction of the metal bands and the hydrogen atom.

Metal d-band interaction

The electronic interaction of the hydrogen atom with the metal surface can be split into two contributions: A contribution stemming from the interaction with the energetically broad metal sp-band and a contribution from the narrow metal d-band. The interaction of the d-band with the adsorbate is a very crucial parameter and determines largely the experimentally observed different catalytic properties of the various metals we consider in this work: Pt, Cu, Au, Ag.

First, the H1s orbital interacts with the metal sp band, which results in a filled bonding state and an empty antibonding state [HN95]. This interaction is quite similar for all the metals considered here [HN95; San+09].

In addition, the hydrogen states interact with the metal d-band, which leads to an additional splitting and an emerging antibonding state lying energetically above the metal d-band. Figure 2.10(a) shows the density of states (DOS) of several selected metals as a function of energy. Note that the zero energy is set to the Fermi level. For 'd-metals' such as Pt, the d-band spreads over the Fermi level. The emerging antibonding state caused by the interaction with the d-band lies above the Fermi level and is, consequently, not filled. This gives rise to an additional attraction in addition to the attractive contribution coming from the coupling to the metal sp-band. For 'coinage metals' such as Cu, Ag, and Au the d-band ends quite below the Fermi level. The emerging antibonding state is also below the Fermi level and both, the bonding and antibonding part of the hydrogen DOS are filled. As a result the coupling to the metal d-band leads to a repulsive contribution and the attractive character of the bonding is only determined by the interaction with the sp-band. [HN95]

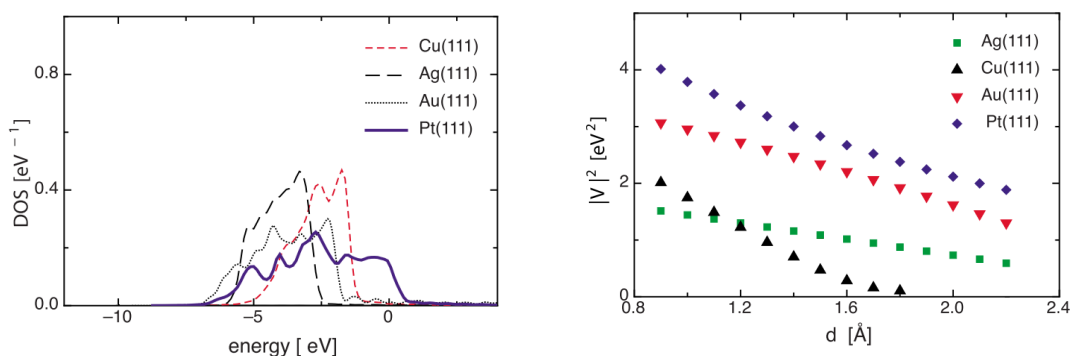


Figure 2.10: (a) Density of states (DOS) of several metal d-bands as a function of the energy. Zero energy is set to the Fermi level. (b) Interaction strength (coupling constant $|V|^2$) of the d-bands of the metals with the H1s orbital as a function of the distance d of the hydrogen atom. Both images are taken from Santos et al. [San+09]

This repulsive contribution is roughly proportional to the coupling strength between the d-band and the H1s orbital, which is denoted as the coupling constant $|V|^2$ by Santos et al. [San+09]. From their model the authors calculated the coupling constant quantitatively as a function of the distance of the hydrogen atom from the surface. Figure 2.10(b) shows the dependence of the coupling constant $|V|^2$ for several metals on the distance. Since the electron transfer occurs at a certain distance in the order of 1.5 \AA away from the electrode surface, a long ranged interaction is also an important parameter for an efficient catalyst. It is visible in the Figure that the coupling strength of Pt(111) and Au(111) are quite comparable, while the coupling strength of Cu(111) decreases much more steeply with the distance. However, since for coinage metals Cu, Ag and Au the coupling between the d-band and the H1s orbital implicates a repulsive contribution, a stronger coupling leads to a weaker bonding. This result is in accordance with Hammer et al. [HN95], who also postulated an increasing repulsive contribution down the periodic table.

Further influences on adsorption kinetics

Besides the aspects already mentioned above, several other effects may influence the adsorption kinetics. These factors do not apply exclusively for the hydrogen adsorption and may also be present in other adsorption reactions. For the sake of completeness the two most important aspects are shortly introduced in the following:

Solvent reorganization (according to the Marcus model). The adsorption of a hydrogen atom is related to a charge transfer and leads to a change of the local charge density close to the electrode surface. As a consequence, the solvent needs to reorganize. This effect is neither specific for hydrogen adsorption, nor depending on the metal species. It is also present for outer-sphere reactions.

Change of the adsorption energy by local electric fields. The energy E of a system in presence of an externally applied electric field F can be expanded as a Taylor series [Che+18]

$$E(F) = E_0 + \left(\frac{\partial E}{\partial \vec{F}} \right)_{F=0} \cdot \vec{F} + \frac{1}{2} \left(\frac{\partial^2 E}{\partial \vec{F}^2} \right)_{F=0} \vec{F}^2 \quad (2.50)$$

where E_0 is the energy of the system in the absence of an electric field \vec{F} . The partial derivatives are evaluated at $F = 0 \text{ V \AA}^{-1}$. This formulation can be used to express the dependence of the adsorption energy of an adsorbate on a locally present electric field at an electrochemical interface:

$$E_{\text{ad}}(F) = E_{\text{ad},0} + \Delta\vec{\mu} \cdot \vec{F} + \frac{1}{2} \Delta\alpha \vec{F}^2 \quad (2.51)$$

where $E_{\text{ad},0}$ is the adsorption energy in the absence of the electric field (due to chemical bonding to the surface), and $\Delta\vec{\mu}$ (or $\Delta\alpha$) is the difference in dipole moment (or polarizability) between the metal surface with adsorbates and the corresponding noninteracting system, i.e. clean surface and gas-phase molecules [Che+18; Wae+19]. Although these values are intrinsic properties of the actual system and not trivially determined experimentally, the equation shows that the adsorption energy of an adsorbed state can be altered by the local electric field present at the interface.

In a typical electrochemical system, a local electric field is intrinsically present due to the double layer formation. This electric field can be controlled by the electrode potential and the properties of the electrolyte, such as cation species and concentration. For example it was shown by Chen et al. that the local electric field induced by the cation species present in front of the electrode can stabilize the adsorbed CO_2 molecule on Ag(111) and shifts the free energy landscape of the CO₂RR on weakly adsorbing metals [Che+16]. Consequently, when modifying the double layer properties, one may vary the local electrical field strength in front of the electrode surface (more precise: at the reaction plane), and, thus, the reaction rate.

Chapter 3

Experimental details

3.1 Fabrication and characterization of nanostructured electrodes

In this section, we first introduce the design and composition of the silicon-based electrodes patterned by an array of metal (catalyst) structures (section 3.1.1). Second, we introduce the technique Lift-Off Nanoimprint Lithography (LO-NIL) used for electrode fabrication (section 3.1.2). Finally, we close this section with a dry characterization of the nanostructured electrodes typically produced by LO-NIL (section 3.1.3).

3.1.1 Design and composition of the nanostructured electrodes

The centerpiece of the nanostructured electrodes investigated in this work is a Metal/Insulator/ Semiconductor (MIS) stack. We use silicon as the semiconductor material and substrate of the electrodes. Depending on the application of the future electrode, we use silicon wafers with either moderately p- or n-doping. The former doping is used for producing photoelectrodes, the latter for photo-inactive electrodes (the theoretical background of the electrical response of MIS junctions can be found in section 2.1.1). The thickness of the silicon substrate is approx. 500 μm . The insulator in the MIS stack is a silicon (plasma) oxide film that covers the silicon substrate. The silicon oxide layer is rather thin (1.6 - 1.8 nm) and allows for tunneling of the charge carriers between the substrate and the metal structures present on the front side. The back side of the substrate is covered by an aluminum (Al) layer. Electrically, this Si/Al interface exhibits an ohmic behavior and is referred to as 'back contact', as typically the electrical contacting of the samples is achieved from the back.

The metal nanostructures on the front side are composed of two different metals: The first layer, which is in contact with the silicon(-oxide) substrate, is made of titanium (Ti) with a typical thickness of 3 nm. This layer fulfills two functions: First, Ti is utilized as an adhesion promoter between the final metal structures and the substrate [Nag18]. Second, it is used to optimize the properties of the electrical contact of the MIS interface, cf. section 2.1.1. Above the titanium layer there is the catalytic active metal, which is either Au or Pt in this work. The typical thickness h_M of the catalyst layer is between 10 and 15 nm.

Most of the electrodes presented in this work further exhibit an additional insulating layer present beside the metal structures. This layer is made of either thermal silicon oxide or low-pressure-chemical-vapor-deposited (LPCVD) silicon nitride. It covers the non-metal-covered silicon surface, thus the metal structures are embedded in this additional layer. Typical thicknesses h_{In} of this insulating layer range from 10 to 15 nm. The first mentioned value is the standard thickness and applies for most of the structured electrodes discussed in this work, if not explicitly stated differently. This oxide- or nitride-based layer is also referred as 'passivation layer' throughout this work, as it 'passivates' the non-metal-covered silicon surface from chemical or electrochemical corrosion when the electrode surface is brought in contact with the electrolyte. This is of great importance in alkaline electrolytes, as silicon oxide of bad quality and silicon dissolve rather quickly in alkaline environment (see section 2.1.3). In addition, this thin layer is rather transparent for solar light, allowing for an efficient photon transmission into the silicon-based absorber when illuminating the sample from the front side. A scheme of the nanostructured electrode is shown in Figure 3.1.

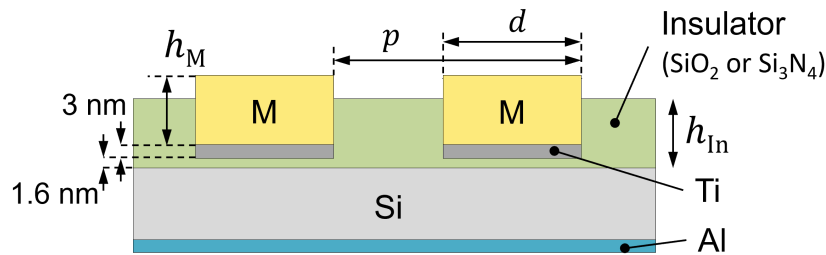


Figure 3.1: Scheme (side cut) of the typical nanostructured electrode investigated in this work. Metal structures composed of M/Ti (yellow/silver) are present on a silicon-based substrate (grey) surrounded by an insulator-based 'passivation' layer (green). Important geometric quantities, such as the pitch p of the array and the structures size d , are given in the scheme. Taken with modifications from Maier et al. [Mai+20]

The size, the shape and the geometric arrangement of the metal structures is determined during the fabrication process of the electrode (see below). The structures are arranged in a very regular array with a total structured area of $5 \times 5 \text{ mm}^2$. The size d of individual metal structures as well as the center-to-center distance between neighboring structures is determined by the stamp used during fabrication. Multiple metal structure sizes are compared within this work: 1400 nm, 350 nm, 200 nm, 75 nm. The shape of the structures is quadratic for the largest three sizes, and circular for the smallest size (75 nm). The term 'size' denotes either the side length for quadratic or the diameter for circular structures. The metal array is designed in a way that the pitch ratio d/p is quite similar for all structure sizes investigated. The pitch p is approx. double the structure size. As a consequence, all electrodes have a very similar filling factor between 20% and 25%. The filling factor gives the share of the gold covered area from the total area ('structured area'). An overview of important geometric parameters of the metal arrays is given in Table 3.1.

Size d / nm	Structure form	Pitch ratio d/p	Filling factor
1400	Squares	0.47	22 %
350	Squares	0.50	25 %
200	Squares	0.46	21 %
75	Circles	0.50	20 %

Table 3.1: Relevant geometric parameters of the metal arrays present on the structured electrodes investigated in this work. The size d labels the size of single structures in the array, the pitch p the center-to-center distance between individual structures.

3.1.2 Electrode fabrication: Lift-Off Nanoimprint Lithography

In this section, the fabrication technique of the metal nanostructure array on the electrode substrate is introduced. The nanostructuring is achieved by the method Lift-Off Nanoimprint Lithography (LO-NIL). This technique has several advantages over other lithographic techniques, such as scalability, cost efficiency, and flexibility, which makes it a good candidate for future large area patterning of commercial electrodes.

Scalability: The method combines advantages of several other lithographic techniques. The patterning of individual structures takes place at the same time (comparable to the full surface exposure done in optical lithography). Thus, the needed surface patterning time does not scale with the structuring area, which makes large-area patterning much less time consuming as patterning by e-beam lithography. In addition, the minimum resolution goes down to the deca-nanometer range. In our team we could reliably produce structures with a size of 45 nm (without passivation layer). In principle, even smaller sizes are possible. Thus, the resolution is higher than achievable by regular optical UV lithography, which is approx. the wavelength of the UV light used.

Cost efficient large scale patterning: The production of the master stamp is performed via e-beam lithography and the only time consuming, i.e. expensive, step in the process. This master stamp can be easily and rapidly replicated to produce a single-use working stamp. Consequently, one master is sufficient for many generations of working stamps and, consequently, of samples. A detailed description of the stamp fabrication technique and replication process goes beyond the scope of this thesis. It is explained very well by Nagel et al. [Nag18] or Golibrzuch et al. [Gol23].

Flexibility in geometry: The (lateral) size and shape of the final structures is determined by the stamp used. Thus, it is fixed for a given master stamp. However, we could vary the fabrication process to tune the feature size of either the stamp [Gol+22] or the imprint in the coating after the imprint process [Nag+17]. Thus, we can change simultaneously the size and the pitch ratio, which gives an additional geometric degree of freedom. However, the absolute pitch of the array remains the same.

Flexibility in materials: LO-NIL can be applied to variety of material-combinations for structured electrodes. It is possible to change: (1) the catalytic active material (Au, Pt, Cu in this work), (2) the substrate material (Si and GC in this work), and (3) the passivation layer material (silicon oxide and silicon nitride in this work). In addition, this method allows for various other combinations, such as the production of insulator structures on a catalytic active metal support (cf. section 6.1.2).

In the following, the fabrication process of the standard structured electrodes (Au structures on silicon-based substrate) is introduced shortly. A schematic overview over the process is given in Figure 3.2. The individual steps are explained below.

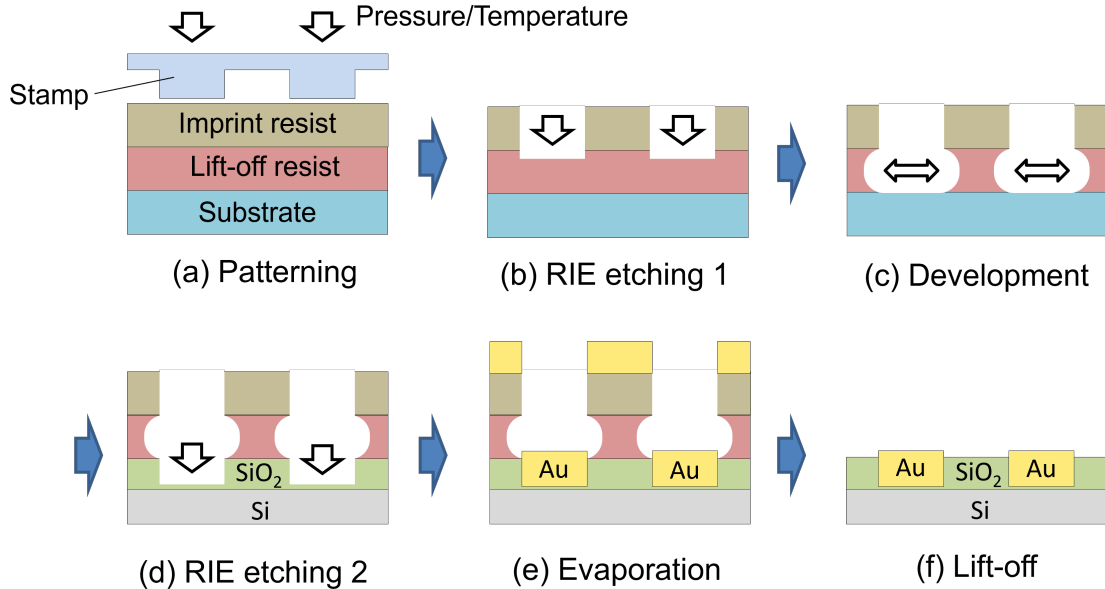


Figure 3.2: Scheme of the fabrication steps of the Lift-off Nanoimprint Lithography (LO-NIL) technique. An explanation of the different steps is given in the text. Adapted from Maier et al. [Mai+20]

Wafer dicing and back contact

For electrodes with silicon oxide as passivation layer, we use two different silicon wafer substrates, depending on the actual application of the respective electrodes: n-doped silicon (FZ:(111), 1-10 Ohm cm, Sil'tronix Silicon Technologies, France), or p-doped silicon (FZ:(111), 1-10 Ohm cm, Si-Mat Silicon Materials, Germany). The production of the silicon oxide passivation layer is done by thermal oxidation. Thus, we oxidize the wafers in an oven (ATV-SRO furnace) at 1000 °C in 100% O_2 atmosphere at ambient pressure for 10 minutes. Afterwards the resulting thermal silicon oxide layer is wet etched in a buffered oxide etch solution (BOE 98-2, 98 parts of 40% ammonium fluoride (NH_4F), 2 parts of 50% hydrofluoric acid (HF)) to the desired thickness, usually approx. 10 nm.

For electrodes with a silicon nitride passivation layer we use n-doped silicon wafers (FZ:(111), 1-10 Ohm cm, Si-Mat Silicon Materials, Germany), which come already covered by a 17 nm LPCVD (low pressure chemical vapor deposition) Si_3N_4 layer on both sides by the supplier. This layer is etched in a reactive ion etching step (RIE, PlasmaLab 80 Plus, Oxford Instruments) to the desired thickness, usually approx. 10 nm.

Next, the wafer is diced into pieces of the desired shape of $10 \times 10 \text{ mm}^2$ (substrates). Prior to this, the front surface is covered with a protective resist coating (AZ5214E, Microchemicals) to protect the surface from particles and dust during the dicing process.

Afterwards, the back contact is fabricated. Therefore, we clean the substrates with 7 minutes of ultrasonification in acetone and 7 minutes in isopropanol. Next, we spin coat a protective layer on the front side. The removal of the passivation layer on the back

side is done by either immersing the sample into a buffered-oxide-etchant (BOE) bath for several tens of seconds for silicon oxide covered samples, or RIE etching for silicon nitride covered samples down to the silicon material. Subsequently, we evaporate an Al layer onto the back side with a thickness of 150 nm. This layer works as the back contact of the electrode.

To assure an ohmic behavior at the back metal/silicon interface, we anneal the samples after evaporation. The annealing step is necessary to force diffusion of Al atoms into the silicon substrate, creating a highly doped n^{++} or p^{++} layer. This treatment establishes an ohmic contact between the silicon substrate and the back side metal. In order to do so, we remove the protective coating on the front side by 7 minutes sonification in acetone and 7 minutes in isopropanol. This step is necessary in order to prevent a deep burning of the coating on the front side during the subsequent annealing of the sample. We anneal the samples made of n-Si at 250 °C and of p-Si at 400 °C in vacuum (10^{-4} mbar) for 15 minutes.

Patterning

Next, we pattern the surface. This is done by a thermal imprint process. After cleaning the samples (7 minutes in acetone, 7 minutes in isopropanol in an ultrasonic bath) we coat the resists:

First, the Lift-off resist. After prebaking the substrates at 250 °C for 1 minute, a lift-off resist (LOR) (PMGI SF6:T-Thinner, vol.% dilution 1:2, microresist technology GmbH) layer is spincoated on the silicon oxide or silicon nitride covered surface. Afterwards, the sample is baked at 250 °C for 3 minutes to vaporize solvent residues. A typical thickness of the LOR is between 40 and 50 nm. This thickness turned out to be useful for the later process, as it needs to fulfill two opposing demands: First, it needs to be thin to ensure a complete exposure of the substrate surface during the later development step, see Figure 3.2(c), before a complete underetching of the later imprint resist happens. Second, it needs to be thick enough to prevent a linking of the evaporated metal on the substrate and on the imprint resist during the evaporation step (e), which would prevent the later lift-off step.

Onto the LOR, the imprint resist is coated. As imprint resist we use either undiluted mr-I 8020R (for 350 nm structure size) or mr-I 8020R:ma-T 1050 with a vol.% dilution of 1:1 (all other sizes). All resists are obtained from microrresist technology GmbH. After spin coating the samples need to be baked at 100 °C for 1 minute to vaporize solvent residues. Typical thickness of the undiluted imprint resist is 150 nm, the diluted imprint resist has a typical thickness of 70 nm. The different thicknesses are necessary, as the available stamps have a different structure protrusion height. The stamp with structures of 350 nm size has a protrusion height of 260 nm, while for all other sizes the structures have a protrusion height of 90-95 nm. The imprint resist thickness is chosen in a way that during the imprinting step the protrusions are completely filled by the resist, but the residual layer of imprint resist below the protruding structures is as thin as possible.

Next, the patterning is achieved in a thermal imprint process: We use a commercial NIL tool (obducat EITRE 3, Obducat), which presses the desired stamp onto the sample (imprint resist) at 165 °C and at a pressure of 30 bar for 180 seconds. After cooling of the samples to room temperature, the stamp is removed carefully by mechanical lifting.

First RIE etching and developing

Next, there is the need to remove of the imprint resist residual layer and partly etching into lift-off resist. This is done by a first RIE etching step. In this step we anisotropically etch the imprint resist. The RIE machine used is a PlasmaLab 80 Plus (Oxford Instruments). We use 27 sccm O₂ and 25 sccm C₄F₈ with plasma RF power of 200 W. The etching step is followed by a pure oxygen plasma (O-plasma) step for 5 seconds. The etching rates of this step are approx. $1.5 \pm 0.1 \text{ nm s}^{-1}$ for the imprint resist layer and $2.0 \pm 0.2 \text{ nm s}^{-1}$ for the LOR layer as determined by T. Angerer [Ang19].

Afterwards, we perform an isotropic wet etching of the exposed lift-off resist (developing step). This step uncovers the substrate surface below the holes in the imprint resist and leads to an artificial undercut below the imprint resist. The developer used is a buffered KOH-based solution (AZ400K, Microchemicals GmbH) diluted by DI-water in 1:5 vol.%. Typical etching times are between 17 s (75 nm structures) and 30 s (1400 nm structures).

Second RIE etching

In case the substrate consists of a passivating layer, which separates its surface from the (semi-)conducting bulk, an additional RIE etching step (second RIE etching step) is applied, see Figure 3.2(d). Here, the passivating layer is anisotropically etched down to the conductive substrate, which then can form an electrical contact with the later evaporated metal layers. Obviously, this step is not needed if the substrate itself is supposed to be covered by the nanostructures, which is the case for samples without passivation layer or for insulating structures on a conductive substrate, cf. sections 6.1.2.

Typical mixtures for dry silicon oxide etching consist of O₂ and CF-based gas [Roo84]. Here, 2 sccm O₂ and 18 sccm C₄F₈ at a plasma RF power of 150 W is applied for a sufficient time. It is followed by a 5 second O-plasma step. The oxygen plasma step is necessary to remove the silicon-fluorine compounds at the sidewalls of the passivation layer and to oxidize the exposed silicon surface (after etching through the thermal oxide) and forming a thin oxide layer below the later metal structures. The vertical etching rates of this step at the given parameters are approx. $0.7 \pm 0.2 \text{ nm s}^{-1}$ for silicon nitride [Ang21], $1.0 \pm 0.1 \text{ nm s}^{-1}$ for silicon oxide and $1.2 \pm 0.2 \text{ nm s}^{-1}$ for the imprint resist [Ang19]. This step is crucial in the process.

Evaporation and Lift-off

After the surface of silicon is exposed at the desired locations, the selected metals are evaporated into the holes. The first layer is a thin Ti layer, which works as an adhesion promoter between the silicon(oxide) and the second evaporated metal layer (the catalytic active materials). The evaporation is done via e-beam evaporation in a UHV physical vapor deposition system (Kurt J. Lesker Company Ltd.) at a high vacuum of 10^{-7} mbar. The evaporation rate is around 1.0 \AA s^{-1} for Ti and 2.0 \AA s^{-1} for the Au or Pt layer.

Finally, the resists are removed in a lift-off step. The lift-off is conducted in a commercial lift-off solution (mr-Rem700, microresist technology GmbH) in an ultrasonic bath for a few minutes. After cleaning with acetone and isopropanol for 7 minutes each in the ultrasonic bath, the nanostructuring process of the electrodes is finally finished.

3.1.3 Dry electrode characterization

After production, the electrodes are usually characterized by four main dry characterization techniques: Scanning Electron Microscopy, Atomic Force Microscopy, X-ray Photoelectron Spectroscopy and electrical profiling technique. In this section, the methods and instruments are introduced and the typical nanostructured electrodes fabricated are exemplarily characterized by the mentioned methods.

As the main focus of this work lies on the electrochemical properties of the fabricated electrodes, the dry characterization performed in this section is just outlined to get a first impression of the composition of the electrodes fabricated by LO-NIL. A detailed dry analysis of structured electrodes, especially regarding the influence of a variation of several process parameters on the reliability of the process and the defect densities in the later metal array, is given in the Master's thesis of T. Angerer [Ang21] or in the PhD thesis of M. Golibrzuch [Gol23].

Scanning Electron Microscopy

With Scanning Electron Microscopy (SEM) we determine the surface topography of the fabricated electrodes. The method works as follows: Electrons are accelerated in an electron gun. In this work, an accelerating voltage of 5 keV is used. Electrostatic and magnetic lenses and apertures are used to reduce the beam size to a small probe, which can raster across the sample surface. The local electron-matter interaction with the sample surface results in, amongst others, the emission of secondary electrons. The emission of secondary electrons is highly localized at the point of impact of the incident electron beam and quite surface specific due to their short mean free path length in matter. Thus, SEM is surface sensitive and a very localized technique, which allows for a lateral resolution (x - y plane) below 1 nm. In order to prevent scattering of electrons with gas molecules present in the chamber, a very high vacuum needs to be established in the chamber. Here, we work below 10^{-6} mbar. After detection of the emitted electrons in a suitable detector, a gray-scale image of the sample surface (map) can be obtained. Brighter pixels in the SEM image indicate a higher rate of ejected secondary electrons. [VG09]

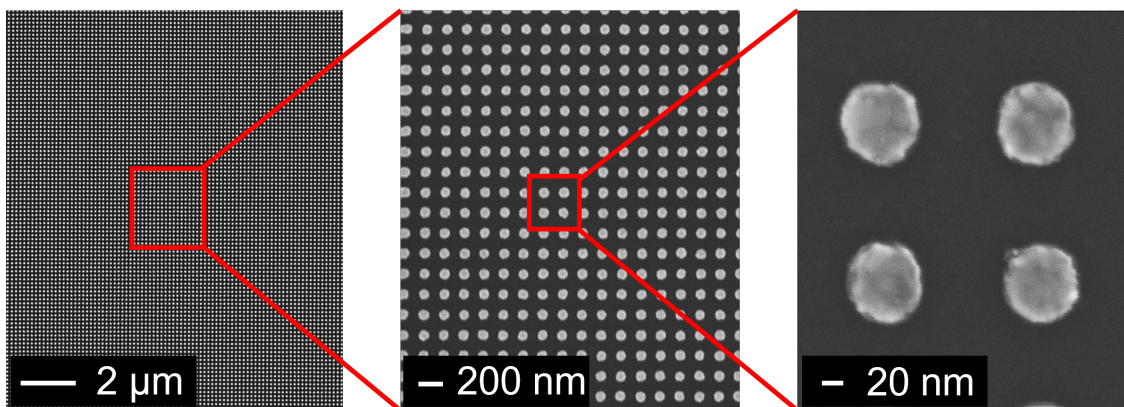


Figure 3.3: SEM images of an array of 75 nm sized gold structures on n-doped silicon in various magnifications. The images show that the fabrication method used can fabricate a very well organized array of structures on a large surface area.

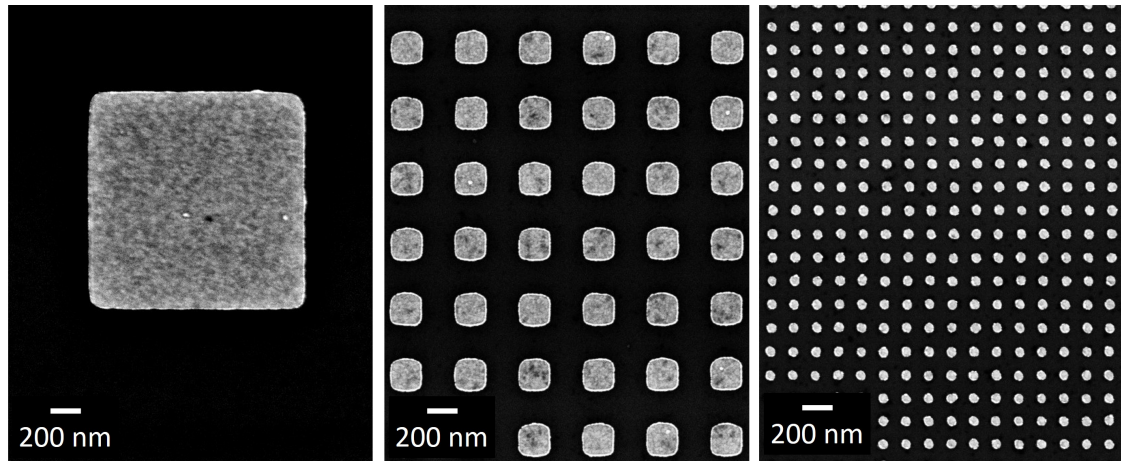


Figure 3.4: SEM images of gold structures on n-doped silicon substrate with structure sizes of 1400 nm (left), 200 nm (middle), and 75 nm (right) at the same magnification. The gold structures (bright area) are surrounded by thermal silicon oxide passivation layer (dark area). [Mai+20]

Typical SEM images of the electrodes fabricated are shown in Figures 3.3 and 3.4. Figure 3.3 shows SEM images of an electrode covered by 75 nm sized Au structures (smallest size investigated in this work) in various magnifications. The bright areas indicate Au, the dark areas the surrounding passivation layer (silicon oxide, SiO_x). From this image, it becomes clear that the fabrication method can produce a very well defined array of metal structures on the silicon surface. We further tried commercially available flat and polished glassy carbon (GC) plates (HTW GmbH, Germany) as a substrate material for the nanostructuring procedure. However, the comparatively high roughness of the GC material leads to a rather inhomogeneous metal array for the structure size investigated (75 nm). An SEM image of a metal nanostructure array fabricated on GC substrate by LO-NIL is shown in the appendix A.4.

Figure 3.4 shows SEM images of silicon-based electrodes with differently sized structures of sizes 1400 nm (left), 200 nm (middle), and 75 nm (right) with similar magnification. This image clearly demonstrates that the fabrication procedure mentioned above is able to produce well defined structures in all three size ranges. In addition, it demonstrates that the coverage is rather constant for all sizes and that the 'interfacial border area' between Au and SiO_x increases significantly with decreasing structure size. The importance of this property of the electrodes will become clear in chapter 5.1.

Atomic Force Microscopy

Atomic Force Microscopy (AFM) can image the surface topography of a sample with nanometer precision. A sharp tip with dimensions of a few nanometer is attached to a force sensitive cantilever. This tip scans across the sample surface governed by piezoelectrics and experiences repulsive interactions from the sample depending on the operating mode. In this work, we use the tapping mode. Here the tip is in periodic contact with the surface. The force between the tip and the sample is kept constant. Thus, from a change of the vibrational amplitude and/or phase of the oscillating tip, information about the surface topography can be acquired. AFM does not necessitate the flow of electrical current between tip and sample, thus it can be used to probe both, conducting and insulating surfaces. [VG09]

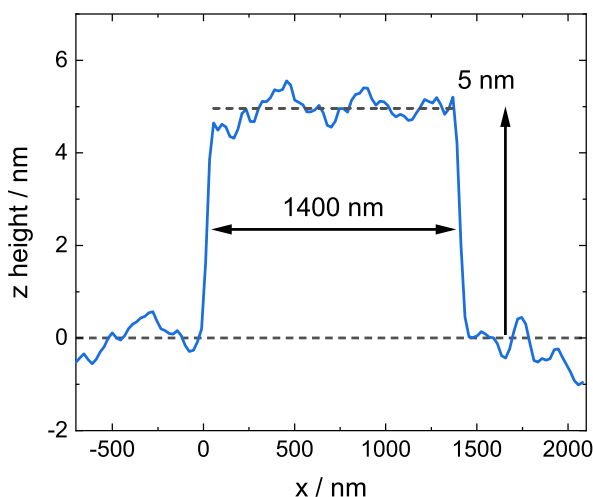


Figure 3.5: Exemplary height profile of an electrode with Au structures of size 1400 nm immersed in a passivation layer measured by AFM. The passivation layer thickness is 10 nm, the evaporated metal layer thicknesses are 3 nm and 12 nm of Ti and Au, respectively. The protrusion of the metal film is well given by the sum the metal layer thicknesses subtracting the passivation layer thickness.

AFM is a very useful technique for determining surface profiles in the nm range. A typical height profile of a metal structure immersed in a silicon oxide layer determined by AFM measurement is shown in Figure 3.5. The thickness of the passivation layer is 10 nm, the thicknesses of the evaporated layers are 3 nm of Ti and 12 nm of Au. The measured protrusion height of the structure is very well given by the difference between the passivation layer height and the sum of the metal layer thicknesses. Thus, it is nicely visible that the metal structures could be successfully embedded in the passivation layer film.

In another work [Ang19] it was shown by AFM measurements that at certain production process parameters, the structures produced show a 'fencing' on the top surface. This means that the metal layer protrudes at the edges of the structures. A typical image of protruding edges is given in the appendix A.5. These protruding metal edges seem to decrease with ongoing electrochemical measurement routine. However, it was shown that the presence or absence of these metal fences does not alter the electrochemical response of the nanostructured electrodes regarding HER significantly [Ang21].

X-Ray Photoelectron Spectroscopy

X-Ray Photoelectron Spectroscopy (XPS) is a method to determine the near surface composition and chemical states of composites of a sample. In this technique, the absorption of X-rays approaching the sample in ultra high vacuum releases electrons, which reach a detector. As the mean free path length of electrons in the solid sample is comparably small (in the order of nanometer), only electrons exited from the near surface atoms are able to leave the sample and can reach the detector. The photoelectrons, which can leave the sample without inelastic losses, lead to the characteristic peaks in the XPS spectrum. Electrons undergoing inelastic collisions lead to the background of the spectrum. The peak positions are characteristic for the kinetic energy of the electrons, which can be directly correlated to their binding energy. The peak heights are proportional to the rate of approaching photoelectrons. [VG09]

In this work, we use an Al $K\alpha$ anode (1486.6 eV) as the X-Ray source with 12 kV and 250 W. The pressure in the analysis chamber during measurements is around 2.2×10^{-10} mbar. All samples analyzed by XPS are previously cleaned by 7 min ultrasonification in acetone and ethanol, followed by 3 x 4 min in ultrapure de-ionized (DI) water. After the wet treatment, the samples are dried by Ar gas flushing.

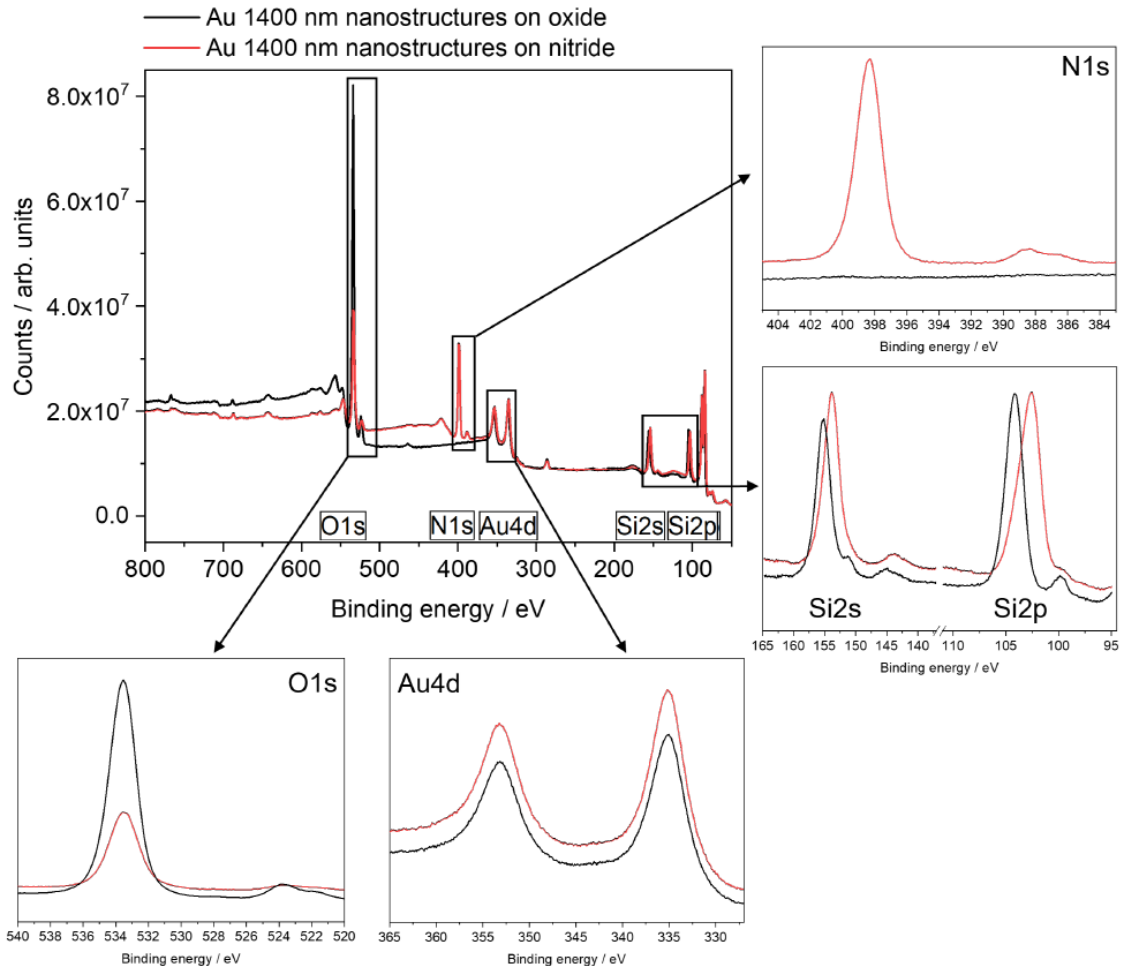


Figure 3.6: Exemplary XPS spectra of nanostructured electrodes with Au structures of 1400 nm size using either thermal silicon oxide (black) or silicon nitride (red) as the passivation layer material beside the structures. The smaller plots on the right side and at the bottom are zoom-ins from the survey. It is clearly visible that the silicon nitride electrode shows signals, which can be attributed to N1s, but also show a signal of O1s, which will be further discussed later in the results section 6.2.2. The image is taken from [Ang21].

Figure 3.6 shows typical XPS spectra of nanostructured electrodes. The black curve is measured for an electrode with 1400 nm structure size and with (thermal) silicon oxide as the passivation layer material beside the metal structures. The red curve is measured for electrodes exhibiting similar Au structures, but using silicon nitride as the passivation layer material. The smaller sized plots on the right side and at the bottom are zoom-ins of the survey spectrum in the respective ranges. Both electrodes show the relevant features, as expected. It is clearly visible, that the relevant gold features are visible and very similar for both electrodes investigated. The electrode with oxide-based passivation layer shows a huge contribution of the O1s signal. The electrode with nitride-based passivation layer

shows additionally a N1s signal and a O1s signal, which is somewhat smaller as observed for the other electrode. This can be explained by an oxidation of the top surface of the silicon nitride layer prior the XPS measurement. Implications of this finding on the electrochemical response of the electrodes will be further described and discussed in the results section 6.2.2.

Electrical characterization (U - I measurements) of nanostructured electrodes

To determine the dry electrical response of the investigated samples, such as dry current-voltage (U - I) or capacitance-voltage characteristics, we probe the samples with a wafer probe stage Keithley 4200-SCS Semiconductor Characterization System.

To facilitate the contacting of the front side of the nanostructured samples, i.e. the structures, we evaporate additional metal pads of the same material as the material of the nanostructures onto the front surface. The evaporated metal pads have a diameter of 100 μm and a thickness of 50 nm. This size allows to contact the front side reliably with the tip of the probe stage. However, the pads shortcut several structures. Note, that the silicon surface of the investigated samples is covered by an insulating layer, i.e. silicon oxide or nitride, with a thickness of at least 10 nm, resulting in a huge electrical resistance at the remaining silicon surface covered by the metal pad. Thus, the DC electrical response of the pad is determined only by the MIS interface below the nanostructures. The back side of the samples is contacted by the stage. The fabrication method of the Al back contact gives a good ohmic contact for both different silicon substrates used in this work (p- or n-doped, 1-10 Ωcm). Thus, the DC electrical response of the sample is dominated by the MIS interface of the front side.

In this work, we investigate two different types of electrodes: (a) Photoelectrodes based on a p-doped silicon substrate and (b) photo-inactive electrodes based on n-doped silicon substrate. The actual metal stack consists of Au/Ti/SiO₂/Si interfaces and constitutes a MIS junction. Properties of the materials used and/or fabrication parameters applied during the fabrication process define the electrical response of the MIS junction. The photoelectrodes fabricated for this work consist of p-doped silicon substrate with 1-10 Ωcm resistivity. The photo-inactive electrodes fabricated consist of n-doped silicon substrate with 1-10 Ωcm resistivity.

Figure 3.7 shows dry current-voltage (U - j) characteristics of (a) photoelectrodes based on p-doped silicon measured in the dark and (b) photo-inactive electrodes based on n-doped silicon for various Au structure sizes. The characteristics of the produced photoelectrodes conducted in the dark, Figure 3.7(a), show that the present MIS junctions exhibit qualitatively the typical Schottky-diode behavior [Sze07] within the relevant current density range: For negative polarization (of the back contact) the MIS junction is reverse biased. Note that there is almost no dependence of the quantitative behavior on the metal structure sizes, i.e. the dry electrical response of the photoelectrodes is similar for all metal structure sizes investigated in the this work. The characteristics of the produced photo-inactive electrodes, Figure 3.7(b), show that the present MIS junctions exhibit a quite linear U - j dependence in the relevant current range, for all metal structure sizes investigated. This is indicative of an (quasi-)ohmic contact at the MIS interface. Note that this behavior is different from the case using p-doped silicon as the substrate material. In the photo-inactive case, the specific resistance (absolute measured resistance per MIS area) of the different sizes are calculated to be 0.6 Ωcm^{-2} (1400 nm), 4.6 Ωcm^{-2} (350

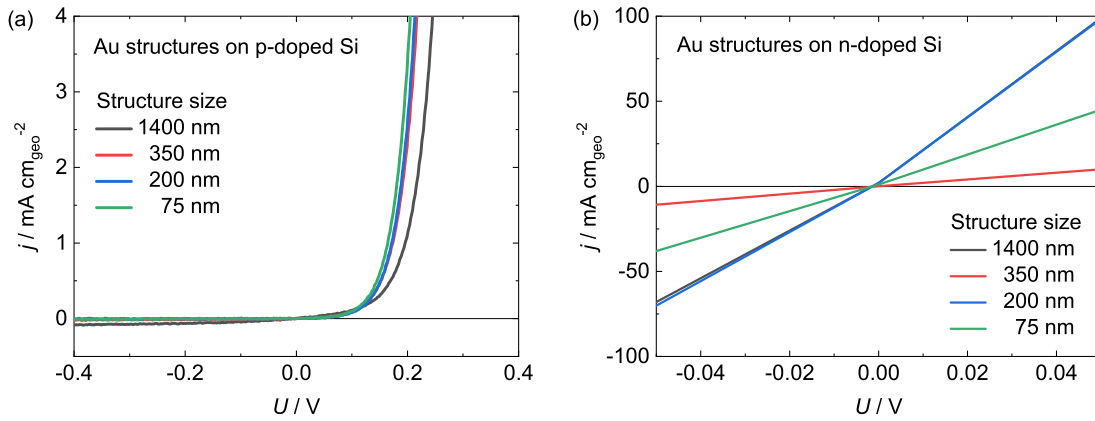


Figure 3.7: Measured dry U - j behavior of structured electrodes for various metal structure sizes. (a) Photoelectrodes based on p-doped silicon ($1\text{-}10 \Omega \text{cm}$) measured in the dark. The photoelectrodes show a Schottky-diode like behavior of the MIS junction, with reverse biasing condition in cathodic direction. Note that the behavior is quite similar for all gold structure sizes investigated. The scan rate is 200 mV s^{-1} . Taken with modifications from [Fil+18]. (b) Photo-inactive electrodes based on n-doped silicon ($1\text{-}10 \Omega \text{cm}$). Note that the curves of the 1400 nm and the 200 nm electrodes overlap. For all structure sizes, the curves show a linear behavior within the relevant current density range, which is indicative of a (quasi-)ohmic contact at the MIS junction. Taken with modifications from [Mai+20].

nm), $0.6 \Omega \text{cm}^{-2}$ (200 nm), $1.1 \Omega \text{cm}^{-2}$ (75 nm). Although these resistances differ slightly in their absolute value, the potential drop at the MIS interface at relevant current densities considered in this work ($j < 5 \text{ mA cm}^{-2}$) can be neglected for all sizes for these kind of electrodes. Consequently, the overpotential applied to the photo-inactive electrodes in the electrochemical configuration is assumed to drop completely at the metal/electrolyte interface.

3.2 Electrochemical investigation

In this section, the techniques, setups and routines used for the electrochemical characterization of the investigated electrodes are introduced.

3.2.1 Three-electrode setup and IR-correction

Most electrochemical measurements performed in this work, except for SECCM and SICM measurements introduced in section 3.2.6, are conducted in a three-electrode setup. The working electrode (WE) is the (structured) electrode of interest. As counter electrode (CE) a coiled wire of the same material as the WE (either Au or Pt) is used. This is necessary to avoid any contamination of the working electrode with another material stemming from the CE, which may alter the catalytic behavior of the WE.

The reference electrode (RE) used is a commercial Mercury/Mercurous Sulfate (MSE) Reference electrode (International Chemistry Co. LTD, Japan). The electrode consists of a long and narrow glass body (approx. 60 mm length from joint to bottom, 5 mm in diameter) and an electrode liquid junction made of porous ceramics at the bottom. The electrode interface is composed of a Hg/Hg₂SO₄/K₂SO₄ (sat.'d) junction. Thus, the actual reference reaction in equilibrium is:



Using a saturated K₂SO₄ solution in the liquid phase leads to a standard potential of $E^0 = 0.64 \text{ V}$ (at 20 °C) [BF01]. After each measurement day, the electrode is stored with its liquid junction immersed in saturated K₂SO₄ solution to assure saturation of the liquid phase. This electrode is chosen as reference, as it shows a very stable reference potential over several months (probably due to its advantageous geometry). This could be observed even when working in acidic (pH 1) or alkaline (pH 13) electrolytes for multiple days. In addition, chloride contamination of the system stemming from the RE choice can be avoided in this case.

The potentials given in this work are often referred to the Standard Hydrogen Electrode (SHE) scale or the Reversible Hydrogen Electrode (RHE) scale. The measured potential against MSE (labeled as V_{MSE}) can be converted into the other scales by:

$$\text{SHE: } E [V_{\text{SHE}}] = E [V_{\text{MSE}}] + 0.64 \text{ V} \quad (3.2)$$

$$\text{RHE: } E [V_{\text{RHE}}] = E [V_{\text{MSE}}] + 0.64 \text{ V} + \text{pH} \cdot 59 \text{ mV} \quad (3.3)$$

Here E being the electrode potential in the respective scale and pH being the pH value of the electrolyte investigated.

Moreover, all electrode potentials displayed in this work are IR-drop corrected. The serial resistance necessary for IR correction is determined by impedance spectroscopy in the double layer region. Thus, the (constant) impedance value at high frequencies ($> 10 \text{ kHz}$) is directly used as the serial resistance. If the behavior in this frequency range was not constant, a fitting of the impedance spectrum has been conducted and the value for the serial resistance extracted. Typical values measured for the serial resistance of the whole system (i.e. consisting of the resistivity of the electrolyte and contact resistances) lied in the range between 30Ω (in $0.1 \text{ M H}_2\text{SO}_4$) and 50Ω (in 0.1 M NaOH) for nanostructured electrodes.

3.2.2 Electrolytes

All electrolytes used in this work are composed of suprapure chemicals. A complete list of the chemicals used is given in the appendix A.6. The electrolytes are mixed using ultrapure DI water of 18.2 M Ω cm (ELGA PURELAB, Veolia Water Technologies, Germany).

Unless stated otherwise, the measurements are performed in an Ar saturated electrolyte. Thus, the electrolyte-filled cell is purged for at least 20 minutes with Ar gas before the measurements to remove traces of oxygen present in the system. The Ar gas used is of purity 5.0 (Westfahlen, Germany). During the measurement, the electrolyte purging with Ar is continued at a smaller flow rate. The cells (the optical cell as well as the ReRDE cell, see below) have a gas outlet system consisting of a bubbler-device. The bubbler enables a well defined atmosphere of the purging gas in the gas overhead of the cell and keeps the pressure in the cell on ambient pressure. Some experiments are conducted in H₂ saturated electrolyte. The same purging process is applied here. The H₂ gas is also of purity 5.0 (Westfahlen, Germany).

3.2.3 Measurement equipment and measurement techniques

Electrochemical measurements are conducted with a Zahner Zennium Pro potentiostat (Zahner elektrik GmbH, Germany). The control software used is 'Thales v5.5.0'.

The standard electrochemical characterization technique conducted in this work is *Cyclic Voltammetry* (CV) or *Linear Sweep Voltammetry* (LSV). In both methods, the potential applied at the working electrode is changed linearly with time and the resulting DC current between working and counter electrode is recorded. Measurement parameters are the turning potentials, i.e scan range in CV experiments and start- and end-potential in LSV experiments, and the potential scan rate ν . The standard scan rate used throughout this work, if not stated differently, is 50 mV s⁻¹. The potentiostat control software 'Thales' also gives the possibility to choose the number of samples/cycle. It is chosen as 400 samples/cycle per 1 V scan range and per 50 mV s⁻¹. This value has been determined experimentally to give no current feedback with the electronics in the potentiostat or the power grid. The specification of this value results in one datapoint every 5 mV during the potential scan for the given parameters and one datapoint every 0.1 s.

Another widely used measurement technique in this work is *Electrochemical Impedance Spectroscopy* (EIS). This technique is used to determine the serial resistance used for IR-drop correction and to determine the capacitive behavior of the electrodes (cf. section 7.2). In this method, an AC sinusoidal pertubation is added to the DC electrode potential. The AC current response of the system is recorded and the (complex) impedance behavior can be determined. Measurements at various pertubation frequencies can give a fittable spectrum (a typical EIS spectrum is given in the appendix in Figure A.10). The aquired EIS spectrum is fitted with the program 'EIS Spectrum Analyser 1.0' developed by Bandarenka et al. [BR05] to a suitable equivalent circuit. Typical elements used in the circuits are resitances R and constant-phase-elements CPE. The impedance of these elements as a function of the pertubation frequency ω is given by:

$$Z_R(\omega) = R \quad \text{and} \quad Z_{CPE}(\omega) = \frac{1}{Q(i\omega)^n} \quad (3.4)$$

Here i is the complex number and R , Q and n are (frequency independent) fitting param-

eters. The typical equivalent circuit used for structured electrodes with n-doped silicon as the substrate material consists of a serial connection of a resistance R_s connected with one or more CPE||R elements, which consist of a parallel connection of a constant phase element and a resistance. The equivalent circuits used for fitting the impedance data are shown in the respective results sections.

3.2.4 Photoelectrochemical measurements

Optical cell/Standard cell

In all photoelectrochemical experiments, which require the illumination of the sample, a self-designed three-electrode optical cell is used. In addition, this cell is used as the 'standard cell' performing most of the electrochemical experiments presented in this work, if not stated differently. A scheme of the cell body is shown in Figure 3.8. It consists of three separated compartments, for the reference, the counter and the working electrode, respectively, which are connected by the electrolyte. In addition, a proton-conducting membrane (here: NAFION, DuPont) can be inserted, which separates the main compartment (WE compartment) from the two other compartments. The separation of the compartments, especially the counter electrode compartment, is necessary to avoid contamination of the working compartment by dissolved chemical compounds and/or ionic metal species stemming from the counter electrode. The main body of the cell is made of PCTFE, which is chemically inert against the electrolytes used here as well as thermally and mechanically very stable.

The front of the cell is covered by a glass window, which is made of mineral glass that has been further chemically and thermally hardened to improve its mechanical stability. Apart from silica (SiO_2 , $> 70\%_{\text{mol}}$), glass of this grade can further consist of alkali oxides ($\text{Na}_2\text{O}/\text{K}_2\text{O}$, $\approx 15\%_{\text{mol}}$), alkaline earth oxides (CaO/MgO , $\approx 13\text{-}16\%_{\text{mol}}$), traces of aluminum oxide (Al_2O_3) and of boroxide (B_2O_3) [SCH20]. It is known that the composition of glass can influence its etching properties in neutral to alkaline electrolytes, see section 2.1.3 and [SCH20]. However, mineral glass (i.e. soda-lime glass) exhibits an etching rate in alkaline media in the same order of magnitude as the one of thermal silicon oxide (see comparison of thermal silicon oxide and soda-lime glass in Table 2.2). As an upper limit of the etching rate we find $1.6 \times 10^{-2} \text{ nm s}^{-1}$ (in 30 wt% KOH, 70°C) in the literature [Sak+13]. However, the optical cell is always operated at room temperature (the temperature strongly influences the etching rate of glass, cf. section 2.1.3) and with much more dilute alkaline electrolytes. Consequently, the actual etching rate of the cover glass is likely to be orders of magnitude lower than the value presented. Thus, we conclude that the choice of the actual cover glass material is not likely to have a relevant impact on the amount of dissolved silica in the electrolyte, although its amount has not been explicitly measured within the scope of this work. However, the great advantage using hardened mineral glass instead of e.g. quartz glass turned out to be its mechanical stability and durability, while it allows for a very good transmittance of light in the relevant optical region. These advantages justified its selection. The glass window used has a transmittance of $\approx 95\%$ (at perpendicular incidence) on a wide spectral range, which is shown in Figure 3.9(a).

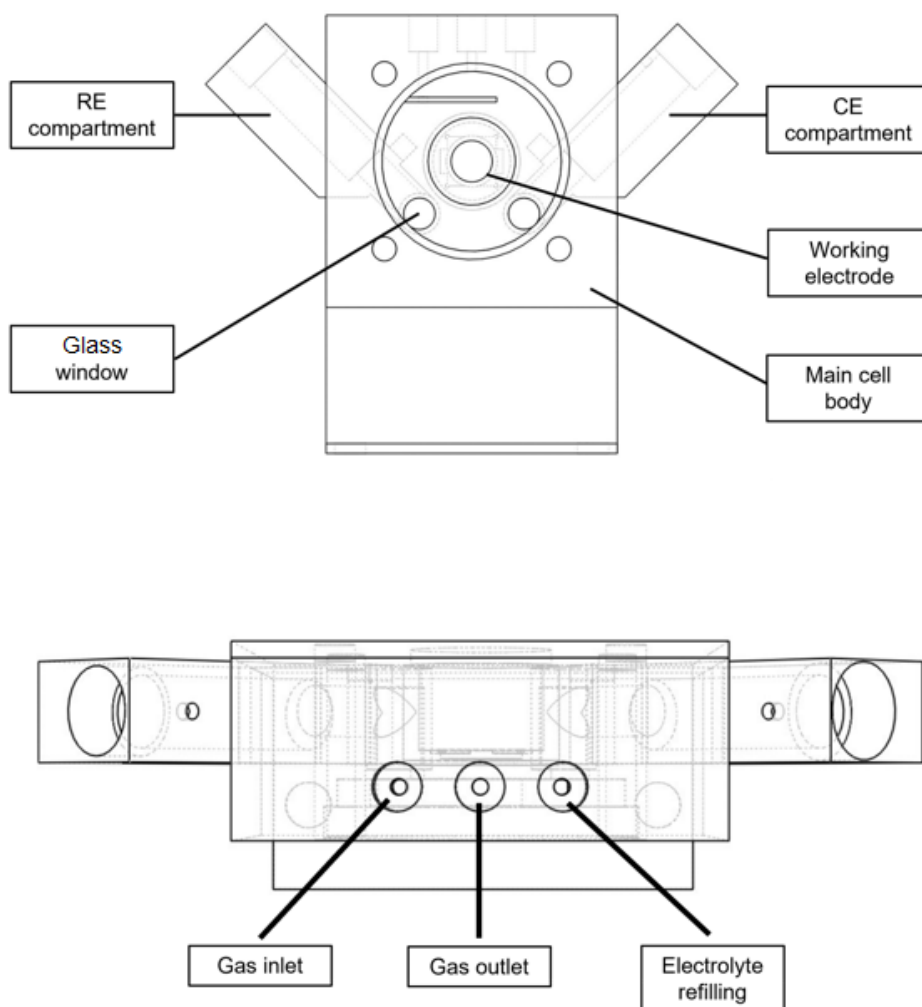


Figure 3.8: Scheme of the optical cell used for most of the electrochemical measurements performed within this work. Top: Front view, Bottom: Top view. Images are taken with modifications from [Ang21].

Illumination

Photoelectrochemical measurements are performed in the optical cell introduced above. The photosensitive working electrode is illuminated from the front (nanostructured surface) through the glass cover and through the electrolyte. In this work, the illumination of the sample is performed with two different light sources: A 'Tunable Light Source' (TLS, Zahner elektrik GmbH, Germany), which can be used to illuminate the sample monochromatically at various wavelengths, and a white light source (LSW-2, Zahner elektrik GmbH, Germany). The illumination intensity approaching the cell is measured by a light detector which is placed in close vicinity of the optical glass (for LSW-2). The spectrum of the white light source ranges from 450 to 700 nm and is plotted in Figure 3.9(b). Both lamps can be controlled via the potentiostat software.

The Zahner software and the light detector use a feedback loop, which adjusts the intensity of the lamp automatically. Consequently, independent of the distance of the lamp or focusing of the beam, the intensity specified in the software approaches the sample, resp.

the glass cover. However, the illumination intensities mentioned in this work are the values specified in the software and measured at the sensor. The actual intensity approaching the sample needs to be reduced by a factor given by the transmittance of the optical glass and the absorbance in the electrolyte. The optical glass used has a transitivity of approx. 95% within the complete optical range (for perpendicular incidence), cf. Figure 3.9. Consequently, the reflection/absorbance of the optical glass as well as the absorbance of light by the thin electrolyte layer (approx. 1 cm) is neglected.

The beam diameter approaching the sample is determined by an aperture in front of the glass window. The aperture has a round shape with a diameter of 4 mm. The resulting beam size is smaller than the usual nanostructured area on a typical sample. Thus, it is made sure that the whole beam approaching the sample covers only structured area.

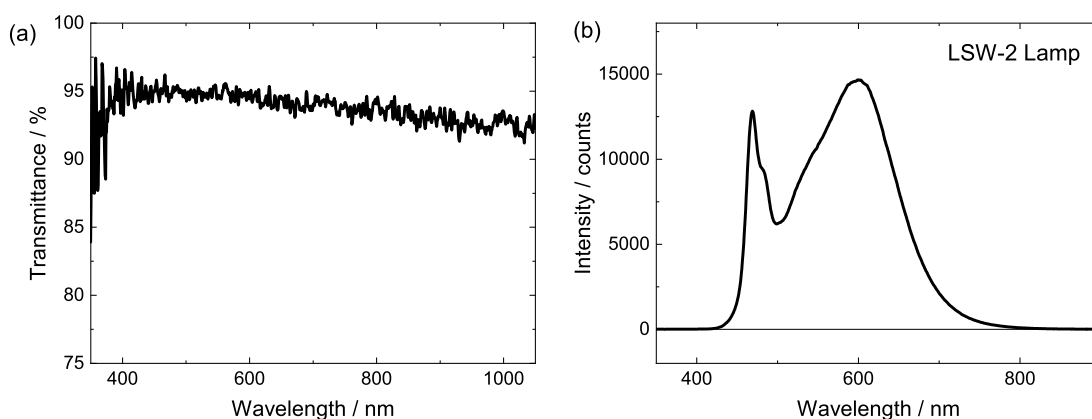


Figure 3.9: (a) Measured transmittance of the optical glass window of the optical electrochemical cell plotted over the wavelength. (b) Measured spectrum of the LSW-2 lamp (Zahner elektrik GmbH).

3.2.5 Recessed Rotating Disk Electrode setup (ReRDE) - Introduction and characterization

For determining the influence of particle transport on the reactions occurring on the flat wafer pieces, i.e. the silicon-based electrodes, a setup is established based on the principle of a Rotating Disk Electrode (RDE), namely a Recessed Rotating Disk Electrode (ReRDE). It is not possible to conduct experiments with the flat silicon wafers in the normal RDE configuration, as there is the crucial need for sealing of the front side of the sample from its back side in order to avoid electrical short circuits. This sealing can be achieved by pressing the sample front side onto an O-ring. However, this way of designing the sealing results in a recess of the electrode surface. A scheme of the ReRDE setup (sample holder) showing the recess and labeling relevant geometric quantities is shown in Figure 3.10.

The use of a recessed electrode instead of a planar electrode surface may lead to a deviation from the actual known RDE-like transport behavior when rotating. There are several studies, which investigated the hydrodynamic and electrochemical behavior of classical ReRDE setups, e.g. Newman et al. [WN91] theoretically and Dinan et al. [DML91] experimentally.

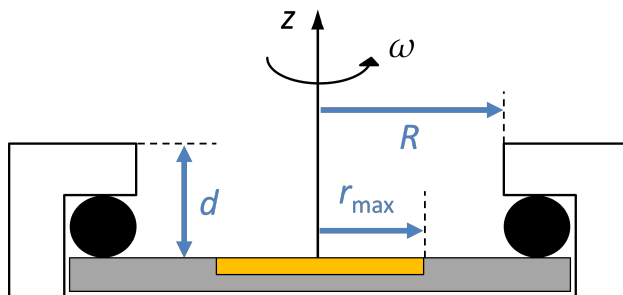


Figure 3.10: Scheme (side-cut) of the ReRDE setup (sample holder) established within the scope of this work and characterized in this section. The electrode (grey/orange area) is pressed from its backside onto an O-ring (black area). The white part is made of PCTFE. The setup rotates around the z -Axis. d : Recess depth, R : Total electrode radius, r_{\max} : Radius of active surface area.

The latter investigated the influence of the aspect ratio d/R on the limiting current density and the current distribution on the electrode surface in the current limited range, which is quite relevant for the system presented here. They performed variations of d/R between 0.0 (ideal RDE case) and 2.0 and could show that ReRDEs generally show a behavior similar to RDEs, meaning that the limiting current density j_{lim} scales linearly with \sqrt{w} , as known for RDE setups, see equation (3.5). However, they observed that for larger aspect ratios the limiting current density becomes smaller, independent of the rotation speed, i.e. the behavior can be empirically modeled by equation (3.6).

$$\text{RDE: } j_{\text{lim}}(w) = 0.62nFc_i^*D_i^{2/3}\nu^{-1/6}\sqrt{w} \quad (3.5)$$

$$\text{ReRDE: } j_{\text{lim}}(w) = B\sqrt{w} - A(d/R) \quad (3.6)$$

Here n is the number of transferred electrons, F is Faraday's constant, c_i^* is the bulk concentration of the reacting species i , D_i is its diffusion coefficient in the solvent (here water), ν is the kinematic viscosity of water and w is the rotation speed. According to Dinan et al. [DML91], B is constant and independent of the aspect ratio and its value is comparable to the value given by RDE theory ahead the \sqrt{w} term in equation (3.5). A is a positive constant and depends on the ratio d/R , but not on w . It becomes larger with increasing aspect ratio.

The authors explained this behavior of ReRDEs by a more restricted mass transfer into the recess as its depth is more increased. To proof this hypothesis, they plated copper electrochemically on the electrode under diffusion limiting conditions, measured the resulting thickness of the deposited copper layer at different positions on the electrode surface and concluded from these measurements the uniformity of the current distribution on the electrode. They could show that for $d/R = 0.0$ (RDE case) the current is uniform on the whole electrode surface, as expected. For $d/R = 0.1$ the current begins to decrease rapidly beyond a relative radius of approx. $r/R = 0.9$, and for $d/R = 0.5$ the current drops at approx. $r/R = 0.8$. Thus, they concluded that the mass transfer at the edges of the electrode is more restricted for larger aspect ratios, which leads to a nonuniform current distribution and, therefore, lowers the limiting current (i.e. the limiting current density for a given and constant surface area) for a given rotation rate.

Characterization of the ReRDE setup used in this work

Figure 3.10 shows the schematic side-cut of the ReRDE setup (i.e. sample holder) established and used in this work. We now characterize the presented ReRDE setup for its mass transfer properties by measuring the limiting current behavior under mass-transfer limiting conditions and compare it with the expected behavior predicted by equations (3.5) and (3.6).

In our setup, the geometric shapes of recess and electrodes are fixed. The recessed depth realized here is $d = 1.60$ mm, the diameter of the electrode surface exposed to the electrolyte is $2R = 8.50$ mm, which is equal to the toroidal inner radius of the O-ring used. These geometric properties lead to an aspect ratio of $d/R = 0.38$. As the aspect ratio d/R is fixed for all electrodes used in our setup, we will investigate the behavior of the ReRDE setup for various extents of the active surface area r_{\max}/R . We analyze samples consisting of a circular and centric aligned platinum surface with radius r_{\max} , which is surrounded by thermal silicon oxide. The oxide passivates the remaining electrode surface. Thus, the investigated electrodes have the same absolute area exposed to the electrolyte (R), but differ in the radius of their electrochemically active surface area (r_{\max}). The samples are fabricated via optical lithography. The relevant geometric properties of the samples investigated here are given in Table 3.2.

$2r_{\max} / \text{mm}$	$A_{\text{geo}} / \text{cm}^2$	$A_{\text{meas}} / \text{cm}^2$	r_{\max}/R
3.0	0.071	0.062 ± 0.005	0.35
5.0	0.193	0.181 ± 0.007	0.59
6.0	0.283	0.255 ± 0.013	0.71
9.5	0.709	0.702 ± 0.029	1.12

Table 3.2: Specifications of the electrodes investigated for characterizing the established ReRDE setup. The (geometric) radius of the active surface area r_{\max} is determined by the fabrication process, A_{geo} is the resulting geometric surface area, A_{meas} is the measured Pt active surface area. The procedure of determining the active surface area is described in the text. The ratio of r_{\max}/R is calculated from the geometric radius of the active surface r_{\max} and the toroidal inner radius of the O-ring used $2R = 8.5$ mm.

The active surface area is determined as described in section 3.2.7, i.e. via H-UPD adsorption and desorption in Ar saturated 0.1 M H_2SO_4 in a potential range between 0.045 and 0.505 V_{RHE} . The active surface determined by this method slightly changed during measurements. The absolute values given in Table 3.2 are the average values of two measurements performed before and after the ReRDE characterization measurements. The error of the values given is the difference between these two measurements. Due to the curvature of the O-ring, which has an toroidal inner diameter of 8.5 mm and a poloidal radius of 0.5 mm, at a finite applied pressure, the total radius of the active area r_{\max} can be larger than the value of R as defined. This becomes clear when looking at the scheme of the setup in Figure 3.10. Consequently, the ratio r_{\max}/R can become larger than 1.

By comparing the measured areas with the geometric areas calculated from the diameter one sees that the measured area is smaller for all samples. This systematic underestimation of the measured area might arise from a non ideal potential window for evaluating the H-UPD charge. Since this error appears to be systematic for all mentioned samples, we consider the difference between A_{meas} and A_{geo} as a further contribution to the error of

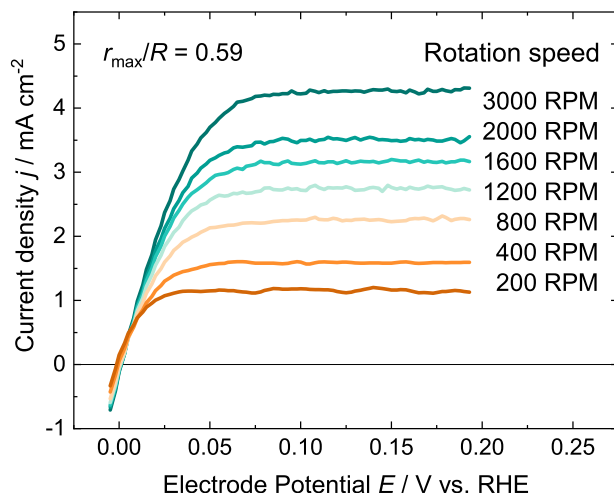


Figure 3.11: LSVs of an exemplary sample ($r_{\max}/R = 0.59$) in the HOR region at various rotation speeds. The measurements are conducted in the presented ReRDE setup. Electrolyte: 0.1 M H_2SO_4 , saturated with H_2 gas at atmospheric pressure. Scan rate: 50 mV s^{-1} . At sufficiently large overpotentials the current is transport limited resulting in constant j_{lim} .

the final data, see below. All current densities mentioned in this section are calculated using the measured surface area. The reaction utilized for determining the current limiting behavior of the ReRDE setup is the hydrogen oxidation reaction (HOR), which is given by:



The electrolyte, in which the measurements are conducted, is based on 0.1 M H_2SO_4 at pH 1 and is continuously purged with H_2 -Gas to assure saturation. The cell used is kept at atmospheric pressure. Exemplary linear potential sweep experiments (LSVs) of an electrode conducted in the HOR region at various rotation speeds are shown in Figure 3.11. The data shows the expected saturation of the current at the respective values j_{lim} at sufficiently large positive overpotential.

Figure 3.12 shows the average limiting current density j_{lim} of HOR as a function of \sqrt{w} for the mentioned samples with the same aspect ratio ($d/R = 0.37$) but different r_{\max}/R . The red solid line in the Figure shows the behavior expected from RDE theory given by equation (3.5). The values used for calculating the theoretical curve are given in the appendix A.7. The errors of the experimental data given in the Figure as error bars consist of the error stemming from the difference of measured and geometric area mentioned above, the change of the measured area during the experiment and the difference between forward and backward scan of j_{lim} in the transport limited region. All errors are added quadratically.

By comparing the different behaviors with \sqrt{w} one sees that for all ratios the behavior is quite linear as indicated by a linear fitting (dashed lines). We first consider the behavior of the sample with the largest active surface area, i.e. $r_{\max}/R = 1.12$. Its y -intercept is slightly negative. Thus, this coincides with the behavior observed by Dinan et al. and predicted by equation (3.6). However, the slope of the linear fitting differs significantly from the one of the other samples investigated. The smaller slope is contrary to the results

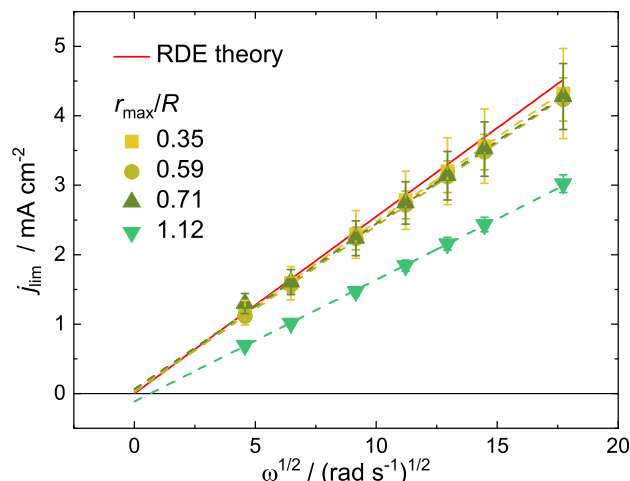


Figure 3.12: Average limiting current density j_{lim} of the HOR as a function of $\sqrt{\omega}$ for different ratios of r_{max}/R . The measurement points are indicated by the symbols, linear fits of the data are given by the dashed lines in the respective color. The red line indicates the theoretical behavior of the mentioned reaction predicted by RDE theory according to equation (3.5). All samples with $r_{\text{max}}/R \leq 0.71$ show a behavior very similar to the behavior predicted by RDE theory.

obtained by Dinan et al. [DML91], who found a similar slope, but only a more negative intercept for higher aspect ratios. One explanation may be the different geometry of the setup presented here. Since $r_{\text{max}}/R > 1$, there exists an area on the electrode surface which is 'shielded' by the O-ring, but is in contact with the electrolyte. The higher the rotation of the system, the more turbulence is introduced in the vicinity of the shielded area. A local appearance of turbulence leads to a local non uniform distribution of the diffusion layer thickness, which directly influences the limiting current behavior. This effect might appear as a decrease of the active area for higher rotation speeds and, therefore, as an underestimation of the current density when normalizing the current to the area determined in the non-rotating case.

Now, we consider the other samples. It is remarkable that the behavior of the samples with smaller ratios r_{max}/R are much closer to the theoretically expected behavior of the RDE (red line). Within the uncertainties, the behavior of all other samples considered, i.e. the samples with $r_{\text{max}}/R = 0.33$, $r_{\text{max}}/R = 0.59$ and $r_{\text{max}}/R = 0.71$ match the curve predicted by RDE theory. This is in accordance with the results presented by Dinan et al. As already mentioned above, the authors showed that the current distribution for an aspect ratio of $d/R = 0.5$ is uniform until a value of $r/R = 0.8$. The aspect ratio of the ReRDE setup established here is $d/R = 0.38 < 0.5$, and the largest active surface area ratio of the considered electrodes is $r_{\text{max}}/R = 0.71 < 0.8$. Thus, the assumption of a homogeneous current distribution on the whole active electrode surface for the three investigated samples with $r_{\text{max}}/R \leq 0.71$ is supported by the results presented here.

Based on these results we can conclude that the presented setup is an appropriate tool for maintaining controlled diffusion towards flat electrodes based on silicon wafers, as investigated in this work. The RDE theory can be applied for electrodes with a circularly shaped active surface area up to a radius of $r_{\text{max}} < 6.0$ mm (i.e. $r_{\text{max}}/R = 0.71$), located centrally on a $10 \times 10 \text{ mm}^2$ silicon wafer chip. The active surface area of all electrodes measured in this setup and considered in this work do not exceed this limit.

3.2.6 Local current mapping - SECCM and SICM measurements

Scanning electrochemical cell microscopy

For localized current measurements (current mapping) we use the Scanning ElectroChemical Cell Microscopy (SECCM) technique [Wil+09]. We prefer this method over other electrochemical scanning methods, such as electrochemical scanning tunneling microscopy (EC-STM) [Lia+18] since the sample surface to investigate consists of areas with high (metal) and very low (silicon oxide) electrical conductivity. Scanning techniques based on tip bias as a feedback mode would crash when scanning over this heterogeneous surface.

In SECCM, a nanopipette filled with an electrolyte and equipped with an electrode is hopping over the sample surface. Here, we use a Ag/AgCl wire as a Quasi Reference/Counter Electrode (QRCE) inside the pipette. The tip of the nanopipette is open and carries a tiny electrolyte droplet at the tip. Once there is contact between the electrolyte droplet and the sample, a locally constrained liquid connection between the target spot on the sample and the QRCE inside the pipette is formed (meniscus). Thus, this technique allows for conducting local electrochemical experiments. A scheme of the configuration used is given in Figure 3.13. In this work, we use this method to determine the HER reactivity locally on our sample surface (current map).

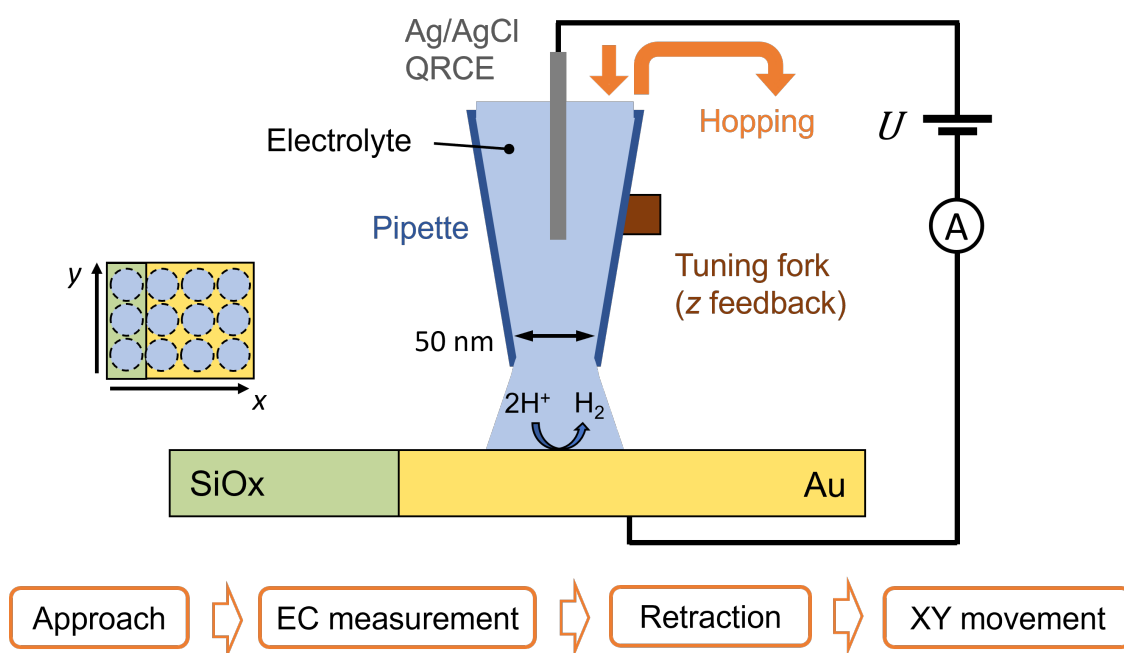


Figure 3.13: Scheme of the SECCM setup and the measurement routine.

The feedback mechanism for the vertical approach of the pipette (z -direction) we use does not necessitate an electrical (or electrochemical) connection, i.e. current, between the sample and the QRCE, since it works mechanically. A commercial tuning fork is in physical contact with the pipette glass. The resonance frequency of the tuning fork is live monitored by a digital multi-frequency lock-in amplifier (Zurich Instruments). During approach, the combined pipette/tuning fork system is moving towards the electrode surface. Once the tip of the pipette approaches the surface and the meniscus is established, the resonance frequency of the tuning fork changes. This is detected by the instrument and stops the

z -movement of the pipette to avoid a crashing of the pipette and the sample. Note that the pipette is *not* in physical contact with the sample. After conducting electrochemical experiments, the pipette is retracted from the surface, which breaks the liquid connection between pipette and sample. The resonance frequency of the tuning fork changes to its prior value. The stage is now moved to the next xy -position and the approach procedure repeats.

In the following, more information about the equipment used is given. The nanopipettes are pulled from quartz capillaries with an outer diameter of 1 mm and an inner diameter of 0.5 mm (QF100-50-10, Friedrich & Dimmock) using a commercial laser pipette puller (P2000, Sutter Instruments). The opening diameter of the pipettes produced by the used program have been determined previously by TEM imaging and were in the range of 45 ± 10 nm. More details about the pipette pulling procedure and its parameters are given by Hengsteler et al. [Hen+21]. The pipette is placed on a custom-made pipette holder placed above the substrate. The coarse z -positioning of the pipette above the electrode surface is done with a micropositioner (MMP1, MadCityLabs), which was optically controlled by an installed microscope camera system (AM7915MZTL - EDGE, Dino Lite). The automatized vertical approach and retraction of the pipette during the scan experiment is performed by a piezo nanopositioner (Nano-MET10, MadCityLabs). The change of the xy -measurement position is realized by nanopositioning of the sample. Thus, the sample is placed on a high precision XY piezo nanopositioning stage (Nano-PDQ250, MadCityLabs). The setup is controlled by a PC with FPGA card (PCIe-7846, National Instrument) and a custom-made LabVIEW program, which is based on the WEC-SPM software package by P. Unwin, University of Warwick. The whole setup is located in a custom-made Faraday cage to reduce electromagnetic noise. To reduce mechanical vibrations, the setup is placed on a benchtop vibration isolation platform (BM-8, Minus K Technology) and the Faraday cage is further coated by acoustic foam to minimize acoustic vibrations.

Scanning ion conductance microscopy

As an alternative method for current mapping we use scanning ion conductance microscopy (SICM). This method can be used to measure indirectly local reactivity by a change in the local ion concentration due to an occurring reaction involving charge transfer [Mom+16]. The setup used (i.e. stages, positioning controller, software etc.) is similar to the one used for SECCM measurements. However, the electrode configuration and measurement routine differs. A scheme of the SICM configuration and the conducted measurement routine is shown in Figure 3.14. The working principle is described in the following.

In SICM, the surface to be analyzed (WE) is immersed in an electrolyte. There are two QRCE electrodes present in the system: One electrode in the bulk of the electrolyte (bulk QRCE), and one in the pipette (pipette QRCE). The pipette is filled with the same medium as the surrounding electrolyte. Here, we use Ag/AgCl wires as QRCEs and work in an electrolyte containing 50 mM KCl. The pipettes we use in this configuration are similar to the ones used in SECCM setup, i.e. the opening diameter is approx. 50 nm. The QRCEs used have macroscopic dimensions. Thus, the areas of both QRCEs are orders of magnitudes larger than the actual opening of the pipette.

Between the two QRCEs a DC voltage U_2 can be applied. The resulting current $|I_1|$ flowing between the bulk QRCE and the pipette QRCE is limited by the pipette opening. More

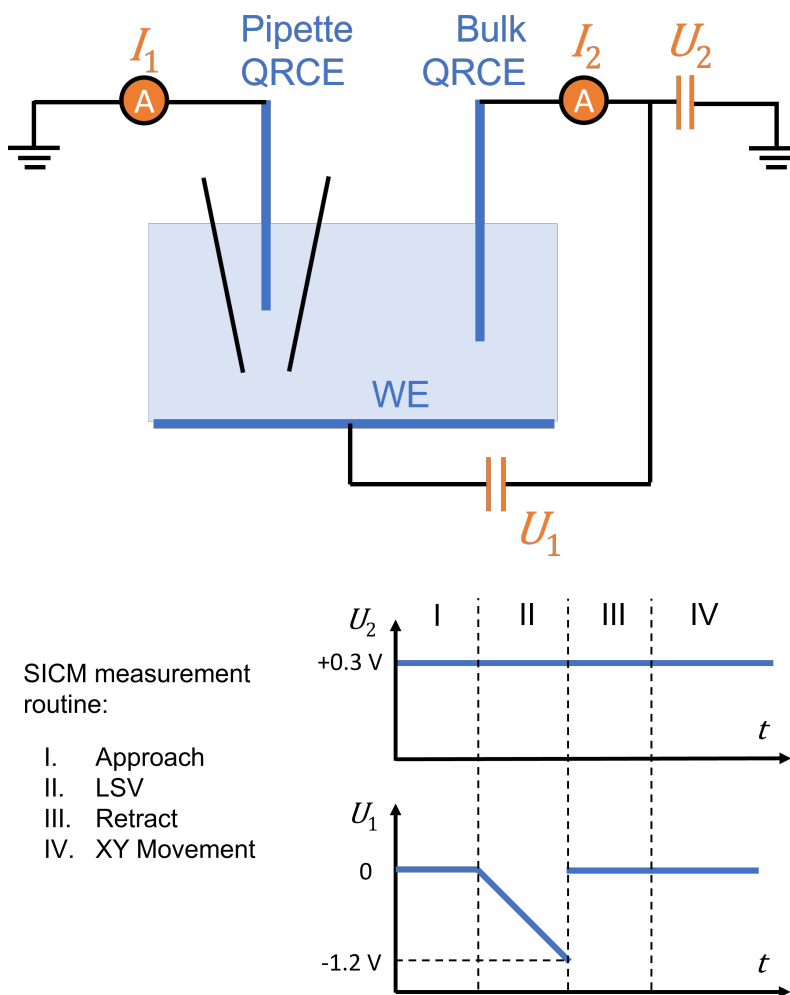


Figure 3.14: Scheme of the SICM configuration (top) and the measurement routine (bottom).

precisely, it depends on the ionic conductivity in the limiting ion conduction channel. This stationary current works as the feedback for the approach of the pipette (I). The pipette moves towards the WE surface. When the pipette approaches the surface, the ion conducting channel gets reduced due to geometric reasons. As a consequence, the measured current $|I_1|$ decreases. Once the measured current falls below a threshold value (here we use 60 percent of the current measured in the bulk), the approach of the pipette is stopped and it remains at the current z -position. The height of the pipette above the WE surface depends on the approach speed of the pipette, the sampling frequency, the set threshold value and the conductivity of the electrolyte [Mom+16].

After approach, a potential sweep (LSV) is applied between the bulk QRCE and the WE substrate (II). Thus, the voltage U_1 between the bulk QRCE and the WE is swept linearly from 0 in cathodic direction. Note that U_2 stays the same. The change of the voltage U_1 leads to a current $|I_2|$ (with faradaic and non-faradaic contribution) between the bulk QRCE and WE. After LSV measuring, the pipette is retracted (III) and moved to the next position (IV).

The principle idea behind this method is that faradaic reactions occurring at the electrode surface change the local ionic concentration in the vicinity of the electrode surface. A

changed ionic concentration modifies the local ionic conductivity. A change of the local ionic conductivity can be probed by the pipette, as $|I_1|$ is supposed to depend on the local ionic conductivity at the pipette tip. Thus, it is in principle possible to probe local reactivity.

3.2.7 Area determination

Geometric and illuminated area

The geometric area can be determined by geometric calculations. However, it does not consider the roughness of the surface and that some nanostructures may be deactivated due to local contact issues at the M/Si interface.

In photoelectrochemical experiments presented here, the measured current is often normalized to the illuminated area. It has been found in a previous work [Mai17] that in photoelectrochemical experiments, the normalization of the current on the illuminated area is more meaningful than the normalization on the actual geometric or active surface area. The reason is that at negative potentials and at moderate illumination intensities, the current is rather limited by the migration of photoexcited charge carriers than by the kinetics of the electrochemical reaction. However, all nanostructured electrodes have a very similar gold coverage on the surface (see filling factor in Table 3.1), which assures a similar proportionality between the illuminated area and the exposed absorber area for all electrode sizes investigated. The illuminated area is given by the size of the aperture used, which has a diameter of 4 mm in this work. Consequently, the resulting illuminated area is $A_{\text{ill}} = 0.126 \text{ cm}^2$. The corresponding normalized current density is denoted by j_{ill} . It is maintained that the whole light beam covers the structured area (see above).

The area used for normalizing the current in typical experiments conducted without illumination (for substrates based on n-doped silicon) is determined electrochemically, which is further explained below for the various metals considered.

Au-based electrodes

The electrochemical active surface area of Au-based electrodes investigated in this work is determined via Au-oxide reduction in acidic electrolyte (0.1 M $\text{H}_2\text{SO}_4/\text{Ar sat.'d}$). This method is preferred over others, such as the determination via capacity measurements [LSC16] or Cu-UPD deposition [Pal+11]. A determination of the area via capacitive experiments (specific capacitance) turned out to be not useful, since experimental results shown later (cf. section 7.2.4) suggest that the capacitance of the electrodes can be altered significantly by electrode structuring. This would lead to a reduced comparability between the different structure sizes. A determination of the active surface area via Cu-UPD deposition also turned out not to be useful. The complete removal of Cu traces from the system is challenging and deposited traces of Cu onto the electrode surface during HER analysis could further influence the experimental HER behavior and lead to misinterpretation of results. Consequently, the area determination via Au-oxide reduction is preferred, as this way further provides an 'online' indication of the area (and its changes), when extending the cycling experiments conducted to determine HER activity into the Au oxidation region.

Figure 3.15(a) shows CV experiments in the Au oxidation region of an evaporated Au layer on n-doped silicon substrate ($A_{\text{Au,geo}} = 0.636 \text{ cm}^2$) in 0.1 M $\text{H}_2\text{SO}_4/\text{Ar sat.'d}$ for

various upper potential limits (upl). The area below the Au-oxide reduction peak increases when increasing the upl. The transferred charge during reduction Q_{red} is calculated by integrating the reduction peak area via:

$$Q_{\text{red}} = \frac{1}{\nu} \int (I(E) - I_{\text{DL}}) dE \quad (3.8)$$

Here ν is the scan rate of the experiment, I is the measured current and I_{DL} is the charging current of the double layer. The charging of the double layer during the scan leads to a constant contribution to the current measured and, thus, is subtracted as a potential independent baseline.

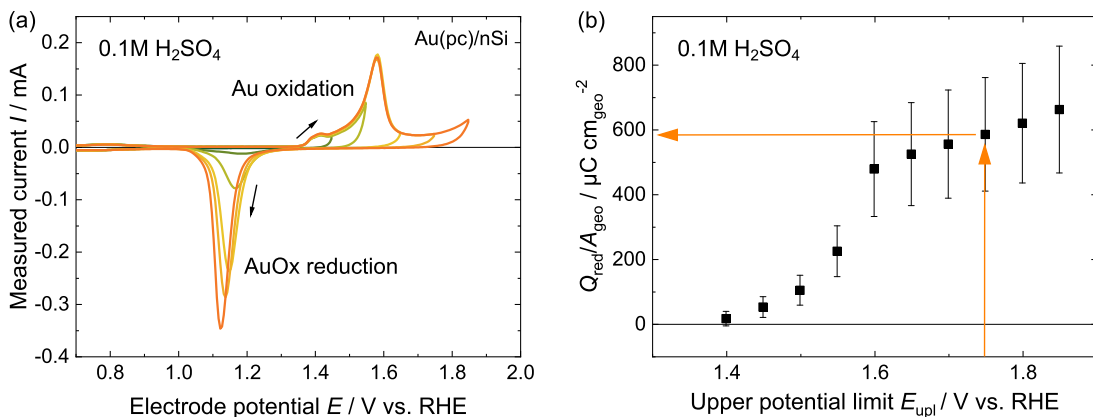


Figure 3.15: (a) Cyclic Voltammograms of a typically evaporated Au film used in this work conducted in the Au oxidation region for various upper potential limits (upl) in 0.1 M $\text{H}_2\text{SO}_4/\text{Ar}$ sat.'d. Scan rate: 50 mV s^{-1} . (b) Transferred charge during Au oxide reduction normalized to the geometric Au area plotted over the respective upl. 'Monolayer' coverage is achieved at $E_{\text{upl}} = 1.75 V_{\text{RHE}}$ (see text), as indicated by the orange arrow.

The reduction charge is a function of the upper potential limit (upl), as it is shown in Figure 3.15(b). In this plot the determined reduction charge normalized to the geometric gold area is plotted over the upl of the corresponding scan. A qualitative similar plot has been obtained by other groups [LC61; Dia+13]. Although the oxidation process of gold is a rather complex process and occurs in multiple oxidation steps at various anodic potentials [Che+13; Dia+13], the determination of the area via reduction charge measurement necessitates a defined 'monolayer'-like coverage of Au-oxide on the surface. From the literature we obtain a upl value of $E = 1.75 V_{\text{RHE}} (= 1.69 V_{\text{SHE}} = 1.05 V_{\text{MSE}})$, at which a 'monolayer' coverage of gold-oxide on the surface is achieved [Ham96; LSC16; GK21b].

Consequently, we determine the electrochemical active surface area (ECSA) via the transferred charge during the Au-oxide reduction Q_{red} obtained in a CV with a scan rate of 50 mV s^{-1} using $E = 1.75 V_{\text{RHE}}$ as the upper potential limit via:

$$A_{\text{ECSA,Au}} = \frac{Q_{\text{red}}}{q_{\text{Au}}} \quad (3.9)$$

Here $q_{\text{Au}} = 390 \mu\text{C cm}^{-2}$ is the well accepted specific surface charge value [TP91; BF01]. In the further course of this work the term 'area' is equivalent to the electrochemical active surface area, if not explicitly labeled differently.

From Figure 3.15(b) we can further determine the roughness factor (RF) of typically evaporated Au films investigated in this work. The RF is defined as:

$$RF = \frac{A_{\text{ECSA}}}{A_{\text{geo}}} = \frac{Q_{\text{red}}/A_{\text{geo}}}{q_{\text{Au}}} \quad (3.10)$$

We determine from the figure $Q_{\text{red}}/A_{\text{geo}} \approx 590 \mu\text{C cm}^{-2}$ (orange arrows). This value divided by q_{Au} results in a roughness factor of $RF \approx 1.5$ for the Au surfaces investigated in this work.

The determination of the area by oxidation/reduction cycling in the mentioned potential range does not lead to a significant dissolution of gold during one oxidation/reduction cycle. It can be calculated from the measurements conducted by Cherevko et al. [Che+13] that during one 50 mV s^{-1} cycle in this range only $10 \mu\text{C cm}^{-2}$ of Au^+ ions are dissolved, which equals approx. 1/40 monolayers of gold atoms. Thus, the gold surface appears to be rather stable for moderate numbers of cycles conducted in the mentioned potential range.

Pt-based electrodes

The ECSA of Pt-based electrodes is determined via the charge transferred during proton adsorption and desorption (H-UPD) in Ar saturated acidic electrolyte (0.1M H_2SO_4 , pH 1). This is widely accepted as the standard method for determining the active surface area of Pt-based electrodes [TP91]. Figure 3.16 shows a CV of a Pt-layer evaporated on a n-doped silicon substrate in the H-UPD region. The appearing cathodic peaks are assigned to proton adsorption, the anodic peaks to proton desorption. The presented peak ensemble shape in the H-UPD region is typical for a poly-crystalline Pt electrode [Rhe+14].

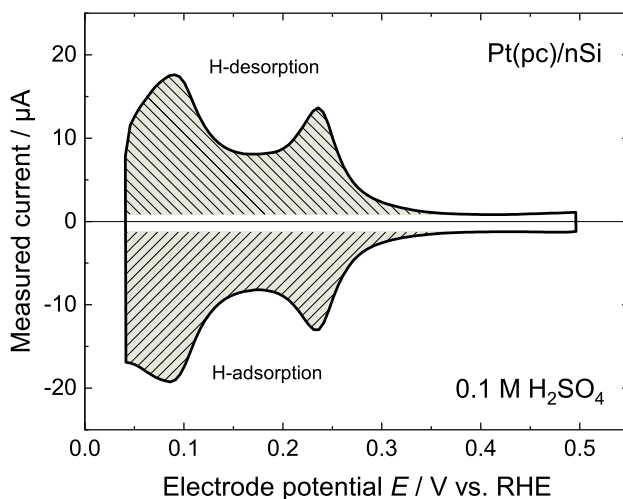


Figure 3.16: CV in the H-UPD region of a Pt(pc) layer deposited on n-doped silicon measured in 0.1M $\text{H}_2\text{SO}_4/\text{Ar}$ sat.'d (pH 1). Scan rate: 50 mV s^{-1} . The charge transferred during H-ad- and desorption (filled areas) is used to determine the electrochemical active surface area (ECSA) for Pt-based electrodes in this work.

The transferred charge during proton ad- and desorption, Q_{ad} and Q_{des} respectively, is calculated by subtracting the respective (constant) double layer charging current $i_{\text{DL},i}$ via:

$$Q_{\text{ad}} = \left| \frac{1}{\nu} \int (i(E) - i_{\text{DL,c}}) dE \right| \quad (3.11)$$

$$Q_{\text{des}} = \frac{1}{\nu} \int (i(E) - i_{\text{DL,a}}) dE \quad (3.12)$$

The scan for determining the area is conducted below $0.5 V_{\text{RHE}}$ to avoid any cathodic parasitic current coming from PtOx reduction and HSO_4^- ad-/desorption. The upper potential limits for integration is chosen where the minimum currents are observed during the scans (around $0.4 V_{\text{RHE}}$), the lower potential limit is chosen as $0.04 V_{\text{RHE}}$. The choice of the lower limit is rather positive to avoid any contribution of HER during the area measurement. We will see later that HER on structured electrodes appears at a more positive potential than observed for continuous Pt electrodes, cf. results in section 6.1.3. However, the choice of the rather positive potential leads to a slight underestimation of the actual real area, when comparing to literature data.

The area is then determined by dividing the average transferred charge by the specific surface charge of H-UPD $q_{\text{Pt}} = 210 \mu\text{C cm}^{-2}$ [TP91]:

$$A_{\text{ECSA,Pt}} = \frac{(Q_{\text{ad}} + Q_{\text{des}})/2}{q_{\text{Pt}}} \quad (3.13)$$

Cu-based electrodes

Cu is deposited onto the Au surface of the sample by electrochemical Cu deposition. The parameters are chosen in a way that much more than one monolayer of Cu atoms is deposited onto the surface. We use the determined area of the underlying Au surface for normalizing the current of electrodes with deposited Cu, although the Au is covered by Cu during the experiment. Consequently, we do not consider any changes in roughness of the surface coming from the Cu deposition. A different roughness may occur when the Cu is inhomogeneously deposited onto the surface, exemplarily caused by transport limitation of Cu ions during deposition.

Chapter 4

Electrochemical behavior of nanostructured metal/p-Si photoelectrodes

In this chapter, we analyze p-doped silicon-based photoelectrodes patterned with a metal nanostructure array in CO₂-saturated and Ar-saturated aqueous electrolyte. First, we examine the electrochemical and electrocatalytic behavior regarding CO₂ Reduction Reaction (CO₂RR) (cf. section 4.1). In order to understand the complex response of the illuminated electrolyte/MIS system, the electrical and electrochemical behavior of this system expected from theory is elaborated by simulation and compared to the experiment (cf. section 4.2). Afterwards, we investigate the Hydrogen Evolution Reaction (HER) on photoelectrodes patterned with Au-based nanostructures (cf. section 4.3). We close this chapter by investigating HER on photoelectrodes with Pt-based nanostructures and with the discussion, under which conditions it is possible to determine the kinetics of cathodic reactions proceeding on the photoelectrodes presented here (cf. section 4.4).

4.1 General behavior of Au/p-Si photoelectrodes

In this section, the general electrochemical behavior of photoelectrodes with Au nanostructures in CO₂-saturated electrolyte is analyzed. The photoelectrodes investigated here consist of an array of Au structures deposited on a p-doped silicon substrate (resistivity 1-10 Ω cm), with a thermal silicon oxide 'passivation layer' surrounding the structures (cf. section 3.1.1 for more information regarding the design of the samples investigated).

The actual metal stack consists of Au/Ti/SiO₂/p-Si interfaces and constitutes a MIS junction. As already shown in section 3.1.3, the electrical response of the MIS junction of the photoelectrodes analyzed here exhibits a typical diode behavior (Schottky diode) in the relevant current density range. The diode is reverse biased in cathodic direction. The operation of the diodic photoelectrodes under reverse bias conditions is of particular interest, since the reduction reactions of interest, i.e. CO₂RR and HER, appear at a negative polarization of the electrode, i.e. in cathodic direction. Thus, there is the need for illuminating the photoelectrodes to make an investigation of cathodic reactions possible. As in cathodic direction the current is limited by illumination, the rate of the reactions can be governed by the intensity of the employed illumination.

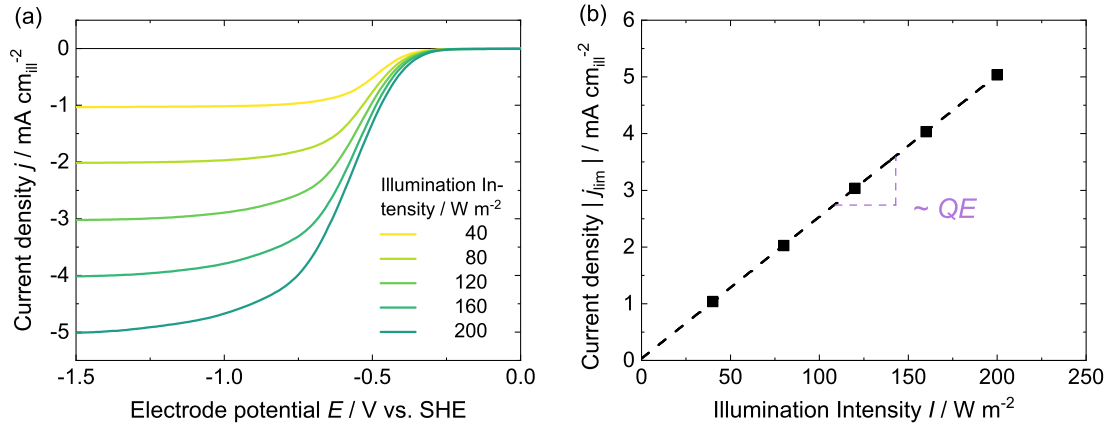


Figure 4.1: (a) LSVs of an illuminated structured photoelectrode (Au structures of size 200 nm) in contact with the electrolyte for different illumination intensities at 444 nm wavelength. (b) Limiting current density j_{lim} (determined at $-1.5 \text{ V}_{\text{SHE}}$) plotted over the illumination intensity. The limiting current density scales linearly with the intensity (dashed black line) due to the constant quantum efficiency of the electrode. Scan rate: 50 mV/s. Electrolyte: 75mM K_2CO_3 , 100mM H_3PO_4 , CO_2 sat. The current is normalized to the total illuminated area. Taken with modifications from [Fil+18].

This becomes clear in Figure 4.1(a), which shows linear scan voltammograms (LSVs) of an exemplary structured photoelectrode (200 nm Au structure size) in contact with an electrolyte (75mM K_2CO_3 , 100mM H_3PO_4 , CO_2 sat.) at various illumination intensities. The illumination is monochromatic with a wavelength of 444 nm. The scans are performed in negative potential direction with a scan rate of 50 mV s^{-1} . The cathodic current present in the LSV starting at small negative overpotentials is composed of HER and CO_2RR , which can both occur in this electrolyte at these overpotentials. When further decreasing the electrode potential, the measured current saturates, i.e. it becomes constant and rather independent of the applied potential. This region is referred as 'saturation region'. The actual 'starting potential' of this regime depends on the illumination intensity and shifts more negatively for increasing illumination intensity.

In the saturation region, the measured current is determined by the Schottky device. The current is limited by the number of photoexcited charge carriers, which do not recombine within their diffusion/migration length, reach the electrode surface, and can participate in the electrochemical reaction. The proportionality between the rate of incoming photons \dot{N}_{ph} and the rate of free charge carriers participating in the reaction \dot{N}_e is given by the quantum efficiency QE of the system.

$$\dot{N}_e \equiv QE \cdot \dot{N}_{\text{ph}} \quad \Rightarrow \quad \frac{i}{e} = QE \cdot \frac{\lambda}{hc} A_{\text{ill}} I \quad (4.1)$$

Here, i is the measured electrical photocurrent, e is the elementary charge, A_{ill} is the illuminated area, λ is the wavelength of the incoming photons, I is the illumination intensity (in W m^{-2}), h is Planks constant, and c is the speed of light. In the saturation region, nearly all excited charge carriers can reach the electrode surface due to the large electric field present inside the device. Consequently, the measured current becomes approx. constant ('saturation current') for very large overpotentials. Plotting the saturation current density j_{lim} over the illumination intensity I should give a linear correlation:

$$j_{\text{lim}} = QE \cdot \frac{e\lambda}{hc} I \quad (4.2)$$

This linear dependence is clearly visible in Figure 4.1(b), in which the limiting current density determined at $E = -1.5 V_{\text{SHE}}$ is plotted over the illumination intensity I . From the linear dependence the quantum efficiency of the system can be determined via the slope of the linear fit. In the given example a quantum efficiency of 70% is calculated for the nanostructured electrode and the given system parameters.

The photoelectrochemical response of these kinds of electrodes at finite illumination under reverse biasing condition is, consequently, not just determined by the properties of the electrode/electrolyte interface, but also by the electrical response of the MIS device. This becomes clear, when conducting chronoamperometric experiments.

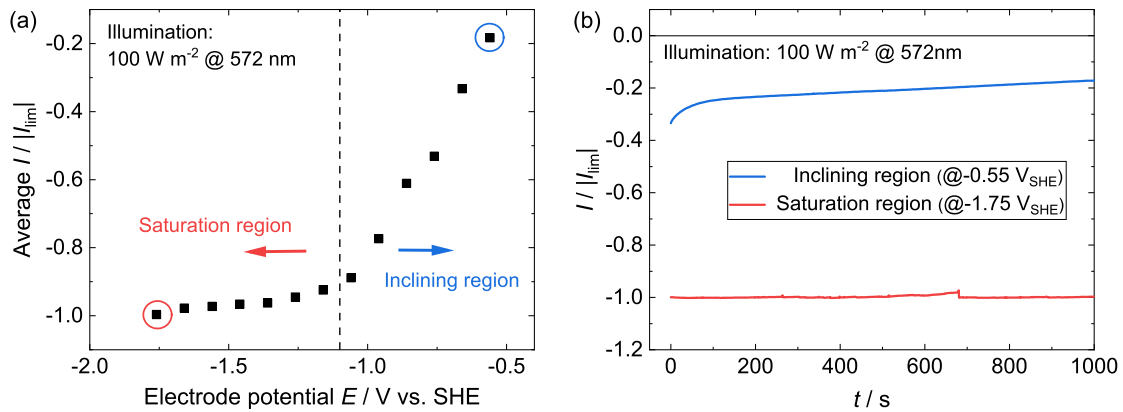


Figure 4.2: Behavior of measured current in potential step experiments conducted at various electrode potentials on a structured photoelectrode (Au structures of size 200 nm). (a) Average current during chronoamperometric potential step experiments plotted over the applied potential. (b) I - t curves at two selected potentials in either the inclining region (blue) or the saturation region (red). The measured current I is normalized to the absolute value of the limiting current $|I_{\text{lim}}|$ measured at $-1.75 V_{\text{SHE}}$. Applied illumination intensity: 100 W m^{-2} ; Wavelength: 572 nm. The images are taken with modifications from [Mai17].

Figure 4.2(a) shows the time averaged current I of chronoamperometric measurements conducted at several applied electrode potentials E , ranging from the 'inclining region' (i.e. the potential region, in which the current increases with decreasing potential, here approx. above $-1.1 V_{\text{SHE}}$), towards the saturation region (here approx. below $-1.1 V_{\text{SHE}}$). The currents averaged over time in postentostatic (i.e. chronoamperometric) measurements plotted over the actual applied electrode potential follow the same qualitative behavior with decreasing potential, as it could be observed in the LSVs mentioned before.

However, the actual chronoamperometric trend, when applying a potential step in either the inclining or the saturation region, exhibits a very different behavior. Figure 4.2(b) shows the I - t curves at two exemplary potentials, at $-0.55 V_{\text{SHE}}$ (in the inclining region, blue) and at $-1.75 V_{\text{SHE}}$ (in the saturation region, red). When applying a potential in the inclining region, the absolute value of the current decreases with time. This behavior is usually expected for electrochemical potential step experiments due to the build-up of the diffusion layer with time known from Cottrell experiments, cf. [BF01]. However, applying a potential in the saturation region exhibits a constant current with time, which is, for now, a rather unexpected behavior. The spike in the red curve at approx. 700 s is probably due to a detaching gas bubble at the electrode surface.

As already mentioned above, in this system the cathodic current drawn consists of both, HER and CO₂RR. Thus, we can analyze the produced product gas in order to determine the share of the two different reactions on the total measured current, which may give further insights. Hori et al. [Hor+87] investigated Au-based electrodes in CO₂-saturated electrolyte and found that the product spectrum of CO₂RR/HER is strongly potential dependent. They found that CO₂RR to CO is dominating at low cathodic overpotential, while for increasing overpotential HER becomes more and more predominant. Thus, the dependence of the product spectrum on the applied potential can give further insights in the occurring reactions appearing at the two distinct potential ranges.

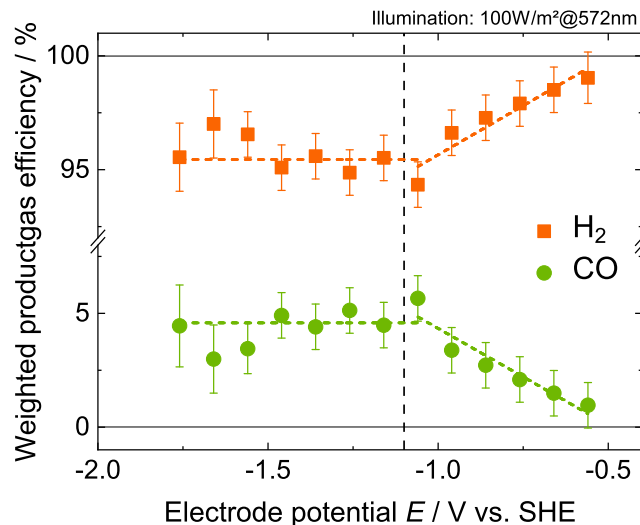


Figure 4.3: Weighted product gas efficiency of electrolysis measurements performed on a photoelectrode with 200 nm structure size in 75mM K₂CO₃, 100mM H₃PO₄, CO₂ sat.'d. Illumination: Intensity 100 W m⁻², wavelength 572 nm. Dashed lines are a guide to the eye. Taken with modifications from [Mai17].

Figure 4.3 shows the product gas distribution (weighted product gas efficiency) as a function of the electrode potential. The product gas is measured with a gas-chromatograph setup [Mai17]. It is visible in the Figure that the product gas distribution changes with decreasing potential in the inclining region, i.e. the ratio of produced CO gas compared to H₂ gas increases. This is the expected behavior according to Hori et al. However, in the saturation region the product ratio is approximately constant, i.e. it does not change with the applied potential. This is indicated by the horizontal dashed lines at potentials below $-1.1 V_{SHE}$. This behavior is not expected considering the results of Hori et al. [Hor+87]. However, this behavior may be attributed to the dominating contribution of the MIS junction to the total electrode behavior.

In order to understand the experimentally observed behavior and to examine, how the Schottky-MIS interface determines the measurable electrochemical response of the photoelectrodes, the overpotential distribution between the electrolyte/metal and the MIS junction is simulated in the following section.

4.2 Simulating the overpotential-distribution in the combined junction

In order to further understand the differing electrocatalytic behavior of the photoelectrodes compared to photo-inactive electrodes (e.g. bare metal surfaces as used by Hori et al.), we model the overpotential distribution in this combined junction system theoretically. When performing potentiostatic/amperometric experiments with this combined system, the *total* applied voltage η_{app} across the whole junction consisting of the electrolyte/metal and the MIS interface is controlled. However, the electrocatalytic properties, e.g. the selectivity, are not determined by the total applied voltage, but by the fraction of voltage dropping at the electrode/electrolyte interface. Nevertheless, both interfaces are coupled as they are placed in series. Here, we model the overpotential distribution in the combined system qualitatively when applying a voltage η_{app} to the whole system.

As shown experimentally, the MIS junction present in the investigated photoelectrodes shows a typical diode behavior (cf. Figure 3.7(a)). Thus, its electrical response can be modeled by the typical response of an illuminated diode. The current-voltage characteristics of an illuminated diode is given by [KS15]:

$$I_{\text{di}}(\eta_{\text{di}}) = I_{\text{lim}} \left[\exp\left(\frac{e \eta_{\text{di}}}{k_B T}\right) - 1 \right] \quad (4.3)$$

Here I_{di} is the current flowing through the diode, η_{di} is the voltage at the diode ($\eta_{\text{di}} = 0$ is tantamount to open circuit condition), $I_{\text{lim}} > 0$ is the limiting saturation current for reverse bias (including the photocurrent induced by illumination). The qualitative current-voltage behavior is shown in Figure 4.4(a).

The electrical response of the electrode/electrolyte interface can be modeled by the Butler-Volmer model, considering that the current is kinetically limited. This approach is quite reasonable, as the electrolyte resistance as well as the absolute current density considered in the experimental configuration is comparatively small. The current-voltage characteristics of the electrode/electrolyte interface is in general given by [BF01]:

$$I_{\text{el}}(\eta_{\text{el}}) = I_0 \left[\exp\left(\frac{\alpha_a F}{RT} \eta_{\text{el}}\right) - \exp\left(-\frac{\alpha_c F}{RT} \eta_{\text{el}}\right) \right] \quad (4.4)$$

Here I_{el} is the current flowing across the electrode/electrolyte interface, I_0 is the exchange current, and η_{el} is voltage at the electrode/electrolyte interface. The other quantities are explained in section 2.3. The qualitative behavior of the reaction kinetics is shown in Figure 4.4(b).

When combining these two interfaces and performing potentiostatic experiments, the total applied voltage η_{app} , which is the sum of the individual voltages dropping at the respective interfaces, is set. The resulting current I flowing through the system is identical at both interfaces, since the interfaces are connected in series. Thus, we get the following conditions:

$$\eta_{\text{app}} = \eta_{\text{di}} + \eta_{\text{el}} \quad (4.5)$$

$$I = I_{\text{di}} = I_{\text{el}} \quad (4.6)$$

This set of equations together with equations (4.3) and (4.4) can be solved easily by root-finding algorithms, which we apply in a self-written Python code.

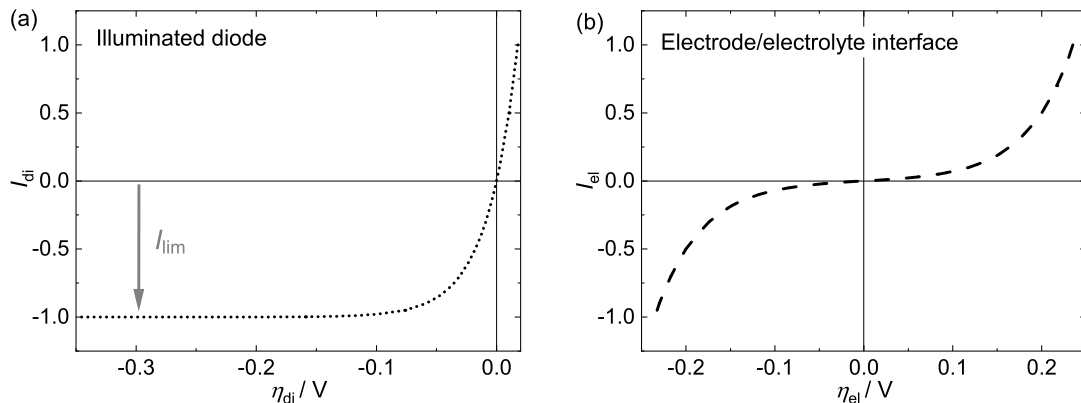


Figure 4.4: Current-voltage characteristics of the individual junctions, modeled as functions of the individual junction (over)voltages η_i . (a) Illuminated diode. Its dependence is given by equation (4.3) with $I_{lim} = 1$. (b) Electrode/electrolyte interface. Its dependence is given by equation (4.4) with $I_0 = 10^{-2}$, $\alpha_a = \alpha_c = 0.5$.

Figure 4.5(a) shows the calculated current I as a function of applied voltage η_{app} on the combined device for an exemplary set of parameters. The exact behavior of the curve depends on the chosen physical parameters of the systems (e.g. I_0 , I_{lim} , etc.). At small negative voltages, the current characteristics follows the Butler-Volmer curve. At far negative voltages, the current saturates, i.e. follows the diode curve. Consequently, the modeled device shows qualitatively the same behavior as we have observed experimentally in Figure 4.1(a).

Figure 4.5(b) shows the calculated individual voltages η_i dropping at the respective interfaces as a function of the total applied voltage η_{app} . We note that at small (negative) voltages most of the applied voltage drops at the electrode/electrolyte interface. With further decreasing voltage, a larger share drops at the diode. At a certain voltage (here at approx. -0.3 V) nearly the whole voltage applied additionally drops at the diode interface and only a minor share of the additionally applied voltage drops at the electrode/electrolyte interface.

Estimation of the I - t characteristics for potential step experiments

We have seen in the previous paragraph that the actual fraction of applied voltage dropping at the individual interfaces changes with the applied voltage for stationary conditions. However, the question remains how the voltage at an individual interface changes with time when performing a potential step experiment.

Consequently, we now model the chronoamperometric (I - t) behavior of the hetero-interface, which comprises the diode and the electrochemical interface in series, in a potential step experiment. The sum of the individual junction voltages is determined by the applied voltage and, thus, is constant in this kind of experiment at $t \geq 0$. However, the individual voltages dropping at the respective junctions can change with time. This implication can further influence the current-time characteristics of the combined junction. Although we explicitly model the time evolution, equations (4.5) and (4.6) still hold.

The time dependence of the system stems from the limited transport rate of reactants towards the surface. It is assumed that the transport of photoexcited electrons participating

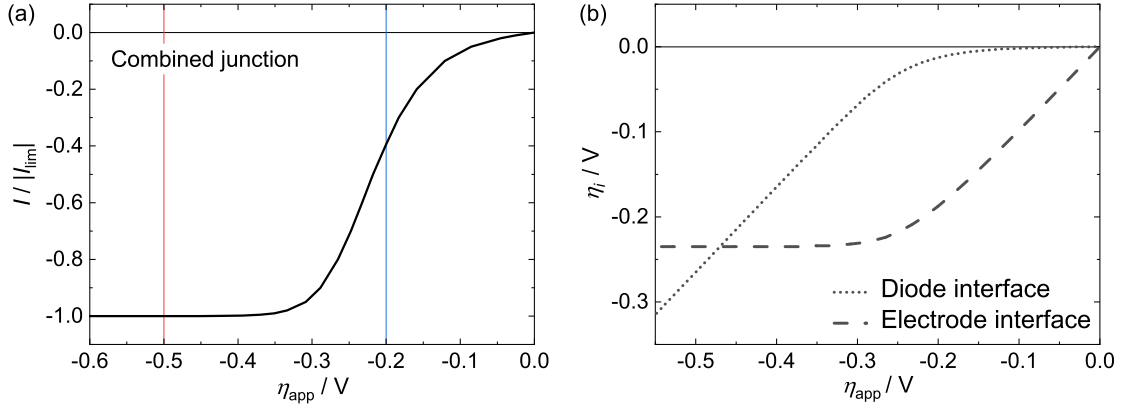


Figure 4.5: Simulated characteristics of the series connection of an illuminated diode and an electrode/electrolyte interface. (a) Current I as a function of the total applied voltage η_{app} . The characteristic shows the same qualitative behavior as the experimentally observed one in Figure 4.1(a). (b) Individual junction voltages η_i dropping at the diode (dotted) and electrode/electrolyte interface (dashed), respectively, plotted over η_{app} . At small applied voltages, most of the voltage drops at the electrode interface. At quite negative voltages ($\eta_{app} < -0.3$ V), the whole voltage applied additionally drops at the diode interface.

in the reaction coming from the semiconductor bulk is very fast. Thus, we assume that I_{di} is still stationary, i.e. not explicitly time dependent and, consequently, is still given by equation (4.3). However, the transport of reactants (here oxidized species) from the electrolyte bulk to the surface may be slow as it is determined by diffusion. Thus, we consider the current at the electrode/electrolyte interface being explicitly potential *and* time dependent and approximate its behavior by the following Cottrell-like equation:

$$I_{el}(\eta_{el}, t) = -I_0 \operatorname{erf}\left(\frac{a}{\sqrt{t}}\right) \exp(-b \eta_{el}) \quad (4.7)$$

with a and b being constants. This equation can be derived from the concentration dependent Butler-Volmer equation considering diffusive transport of reactants. Its derivation is given in the appendix A.8. The set of the mentioned equations can, again, be solved by root-finding algorithms. Here, we use $a = 0.5 \times 10^{-5} \text{ s}^{1/2}$ and $b = 20 \text{ V}^{-1}$ for the simulation. All other constants remain the same.

Figure 4.6(a) shows current-time dependencies of the modeled combined junction when conducting potentiostatic experiments in either the inclining region, exemplary at $\eta_{app} = -0.2$ V (blue line), or in the saturation region, exemplary at $\eta_{app} = -0.5$ V (red line). These two voltages are also indicated in the current-voltage characteristics of the combined device in Figure 4.5(a) by the blue and red line, respectively. It can be seen that the current decreases with time for a voltage applied in the inclining region, while it stays constant for a voltage applied in the saturation region. This is remarkable as the behavior of this modeled device depicts qualitatively the same time dependencies as observed experimentally, cf. Figure 4.2(b).

In order to understand this behavior, we analyze the individual junction voltages as a function of time. Figure 4.6(b) shows the time dependencies of the individual voltages at the two junctions normalized to the total applied voltage. Their behavior now further clarifies the observed behavior of the combined device: When conducting potentiostatic experiments in the inclining region (blue), a large share of the applied voltage drops at

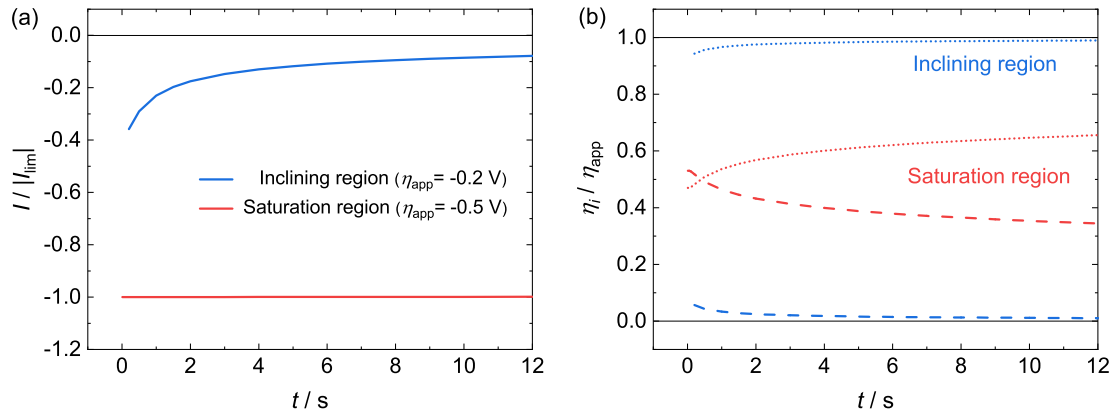


Figure 4.6: Time dependencies of the modeled combined junction device for potentiostatic experiments. (a) Current as a function of time when applying a total overpotential η_{app} in the inclining (blue) or saturation (red) region. The simulation shows qualitatively the same behavior as it could be experimentally observed in Figure 4.2. (b) Share of the respective overpotential dropping at either the electrode/electrolyte interface (dotted) or the MIS (dashed) interface as a function of time. Note that still condition $\eta_{app} = \eta_{di} + \eta_{el} = \text{const.}$ applies here.

the electrode/electrolyte interface (dotted lines), already from the start of the experiment at $t = 0$. The voltage dropping at the diode (dashed lines) is comparatively small. Both voltages stay approx. constant with time and show only minor changes. Thus, the behavior of the device is dominated by the electrode/electrolyte interface, which limits the current. This results in the typical $1/\sqrt{t}$ behavior of the current flowing through the whole device, which can be observed in Figure 4.6(a) as the blue line. When conducting potentiostatic experiments in the saturation region (red), the voltage dropping across the electrode/electrolyte interface increases with time (dotted red line). The voltage dropping at the diode interface decreases with time (dashed red line), which is necessary to keep condition (4.5) fulfilled. Thus, the diode interface is able to 'buffer' the electrode interface. This means it can enable an increasing voltage drop at electrode/electrolyte interface, while keeping the current flowing through the device almost constant at the same time. This is due to its saturating behavior at far negative potentials. This circumstance finally leads to a constant current-time dependence of the combined electrolyte/MIS system, as observable in Figure 4.6(a), red line.

We can conclude from this simulation: In the saturation region, the measured current is almost independent of the actual applied voltage η_{app} , as most of the additionally applied voltage drops at the diode junction. As a consequence, the voltage dropping at the electrode/electrolyte interface is also nearly independent of the actual applied voltage in this region. This further explains, why the product distribution of electrolysis experiments conducted in the saturation region do not change when further decreasing η_{app} : As most of the additionally applied voltage drops at the diode interface and not at the electrode/electrolyte interface, the selectivity of the electrode stays constant within the saturation region. In addition, the diode interface buffers the time dependence of the system, as it counteracts the decreasing concentration of educts at the electrode surface by increasing the potential drop at the electrochemical interface such that the current is kept constant. This leads to an almost constant behavior of the measured current with time of the combined electrolyte/MIS device in potentiostatic experiments.

4.3 Increasing HER activity with decreasing structure size

In the previous section we showed that, at current densities well below the limiting current density for a given illumination, the electrochemical response of the electrodes is determined by the electrode/electrolyte interface, as most of the applied voltage drops at this interface. Let us now take a closer look on the electrocatalytic behavior of the photoelectrodes with Au structures of various sizes. We change the diameter of the gold structures present on the electrode surface, while keeping the coverage of the gold structures on the surface constant. A similar coverage is necessary for comparing the different photoelectrodes, as this ensures a similar absorption area and, thus, a similar rate of absorbed photons.

In previous works [Mai17; Fil+18], we analyzed the behavior of these nanostructured photoelectrodes in CO_2 containing neutral electrolyte (75 mM K_2CO_3 , 100 mM H_3PO_4 , CO_2 sat.'d) for different sizes of gold structures present on the surface regarding HER and CO_2RR . As already mentioned, in this system both HER and CO_2RR can proceed at negative overpotential. We measured the current-potential curves of the structured photoelectrodes as well as the product spectrum of potentiostatic electrolysis measurements performed in the saturation region: Figure 4.7(a) shows LSVs of the structured photoelectrodes in the mentioned system. The scan goes in negative direction with a scan rate of 100 mV s^{-1} . The illumination intensity is 200 W m^{-2} at 444 nm for all measurements considered here. In addition, we performed potentiostatic chronoamperometric measurements in the saturation regime and analyzed the produced gas in a gas chromatograph setup [Mai17]. Note that we applied the same overpotential in each measurement (far in the saturation region, at $-1.76 \text{ V}_{\text{SHE}}$), but could vary the drawn current at this potential by varying the illumination intensity. Figure 4.7(b) shows the weighted product gas efficiency as a function of the (saturation) current density measured during electrolysis, whereby the current was set by the illumination intensity, not by the applied potential.

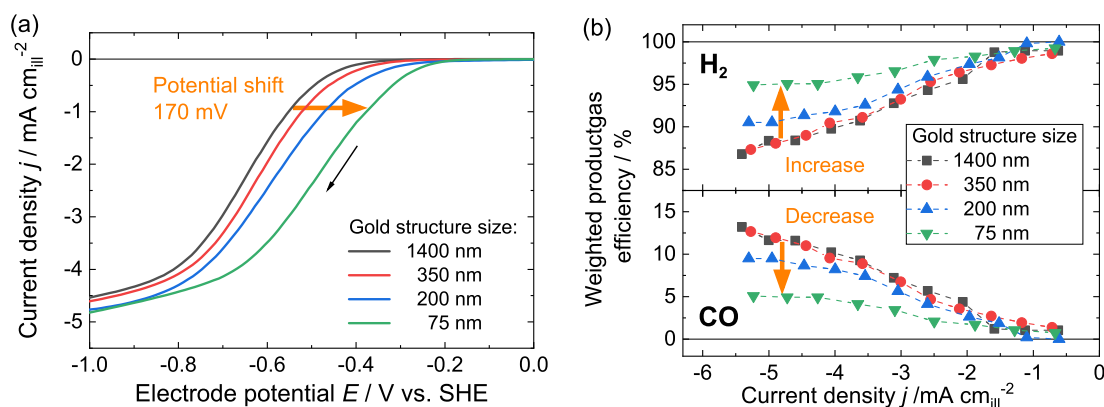


Figure 4.7: Electrocatalytic behavior of illuminated Au structured photoelectrodes with various structure sizes. (a) LSVs in 75 mM K_2CO_3 , 100 mM H_3PO_4 , CO_2 sat.'d electrolyte. Illumination: Intensity 200 W m^{-2} , 444 nm peak wavelength (FWHM: 12 nm). Scan rate 100 mV s^{-1} . (b) Weighted product gas efficiencies of electrolysis measurements plotted over the average current density during electrolysis (i.e. the limiting current density). Taken with modifications from [Fil+18].

We could make the following observations:

1. In the kinetically limited region, the overpotential necessary to draw a certain current density decreases with decreasing structure size (Figure 4.7(a), orange arrow). A potential shift of ≈ 170 mV can be observed at -1 mA cm $^{-2}$.
2. The share of the hydrogen gas production rate increases compared to the share of the CO gas production rate with decreasing structure size, i.e. HER is preferred over CO₂RR (Figure 4.7(b), orange arrows).

The decrease of overpotential necessary to draw a certain current density occurs at current densities well below the saturation current. At these potentials, the response of the system is determined by the kinetics at electrode/electrolyte interface (see previous section). In addition, experiments conducted with electrodes consisting of differently doped silicon substrates (p⁺⁺ doping) showed a similar trend: The overpotential necessary to draw a certain current density decreased with decreasing structure size [Fil+18]. Thus, we concluded that this improvement with decreasing structures size does not stem from changed properties of the MIS junction at the diode interface, but is caused by a mechanism occurring at the electrode/electrolyte interface. Together with the observation that the hydrogen production rate increases with decreasing structure size, we could conclude that there is some mechanism which selectively increases the hydrogen evolution reaction activity.

Although the electrodes are designed in a way that the absorption efficiency is approx. similar for all geometries due to their similar gold coverage, the individual electrodes may have different contact properties, such as the defect density at the MIS interface, which can lead to a different photoresponse. Consequently, a further quantitative analysis of the electrodes with each other and, thus, a more detailed analysis of the HER improvement is hardly possible in this configuration.

To further confirm the conjectured enhanced HER activity for smaller structures, we investigate Au structured photoelectrodes under various electrochemical conditions in the absence of CO₂: HER in acidic electrolyte based on 0.1 M H₂SO₄ (pH 1) and in alkaline electrolyte based on 0.1 M NaOH (pH 13). The electrolytes are continuously purged by Ar gas in order to avoid O₂ or CO₂ reduction in the signal. In these two very different pH regimes HER occurs via two different mechanisms: In acidic electrolyte the hydrogen evolution occurs from the reduction of protons, while in alkaline electrolyte it occurs from water reduction. The respective mechanisms are shown in section 2.4.1. In this configuration, appearing differences can be directly attributed to the electrode/electrolyte interface, as illumination properties are kept constant and the MIS contact behavior is supposed to be independent of the electrolyte properties.

Figure 4.8 shows LSV curves of an electrode with (a) 1400 nm gold structure size and (b) 75 nm gold structure size in the two mentioned electrolytes. The measured photocurrent j_{photo} is normalized to the limiting current $|j_{\text{sat}}|$ determined at -0.8 V_{RHE}. Comparing the curves of the 1400 nm electrode, one sees that the black dashed curve measured at pH 13 is shifted towards more negative potentials compared to the black solid curve measured at pH 1, i.e. a larger overpotential has to be applied to draw the same current density. This is the expected behavior, since the hydrogen evolution at pH 13 occurs via water splitting. This mechanism is supposed to be kinetically slower than HER from protons at pH 1. Consequently, a larger overpotential needs to be applied to draw the same current.

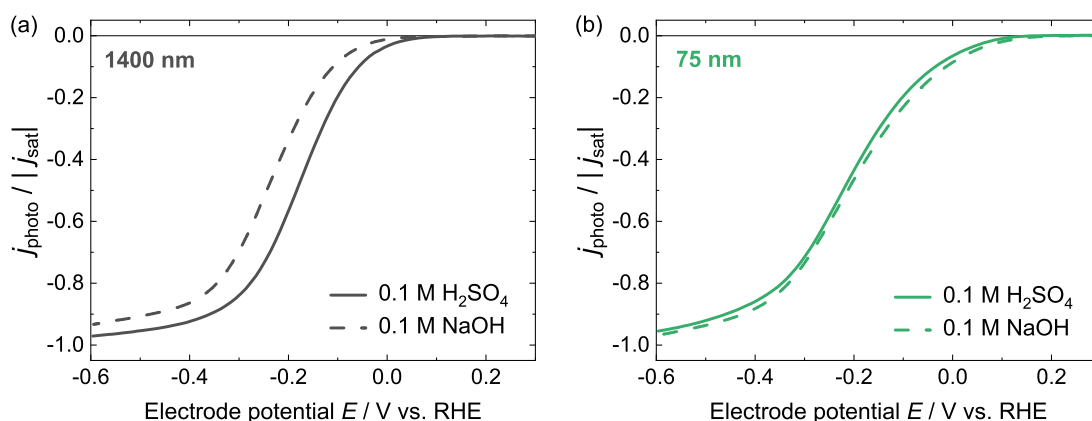


Figure 4.8: LSVs of two structured photoelectrodes with (a) 1400nm structure size and (b) 75nm structure size in either 0.1 M H_2SO_4 (pH 1) (solid lines) or 0.1 M NaOH (pH 13) (dashed lines). Scan rate: 50 mV s^{-1} . Illumination: Intensity 100 W m^{-2} , 444 nm peak wavelength (FWHM: 12 nm). Taken with modifications from [Mai+20].

The 75 nm electrode shows a contrary behavior. The green dashed curved measured at pH 13 lies nearly on top of the solid green curve measured at pH 1. In the alkaline electrolyte no additional overpotential has to be applied at the 75 nm electrode in order to drive the same currents as in acidic electrolyte.

Consequently, we can conclude that HER in alkaline electrolyte is (more) enhanced for the 75 nm photoelectrode than it is for the 1400 nm photoelectrode. Note again that this effect can not be caused by the photoresponse of the photoelectrodes, as illumination is kept constant for both media. This effect has likely the same underlying mechanistic reason as the structure size dependent HER improvement shown in Figure 4.7, since in neutral pH the HER reaction likely occurs via water reduction due to the rather low concentration of protons in the electrolyte. However, since there is still the need for illumination of the system and there is, consequently, a photoresponse of the photoelectrode, a quantitative analysis is challenging. A more detailed analysis of the underlying mechanism is given in the next chapter 5. In this chapter, MIS electrodes with an ohmic contact are employed, where the direct comparison between the different electrodes can be conducted easier.

4.4 Investigation of Pt-based structures

The flexibility of the electrode fabrication method further allows for a straight forward fabrication of nanostructured photoelectrodes, which use Pt as the catalyst material, but are similarly composited otherwise. The electrical contact at the Pt/silicon interface is still dominated by the Ti adhesion layer (cf. chapter 2.1.1), which leads to a very similar photoresponse of these kinds of electrodes with respect to the Au-based photoelectrodes mentioned in the section before. However, the electrochemical and electrocatalytic properties of the electrodes, especially regarding HER, change significantly. This is further analyzed in the following.

Figure 4.9 shows a CV of an illuminated photoelectrode with Pt structures of size 1400 nm in 0.1 M H_2SO_4 . Here, the illumination is 15 W m^{-2} using the non-monochromatic LSW-2 lamp (spectrum is shown in Figure 3.9(b)). The CV clearly shows the distinct features of

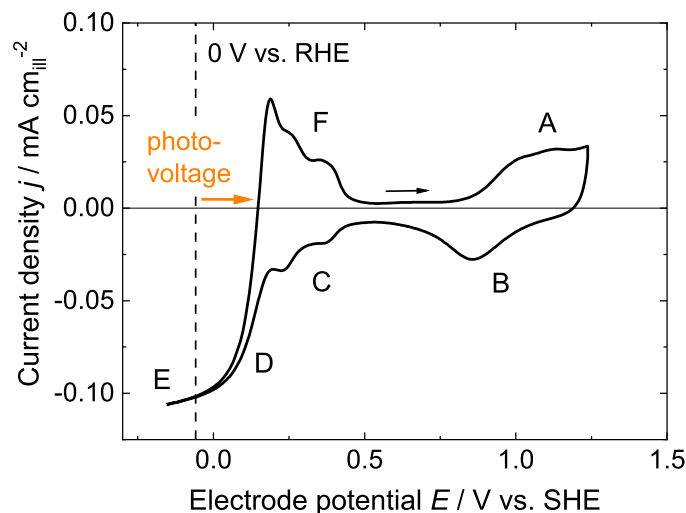


Figure 4.9: CV of an illuminated photoelectrode with Pt structures of size 1400 nm at 15 W m^{-2} (multispectral LSW-2 lamp). Electrolyte: $0.1 \text{ M H}_2\text{SO}_4/\text{Ar sat.}$ Labeled features are explained in the text. Scan rate: 50 mV s^{-1} . The measured current is normalized to the total illuminated area determined by the aperture used.

a Pt(pc) electrode in acidic electrolyte [Rhe+14]: The positive anodic peak A is due to the oxidation of the Pt surface. The Pt oxide is subsequently reduced in the downward scan, visible in peak B. After the valley the characteristic cathodic peak pair C of hydrogen under potential deposition (H-UPD) is visible, which pass over into the hydrogen evolution reaction D. The current starts to saturate at E, which is known behavior indicative of a Schottky-diode contact at the M/SC interface and already discussed in the previous sections. The anodic peak ensemble F consists partly of the oxidation of the produced hydrogen gas as well as the desorption of the under-potential-deposited hydrogen. It appears that the whole CV is shifted towards positive potential compared to literature data. This is clearly visible in the zero-crossing of the upwards scan between E and F. This zero crossing is indicative of the equilibrium potential of the $2\text{H}^+ + 2\text{e}^- \rightleftharpoons \text{H}_2$ reaction and is supposed to be around 0 V_{RHE} . The positive shift is due to photovoltage induced in the device.

The graph shows that photoelectrodes consisting of Pt structures exhibit the electrochemical features of Pt as well as the photosensitive behavior. Furthermore, the saturation current also scales linearly with the illumination intensity (not shown), which makes a calculation of the quantum efficiency straight forward. The determined QE s for the electrodes fabricated at the given parameters range from 17% (1400 nm) to 27% (75 nm). This difference is probably caused by the different diffusion length of electrons. For a larger pitch of the array photo-generated electrons need to cover a greater distance to reach the reaction site. A longer diffusion length leads to higher recombination rates and, consequently, to a lower QE . Moreover, the difference of individual electrodes may stem from minor differences in the fabrication procedure, i.e. the defect density at the MIS interface. Although the difference in the QE s reduces the comparability of the electrodes regarding electrocatalytic properties slightly, a qualitative comparison of the HER kinetics between the different structure sizes is still possible. The reason is that Pt has a good activity for the oxidation of hydrogen gas, contrary to Au. Thus, when using an hydrogen saturated electrolyte, the equilibrium potential of HER/HOR is well defined, which makes it possible to analyze the kinetics of HER/HOR via Tafel analysis, as the 'zero crossing'

with the y -Axis (the intercept) in the logarithmic plot of the current density is known. A different photoresponse of the system, which can lead to an altered induced photovoltage at similar illumination intensity, does not lead to a miss-interpretation as an altered electrode kinetics.

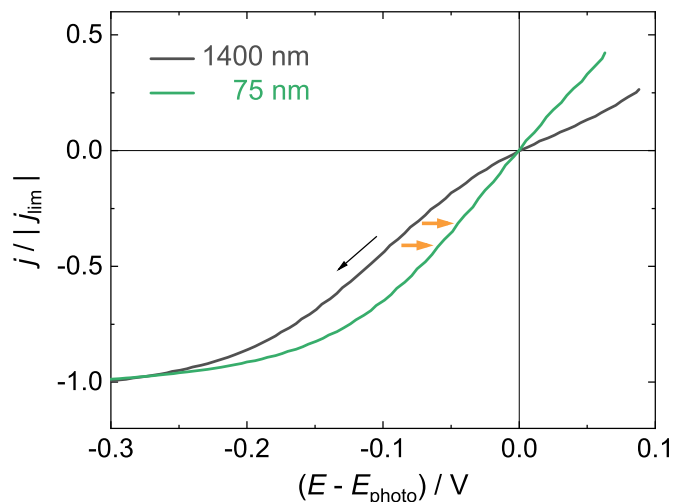


Figure 4.10: LSVs of illuminated photoelectrodes covered with Pt structures of sizes 1400 nm and 75 nm in buffered neutral electrolyte (0.18 M NaOH + 0.12 M H₃PO₄, pH 7) saturated with H₂ gas at ambient pressure. The illumination intensity is 100 W m⁻² (non-monochromatic LSW-2 lamp). The measured current is normalized to the limiting current in the scan. The electrode potential is corrected by the induced photovoltage in order to account for a different photoresponse of the two electrodes. Scan rate: 50 mV s⁻¹.

This becomes clear in Figure 4.10. The Figure shows LSVs of two different photoelectrodes with 1400 nm and 75 nm sized structures in buffered neutral electrolyte (0.18 M NaOH + 0.12 M H₃PO₄, pH 7) saturated with hydrogen gas. The illumination of both photoelectrodes is chosen to be the same, i.e. 100 W m⁻² (LSW-2 lamp). In order to account for the different photoresponse of the two electrodes (i.e. differences in the quantum efficiency), the electrode potential is corrected by the induced photovoltage E_{photo} and the current is normalized to the saturation current j_{lim} at a potential below the plotted potential range. It appears that the 75 nm electrode shows an improved HER kinetics compared to the 1400 nm electrode. This is visible in the split up of the two curves quite below 0 V. At small overpotentials the curve of the 75 nm electrodes shows a higher current at the same overpotential, while both approach the limiting current in the saturation regime, which is independent of the HER kinetics and solely determined by the quantum yield.

Tafel analysis

This HER/HOR kinetics is further analyzed by a Tafel analysis. However, determining the HER kinetics quantitatively is still hardly possible. Determining the exchange current density via the Tafel analysis necessitates a sufficiently large overpotential in order to neglect the anodic exponential term present in the Butler-Volmer equation, since now both, oxidized as well as reduced species, are present in the electrolyte. However, we showed in one of the previous sections 4.2 that the HER rate of photoelectrodes at 'sufficiently large' overpotentials is not solely limited by the kinetics of the electrochemical reaction, but it is also influenced by the rate of photoexcited electrons approaching the surface. This can

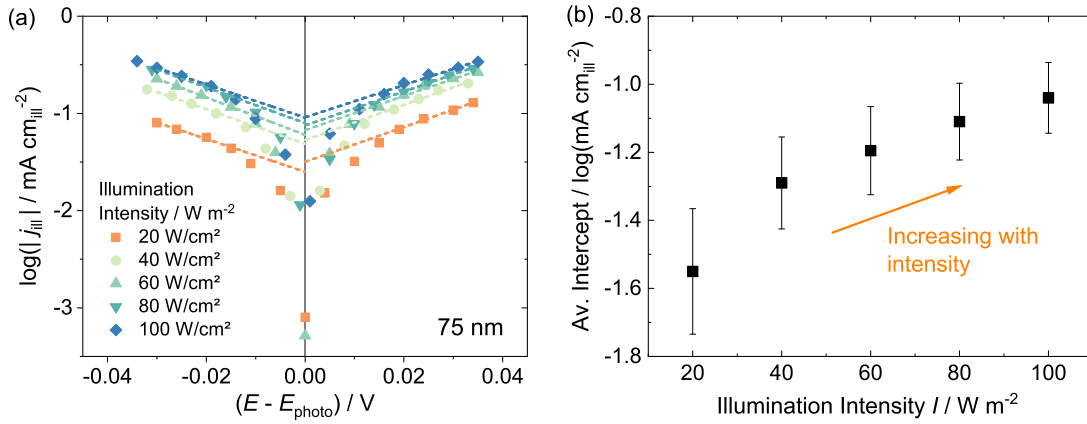


Figure 4.11: (a) Logarithm of the current density of HER/HOR on a photoelectrode covered with Pt structures of sizes 75 nm plotted over the electrode potential (Tafel plot) at various illumination intensities (non-monochromatic LSW-2 lamp). (b) The intercept of the fitted slopes (dashed lines in left image) plotted over the illumination intensity. It is visible, that the intercept increases with increasing intensity, which indicates that the rate is not solely limited by the reaction kinetics at finite illumination.

Illumination Intensity W m^{-2}	b (anodic) dec/V	b (cathodic) dec/V	a (average) $\log(\text{mA}/\text{cm}^2)$
20	17.9	16.9	-1.55
40	18.1	17.8	-1.29
60	17.6	19.2	-1.20
80	17.4	18.3	-1.11
100	16.6	17.1	-1.04

Table 4.1: Fit values of the Tafel analysis of the linear behavior of the logarithmic current density, i.e. of the fits shown in Figure 4.11(a) (dashed lines).

be directly observed in Figure 4.11. Figure 4.11(a) shows the logarithm of the HER/HOR current density on a photoelectrode covered with 75 nm Pt structures plotted over the photovoltage corrected electrode potential (Tafel plot) for various illumination intensities. At sufficiently large overpotentials (here: $|E - E_{\text{photo}}| > 15 \text{ mV}$ for all intensities) the dependence becomes approx. linear and can be fitted with the Tafel equation:

$$\frac{\partial \log(|j_{\text{ill},a/c}|)}{\partial E} = \text{const.} =: \pm b \quad (4.8)$$

$$\Rightarrow \log(|j_{\text{ill},a/c}|) = a \pm b(E - E_{\text{photo}}) \quad (4.9)$$

The slope b and the intercept a are fit parameters, which can be determined from the data (dashed lines in the left image). The actual fit parameters are given in Table 4.1.

Figure 4.11(b) shows the average intercept (average value of the intercepts of the cathodic and anodic fitting) as a function of the illumination intensity. It becomes visible that the intercept increases with increasing illumination intensity, but it does not saturate within the investigated intensity range. In case the reaction rate would be limited by

reaction kinetics, the intercept is supposed to be independent of the illumination intensity. Consequently, the method applied here is not suitable to determine the exchange current density correctly, since, even at the highest illumination intensity chosen, the measured reaction rate is not fully limited by kinetics.

In summary, the photoelectrodes patterned with Pt nanostructures show qualitatively a similar trend with the structure size regarding HER in neutral buffered electrolyte as the photoelectrodes containing Au structures, i.e. with decreasing structures size the necessary HER overpotential to draw a certain reaction current decreases. However, a quantitative comparison between the electrodes is not possible, since, even at the highest illumination intensity applied here, the rate was not fully limited by reaction kinetics. The finite illumination needs to be chosen very high to assure full limitation by reaction kinetics. In addition, the larger the resolvable exchange current density is supposed to be, the higher needs the illumination of the electrode to be chosen.

4.5 Summary

In this chapter, we investigated the electrocatalytic behavior of nanostructured photoelectrodes based on p-doped silicon substrate consisting of Au or Pt nanostructures. In order to analyze cathodic reactions (here: HER and CO₂RR) on the electrode surface, illumination is necessary, as the Schottky-contact present at the MIS interface of the investigated photoelectrodes is operated under reverse bias at the relevant polarization condition. The devices are photosensitive, i.e. they show photovoltage and a linear scaling of the saturation current (at reverse biasing) with illumination intensity.

At low cathodic overpotentials, the electrocatalytic response of the illuminated photoelectrodes regarding HER and CO₂RR behaves as expected from the literature and, consequently, we concluded that it is determined by the electrode/electrolyte interface. Contrary, in the illumination limited regime the electrocatalytic properties of the electrodes become rather independent of the applied overpotential. The reason is that most of the overpotential, which is applied additionally, drops at the Schottky diode interface and not at the electrode/electrolyte interface. In addition, during potentiostatic measurements in the illumination limited regime, the diode interface can "buffer" the limiting diffusive transport of reactants by increasing the overpotential dropping at the electrode/electrolyte interface with time, while maintaining a constant current. This leads to a constant reaction current with time. This behavior is seen experimentally and could be additionally verified theoretically by simulations.

The structured photoelectrodes show an enhancement of HER with decreasing structure size. This is observed for Au- as well as for Pt-based nanostructures. In addition, for Au structures HER in alkaline media is enhanced to a larger extent than HER in acidic media. It is shown that this behavior is due to an so far unidentified effect occurring at the electrode/electrolyte interface and cannot be solely explained by a different photoresponse of the individual electrodes. However, because the photoresponse of individual electrodes may be different, a reliable quantitative analysis of HER kinetics via Tafel analysis in order to investigate the unidentified effect further is not possible for the photo-active nanostructured electrodes investigated here. In the following chapter, the dependence of the catalytic HER activity on the Au structure size will be further analyzed on photo-inactive electrodes.

Chapter 5

Enhanced HER kinetics at the gold/silicon oxide interface

In this chapter, we analyze the HER reactivity enhancement with decreasing gold structure size on photo-inactive nanostructured electrodes, as discussed in the last chapter on photo-active nanostructured electrodes. The investigation of photo-inactive electrodes makes a comprehensive kinetic analysis possible in the absence of illumination. In detail, we will analyze the occurring HER reaction mechanism and its kinetics in acidic and alkaline medium (section 5.1), verify the appearance of a locally increased reactivity by local current mapping of the metal structure array (section 5.2), and shed light on the role of particle transport on the enhancement (section 5.3). An investigation of the influence of several other electrode and electrolyte parameters on the HER reactivity of the metal structure arrays is part of the following chapter, in which we further elaborate the origin of the observed enhancement.

Electrochemical behavior of a typical Au film on n-Si silicon substrate

The substrate material used in this chapter, which gives photo-inactive metal array electrodes, is n-doped silicon with a resistance of 1-10 Ω cm (see section 3.1). This choice of substrate material gives two main advantages: (1) There is a comparatively high density of electrons in the conduction band of silicon, which can participate in cathodic reactions on the electrode surface and make illumination redundant. (2) The MIS interface exhibits a (quasi-)ohmic contact for all structure sizes at relevant current densities (see section 3.1.3), which allows for an investigation of the catalytic properties of the metal/electrolyte interface without a significant or non-linear contribution to the measured U - I data from the MIS interface.

However, before we look closer at the electrocatalytic behavior of the differently sized Au nanostructures, we introduce the typical electrochemical behavior of a continuous gold film evaporated on an n-doped silicon (111) substrate in acidic and alkaline electrolyte. This system works as the reference when analyzing the behavior of Au nanostructured electrodes. The film is produced in the same way as the electrodes with Au nanostructures, i.e. by evaporation with the same parameters. Thus, we will consider this system as the benchmark in the further course of this work.

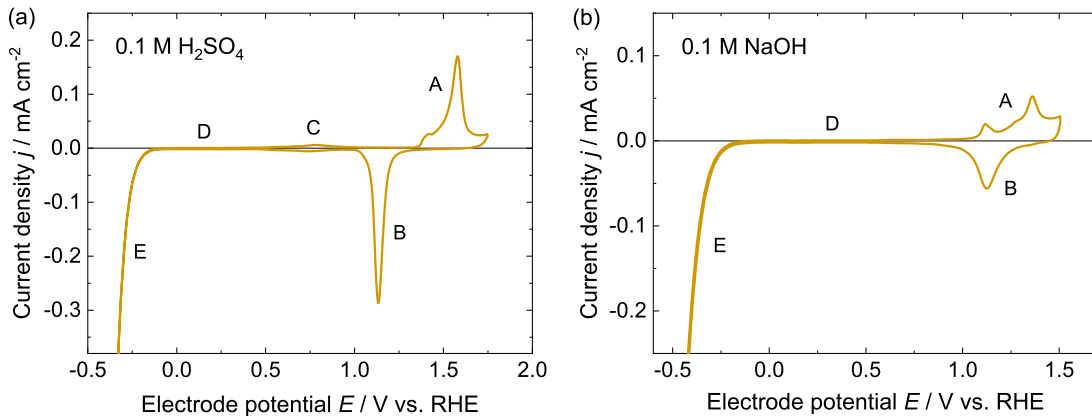


Figure 5.1: CVs of an evaporated Au film (continuous Au layer) in (a) 0.1 M $\text{H}_2\text{SO}_4/\text{Ar}$ sat.'d (pH 1) and (b) 0.1 M NaOH/Ar sat.'d (pH 13). The scan rate is 50 mV s^{-1} . The thickness of the evaporated layer is 30 nm, the substrate is n-doped Si wafer with (111) orientation.

Figure 5.1 shows CVs of a typical evaporated gold film (30 nm thickness) in (a) 0.1 M H_2SO_4 acidic electrolyte (pH 1) and in (b) 0.1 M NaOH alkaline electrolyte (pH 13). The scan rate is 50 mV s^{-1} . Important features are labeled by capital letters in the Figure, which we assign to:

- A: Oxidation of the Au surface
- B: Reduction of Au-oxide
- C: Sulfate ad-/desorption (cf. [AO98])
- D: Double-layer region
- E: Hydrogen Evolution Reaction

The shapes of the CVs are in good agreement with typical gold CVs presented in the literature using the respective electrolytes, as they show all expected features [Ang+87; Ham+90; Ham96]. Beside of the HER region, which will be extensively discussed in the following chapters, also the gold oxide region (A/B) is of particular interest for this work. In acidic and oxygen free electrolyte, the oxidation of gold occurs through the reaction with water. The actual oxidation mechanism and the structure of the oxide formed is rather complex [Che+13; Dia+13]. However, the shape of the gold oxidation peak ensemble A is characteristic for the structure of the Au surface. A good overview of the peak shape on the Au surface structure, i.e. the peak shape of different low-index facets on mono-crystalline Au electrodes, is given by Hamelin et al. [Ham96]. Here, we classify the surface of the evaporated Au film to be dominated by (111) adsorption sites, which is indicated by the pronounced anodic peak at $1.58 V_{\text{RHE}}$ attributed to the oxidation of (111) terrace sites [Zhu+13]. However, we will term the surface of this benchmark system as 'poly-crystalline' (pc) in the following, as we do not explicitly investigate the mono-crystalline quality of our film surface.

5.1 Increased HER activity of laterally patterned Au-SiO_x/n-Si electrodes

In the previous chapter, we could already see that nanostructured Au-SiO_x/p-Si photoelectrodes show an increased activity for HER with decreasing structure size in neutral and alkaline medium. In this section, we will further analyze the mechanisms and kinetics of HER on chemically similarly composited, but photo-inactive Au-SiO_x/n-Si electrodes. Thus, we analyze the dependence of the HER activity in alkaline and in acidic electrolyte when varying the Au structure sizes.

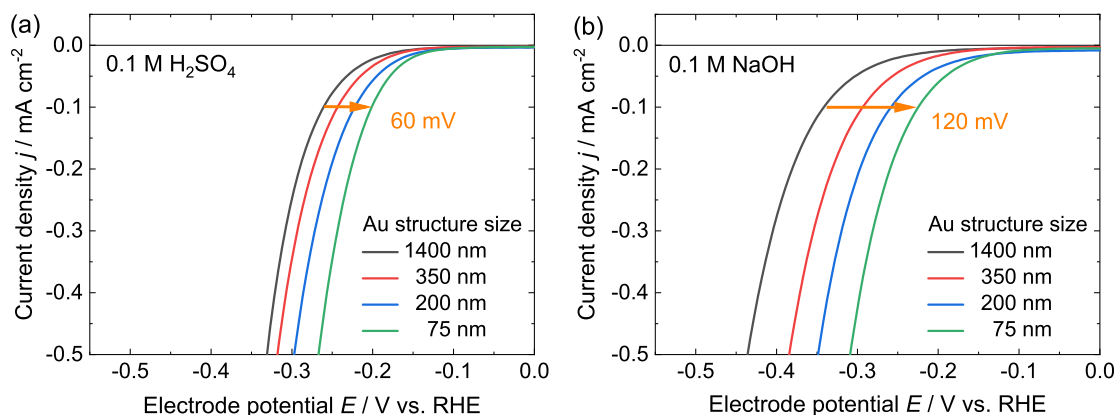


Figure 5.2: LSVs of structured electrodes with Au structures with different sizes performed in (a) 0.1 M H₂SO₄/Ar sat.'d (pH 1) and (b) 0.1 M NaOH/Ar sat.'d (pH 13). The necessary overpotential for HER decreases with decreasing structure size in both media. Adapted with modifications from [Mai+20].

Figure 5.2 shows linear sweep voltammograms (LSVs) performed on electrodes with various Au structure sizes in (a) acidic and (b) alkaline electrolyte. The measured cathodic current is due to HER in both cases. Contrary to the case using p-doped silicon substrate, no saturation of the current at rather large negative overpotentials is visible here, which is due to the high density of electrons in the silicon conduction band in the n-doped substrate. However, it is clearly visible that the overpotential necessary to draw a certain current density decreases with decreasing structure size. This is visible in acidic as well as in alkaline medium. Exemplary at a current density of -0.1 mA cm^{-2} we see an potential shift of 60 mV in acidic and 120 mV in alkaline medium from the largest to the smallest structures (orange arrows). This behavior is qualitatively similar as observed for photoelectrodes in neutral electrolyte, c.f. Figure 4.8. Admittedly, these values are quantitatively lower than the value seen for photoelectrodes in neutral medium, which is likely due to the different pH values of the electrolytes. The reason will become clear at a later point (cf. section 6.3.1).

In order to analyze the kinetics of HER on the structured electrodes in more detail, a Tafel analysis (see section 2.3) is conducted. A necessary requirement for interpreting the fitting parameters achieved in the Tafel analysis as mechanistic and kinetic indicators is that the reaction needs to be fully determined by kinetics, and is not determined by transport of species involved in the reaction. It appears to be clear that due to the comparably high density of electrons in the conduction band and the ohmic MIS contact, no transport effects of electrons towards the metal/electrolyte surface need to be considered here. In addition,

we assume at this point that at these comparatively low current densities shown in Figure 5.2 the transport effect of ionic species (H^+ or OH^-) towards or from the electrode surface can be neglected as well. This assumption will be justified in section 5.3.

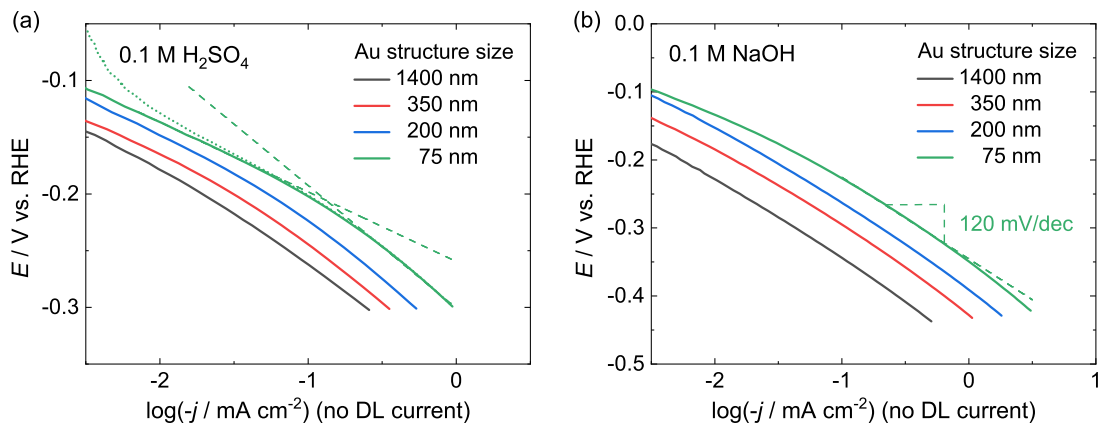


Figure 5.3: Logarithmic plots (Tafel plots) of the LSV curves shown in Figure 5.2, (a) in 0.1 M H_2SO_4 and (b) in 0.1 M NaOH . The non-faradaic current, i.e. double layer (DL) charging current determined at 0 V_{RHE} , is subtracted from the data prior to logarithmizing. In (a), the dotted line shows the data of the 75 nm electrode without prior subtraction of the DL current for comparison and the dashed lines indicate two regions with different slopes of the curve. Adapted with modifications from [Mai+20].

Figure 5.3 shows the corresponding Tafel plots of the LSV scans shown in Figure 5.2. The Tafel plots of the data measured in 0.1 M NaOH , cf. Figure 5.3(b), show a linear behavior within the whole potential range investigated. In 0.1 M H_2SO_4 , cf. Figure 5.3(a), the curves are not linear within the entire potential range. However, there seems to be two distinct potential ranges with linear propagation. In the following two sections, the kinetic properties of the electrodes in both electrolytes are analyzed, interpreted and discussed in detail.

5.1.1 Tafel analysis in alkaline electrolyte - Enhanced border activity

As already mentioned before, the curves in the Tafel plot for 0.1 M NaOH alkaline electrolyte, cf. Figure 5.3(b), propagate very linearly within the whole potential range. The parameters of the Tafel fit performed (fitting range between $-0.25 \text{ V}_{\text{RHE}}$ and $-0.4 \text{ V}_{\text{RHE}}$) for the various electrodes are given in Table 5.1. Figure 5.4 shows the determined parameters, (a) the Tafel slope and (b) the exchange current density j_0 , plotted over the inverse of the respective structure size d . Note that the fitting parameters given here are averaged over three electrode sets, i.e. each data point is the average over three individual electrodes and independent measurements. The error given consists of the individual fitting error of each measurement as well as the statistical error stemming from averaging.

The Tafel slope is quite constant for all electrodes investigated, independent of the actual structure size, and has a value close to 120 mV dec^{-1} . It is well in accordance with the value determined by other groups for $\text{Au}(\text{pc})$ electrodes in alkaline electrolyte [OE92; GK21a]. A Tafel slope value of 120 mV dec^{-1} is tantamount to $\alpha_c \approx 0.5$ (at room temperature) and, thus, is indicative of the first electron transfer being the rate determining step. The first

Structure size d	Fitted slope [mV dec ⁻¹]	j_0 (from intercept) [10 ⁻⁴ mA cm ⁻²]
1400 nm	122	(2.0 ± 0.7)
350 nm	121	(4.7 ± 1.5)
200 nm	121	(9.2 ± 3.4)
75 nm	119	(20 ± 5)

Table 5.1: Fitting parameters of the Tafel analysis of the LSV curves measured in 0.1 M NaOH, i.e. the data shown in Figure 5.3(b). The data is fitted between $-0.25 V_{\text{RHE}}$ and $-0.4 V_{\text{RHE}}$.

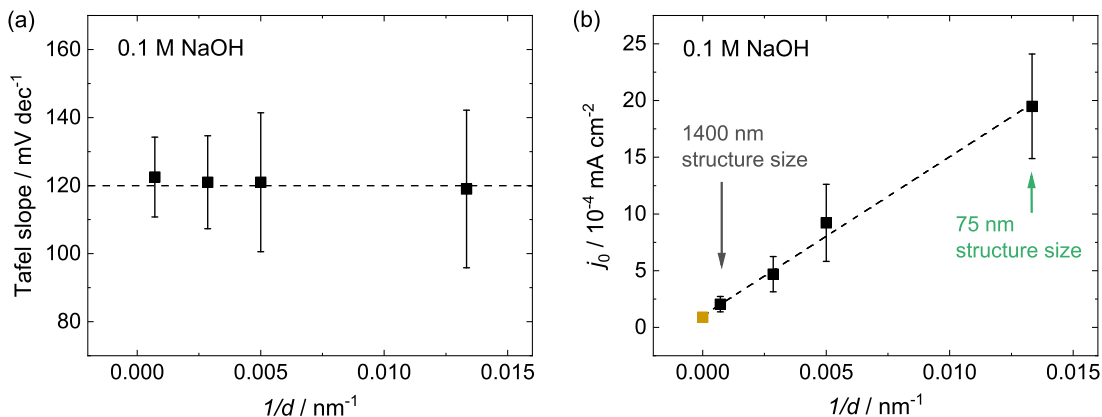


Figure 5.4: Tafel analysis of HER on the structured electrodes in 0.1 M NaOH. (a) Tafel slopes and (b) exchange current densities j_0 plotted over the inverse of the Au structure size d . The Tafel slope is quite similar for all electrodes with a value close to 120 mV dec⁻¹. This is indicative of the first electron transfer step (Volmer step) being the RDS. The exchange current density increases linearly with the inverse of the structure size. This behavior is further discussed in the text. The yellow data point is the experimentally determined j_0 of the continuous gold layer described in the beginning of this chapter. Its value coincides very good with the extrapolation of the linear behavior (dashed line) towards $1/d = 0$. Adapted with modifications from [Mai+20].

electron transfer step in alkaline electrolyte at these moderate overpotentials is likely the Volmer step, as widely accepted in the literature [Rhe+14; Led+17; Zhe+18; GK21a]. It needs to be mentioned that this value can also be indicative of the Heyrovsky step being the RDS when assuming a high coverage of protons on the electrode surface at the evaluated potentials (see next section). However, the energetic barrier for the reduction of water is comparably high. Thus, we consider it is more likely that the surface is not predominantly covered by hydrogen atoms at these moderate overpotentials and, consequently, that the Volmer step is the RDS here. The Tafel slope is similar for all electrodes with differently sized Au structures. Thus, we conclude that there is no difference in the HER reaction mechanism for the different structure sizes.

Contrarily, the exchange current density increases with decreasing structure size. Figure 5.4(b) clearly shows, that there is an approx. linear increase of the exchange current density with $1/d$, which is indicated by the dashed line as a guide to the eye. In addition, the intersect of this linear fitting at $1/d = 0$ matches very well the measured exchange current density of the continuous gold layer electrode (yellow data point). A continuous layer can be imagined as an infinitely large structure and perfectly fits in the trend. This size dependence of the exchange current density is quite remarkable and further discussed in the following.

Discussion: Enhanced reactivity on sturcture border

The increase of the exchange current density with decreasing structure size at constant gold coverage suggests, that the Au/SiOx border area between gold and the adjacent silicon oxide may be a crucial aspect for explaining the observed trend. In order to understand the implication of the linear dependence of j_0 with $1/d$ better, we make some geometric considerations. Let us assume that there are at two distinct areas on the structures which show different HER kinetics. We hypothetically split the total electrochemically active (gold) area A on the electrode into an area a and an area b .

$$A = a + b \quad (5.1)$$

We chose these areas in a way that area a accounts for the 'bulk surface part' of the gold structures, and area b accounts for the 'border surface part' of the structures, i.e. the Au area of the structures, which is in close contact to the surrounding SiOx. A scheme of this splitting with important geometric quantities is shown in Figure 5.5.

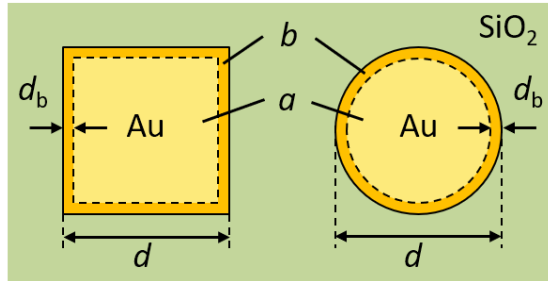


Figure 5.5: Geometric splitting of the gold area into two parts a and b . Part a considers the 'bulk part' of the structures, whereas part b considers the 'border part' of the structures, i.e. the Au area in close contact to the surrounding SiOx. The actual structure size is labeled with d , the (hypothetical) thickness of the border area b is labeled by d_b . [Mai+20]

The total measured current i_{total} is given by the sum of the two individual currents on the respective areas, which we write in terms of the respective current densities.

$$i_{\text{total}} = i_a + i_b \quad (5.2)$$

$$\Rightarrow j_{\text{total}} = \frac{i_{\text{total}}}{A} = \frac{a}{A}j_a + \frac{b}{A}j_b \quad (5.3)$$

Here, j_{total} is the total (i.e. measured) current density, and $j_{a,b}$ is the current density of area a or b , respectively. The experimental data showed that there is a similar Tafel slope present for all electrodes, independent of the actual structure size, cf. Figure 5.4(a). Thus, we can conclude that there is a similar α_c for both distinct parts of the Au structures. When writing the current density on part k explicitly in the Tafel form

$$j_k = -j_{0,k} \exp\left(-\frac{\alpha_c F}{RT}\eta\right) \quad (5.4)$$

we recognize that the second exponential term is then the same for both areas a and b . After factorization we get an dependence of the total (determined) exchange current density j_0 on the individual exchange current densities $j_{0,a}$ and $j_{0,b}$:

$$j_0 = \frac{a}{A}j_{0,a} + \frac{b}{A}j_{0,b} \quad (5.5)$$

Inserting equation (5.1) into equation (5.5) we obtain

$$j_0 = j_{0,a} + \frac{b}{A}(j_{0,b} - j_{0,a}) \quad (5.6)$$

We can now make some further geometric calculations. Independent of the actual shape of the structure, i.e. this applies for structures with quadratic as well as circular shape, we can further simplify the factor b/A :

$$\frac{b}{A} = \frac{4d_b d - d_b^2}{d^2} \approx \frac{4d_b}{d} \quad \text{for } d_b \ll d \quad (5.7)$$

where d is the structure size (i.e. the diameter for circular or the side length for quadratic structures) and d_b the 'border thickness' (thickness of a surrounding ring for circular or a surrounding frame for quadratic structures). We finally obtain:

$$j_0 = j_{0,a} + \frac{4d_b}{d}(j_{0,b} - j_{0,a}) \quad (5.8)$$

According to this equation, the measured exchange current density would, indeed, scale linearly with the inverse of the structure size $1/d$. This behavior is experimentally observed and proves the conjecture that the border part b of the structures exhibits a larger exchange current density than the bulk part a .

In principle, the actual values for $j_{0,b}$ and $j_{0,a}$ can be calculated from the experimental data. However, in order to do so one needs to make an assumption for d_b . The 'border thickness' is a hypothetical construct needed for calculation and should obviously not be understood as a sharp and well defined border. Instead, it can be more understood as an 'effective range' of the enhancement effect occurring at the Au/SiOx interface. To get an impression for the anticipated huge difference between $j_{0,b}$ and $j_{0,a}$, we calculate their value assuming $d_b \approx 5$ nm. From the fitting in Figure 5.4(b) we calculate values of $j_{0,a} \approx 1 \cdot 10^{-4}$ mA cm⁻² and $j_{0,b} \approx 7 \cdot 10^{-3}$ mA cm⁻². Thus, even with this rather 'conservative' assumption for d_b , the exchange current density of alkaline HER on the Au/SiOx interface is more than one order of magnitude larger than it is on the Au bulk surface.

5.1.2 Tafel analysis in acidic electrolyte - Change of reaction mechanism

The dependence of the logarithmic current density with the electrode potential in acidic electrolyte, cf. Figure 5.3(a), shows two distinct potential ranges, which exhibit different slopes: One below approx. $-0.2 V_{\text{RHE}}$ and one above. This is clearest for the 75 nm electrode and indicated by the green dashed lines in Figure 5.3(a), but may be present for all electrodes shown here. In order to investigate this further, the slope of logarithmized current as a function of the electrode potential is analyzed. The dependence of the slope (i.e. the inverse of the Tafel slope) on the electrode potential is shown in Figure 5.6. Figure 5.6(a) shows the derivative of the LSV data as measured, i.e. without subtraction of the non-faradaic current at $0 V_{\text{RHE}}$. Note that the data without current subtraction is not shown for all electrodes investigated. For comparison, only the data of the 75 nm electrode without subtraction is given in Figure 5.3(a), dotted line. Figure 5.6(b) shows the slopes as a function of the electrode potential with the previous subtraction of the non-faradaic current at $0 V_{\text{RHE}}$ from the LSV data, i.e. the slopes of the data as shown in Figure 5.3(a).

It needs to be mentioned at this point that the data considered here is determined from a potential scan with a rather high scan rate of 50 mV s^{-1} . However, a very similar behavior of the slope with the potential is achieved when scanning with a much smaller rate of 10 mV s^{-1} , which we show in the appendix A.9. Thus, the behavior of the slope and consequently all implications from the data made here necessary for the later Tafel analysis, are assumed to be also valid when measuring with the comparably high potential scan rate of 50 mV s^{-1} used here. In addition, the data shown has been smoothed by a 10 point Savitzky–Golay method.

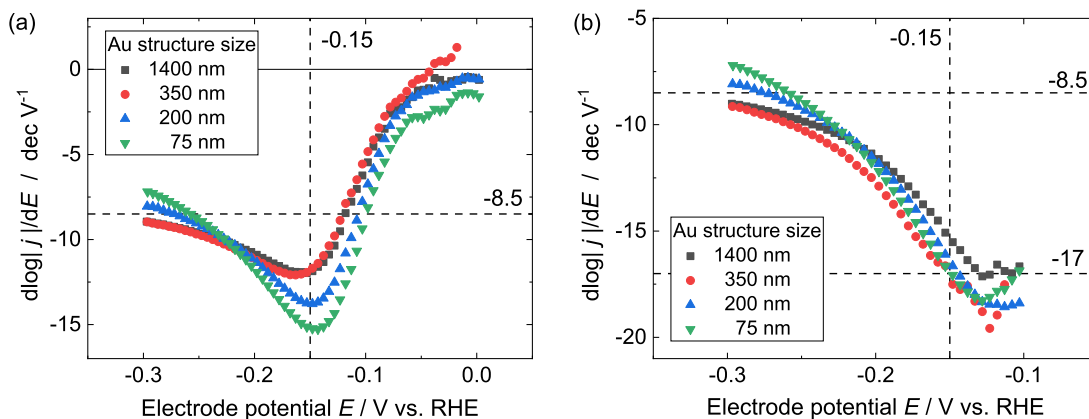


Figure 5.6: Derivative of the logarithmic current density $d \log |j|/dE$ (i.e. slope) plotted over the electrode potential E . (a) Data as measured, i.e. without prior subtraction of the non-faradaic current. (b) After subtraction of the non-faradaic current (the double layer charging current) at 0 V_{RHE} . These data are determined from the data shown in Figure 5.3(a). It is evident that the slopes change during the potential scan from approx. -17 dec V^{-1} at low overpotentials to approx. -8.5 dec V^{-1} at high overpotentials. This behavior is present for all structure sizes. Electrolyte: $0.1 \text{ M H}_2\text{SO}_4$. Potential scan rate: 50 mV s^{-1} .

In Figure 5.6(a), the curves of all electrodes exhibit a qualitatively similar behavior: First, the slope at zero overpotential gives a value around zero, and decreases with decreasing potential until it passes a minimum. The minimum lies around $-0.15 \text{ V}_{\text{RHE}}$. When further decreasing the potential, the slope increases again and approaches a value around -8.5 dec V^{-1} . The potential of the minimum observed coincides very well with the potential at which the coverage θ of the hydrogen atoms on the surface of poly-crystalline gold becomes predominant in acidic electrolyte, i.e. $\theta > 0.5$, according to the Chun et al. [CRK03]. The authors estimated the surface coverage of protons as a function of the electrode potential in sulfuric acid based acidic electrolyte from impedance measurements. The coverage determined by the authors as a function of the electrode potential is shown in Figure 5.7. It is visible, that the behavior can be well fitted by a Langmuir isotherm considering the equilibrium constant $K_{\text{ad}} = 7.3 \cdot 10^{-3}$ in RHE scale. It needs to be mentioned here that the authors stated a value of $K = 2.3 \cdot 10^{-6}$ in their publication. However, it is likely that this reported value is the fitted value when using SCE as the reference potential ($E_{\text{SCE}}^0 \approx 0.244 \text{ V}$). For adsorption isotherms multiple pairs of equilibrium constants and reference potentials can be used to describe the same system. Unfortunately, this does not become clear in the publication. However, otherwise the data provided would not correspond to their proposed fit in RHE scale.

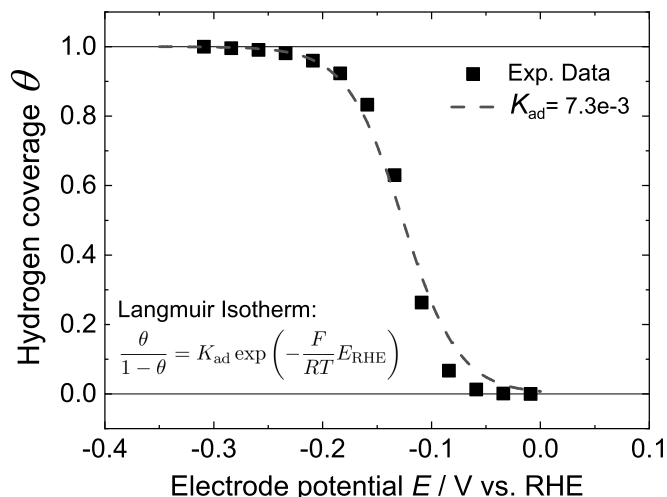


Figure 5.7: Relative coverage θ of hydrogen atoms on a poly-crystalline gold surface plotted versus the electrode potential E in RHE scale in 0.5 M H_2SO_4 . The measured data shown is taken from Chun et al. [CRK03]. The dashed line shows a Langmuir isotherm as described by the inset equation with $K_{\text{ad}} = 7.3 \cdot 10^{-3}$. It is visible that the data measured can be approximated quite well by the Langmuir isotherm.

Discussion: Change of reaction mechanism

The minimum of the slope observed in Figure 5.6(a) at approx. $-0.15 \text{ V}_{\text{RHE}}$ may be indicative of a change in the reaction mechanism appearing at this potential, i.e. the reaction mechanism at small overpotentials may differ from the mechanism at high overpotentials. Let us first consider the non-corrected data in Figure 5.6(a): At low overpotentials, the corresponding Tafel slope is not well identifiable in the graph, since the slope changes continuously during the scan. This effect is likely due to a comparably small exchange current density of the RDS in this potential range. The non-faradaic current (i.e. double layer charging current) present in the potential scan overlays the faradaic current signal significantly. This makes a slope analysis in this potential range not reliable without correction. However, after subtracting the non-faradaic current at 0 V_{RHE} , the slope has a distinct and constant value, even in the low overpotential window, cf. Figure 5.6(b). At low overpotential, i.e. above $-0.15 \text{ V}_{\text{RHE}}$, the value of the slope is approx. -17 dec V^{-1} . This value is similar for all structure sizes investigated. It is tantamount to a Tafel slope of approx. 60 mV dec^{-1} and equivalent to $\alpha_c \approx 1$ at room temperature. According to microkinetic modelling based on the assumption of quasi-equilibrium of all involved reaction steps except for the RDS [SGT15; ESO18; Gui+14], this indicates that the RDS is determined neither by the first, nor the second electron transfer step, but by an intermediate chemical step. However, at sufficiently high overpotential (i.e. below $-0.15 \text{ V}_{\text{RHE}}$) the slopes start changing and converge towards a value of approx. -8.5 dec V^{-1} . This is, again, similar for all sizes investigated. A slope of -8.5 dec V^{-1} is tantamount to a Tafel slope of 120 mV dec^{-1} and, at room temperature, equivalent to $\alpha_c \approx 0.5$. This value indicates that the RDS is now determined by the 'first' electron transfer step in the catalytic cycle.

The presented data showing a changing HER Tafel slope of gold-based electrodes in acidic electrolyte is well in accordance with results obtained by other groups [Bru+84b; KB71; CRK03; KK11]. It is proposed by Kahyarian et al. [KBN17] that the changing Tafel slope

Structure size d	Fitted slope [mV dec^{-1}]		j_0 (from intercept) [$10^{-4} \text{ mA cm}^{-2}$]	
	$E > -0.15 \text{ V}$	$E < -0.25 \text{ V}$	$E > -0.15 \text{ V}$	$E < -0.25 \text{ V}$
1400 nm	65	105	(0.14 ± 0.1)	(4.8 ± 3.1)
350 nm	60	110	(0.18 ± 0.1)	(8.3 ± 3.7)
200 nm	65	120	(0.39 ± 0.2)	(16.2 ± 3.7)
75 nm	60	125	(0.51 ± 0.2)	(35 ± 11)

Table 5.2: Fitting parameters of the Tafel analysis of the LSV curves measured in 0.1 M H_2SO_4 , cf. Figure 5.3(a). The electrode potentials E are given in RHE scale, i.e. in V_{RHE} . The slopes are given with a precision of $\pm 5 \text{ mV dec}^{-1}$ to avoid the impression of pseudo-correctness.

of HER on Au(pc) surface in acidic medium comes from a change of the mechanism during the scan: At low coverage, i.e. at low cathodic overpotential, the reaction is determined by an additional surface diffusion step of adsorbed hydrogen atoms. Protons adsorbed on adsorption sites A (majority of active sites present on the Au surface) diffuse towards adsorption sites B (minority sites on the surface). Sites B show a significantly increased activity for the Tafel recombination step compared to A. A detailed introduction in the mechanism proposed here is given in the appendix A.3. At rather high overpotentials, the surface is assumed to be considerably covered by adsorbed hydrogen atoms. The rate determining step is now likely the first electron transfer step in the catalytic cycle, which is now the Heyrovsky-step, as the surface approaches full coverage by protons.

Discussion: Enhanced reactivity on the structure border

From the Tafel fit we can determine the intercept by extrapolating the linear fitting towards zero overpotential. This intercept can be attributed to the logarithm of the exchange current density if the current is fully kinetically limited. As there are two distinct potential ranges with different Tafel slopes, we determine the intercept for each potential range individually. The determined fitting parameters (slopes and intercepts) are given in Table 5.2. Note that the fitting data shown is averaged over three electrode sets, i.e. each data point is the average over three individual electrodes and independent measurements. The errors given consist of the individual fitting error of each measurement as well as the statistical error stemming from averaging.

Figure 5.8 shows the determined exchange current densities in both potential ranges plotted over the inverse of the structure size d . It is visible that the exchange current density increases with decreasing structure size. This holds for both potential ranges with distinct Tafel slopes. In the high overpotential range with $E < -0.25 V_{\text{RHE}}$, cf. Figure 5.8(b), there is a clear linear dependence of j_0 on $1/d$. This behavior is indicated by the dashed line as a guide to the eye. A similar trend has already been observed in alkaline electrolyte. In the low overpotential range, there is no clear linear trend. In addition, the relative error of the datapoints is considerably larger, because the absolute value of the measured current in this range is considerably smaller. Consequently, the Tafel fitting gives a much larger relative uncertainty.

However, these findings imply that HER is enhanced on smaller sized structures, independent of the dominating mechanism, i.e. independent of the potential range considered. With the same argumentation as given in the previous section, the linear dependence of j_0

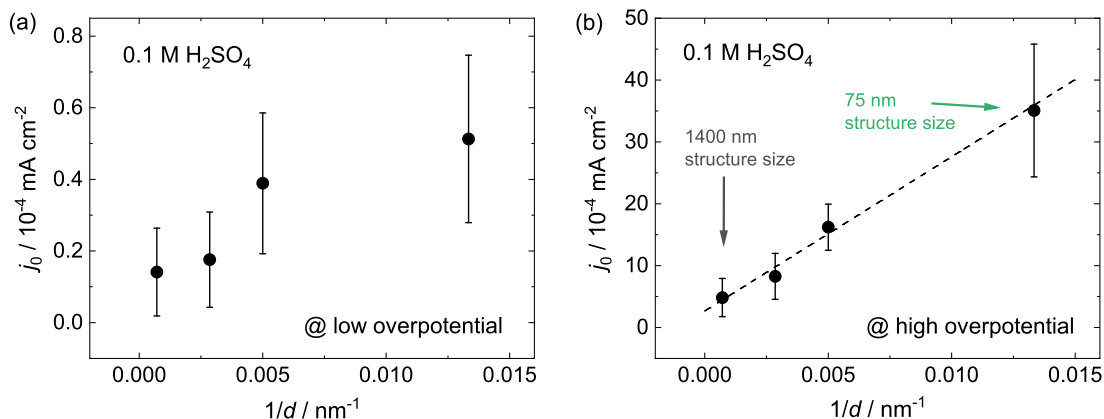


Figure 5.8: Exchange current densities (calculated from intercept of Tafel fittings) of the structured electrodes in 0.1 M H_2SO_4 plotted over the inverse of the Au structure size d . (a) Fit in the low overpotential range (E between $-0.10 \text{ V}_{\text{RHE}}$ and $-0.15 \text{ V}_{\text{RHE}}$). (b) Fit in the high overpotential range ($E < -0.25 \text{ V}_{\text{RHE}}$).

with $1/d$ suggests that the rate increase is due to an enhanced reaction rate at the border of the structures. This holds at least for the case, in which the Heyrovsky step is the RDS, i.e. at 'large' cathodic overpotentials.

Discussion: Mechanistic reasons for enhanced reactivity

Here, we will discuss possible reasons for the enhancements observed in the two distinct potential ranges considering the reaction mechanism proposed by Kahyarian et al. [KBN17], cf. appendix A.3. We will see that, on the basis of the given experimental data, it is not possible to narrow the origin of the observed increased reaction rate on smaller structures.

Considering low cathodic overpotentials, the rate of the rate determining surface diffusion step, cf. equation (1.15), and consequently of the total reaction rate at low overpotentials, can be increased by either (1) an increased concentration of adsorbed protons (coverage), or (2) a faster surface diffusion (i.e. increased forward reaction rate of the RDS). The former could be achieved by a reduced (average) adsorption energy of the surface, or by an increased concentration of protons present at the reaction sites, as both circumstances would shift the equilibrium of the preceding Volmer step more towards the right hand reaction side, cf. equation (1.14). A reduced (average) adsorption energy, however, is unlikely, although the surface of the different gold structure sizes is not necessarily similar, as they may exhibit different ratios of various adsorption sites due to the electrode fabrication process (this point will be further addressed in section 6.1). A lower adsorption energy would lead to an increased surface coverage at a certain potential. Since the change of the mechanism observed in this section is directly linked with the coverage, this would shift the presumed change of the reaction mechanism towards more positive potentials. However, Figures 5.6(a) and (b) show that the change of the mechanism occurs at roughly the same potential, i.e. at approx. $-0.15 \text{ V}_{\text{RHE}}$, for all structure sizes. Therefore, a structure-size dependent adsorption energy is rather unlikely as an explanation for the observed increased rate. Further evidence for this conclusion will be given in section 6.1. A faster surface diffusion could be achieved by a higher concentration of sites B on the surface. A higher concentration of sites B would lead to an reduced diffusion length of adsorbed protons and, consequently, to a larger surface diffusion rate. As there is no further

information about the ratio of adsorption sites A to B, this hypothesis could neither be confirmed or disproved.

Considering high cathodic overpotentials, the rate of the rate limiting Heyrovsky step, cf. equation (1.16), can be enhanced by either (1) an increased concentration of protons (reactants) at the reaction site, or (2) an increased reaction rate of the Heyrovsky step. In principle, an increased surface concentration of adsorbed protons can also accelerate this step, as it shifts the equilibrium. However, this is rather unlikely, since the concentration of adsorbed protons at evaluated potentials is assumed to be already very high and the adsorption energetics do not seem to be size dependent (see above). Note that a higher ratio of sites B to A at the electrode surface cannot be the reason for the observed enhancement in this potential range, as the reaction at higher overpotentials is supposed to be independent of sites B.

At this point, it becomes clear that multiple reasons can lead to an increased HER reaction rate in acidic medium, as observed for smaller metal structures. On the basis of the data shown so far it is not possible to further localize a mechanistic reason, and to explain an increased reaction rate observed for smaller structures. However, before we can carve out the actual mechanism in chapter 6, we need to verify some of the conjectures made above. Thus, in the next section 5.2 we will focus on the conjecture that the reaction rate at the border of the structures is really increased compared to the bulk part of the structures. We prove this by local current mapping. In the following section 5.3 we see that transport of reactants cannot serve as a possible explanation for the enhanced reaction rate.

5.2 Local current mapping

In this section, we prove that the scaling of the exchange current density with the inverse of the structure size $1/d$ observed in the last section, cf. Figures 5.4(b) and 5.8(b), really indicates an enhanced reaction rate at the border of the structures. Consequently, we need to prove that the reaction rate at the border of the structures is really larger than the rate at the bulk part. This can be achieved by measuring the HER reaction current locally on the electrode surface (current mapping). If the conjecture is true, the border of the structures should exhibit an increased reaction current compared to the bulk part of the structures.

5.2.1 Acidic medium - SECCM measurement

For mapping the current locally under potentiostatic conditions in acidic electrolyte on the presented nanostructured electrodes, we use Scanning ElectroChemical Cell Microscopy (SECCM). A detailed introduction to this measurement technique is given in section 3.2.6. Here, it is introduced shortly again.

In this method, a glass pipette filled with electrolyte and an Ag/AgCl wire, which works as a quasi-reference/counter electrode (QRCE) is hopping over the electrode surface. The tip of the pipette is open (opening diameter: 50 nm) which gives a tiny electrolyte droplet at the tip. The approach of the pipette towards the electrode surface stops once the droplet makes contact with the surface (meniscus). Note that we use a feedback method, which does not necessitate any current flow. In contact, a liquid channel between the local meniscus position on the electrode surface (WE) and the QRCE is established. Since the

connection between the WE and the QRCE is locally constraint and just obtained at the position of the droplet, this technique can be used to conduct local electrochemical measurements. The area of the QRCE/electrolyte interface is orders of magnitude larger than the opening of the pipette or the droplet covered area on the WE. Thus, one can assume the the whole applied voltage U between QRCE and WE drops at the WE/electrolyte interface.

Here, we perform a chronoamperometric experiment. The measurement procedure conducted at each spot is as follows: The pipette approaches the surface at $U = -0.8$ V vs. Ag/AgCl applied between the WE (structured electrode) and the QRCE in the pipette. The WE is negatively polarized. Once the droplet is in contact with the substrate, i.e. the WE is in contact with the QRCE, a current flows, which is recorded as a function of time (I - t -measurement), while keeping the applied potential constant. Next, the tip is retracted which leads to the breakdown of the droplet contact. Afterwards, the pipette is moved to the next measurement spot ('hopping') and the procedure is repeated.

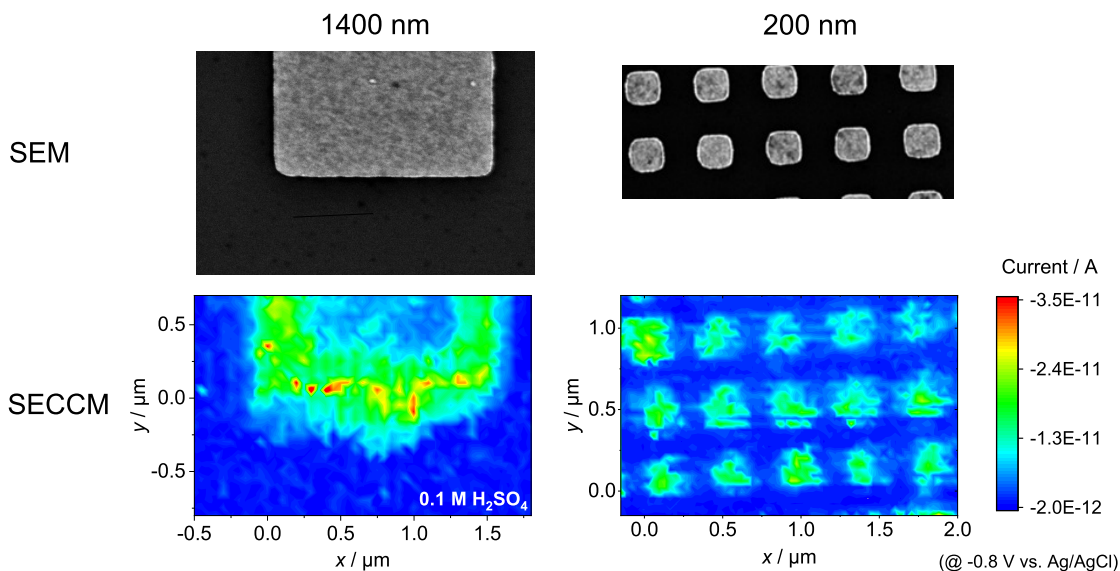


Figure 5.9: SEM (top) and SECCM (bottom) images of structured electrodes with 1400 nm (left) and 200 nm (right) Au structure size. The SECCM image shows the current signal in a potentiostatic I - t -measurement at 10 ms after contact. The potential applied at the electrodes is -0.8 V vs. Ag/AgCl. The electrolyte is 0.1 M H_2SO_4 , without gas purging. Hopping distance: 50 nm

This procedure is conducted in 0.1 M H_2SO_4 (electrolyte in the pipette) on two different electrodes patterned with Au structures of sizes 1400 nm and 200 nm, respectively. Figure 5.9 (bottom) shows exemplary current maps of the two electrodes conducted at the potentiostatic condition of -0.8 V vs. Ag/AgCl. The data shown in the Figure is the current data measured 10 ms after the contact is established. This shifted readout is necessary to minimize the contribution of non-faradaic current (double layer charging current), which is present once contact is made. For better comparison, SEM images with the same scale at similar positions on the structured electrodes are shown above the SECCM images. The lateral resolution (lateral distance between two measurement spots, i.e. hopping distance) is 50 nm, which is similar to the opening diameter of the pipette. The current is given as

measured and not normalized to any area, as the actual diameter of the contact area is not known (this issue is further discussed below).

The SECCM image of the 200 nm sized structure, cf. Figure 5.9(bottom right), shows several spots (green), which exhibit a higher measured current than measured at their surrounding (blue). Since these spots appear in a very regular pattern, they are identified as the 200 nm sized gold nanostructures present on the electrode surface. The SECCM image of the 1400 nm sized structure, cf. Figure 5.9(bottom left), shows a bright halo (green) surrounding an area with a considerable current signal (light blue). We identify this area as the 1400 nm structure. Note that the surrounding halo indicates that the absolute current measured at the border of the structure is larger than the measured current at the bulk of the structure. This behavior could be repeatably observed by multiple measurements performed on different structures and is, thus, statistically relevant.

We can further make the following experimental observations (not explicitly shown here):

- The (qualitative) presence of the surrounding halo does not depend on the time at which we collect the current data, after the contact is established. From this observation we can conclude that the appearance of the halo is not (completely) caused by non-faradaic current, but it is furthermore determined by faradaic reaction current, which is most likely HER reaction current at the potential applied here.
- When applying a more negative potential on the electrode, the absolute measured current is higher. This is valid for the 'halo current', i.e. at the edge, as well as for the current measured at the bulk of the structure. This further indicates, that the current measured is determined by a cathodic faradaic reaction, as this is supposed to be strongly potential dependent.

Thus, the data shown in Figure 5.9 further confirms the conjecture, that the HER activity at the border of the structures, i.e. at the Au/SiO_x interface, is enhanced compared to the bulk of the structures.

Discussion: Enhanced HER reactivity or droplet spreading?

As already mentioned before, the shape of the droplet and, consequently, the area covered by the liquid droplet is not known. Moreover, it is not known if the droplet size changes when scanning across the surface, as the wetting of the surface may be different. This would not be unexpected, since the droplet shape, i.e. the contact angle θ , cf. Figure 5.10, can depend on multiple system parameters such as: The potential applied ('electrowetting') [MH19], the material/structure of the surface to investigate ('hydrophobicity') [MH19], the ambient atmosphere [Shk+20], etc. A changing droplet size, i.e. a varying contact angle, would directly influence the measured current signal, as the covered area changes, although the actual local reactivity does not differ.

Let us first consider the situation on a pure gold surface. Variations of the microscopic roughness of metal films do not significantly influence the contact angle of the droplet and, thus, it is possible to investigate poly-crystalline surfaces as shown by Aaronson et al. [Aar+13]. Other experiments conducted with the same setup as used here showed that the area covered by the formed meniscus on a gold surface at moderate electrode potentials is in the same order of magnitude as the opening of the pipette tip [Hen+21]: At $-0.5\text{ V vs. Ag/AgCl}$, the droplet size is approx. 100 nm when using a pipette with 50 nm opening diameter. The PZC of Au(pc) is approx. at $+0.2\text{ V}_{\text{SHE}}$ (see section 7.2.3)

and, thus, more positive than the potential applied here. As a consequence, the droplet size should increase with further decreasing potential, as the cosine of the contact angle θ is supposed to scale quadratically with the applied potential according to the Young-Lippmann equation [MH19]:

$$\cos \theta(E) = \cos \theta_{pzc} + \frac{\varepsilon \varepsilon_0}{2\lambda_D \gamma} (E - E_{pzc})^2 \quad (5.9)$$

Here, θ is the contact angle, E the electrode potential, θ_{pzc} the contact angle at the potential of zero charge, E_{pzc} the potential of zero charge, λ_D the Debye screening length in the electrolyte, ε is the relative permittivity of the medium, and γ the surface tension of the electrolyte/atmosphere interface.

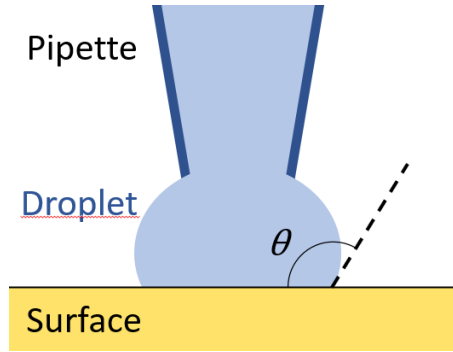


Figure 5.10: Visualisation of the contact angle θ of the droplet in the SECCM experimental configuration. According to the Young-Lippmann equation (5.9), the contact angle decreases when increasing the applied potential relative to the potential of zero charge. This results in a spreading of the droplet and an increasing surface coverage.

Let us come back to the experimental data. We note that the 'halo' thickness visible in the data of the 1400 nm structure in Figure 5.9 is approx 5 data point wide (approx. 250 nm). If we assume that the larger current signal stems from a higher reactivity at the edges of the structure, we can expect a droplet size in the same range, so approx. 250 nm. Considering the droplet size given by Hengsteler et al. [Hen+21] and the more negative potential applied here, this droplet size seems quite reasonable in the present setup. A forming droplet of this comparatively large size can also be the reason, why the enhanced rate at the electrode edges cannot be seen for the smaller structures (200 nm diameter). The droplet would always cover 'edge parts', independent of the actual position of the pipette on the structure. This would lead to an increased current signal seen for the whole 200 nm structures compared to the signal at the bulk part of the 1400 nm structure. This behavior is, indeed, visible in the data.

However, the question remains, if a droplet spreading at the Au/SiOx interface could lead to an increased current signal at the edges and to misinterpretations of the enhanced current signal. An important quantity for this consideration is the contact angle on the pure SiOx interface. Macroscopic observations of the surface wetting behavior suggest that the SiOx surface is hydrophobic for the solution used here, i.e. the surface is not wetted by the electrolyte in the absence of an external potential (at OCP). The contact angle response of a dielectric layer in contact with an electrolyte is rather insensitive to surface chemical processes and dominated by the electrostatic properties of the dielectric [MH19]. Consequently, it also scales with the applied voltage according to [MH19]:

$$\cos \theta(U) = \cos \theta_0 + \frac{c_d}{2\gamma} U^2 \quad (5.10)$$

Here, c_d is the differential capacitance of the interface. Most of the variables are not known for our system, so a theoretical estimation is not possible. However, it can be concluded from the measurement of the array with 200 nm structures that the droplet size present on the SiOx surface is at least smaller than 200 nm. Otherwise the structure array could not be resolved by the measurement. Consequently, it is likely that the contact angle on the bulk SiOx interface is at least similar or larger than it is at the bulk Au interface. Thus, a droplet spreading at the Au/SiOx interface is rather unlikely and does not serve as a reasonable explanation for the higher current measured at the border of the 1400 nm structure. Consequently, we can conclude that the borders of the 1400 nm structures, indeed, exhibit an increased reaction rate for acidic HER compared to their bulk part.

5.2.2 Neutral medium - SICM measurement

From the considerations made above, it becomes clear that it is very challenging to conduct reliable measurements with the SECCM method at higher electrolyte pH values, since higher pH values necessitate a more negative absolute electrode potential to be applied to supply the same electrode potential in the RHE scale. An investigation of the local HER activity at higher pH values would be desirable, as the data presented in the previous section 5.1 suggests a larger difference between 'bulk activity' and 'border activity' regarding HER of the gold structures with increasing pH. However, the position of the PZC in SHE scale is rather independent of the pH [Led+17]. Thus, the contact angle at a similar HER overpotential increases with increasing pH according to equation (5.9). Indeed, conducting SECCM measurements in neutral electrolytes turned out to be very challenging and could not be performed reliably within the scope of this work.

However, to prove if there is an enhanced reactivity at the structure borders in neutral electrolyte as well, we conduct Scanning Ion Conductance Microscopy (SICM). This technique is conducted completely in liquid phase and, thus, a wetting behavior, which scales with the applied electrode potential, can be avoided. In our setup, we use an electrode configuration comparable to the configuration used by Momotenko et al. [Mom+16] and Page et al. [Pag+16]. The actual method procedure applied in this work slightly differs from the mentioned references. It is described in detail in section 3.2.6, and briefly introduced here.

The basic principle behind the local reactivity mapping in the SICM configuration is that the occurrence of an electrochemical reaction on the surface of the WE to investigate changes the local ionic concentration. This can be probed by SICM. We use two QRCEs in the setup, one present in the bulk of the electrolyte, in which the WE surface is immersed, and one in the pipette, which is hopping over the WE surface. The QRCEs used consist of a Ag/AgCl wire with macroscopic dimensions, i.e. their actual area is orders of magnitude larger than the opening of the pipette tip (again approx. 50 nm). In addition, the bulk QRCE has a much larger area than the gold area of the structured electrode to investigate, which is a nanostructured electrode with 1400 nm sized structured. The electrolyte used is 50 mM KCl. We chose an electrolyte containing Cl^- ions in order to assure a stable equilibrium at the two QRCEs.

Between the two QRCEs, a constant DC voltage U_2 of 0.3 V is applied (positive polarization at the bulk QRCE) throughout the whole mapping measurement. The resulting current I_1 is limited by the ionic conductivity at the pipette opening. When the pipette tip approaches the electrode surface, the ion conducting channel becomes smaller due to geometric reasons. Once the current I_1 falls below a certain reference value (here we use

60% of the bulk current), the approach is stopped. The pipette now remains at this z -position (the actual height of the pipette over the WE surface can just be estimated and is in the order of < 150 nm [Mom+16]) and a LSV scan is performed. In the LSV scan, the DC voltage U_1 between the bulk QRCE and the WE is swepted linearly. The voltage U_1 can also be interpreted as a WE potential vs. Ag/AgCl. We chose 500 mV s^{-1} as the scan rate. The WE is negatively polarized in this sweep. Two current feedbacks of the system are recorded: The current I_1 measured at the pipette QRCE and the current I_2 measured at the bulk QRCE. Figure 5.11 shows an exemplary current feedback of the system during one scan.

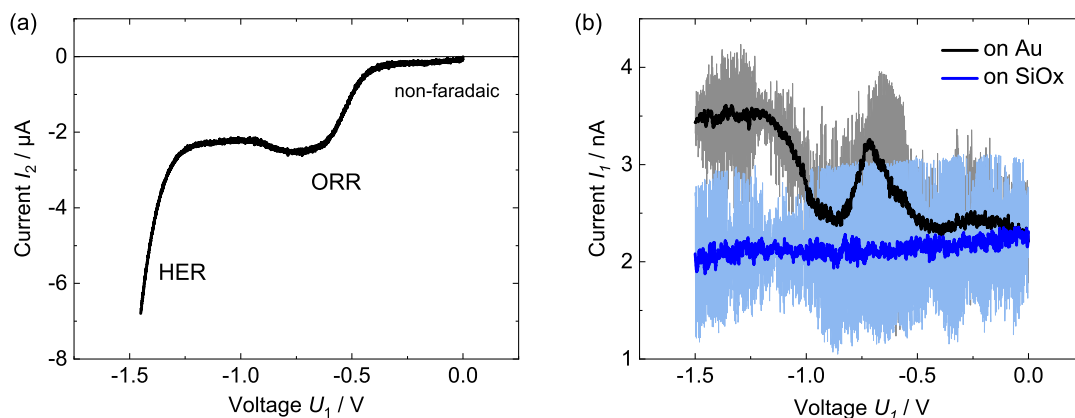


Figure 5.11: Single point SICM measurements. Response of (a) the bulk QRCE current I_2 and of (b) the pipette QRCE current I_1 during the LSV scan of U_1 going in negative direction. The I_1 feedback is shown at two different pipette positions: When the pipette is located 'in contact' over the Au surface (black), and when the pipette is located 'in contact' over the silicon oxide surface (blue). The I_2 feedback is similar in both cases. Scan rate: 500 mV s^{-1} . Electrolyte: 50 mM KCl .

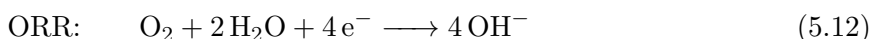
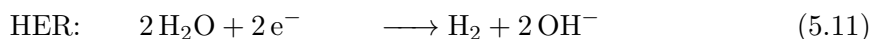
The current I_2 shown in Figure 5.11(a) clearly exhibits the typical features expected from a scan in negative potential direction on a Au surface. Between 0 and -0.4 V a small non-faradaic current is observed due to the charging of the double layer. At -0.4 V an increasing faradaic current is observed, saturating at around -0.7 V. This current is probably due to oxygen reduction reaction (ORR) since the measurement is not conducted in a controlled atmosphere and, consequently, the electrolyte is in equilibrium with ambient air. At around -1.3 V the current increases again due to HER. Since the current feedback shows the typical features expected for an Au electrode and the WE area is much smaller than the bulk QRCE area, we can conclude that most of the potential U_1 applied drops at the WE/electrolyte interface in the potential range investigated.

The influence of the potential sweep at the WE on the current I_1 measured at the pipette QRCE is shown in Figure 5.11(b). The noisy lighter lines are the raw data, the darker lines represent the moving average of the raw data over 50 points using the Savitzky-Golay smoothing method. We look at the current feedback at two selected positions: When the pipette is located over the SiOx/electrolyte interface on the WE (blue), and when it is located over the Au/electrolyte interface (black).

Let us first consider the I_1 feedback when the pipette is located over the SiOx interface (blue). During the potential sweep, the current stays almost constant, resp. it slightly decreases. This is the expected behavior. I_1 consists of two contributions, the current flowing between the pipette and the bulk QRCEs (major contribution) and the current

flowing between the pipette QRCE and the WE (minor contribution). When the pipette is at a position at which there is no change of the ionic conductivity due to local reactivity while sweeping U_1 (e.g. in the electrolyte bulk or over the SiOx), the I_1 signal only changes marginal. As the potential difference between the pipette QRCE and the bulk QRCE stays the same, the stationary current between these two is supposed to stay the same. However, the contribution of the WE/pipette QRCE current is supposed to change as their potential difference changes. From the data one can conclude that this contribution is only marginal (due to the small pipette opening) as the current only changes by approx. 10%. Thus, we can conclude that the main contribution of current I_1 is really caused by the current between the pipette QRCE and the bulk QRCE.

The behavior clearly changes when the pipette is located over a catalytic active surface during the potential scan, see black line in Figure 5.11(b). Starting from 0 V, the measured current changes during the sweep. We locate a maximum around -0.7 V and an increase of the current below -1.0 V after passing a valley. The features visible in I_1 clearly correlate with the macroscopic features observable in I_2 , see Figure 5.11(a). Consequently, we can conclude, that we probe the local change of the ionic conductivity due to the changing of the local ionic concentration. We see both reactions in the data, ORR as well as HER, as both reactions involve the production of hydroxide ions:



The recorded current caused by ORR at each pixel can be treated as a background current.

Current maps

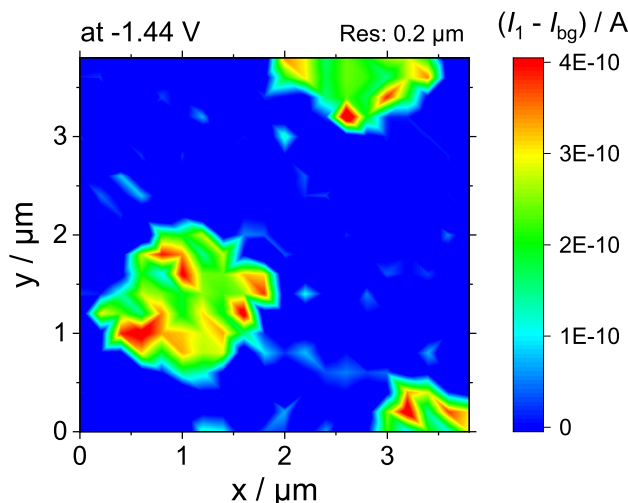


Figure 5.12: SICM current I_1 map of an Au structured electrode with 1400 nm structure size at voltage $U_1 = -1.44$ V, i.e. in the HER region, cf. 5.11. The structures are clearly identifiable from the silicon oxide surrounding. Resolution: $0.2 \mu\text{m}$. Electrolyte: 50 mM KCl.

Figure 5.12 shows an exemplary current map of a section of the metal array with 1400 nm sized structures. The data shown is collected at a potential of $U_1 = -1.44$ V, thus, in the HER region. The current I_1 is corrected by the background current I_{bg} , which is the average current measured between -0.6 V and -1.1 V. This background current accounts

for the non-faradaic contribution and the faradaic ORR contribution and is determined at each pixel individually. Here, the resolution (distance between pixels) is $0.2\ \mu\text{m}$. One can clearly identify areas, where an increased current can be measured (green to red area). These areas have a quadratic shape with a sidelength of approx. $1.2\ \mu\text{m}$. This sidelength coincides well with the sidelength of the Au structures ($1400\ \text{nm}$) within the resolution of the measurement. Thus, the structures in the array can be clearly identified by the ionic conductivity mapping, i.e. the local HER current.

Looking more carefully at the data, the current measured at the edges of the structures appears to be slightly increased (red) compared to the bulk (green). However, the difference between edges and metal bulk is not as clearly visible as observed in the SECCM data. In addition, the data shown is not statistically representative. We collected multiple maps at various positions on the sample but could neither verify or disprove the conjecture of the increased ionic conductivity at the edges of the structures, as the difference between edges and bulk, if observed, has been only very little and was within the measurement uncertainty. Unfortunately, due to an inherent drift in the system while performing measurements, a reliable mapping with higher resolution turned out to be very challenging.

However, we further tried to evaluate the local HER kinetics by performing line scans across individual structures. In order to account for the local uncertainty, we average the local data over multiple scans. Figure 5.13(top) shows multiple scans across a single structure (linescans) performed in x -direction with $0.1\ \mu\text{m}$ resolution plotted over each other (y -direction). The measured current is normalized to the average background current I_{bg} at each pixel. The individual lines are averaged over the y -coordinate and the resulting averaged current is plotted over the x -coordinate (bottom image). Looking carefully at the I - x plot shows that after averaging there is no statistical relevant higher rate at the edge of the structure. Scans with higher resolution in x direction give similar results.

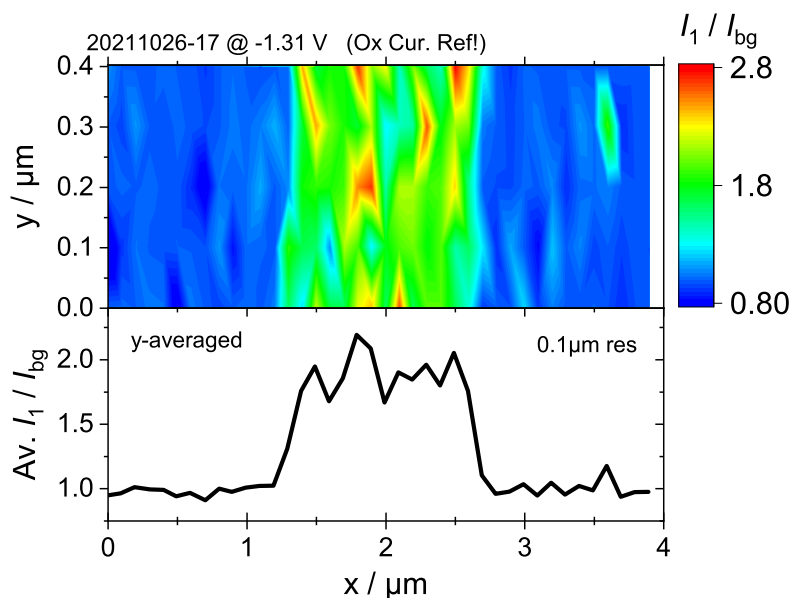


Figure 5.13: SICM line scans (top) across an Au structure with $1400\ \text{nm}$ size. The resolution is $0.1\ \mu\text{m}$. The measured current I_1 is normalized to the background current I_{bg} at each individual pixel. The green to red area shows the presence of the nanostructure. This data is averaged over the y -coordinate and the resulting averaged current is plotted over the x -coordinate (bottom image). No increased current at the edges can be observed.

Discussion: Does SICM resolve kinetics?

The question remains: Does the lack of evidence for the proposed increased HER reactivity at the structure edges necessitate a rejection of the conjectured effect, or does the method not resolve the conjectured effect? In other words, can the method provide a measurement of the local kinetics with the necessary resolution? Let us look again carefully at the I - U data shown in Figure 5.11. The detectable local response of I_1 appears below -0.5 V, cf. Figure 5.11(b). Contrary, the (kinetically determined) response of the macroscopic system I_2 appears at a more positive potential, i.e. above -0.5 V, cf. Figure 5.11(a).

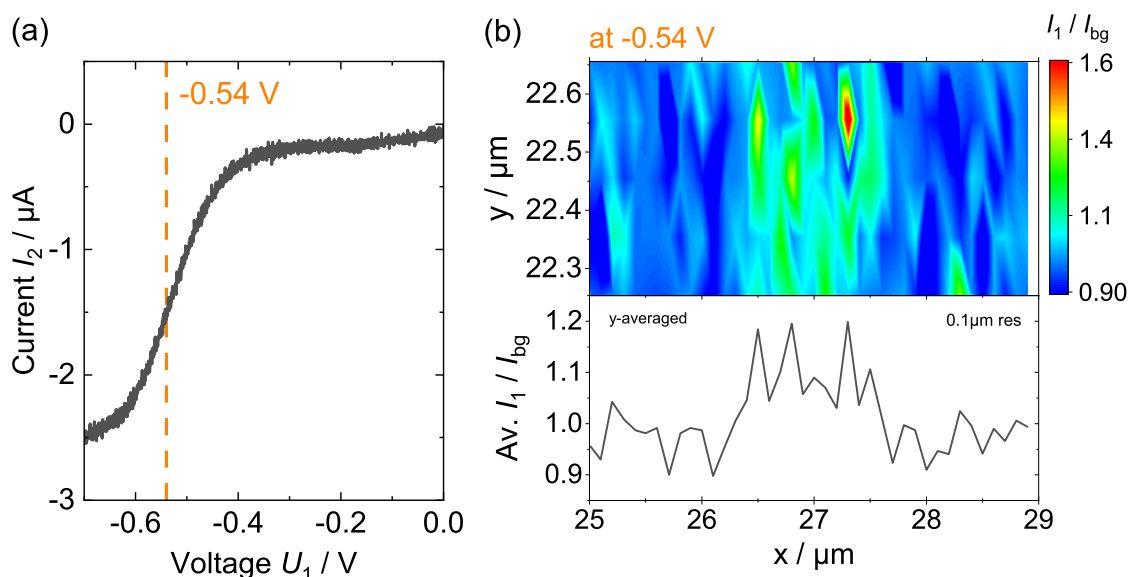


Figure 5.14: SICM mapping scan. (a) Macroscopic current response I_2 for a linear scan of U_1 , collected at an exemplary position during the conducted line scan. (b) Corresponding map of current I_1 (top) at $U_1 = -0.54$ V (normalized to the background current), and averaged current I_1 (bottom) over the y -coordinate (over one structure). The current measured at this potential is caused by ORR.

This becomes even more clear, when looking at the current map of the starting ORR. Figure 5.14(a) shows the macroscopic current response I_2 in the ORR region plotted over voltage U_1 collected at an exemplary position during an SICM mapping scan. Figure 5.14(b) shows the current map of the current I_1 in an SICM scan normalized to the background current at each position (top) and the averaged lateral current distribution at $U_1 = -0.54$ V (bottom). This potential was determined to be the lowest overpotential, at which we could observe statistical relevant indications of mapping faradaic currents in the data. It is clearly visible from the LSV shape in Figure 5.14(a) that at this potential the current is not limited by kinetics anymore, but already determined by species transport. This is a strong hint that it is not possible to determine the kinetics in the necessary precision by this method. The measurement procedure may identify areas with and without reactivity in the relevant size dimension of the array (1 μm) indirectly due to a change in local ion concentration. However, the method as applied here does not seem to resolve the kinetics in the necessary length-/timescale.

5.3 Influence of particle transport

The interpretation of the kinetic data of nanostructured electrodes in section 5.1 has been conducted with the assumption, that the current feedback is completely determined by reaction kinetics. However, the measurements considered in this section have not been conducted under transport controlled conditions. It is known that the transport of particles, which participate in the reaction, towards/from the electrode surface can determine the current response of an electrochemical system during a potential scan significantly. Thus, a size-dependent transport behavior, i.e. a different transport behavior at the edges of the structures compared to the bulk surface, may lead to miss-interpretations, when performing kinetic analyses as conducted. Consequently, in this section we investigate if, respectively how, particle transport affects the macroscopic current feedback of the investigated nanostructured electrodes.

The local ionic flux \vec{J}_i of a species i in the electrolyte is given by the Nernst-Planck-Equation [BF01]:

$$\vec{J}_i = -D_i \vec{\nabla} c_i + D_i c_i \frac{z_i e}{k_B T} \vec{\nabla} \phi + c_i \vec{v} \quad (5.13)$$

Here, D_i is the diffusion coefficient, c_i is the local concentration, ϕ is the local electrostatic potential, z_i is the ionic charge number, e is the elementary charge, k_B is the Boltzmann constant, T is the temperature, and \vec{v} is a local velocity field. The first term of the equation is known as the diffusion term, the second as migration and the last term as convection. Considering a flux of charged species, the connection between the particle flux J_i and the actual (electrical) current density j_i is given by

$$\vec{j}_i = z_i F \vec{J}_i \quad (5.14)$$

5.3.1 Primary current distribution

Let us first consider only the primary current. Primary current is the response of the electrochemical system at potentiostatic or -dynamic conditions, if the current is determined by the conductivity of the electrolyte:

$$\vec{j}(\vec{x}) = -\kappa \vec{\nabla} \phi(\vec{x}) \quad (5.15)$$

This is basically Ohm's law. A comparison with the Nernst-Planck-equation makes clear that this description is valid if migration is the dominating contribution to the local particle flux. In the case of two electrodes immersed in an electrolyte, where the electrodes work as ion source and sinks, the ionic current flowing across the electrolyte is determined, among others, by the reacting species. Consequently, for acidic HER it is determined by proton conduction. Newman et al. [New66; SN89] calculated the primary current profile on a planar rotating disk electrode. They showed, that the current profile is not homogeneous on the electrode surface, but the current increases when approaching the disk/insulator interface, i.e. the border of the conducting disk. This behavior strongly reminds of the increased reactivity measured at the border of the Au nanostructures compared to their bulk area, shown in the previous section 5.2.

However, only considering the primary current distribution is not sufficient to describe the 'real' system investigated here: First, the electrolytes investigated experimentally are rather highly concentrated, i.e. the conductivity κ is comparatively high: $\kappa(0.1 \text{ M H}_2\text{SO}_4) \approx 4 \Omega^{-1} \text{ m}^{-1}$, $\kappa(0.1 \text{ M NaOH}) \approx 2.5 \Omega^{-1} \text{ m}^{-1}$ (the values were calculated on a basis of

the molar conductivities given in [Rum17] of the individual ionic species present in the respective electrolyte). In addition, the measured current can just be correlated with the primary current distribution if migration is the rate determining process. This is just the case, if most of the applied potential drops inside the electrolyte. However, in rather non-dilute electrolytes (high κ) and/or at low current densities this is not valid. In this cases, the potential drop across the electrolyte is negligible and, thus, the current is not determined by migration, which makes the primary current insufficient to describe the current distribution correctly. Most of the applied overpotential drops across the double layer. However, considering a non-zero current across the metal/electrolyte interface, the current can still be determined by either kinetics or diffusion. The influence of diffusion in our system is presented in the next sections.

5.3.2 Macroscopic diffusion - ReRDE measurement

A common method in electrochemistry to govern transport conditions is the rotating disk electrode (RDE). The rotation of a disk electrode forces convection of fluid towards the electrode surface, cf. third term in equation (5.13). Thus, by variation of the rotation speed, the diffusion layer thickness can be tuned in the micrometer range and allows for defined transport condition [BF01].

The macroscopic shape of the electrodes investigated here is planar. In addition, the back contact of the electrodes needs to be sealed from the electrolyte at the front side. Thus, a standard rotating disk configuration is not applicable to our samples. Within the scope of this work, we adapted the approach of a recessed rotating disk electrode (ReRDE) setup to our samples. A detailed characterization of this experimental configuration is given in the experimental section 3.2.5. Furthermore, we show in section 3.2.5 that the developed ReRDE configuration in combination with the electrodes investigated here yields the behavior known from a typical RDE setup, which allows for an application of the known equations.

In a RDE experiment, the diffusion layer thickness δ can be controlled via the rotation speed ω according to the equation [BF01]:

$$\delta = 1.61D^{1/3}\nu^{1/6}\omega^{-1/2} \quad (5.16)$$

Here, D is the diffusion coefficient of the reactant, and ν is the kinematic viscosity of the medium ($\nu \approx 10^{-6}\text{m}^2\text{s}^{-1}$ for water at 20°C [Rum17]). Assuming the diffusion coefficient of OH^- ions in water ($D_{\text{OH}^-} = 5.3 \times 10^{-9}\text{m}^2\text{s}^{-1}$ [Rum17]) and a rotation speed of 2000 RPM, the diffusion layer thickness is in the range of 20 μm . Thus, even at this comparatively high rotation speed, the diffusion layer thickness is approx. one order of magnitude larger than the pitch of the largest structures investigated (1400 nm Au structure size). Consequently, the transport properties, which can be altered by the ReRDE rotation, are labeled by the term 'macroscopic diffusion properties' in the following. As the maximum array pitch is much smaller than the thickness of the diffusion layer with maximum rotation speed applicable, the current-voltage behavior of the nanostructured electrode is likely to be independent of the RDE rotation at the low to moderate current densities investigated here, i.e. it is independent of the macroscopic diffusion properties. In the following, we will analyze, how rotation influences the behavior of a (i) continuous layer electrode with an active surface area much larger than the calculated diffusion layer thickness and (ii) a nanostructured electrode with the smallest structure size investigated

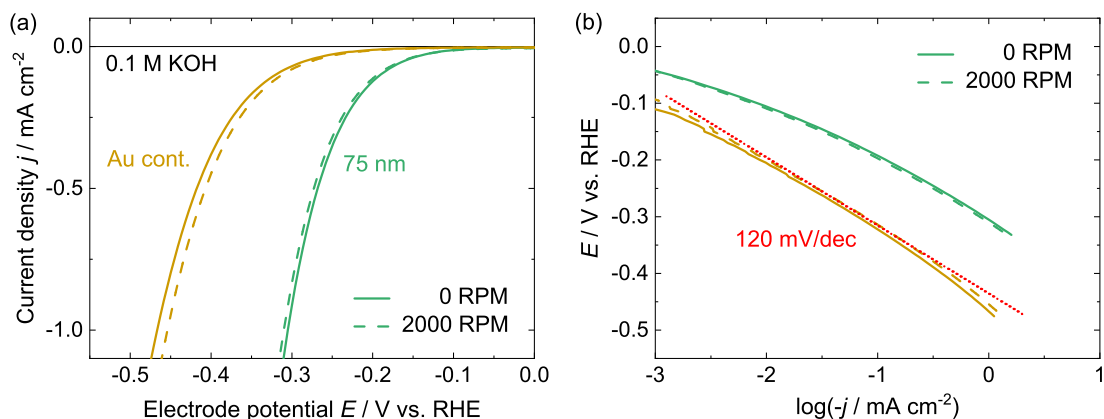


Figure 5.15: (a) LSVs of a continuous Au layer electrode (Au cont., yellow) and 75 nm sized structured electrode (green) measured in 0.1 M KOH (pH 13) in the recessed rotating disk electrode (ReRDE) configuration with and without rotation. Scan rate: 50 mV s^{-1} . (b) Associated Tafel plots. For the continuous Au layer the overpotential necessary for a certain HER current density becomes slightly smaller with increasing rotation rates. The behavior of the 75 nm structures is rather independent of the rotation rate. Consequently, the current-potential characteristics of nanostructured electrodes without rotation is not determined by the macroscopic diffusion properties in the current density range investigated in this work.

in this work.

Figure 5.15(a) shows the LSV curves of a continuous Au layer with 5 mm pad diameter of the active surface area (Au cont., yellow) and a nanostructured electrode with 75 nm structure size (75 nm, green) in the ReRDE configuration in alkaline electrolyte containing 0.1 M KOH with and without rotation of the electrode. Figure (b) shows the associated Tafel plot.

Let us first consider the continuous Au layer electrode (yellow curves). It appears that with rotation (dashed line) slightly less overpotential needs to be applied to draw a certain current density compared to the curve without rotation (solid line). At -1.0 mA cm^{-2} the difference between the curves is approx. 13 mV. This difference is well reproducible and, thus, not solely explainable by measurement uncertainty. However, the Tafel slope of both curves is very similar in the range of low current densities and has a value very close to 120 mV dec^{-1} , as indicated in Figure 5.15(b) by the red dotted line. As convection is forced by rotation, the diffusion layer thickness is decreased according to the standard RDE theory given by equation (5.16). Consequently, in the transport influenced regime an increasing current at a fixed potential is expected, if the transport rate towards/from the surface of species participating in the reaction is increased by rotation. This behavior can be observed in Figure 5.15(a) for Au cont.

Although this result is quite expected, it needs to be mentioned that it differs from the results obtained by Goyal et al. [GK21b]. The authors observed a decreasing current at a fixed potential when increasing the rotation speed in 0.1 M KOH at pH 13 (same electrolyte as used here) for an Au(pc) electrode (comparable to Au cont. investigated here). As an explanation for this counter-intuitive behavior they suggested that the increasing rotation rate decreases the surface pH at HER conditions, which leads to a repulsion of cations in order to fulfill the charge neutrality condition locally. As "the cations near the surface play a central role in stabilizing the transition state for the rate determining Volmer step" [GK21b], an increasing rotation would result in the suppression of HER. However,

this behavior could not be reproduced experimentally here and, consequently, the given hypothesis could not be verified.

Next, we consider the behavior of the 75 nm electrode (green curves). It is clearly visible that both curves, with and without rotation, lie quite close to each other. The curve for zero rotation appears to be slightly shifted towards more positive potentials by 5 mV at the comparatively large current density of -1.1 mA cm^{-2} . However, this slight difference may be explainable by the measurement uncertainty. In addition, the trend of both curves in the Tafel plot is very similar in the whole potential range investigated. The behavior appears to be rather independent of the rotation speed. This further justifies the assertion given above that the current response is not affected by (macroscopic) diffusion in the current regime investigated here, i.e. below -1 mA cm^{-2} . This holds at least for the rather 'strong' electrolyte with an ionic concentration 0.1 M of product species investigated here.

Consequently, we conclude two important points: First, the change of the Tafel slope with increasing overpotential observed at low current densities in several systems presented earlier, cf. Figures 5.3(a) and (b), cannot be explained by differences in the macroscopic diffusion properties of differently sized Au structures. Second, even more relevant, the observed decrease of overpotential with decreasing structure size, cf. Figures 5.2(a) and (b), is not explainable by differences in the (macroscopic) diffusion profile, i.e. the transport towards/from the structures of various sizes. Consequently, the result obtained here strengthens the hypothesis that the HER enhancement observed for smaller structures is caused by a variation of the reaction kinetics.

5.3.3 Microscopic diffusion - Diffusion in microelectrode arrays

The electrodes investigated here consist basically of an array of micro-/nanoelectrodes. Especially at low current densities during a potential scan, i.e. during the build up of the diffusion layer, the diffusion of reactants towards the individual structures may play a crucial role, as the local diffusion profile at the edges can differ from the bulk part of the structures. Consequently, we analyze 'microscopic diffusion properties' of the variously sized nanostructures, i.e. the diffusion properties of the microelectrode arrays, in this section.

Guo et al. [GL08] simulated the evolution of concentration profiles in 2D co-planar microelectrode arrays during cyclic voltammetric experiments. They recognized that, depending on the geometric, physical, and measurement parameters, the emerging concentration profile and, consequently, the shape of a recorded CV varies. An overview of the different possible transport-profiles for microelectrode arrays and the respective CV shape is given in Figure 5.16(a). Relevant parameters, which influence the transport profile, are: The radius of an individual structure $d/2$ in the array, the center-to-center-distance (pitch) p between two structures (hexagonally ordered in this case), the scan rate ν of the potential scan, and the diffusion coefficient D of the analyte. They introduced the dimensionless scan rate V

$$V = \frac{nF}{4RT} \frac{(d/2)^2}{D} \nu \quad (5.17)$$

which works as a parameter for classifying a certain system/experiment into various 'transport-profile classes'. The classification depends on the actual value of V and the pitch-to-radius ratio $p/(d/2)$ of the array. A zone diagram, which assigns sets of the two parameters to a certain transport class, is shown in Figure 5.16(b).

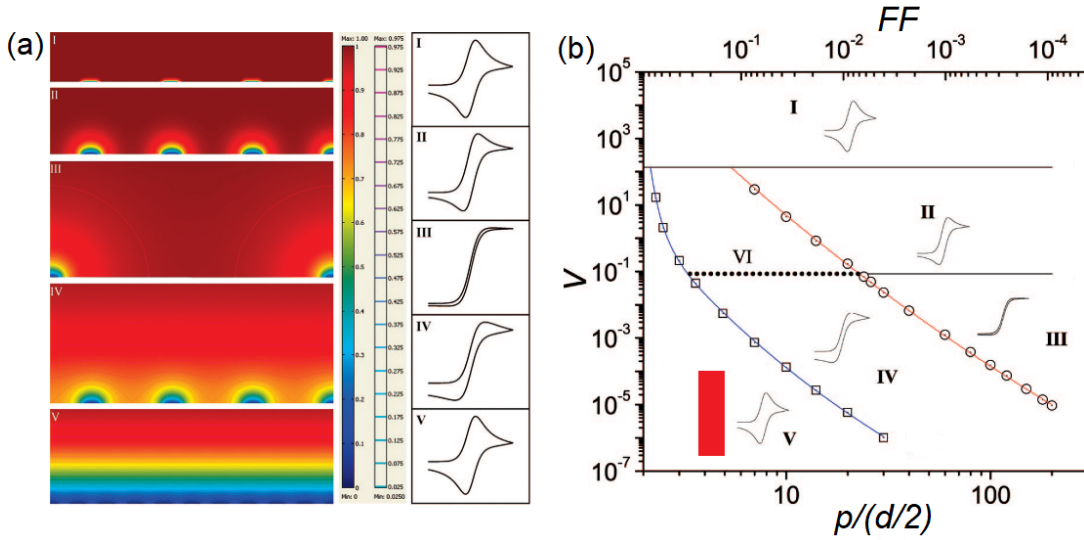


Figure 5.16: Transport-profile classification of a coplanar microelectrode array for various geometric and measurement parameters according to Guo et al. [GL08]. (a) Concentration profiles for various transport profiles and (b) Zone diagram (classification) as a function of the pitch-to-radius ratio $p/(d/2)$ or the filling factor FF of the array and the dimensionless scan rate V . Relevant transport profiles are: (I) Planar diffusion on individual structures, (III) Hemispherical diffusion on individual electrodes, and (V) Planar diffusion layer over the entire array. (II) and (IV) are mixed profiles. The red rectangle in image (b) indicates the zone in which the nanostructured electrodes investigated in this work are located (see Table 5.3). Thus, all electrodes investigated in this work are supposed to show a planar concentration profile. Images are taken with modifications from [GL08].

We can estimate the sets of the two parameters, i.e. the dimensionless scan rate and pitch-to-radius ratio, for the nanostructured electrodes presented in this work. We assume $T = 298\text{ K}$, $n = 2$ (HER), the diffusion coefficient of OH^- ions in solution $D_{\text{OH}^-} = 5.3 \times 10^{-9}\text{ m}^2\text{ s}^{-1}$ [Rum17] and the scan rate 50 mV s^{-1} , which is the standard scan rate used throughout this work. The geometric parameters of the arrays are determined by the stamps used for electrode fabrication and relevant geometric properties are explained in section 3.1.1. The calculated parameters $V(d)$ and $p/(d/2)$ are shown in Table 5.3.

Due to the design of the metal arrays, the pitch-to-radius ratio $p/(d/2)$ is quite similar for all electrodes. However, the dimensionless scan rate differs by approx. two orders of magnitude. This is mostly caused by its quadratic dependence on the radius of individual structures. However, the assignment of the various electrodes to their respective transport

Structure size d	V	$p/(d/2)$
1400 nm	$9.3 \cdot 10^{-5}$	4.3
350 nm	$5.8 \cdot 10^{-6}$	4.0
200 nm	$1.9 \cdot 10^{-6}$	4.3
75 nm	$2.7 \cdot 10^{-7}$	4.0

Table 5.3: Relevant microelectrode array parameters of the nanostructured electrodes investigated in this work: Dimensionless scan rate V and pitch-to-radius ratio $p/(d/2)$. The potential scan rate used for calculation of the dimensionless scan rate is the standard scan rate of 50 mV s^{-1} .

Structure size d	Share of	
	top area	lateral area
1400 nm	96%	4%
75 nm	54%	46%

Table 5.4: Calculated share of top and lateral Au area for protruding structures with two selected sizes. Protruding structures are not embedded in an insulating passivation layer. The scheme of both electrode types, i.e. with embedded and protruding structures, is shown in Figure 5.17(a). Considered metal layer thickness for calculation: 16 nm.

profile using the classification zone diagram in Figure 5.16(b) shows that all electrodes fall into the same zone of profile (V), classified as 'planar diffusion layer over the entire array', cf. red rectangle in the Figure 5.16(b). Consequently, according to this classification, the (microscopic) diffusion properties of all electrodes is similar and is supposed to be planar.

The mentioned classification assumes (1) a hexagonal arrangement of structures and (2) a co-planar microelectrode array. The first requirement is not fulfilled, as the structures are arranged in a rectangular array. However, the error made by this simplification is supposed to be only minor, as small deviations in the pitch-to-radius ratio do not change the classification. The second requirement is fulfilled, since there is no recess between the structures, which is due to their incorporation in the surrounding passivation layer.

However, in order to further investigate the influence of microscopic diffusion in our system, we can analyze electrodes consisting of arrays without embedding the nanostructures in a passivation layer. The structures then protrude from the planar electrode surface by the thickness of their metal stack. A scheme of these electrodes is shown in Figure 5.17(a). Changing the structure size d while keeping the metal thickness constant now changes the share of the top metal surface of the structures to their lateral metal surface. Considering a metal height of 16 nm, the share of the lateral structure surface is approx. 4% for the largest structures investigated (1400 nm) and more than 40% for the smallest structures investigated (75 nm). The actual share is given in Table 5.4. Consequently, microscopic diffusion present in the low current range during a potential scan should be more pronounced for electrodes with a larger share of lateral surface area.

Figure 5.17(b) shows LSV diagrams of electrodes with the two different structure sizes in acidic 0.1 M H_2SO_4 electrolyte at a scan rate of 50 mV s^{-1} . The solid lines show the curves for electrodes with protruding structures, i.e. without passivation layer, the dashed lines show electrodes with embedded structures, i.e. with passivation layer, for reference.

Let us first consider the large structures with 1400 nm diameter (black curves). The curves of the protruding structures and the embedded structures lie well over each other. Thus, there appears to be no significant difference in transport properties of the two electrodes. However, the situation is different considering the small structures with 75 nm diameter (green curves). At very low current densities ($|j| < 0.1 \text{ mA cm}^{-2}$), the curves of the electrodes lie above each other. At higher current densities the curves separate. The incline of the curve of protruding structures is less steep and even crosses the curves of the 1400 nm sized structures at approx. -1.5 mA cm^{-2} .

This behavior can be explained by the emerging diffusion layer at the nanoelectrode array. During the downwards scan in the faradaic regime, the diffusion layer starts building up.

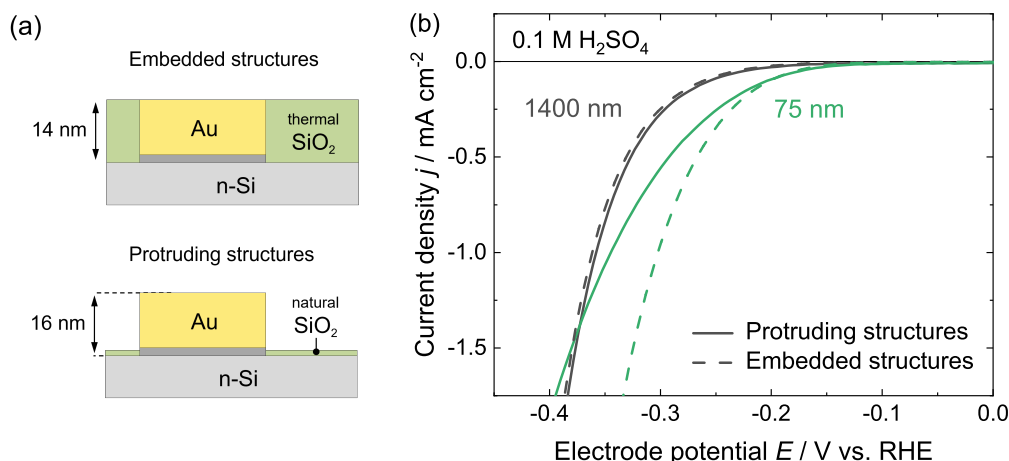


Figure 5.17: Comparison of embedded and protruding metal structures regarding HER in acidic electrolyte. (a) Schematic side-view of the two electrodes types investigated, consisting of either embedded (top) or protruding (bottom) Au structures. The gray area below the Au structures is the Ti based adhesion layer (thickness: 3 nm). (b) LSVs of the two different types of electrodes for two different Au structure sizes of 1400 nm and 75 nm in 0.1 M H₂SO₄. Scan rate: 50 mV s⁻¹

At small current densities, the diffusion profile is still emerging hemispherically around the individual structures, i.e. the iso-concentration plane is perpendicular to the surface normal, at the top surface as well as at the lateral surface. After some time, the hemispheres around the structures start to merge and the diffusion profile begins to evolve planar across the entire (macroscopic) electrode surface. As a consequence, the transport towards the lateral surface is suppressed. As the diffusion profile evolves planar, the predominant active surface becomes the top surface. Consequently, if the share of the lateral surface is high as for the small structures, cf. Table 5.4, the active area gets significantly reduced. This leads to a less steep incline of the actual measured current, even though the current density on the (top) surface still increases with increasing overpotential as expected. This effect is supposed to be even more increased considering a higher reactivity of the area, where metal and oxide is in close contact, i.e. at the bottom of the protruding structures.

There are two major conclusions, which can be deduced from the data presented here. First, the microscopic diffusion present in nano- and microelectrode arrays does not need to be considered for the embedded structures considered in this work. All structure sizes show a planar diffusion behavior and can, thus, be treated equally. This is verified by the comparison between embedded and protruding structures shown above. Second, *both* kinds of electrodes, i.e. consisting of embedded and protruding structures, with the smallest structures investigated of 75 nm size show a shift of the HER onset towards more positive potentials compared to the curves of the respective large structures. The curves of both types of electrodes even lie above each other at low current densities. Thus, we can conclude that the observed overpotential difference between the largest and the smallest structures investigated here is not caused by microscopic diffusion, but is of kinetic origin.

It needs to be mentioned at this point, that it is not fully clear how the actual gold/oxide interface in the case of the protruding structures is composed. It is unclear if the lateral surface of the titanium layer is covered by Au atoms, due to the Au evaporation step in the production process, or, if not, to which extent the titanium layer is embedded in a layer of native silicon oxide, which forms already at ambient conditions [Mor+90]. The influence of a Au/Ti/SiO_x layer on the HER onset shift will be discussed at a later point.

5.4 Summary

In this chapter, we measured the HER reactivity of (photo-inactive) n-type silicon-based electrodes consisting of arrays of Au nanostructures in various structure sizes. We could observe that smaller Au structures exhibit a larger HER reactivity than larger Au structures, in both acidic as well as alkaline media. The absolute overpotential difference at a current density of -0.1 mA cm^{-2} between the largest and the smallest size investigated is larger in alkaline electrolyte (120 mV) than in acidic electrolyte (60 mV).

A Tafel analysis revealed that this enhancement is not caused by different reaction mechanisms present for various structure sizes, as the obtained Tafel slopes are (within the error) the same for all electrodes investigated. In alkaline media, the determined slope of approx. 120 mV dec^{-1} indicates that the Volmer step is the rate determining step for all Au-based electrodes investigated. In acidic media, we observed two potential regimes with different Tafel slopes, approx. 60 mV dec^{-1} at low and approx. 120 mV dec^{-1} at rather high cathodic overpotential. However, the dependence of the Tafel slopes on the overpotential appears to be similar for all structure sizes investigated in acidic electrolyte.

We further showed that the determined exchange current densities of nanostructured electrodes scale linearly with the inverse of the respective structure size $1/d$. Geometric considerations suggest that this dependence is evident if the edges (border) of the metal structures exhibit an increased HER reactivity compared to the bulk of the metal structures. By probing the HER reactivity locally on the heterogeneous electrode surface by SECCM (in acidic medium) we could directly show that the HER reaction current at the border of the structures is increased compared to the bulk of the structures. Moreover, we showed that the HER enhancement at the border is not caused by the transport properties of particles involved in the reaction. Consequently, we attributed the observed higher HER reactivity to a locally increased reaction kinetics.

The findings in this chapter suggest the conclusion that the observed HER enhancement for smaller Au structures is caused by an increased HER kinetics at the border of the structures. This enhancement may be due to special properties of the lateral gold/silicon oxide interface. However, the further localization of the mechanistic origin of this effect will be part of the next chapter.

Chapter 6

Influence of various system parameters on the HER enhancement

In the last chapter we showed that the enhancement of the HER reactivity observed for smaller Au structures is due to an increased kinetics of the reaction at the border of the structures. However, there is still a variety of possible explanations, which could be invoked to explain the increased reactivity at the edges of the structures.

In this chapter, we analyze the influence of various system parameters on the enhancement of HER kinetics on nanostructured metal/silicon electrodes. From the dependence of the reaction enhancement on various system parameters, we further localize the mechanistic origin of the HER enhancement observed. In section 6.1, we investigate and discuss the role of the electrocatalyst material and its surface structure. In section 6.2, we look at the influence of the passivation layer surface and material. We close this chapter with section 6.3, in which we determine the influence of various parameters of the electrochemical environment, i.e. the properties of the electrolyte.

The findings in this chapter form the basis for the elaboration of a bifunctional mechanism present at the metal/insulator interface, which will be finally proposed in chapter 8.

6.1 Electrocatalytic surface and catalyst material

In the last chapter we showed that the edges of the Au structures exhibit an increased HER reactivity in acidic as well as alkaline medium. An obvious explanation of the observed effect may be that the edges of the structures may display an altered hydrogen adsorption energetics compared to the structure bulk, which, in turn, would lead to the observed higher local reactivity. Consequently, we discuss this aspect in this section.

First, we investigate in sections 6.1.1 and 6.1.2 to which extent the enhancement of HER kinetics in acidic (and alkaline) medium present at the border/edges of gold nanostructures is caused by a locally different nature/topography of the gold surface. More precisely: We examine, if the enhancement can be explained *only* by an accumulation of undercoordinated gold sites exhibiting lower hydrogen adsorption energetics at the edges of the structures. We will conclude in section 6.1.2, in which we analyze arrays of silicon oxide patches of various sizes on Au(pc) surfaces that the HER enhancement cannot be ascribed to this explanation.

Second, we investigate in sections 6.1.3 and 6.1.4, how the HER enhancement of metal structures depends on the actual catalyst material, i.e. we investigate if/how the HER enhancement is present for various other electrocatalyst materials exhibiting very different hydrogen adsorption energies. Here, we consider Cu and Pt based nanostructures. We will see that the enhancement is not restricted to Au as the catalyst material, but it is also present for HER on nanostructured electrodes based on Pt or Cu.

6.1.1 Au surface topography of nanostructured electrodes

The nature of the Au electrode surface is known to have a huge influence on the measured HER activity. Since the adsorption of hydrogen atoms is strongly dependent on the adsorption energetics at the reaction site, the variation of reaction sites by altering the surface morphology is a fundamental parameter for changing catalytic reactivity. Many groups studied the HER activity on poly-crystalline [SM82; KBN17] or different mono-crystalline [HW87; PGM98; Kib+18] Au surfaces. These studies clearly reveal that HER activity on Au is dependent on the crystallographic orientation of the Au surface. The activity of the low-index surface facets Au(111), Au(100) and Au(110) show worse HER activity compared to higher index facets. However, the kinetics on the (111) facet, which exhibits the lowest HER activity among the investigated facets, is just a factor of 2 slower compared to the one with the highest activity, which is the (332) facet [HW87]. The kinetics of poly-crystalline Au surfaces further appears to be a superposition of the most dominant low-index facets [HW87]. In addition, on the atomic level a poly-crystalline Au surface exhibits a comparatively high surface concentration of low-coordinated atoms at steps and kinks, which are also known to improve the catalytic activity [Fuj+12].

Due to the design of the nanostructures, the smallest structures exhibit the largest interfacial area between the Au structures and the SiO_x surrounding. However, the surface at the edges of the structures is likely to consist of a larger density of step and kink sites compared to the bulk surface due to the fabrication process of the structures. Consequently, smaller structures may consist of a larger absolute number of undercoordinated sites on the surface, which may, in turn, explain the observed improved HER kinetics.

Figure 6.1 shows the oxidation region of nanostructured electrodes with differently sized Au structures in 0.1 M H₂SO₄. The anodic peak ensemble shape is characteristic for the surface topography [Ang+87; Ham96]. It is visible that the peak ensemble shape is different for the different structure sizes. While the largest structures (1400 nm) show a more pronounced peak at 1.58 V_{RHE} (A2), the smallest structures (75 nm) show a decreased peak at this potential and a more pronounced peak at approx. 1.4 V_{RHE} (A1). The intermediate structure sizes further confirm the appearing trend. A sharp A2 peak is attributed to a higher concentration of Au(111) sites on the surface, while a less sharp peak A2 and more pronounced peak at A1 hints towards a higher poly-crystalline surface fraction [PAI86]. Consequently, the largest structures sizes appear to behave more like a Au(111)-dominated system, while smaller structures appear to behave more like a Au(pc)-dominated system. As it is known from the literature (see above), the Au(111) facet gives the worst activity regarding HER. Thus, we would expect, already from this consideration, an increasing HER activity with decreasing structure size. Indeed, this trend has been observed in the previous section 5.1 in acidic media.

One needs to mention at this point that the argumentation above is just valid if the hydroxide adsorption on the Au surface, i.e. the oxidation of the gold surface, is only

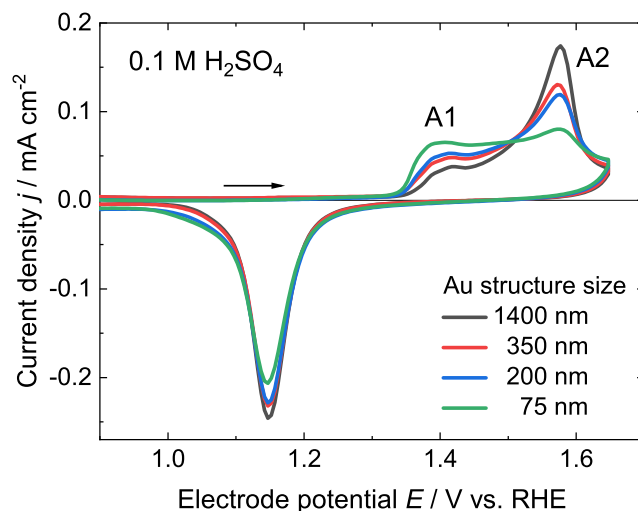


Figure 6.1: Au oxidation region in 0.1 M H_2SO_4 for electrodes containing Au nanostructures in different sizes. The shape of the anodic peak ensemble changes with decreasing structure size. While the peak A2 at approx. $1.55 V_{\text{RHE}}$ is more pronounced for the larger structure sizes, the peak A1 at approx. $1.4 V_{\text{RHE}}$ is more pronounced for smaller structure size.

determined by the properties of the Au surface. If the silicon oxide in close contact with Au further influences the hydroxide adsorption energetics on Au (as it may be caused by an appearing 'bifunctional mechanism' as the one proposed later), this argumentation would not be valid anymore. Consequently, the appearance of such a mechanism would further change the Au oxidation peak shape. However, a study of this effect needs to be part of future work.

To further elucidate the effect of the Au surface state of the nanostructured electrodes on their HER activity, we compare structures, which are of similar size, i.e. both electrodes have a similar 'border length' of the Au/SiO_x interface, but exhibit an altered ratio of the respective surface sites. By changing the parameters during the Au evaporation step, we could produce samples consisting of 1400 nm sized Au structures, but exhibiting a smaller share of Au(111) surface sites. Figure 6.2 shows CVs of three different electrodes in 0.1 M H_2SO_4 : A typical 1400 nm electrode with dominating Au(111) contribution (black), a typical 75 nm electrode (green) for comparison, and the mentioned 1400 nm electrode, which shows an altered Au surface topography (gray). The fact that the latter electrode is less dominated by Au(111) sites becomes evident, when comparing the anodic peak ensemble above $1.3 V_{\text{RHE}}$ between the typical 1400 nm electrode (black) and the altered one (gray). The latter curve shows a less pronounced peak A2, while the contribution of peak A1 is larger. Considering the HER reaction current (see inset), one recognizes that the activity of the altered 1400 nm electrode is slightly improved compared to the typical 1400 nm electrode. The HER overpotential is about 15 mV lower (see orange arrows). As both electrodes exhibit a similar Au/SiO_x interfacial length, this difference is now not caused by any interfacial effect and can now be fully attributed to the changed surface topography at the bulk part of the Au structures.

In the CV, it is also visible that the 75 nm electrode still shows the highest HER activity compared to both 1400 nm electrodes. However, it is also visible in the oxidation peak ensemble that the Au surface configuration of the 75 nm electrode still exhibits more

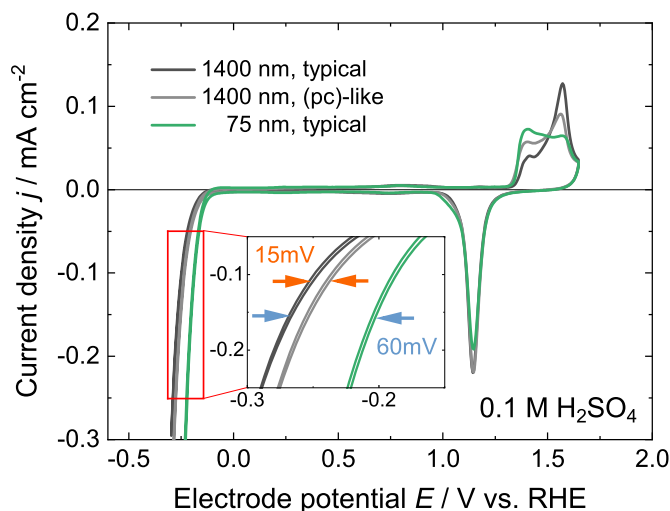


Figure 6.2: CVs of three different electrodes in 0.1 M H_2SO_4 . Black: Typical Au structures with 1400 nm structure size. Gray: 1400 nm sized Au structures, exhibiting a lower density of (111) adsorption sites on the surface. Green: Typical Au structures with 75 nm structure size.

under-coordinated sites compared to the altered 1400 nm (pc)-like electrode. Thus, we can conclude that the increasing HER activity with decreasing structure size observed in acidic medium can be attributed, at least partly, to a different surface morphology, which is intrinsically caused by reducing the Au structure size. However, the question remains, to which quantitative extent the altered Au surface itself contributes to the observed activity difference in acidic medium. Nevertheless, the quantitative comparison of the activities obtained in section 5.1 indicates that the enhancement at the edges in acidic medium cannot be fully explained by the altered surface morphology, as the measured activities of the smallest structures investigated are around one order of magnitude larger compared to the ones of the largest structure sizes. This large difference appears to be rather high to fully assign it to altered hydrogen adsorption energy at the edges. However, in the next section we demonstrate that the presence of an array of oxide structures enhance the HER activity on a homogenous Au surface. In a later section 6.2.1 we will elucidate, if/how the presence of silicon oxide itself influences the activity of nanostructured electrodes.

6.1.2 SiO_x nanostructures on Au(pc) electrode

Still the question remains, if the enhanced HER kinetics in acidic media at the edges of the Au nanostructures is caused by an altered surface morphology at the edges compared to the bulk, which leads to optimized proton adsorption properties, or, if the close presence of oxide to the Au phase itself may lead to an enhancement at the edges, i.e. at the Au/oxide interface.

In this section, we follow a different approach: We investigate arrays of silicon oxide nanostructures with various sizes on a homogeneous Au(pc) surface. With this system, it is possible to estimate the influence of the oxide/Au interface directly, as the Au layer is supposed to have rather homogeneous surface properties across the entire electrode surface. The production method of SiO_x structure arrays on Au(pc) substrates is straight forward and also employs the LO-NIL fabrication method. Instead of using a pure silicon substrate and evaporating Ti/Au metal films as done for the 'standard' nanostructured

electrodes, we use a metal covered silicon substrate and evaporate, after patterning, a Ti/SiO_x film onto the sample. As we use the same stamps for patterning as we use for the 'standard' electrodes, the pitch p and the sizes d are similar. A more detailed description of the actual modified fabrication procedure is given by Maier et al. in [Mai+20]. A schematic side-view of the electrode surface consisting of SiO_x nanostructures is shown in Figure 6.3(a). SEM images of the produced SiO_x structures on Au(pc) surface are shown in Figure 6.3(b).

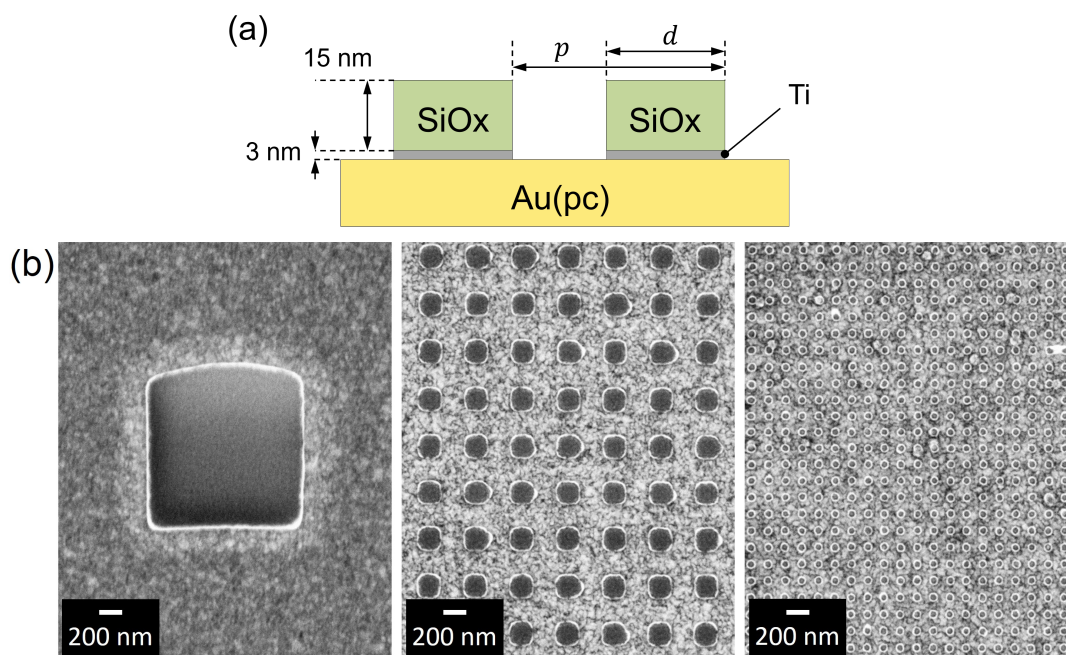


Figure 6.3: Silicon oxide (SiO_x) nanostructures on a Au(pc) surface. (a) Schematic side-view of the electrode surface, giving important geometric quantities. (b) SEM images of the fabricated SiO_x arrays on Au(pc) with structure sizes of 1400 nm (left), 200 nm (middle), and 75 nm (right). The dark and smooth area is the evaporated SiO_x, the light and rough area is the Au(pc) surface. Taken with modifications from [Mai+20].

The great advantage of this system is that the topography of the catalytic active surface, i.e. of the Au(pc) surface, is similar for all different SiO_x structure sizes investigated. In other words, there is no intrinsic difference in the surface concentration of undercoordinated sites caused by the fabrication, as no 'Au edges' are present on the electrode surface. Since the catalytic active surface is similar for all electrodes with differently sized SiO_x structures, the difference in the electrocatalytic response of the system can be directly attributed to the presence of oxide close to the Au catalyst.

Figures 6.4(a) and (b) show LSVs of differently sized SiO_x structures on a Au(pc) substrate in acidic and alkaline electrolyte, respectively. In both electrolytes, the necessary HER overpotential decreases with decreasing SiO_x structure size. This difference in overpotential is larger in alkaline electrolyte than in acidic electrolyte. In acidic electrolyte, the potential difference between the largest structure size 1400 nm and the smallest 75 nm at -0.1 mA cm^{-2} is 15 mV, whereas it is 55 mV in alkaline electrolyte. Thus, the qualitative decrease of necessary overpotential with increasing oxide/Au interface is similar to the case of the 'standard' electrodes containing Au-based nanostructures.

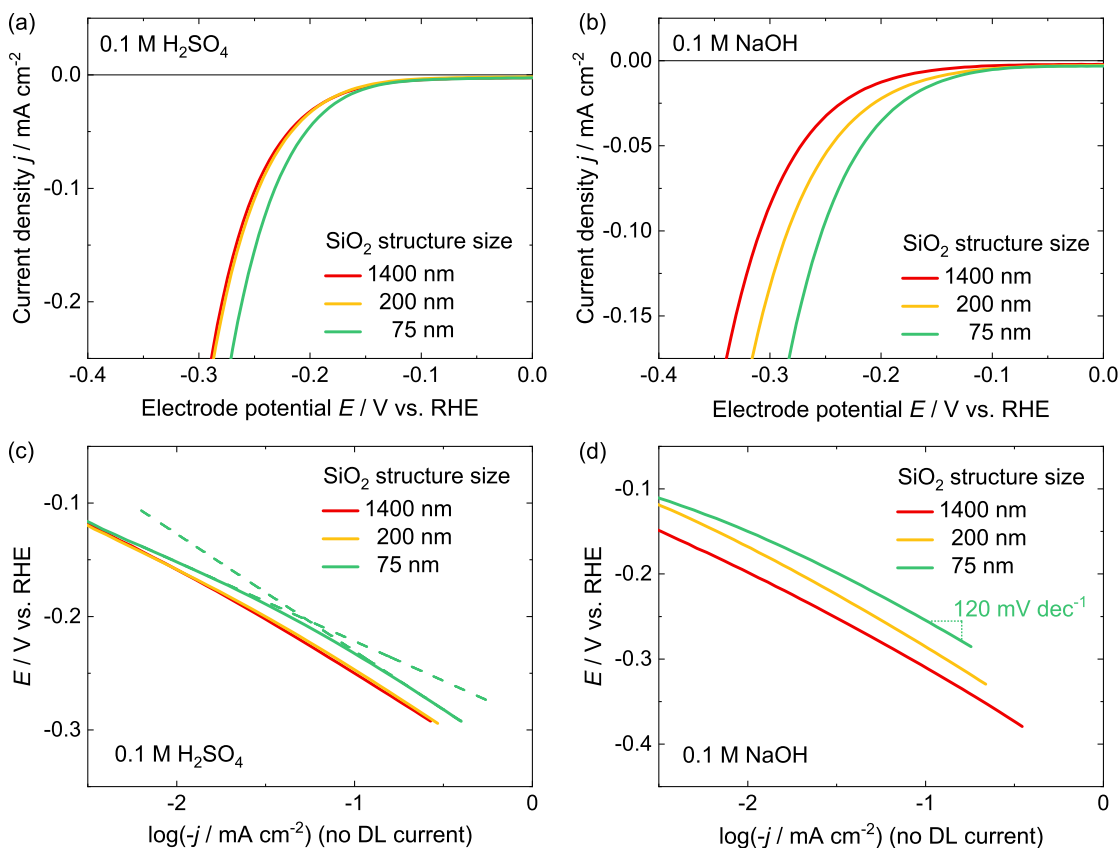


Figure 6.4: LSVs of differently sized silicon oxide (SiO_x) structures on Au(pc) surface in (a) acidic electrolyte at pH 1 containing 0.1 M H₂SO₄ and (b) in alkaline electrolyte at pH 13 containing 0.1 M NaOH. Scan rate: 50 mV s⁻¹. (c) and (d) show the associated Tafel plots of the data in the respective figure above after subtraction of the double layer charging current (DL current) present at $E = 0$ V_{RHE}. Images are taken with modifications from [Mai+20].

Figures 6.4(c) and (d) show the associated Tafel plots of the respective LSV curves in acidic and alkaline electrolyte. In alkaline electrolyte the curves proceed parallel with a slope of approx. 120 mV dec⁻¹ throughout the whole analyzed potential region. In acidic electrolyte the curve of the 75 nm electrode shows two distinct slopes in the range of comparably low and high overpotential (dashed lines). For the other two sizes, this difference is not as clearly visible. However, the qualitative behavior of the slopes in both electrolytes is very similar to the data shown in Figure 5.3 of the electrodes with Au nanostructures. Consequently, the mechanistic discussion of the data made in section 5.1 can also be applied here for oxide nanostructures on Au(pc).

In summary, we can conclude that the observed enhanced HER on nanostructured electrodes is, at least qualitatively, similar for SiO_x structures on an Au(pc) film. The quantitative difference between SiO_x structures on Au and Au structures on silicon may stem from an altered geometry of the active surface between the two systems, i.e. an altered ratio of Au/Ox border area to the Au bulk area. However, the results presented here now clearly give evidence that the HER enhancement present at the border of the Au nanostructures, i.e. at the Au/oxide interface, is really caused by the close presence of both materials, oxide and Au. It cannot be (solely) assigned to an altered proton adsorption energy present at the edges of the Au nanostructures, as this explanation cannot be applied to the results presented in this section.

6.1.3 Pt-based structured electrode

In the previous section we showed that an altered hydrogen adsorption energetics is not the main reason for the improved HER kinetics at the Au/SiO_x interface compared to the activity at bare Au surfaces. This result suggests the hypothesis that the appearance of the HER enhancement occurring at this interface may not necessarily depend on the Free Energy of adsorption of the actual catalyst material. The improvement of the HER kinetics in a metal/SiO_x system may also be present when using a different metal than Au as the HER catalyst. In this and the following section, we proof this hypothesis.

First, we investigate structured electrodes with Pt-based nanostructures, i.e. they consist of Pt as the catalyst material. Since Pt exhibits a very different hydrogen binding energy than Au (cf. section 2.4.2), we can get further insights in the actual mechanism occurring at the metal/oxide interface. The flexibility of the electrode fabrication process allows a straight forward fabrication of Pt nanostructures. The Pt nanostructured electrodes are produced with the same process parameters as applied for the Au nanostructures. Consequently, the geometric parameters (structure size, structure height, oxide height, etc.) are similar to the structured electrodes based on Au.

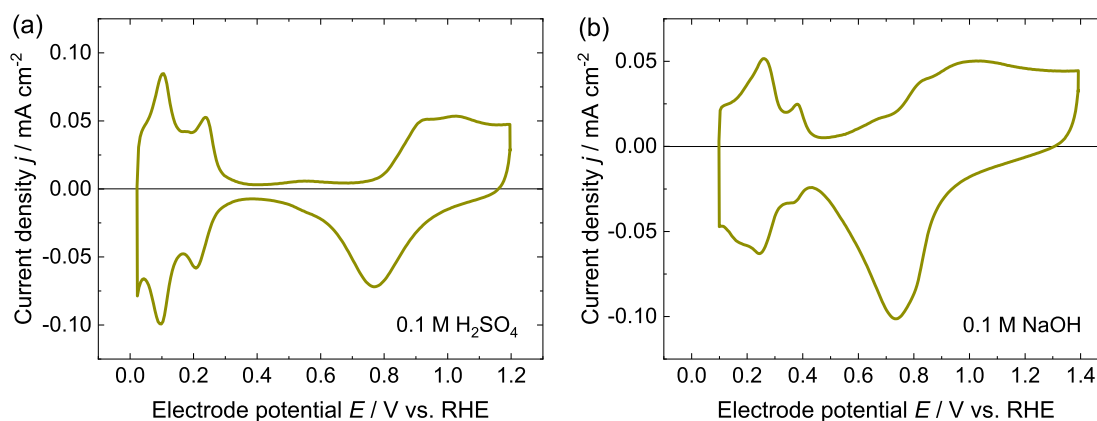


Figure 6.5: Exemplary CVs of a continuous Pt layer evaporated on n-doped silicon substrate in (a) 0.1 M H₂SO₄, pH 1.0, and (b) 0.1 M NaOH, pH 12.8. Both electrolytes are saturated with Ar. Scan rate: 50 mV s⁻¹. Typical Pt(pc) features can be well seen in both electrolytes, confirming the good quality of the evaporated film.

Figure 6.5 shows CVs of a continuous Pt film (50 nm thickness + 3 nm Ti layer below) evaporated onto the n-doped silicon substrate (a) in acidic (0.1 M H₂SO₄, pH 1) and (b) in alkaline (0.1 M NaOH, pH 13) electrolyte. The electrolytes are saturated by Ar gas and the current is normalized to the measured surface area by H-UPD in H₂SO₄-based electrolyte, as described in section 3.2.7. All measurements are conducted at room temperature. As expected, the CVs show the typical features known from Pt(pc) surfaces in Ar saturated acidic [Rhe+14] and alkaline [MWA08; SGS10; Rhe+14; WJO19] media, confirming the good quality of the evaporated film.

Next, we investigate HER on Pt nanostructured electrodes. First, we analyze the LSVs of the structured electrodes in acidic electrolyte (0.1 M H₂SO₄/Ar sat.'d, pH 1.0). Figure 6.6 shows LSVs ranging from the double layer region towards the HER region. A comparison of the full CVs of the electrodes in acidic electrolyte can be found in the appendix A.10.

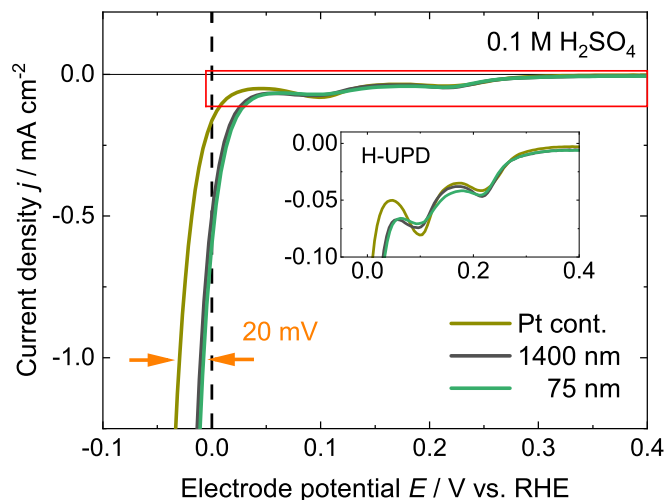


Figure 6.6: LSVs of a continuous Pt layer (olive curve), Pt structures with 1400 nm size (black curve) and Pt structures with 75 nm size (green curve) in 0.1 M $\text{H}_2\text{SO}_4/\text{Ar}$ sat.'d (pH 1.0). The inset shows a zoom of the H-UPD region (red rectangle). Scan rate: 50 mV s^{-1} .

Let us first consider the H-UPD region (inset in the Figure). All electrodes show the characteristic peaks for H-UPD at approx. $0.10 V_{\text{RHE}}$ and approx. $0.22 V_{\text{RHE}}$. In addition, the peak positions as well as their height are very similar for all three systems investigated. Thus, we can conclude that the adsorption characteristics of the under potential deposited hydrogen atoms is very similar for all three electrodes. Contrary, considering the inclining HER current slightly above $0 V_{\text{RHE}}$, the current increase due to HER starts at a more positive potential for the two structured electrodes, than it is observed for the electrode with the continuous Pt layer. This becomes very present at larger HER current densities. The overpotential difference at -1.0 mA cm^{-2} is approx. 20 mV between the continuous layer electrode and the structured electrodes (see orange arrows). It needs to be mentioned at this point that the measurements shown in this section have not been conducted in a transport controlled setup. Thus, we will not conduct a systematic kinetic analysis, but stay with the semi-quantitative analysis of the HER kinetics given here. Moreover, a kinetic analysis of HER in acidic medium on Pt is not easily possible. The kinetics is usually so fast that the applied kinetic overpotential cannot be reliably separated from the diffusion overpotential [SGS10].

In alkaline medium, a similar trend can be observed. Figure 6.7 shows LSVs of the three electrode types in 0.1 M NaOH/Ar sat.'d (pH 12.8) electrolyte. Similar to the measurements performed in acidic medium, it is visible that less overpotential needs to be applied for structured electrodes compared to the continuous layer electrode to reach the same HER current density. Moreover, the overpotential, which needs to be applied to drive a certain current, is clearly smaller for the smallest structure size investigated (75 nm) than the one needed for the largest structure size investigated (1400 nm). At -1.0 mA cm^{-2} , the total overpotential difference between the continuous layer and the smallest structure sizes is 30 mV (see orange arrow).

Although no detailed kinetic analysis is performed at this point, we can determine semi-quantitative kinetic parameters from these scans. The measured current density at $0 V_{\text{RHE}}$ (dashed line) is supposed to scale with the exchange current density. Due to the absence

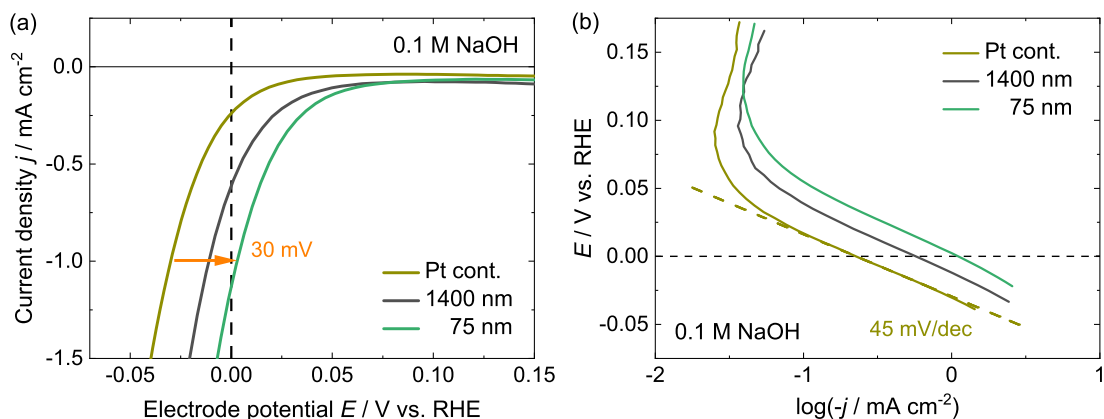


Figure 6.7: (a) LSVs of a continuous Pt layer and nanostructured electrodes with Pt structures of size 1400 nm and Pt structures of size 75 nm in 0.1 M NaOH/Ar sat.'d (pH 12.8). Scan rate: 50 mV s^{-1} . (b) Tafel plot of the LSVs. Smaller Pt structures exhibit an increased activity for alkaline HER (cf. orange arrow).

of hydrogen gas in the electrolyte, a non-zero current signal of HER can be measured at 0 V_{RHE} . At this potential, we determine values of -0.24 mA cm^{-2} (Pt cont.), -0.61 mA cm^{-2} (1400 nm), and -1.1 mA cm^{-2} (75 nm). We recognize that the values differ by a factor of approx. 4. Sheng et al. [SGS10] obtained an exchange current density of $\approx 0.6 \text{ mA cm}^{-2}_{\text{Pt}}$ in 0.1 M KOH at 294 K for of Pt(pc) electrode. Thus, this value is at least in the same range as the value determined for the Pt cont. sample. Considering the uncertainties made by the area determination and the missing detailed kinetic analysis, the values are even quite well comparable.

Figure 6.7(b) shows the LSVs conducted in alkaline electrolyte in a logarithmic plot (Tafel plot). Although interpretations of the determined slopes need to be made carefully, one recognizes that the curves proceed in parallel. Similar to the case of Au structures, there appears to be no difference of the HER mechanism between the samples. The determined slope is around 45 mV dec^{-1} . A slope of 40 mV dec^{-1} suggests a transfer coefficient of $\alpha_c = 1.5$ at room temperature, which would be indicative of the second electron transfer step being the RDS. In a Volmer-Heyrovsky mechanism, this slope implies that the Heyrovsky step is the rate determining step [Led+17]. The same RDS is found in the literature for HER on Pt(pc) in alkaline media (pH 13) [Mon+21]. Note that this conclusion is just valid, if we assume that not the strongly adsorbed hydrogen (H_{upd}) does participate in the reaction, but that weakly adsorbed hydrogen (H_{opd}) is the reaction intermediate in HER [NB88; Mar+96].

6.1.4 Cu-based structured electrode

To further confirm that the enhanced HER activity on nanostructured electrodes is rather independent of the actual (metal) catalyst material, we investigate Cu-based structured electrodes in the following. Contrary to the previous case, where we considered Pt-based structures, we do not evaporate Cu instead of Au during the fabrication process of the samples, but perform an electrochemical Cu deposition onto the Au-based electrodes. The advantage of utilizing an electrochemically deposited Cu layer instead of an evaporated layer is that the Cu surface does not need to be exposed to ambient air between its deposition and the execution of electrochemical measurement. Exposure to air leads to

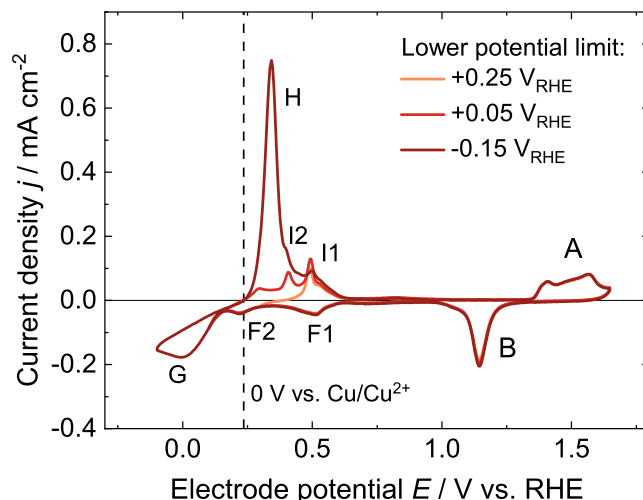


Figure 6.8: CVs of a continuous Au layer in 1 mM $\text{CuSO}_4 + 0.1 \text{ M H}_2\text{SO}_4 / \text{Ar sat.'d}$ (pH 1) for various lower potential limits. Scan rate: 50 mV s^{-1} . Peaks A and B are due to Au oxidation and Au-oxide reduction, respectively. Peaks F are due to Cu-UPD and Peaks I are caused by Cu-UPD stripping. Peak G is due to the bulk deposition of Cu^{2+} onto the electrode surface, and H is the respective (bulk) stripping. The dashed line indicates the determined equilibrium potential of the Cu^{2+}/Cu reaction at $+0.235 \text{ V}_{\text{RHE}}$.

oxidation of the Cu surface, already at ambient conditions [Pla+08], which can alter its electrocatalytic properties and makes a reliable comparison between different samples challenging.

Here, Cu^{2+} atoms are deposited onto the Au surface from solution during a galvanostatic deposition experiment. The electrolyte used for deposition is 1 mM $\text{CuSO}_4 + 0.1 \text{ M H}_2\text{SO}_4 / \text{Ar sat.'d}$ (pH 1), containing a concentration of 1 mM Cu^{2+} ions in solution. CVs of a typical Au electrode (continuous layer) in this electrolyte for different lower potential limits (LPLs) are shown in Figure 6.8. The CVs show the typical features of Au oxidation (peak A) and Au-oxide reduction (peak B), which have already been discussed before. In addition, there appear several other peaks: The peak ensemble F1/F2 can be attributed to the Cu-UPD at the gold surface. The Cu-UPD stripping is assigned to the peak ensemble I1/I2, which is most visible for the two curves exhibiting LPLs in the positive potential range (in RHE scale). The position and shape of the Cu-UPD and stripping peaks is quite similar to CVs obtained by other groups conducted in a similar electrolyte with a poly-crystalline Au surface, which is dominated by the Au(111) facet [HHI91; Nak+02; Pal+11]. The peak G is due to the bulk deposition of Cu^{2+} ions onto the Cu-covered electrode surface. The reaction is given by:



The equilibrium of this reaction can be seen in the dark red CV as the zero crossing of the potential scan in positive direction, which is at approx. $+0.235 \text{ V}_{\text{RHE}}$ and indicated by the dashed line in the Figure 6.8. The peak H can be assigned to the (bulk) stripping of deposited Cu and is, thus, reaction (6.1) in backward direction.

The galvanostatic Cu bulk deposition is conducted at a comparably small current density of $-120 \mu\text{A cm}^{-2}$, as the comparatively low concentration of Cu^{2+} in solution used here leads to a transport limitation already at rather low current densities. The $I-t$ and $E-t$ curves

of a typical copper deposition performed here is shown in Figure 6.9(a). The deposition time is chosen in a way, that we achieve a deposition charge of approx. $1.4 \times 10^4 \mu\text{C cm}_{\text{meas}}^{-2}$. Assuming a specific charge of $460 \mu\text{C cm}^{-2}$ [HHI91] for one monolayer of Cu atoms on a Au(111) surface, we deposit approx. 30 MLs. Considering a lattice constant of $a = 0.362 \text{ nm}$ of the copper lattice [Wyc63](SI, p. 3), this is tantamount to a copper layer thickness of approx. 11 nm deposited onto the Au surface. Due to this quite large coverage of the Au surface by Cu, the electrocatalytic properties of the electrodes are supposed to be dominated by the Cu properties.

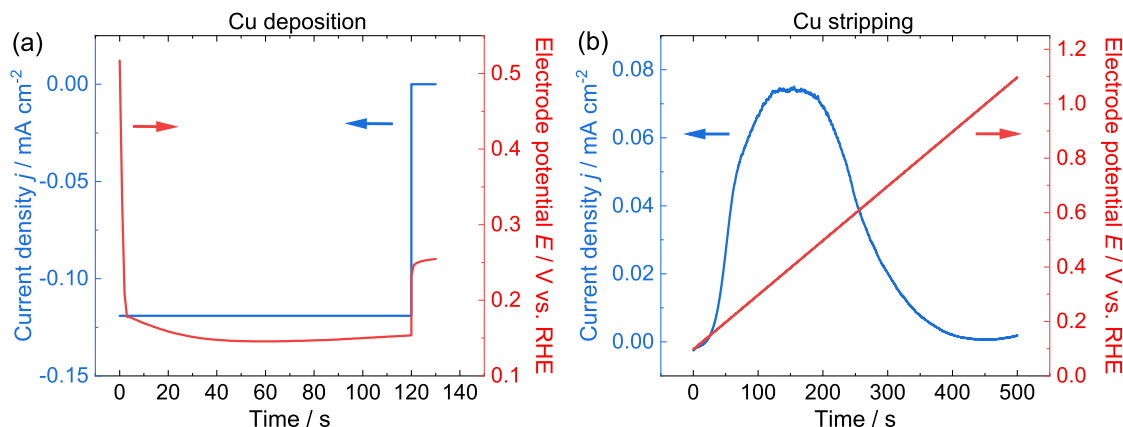


Figure 6.9: (a) Galvanostatic deposition and (b) stripping of a Cu layer onto/from a nanostructured Au surface with 1400 nm structure size. The deposition is conducted in 1 mM CuSO_4 , 0.1 M H_2SO_4 , Ar sat.'d (pH 1) and a constant current density of $-120 \mu\text{A cm}^{-2}$. The stripping is conducted after exchanging the electrolyte to 0.18 M NaOH, 0.12 M $\text{H}_2\text{PO}_4^-/\text{HPO}_4^{2-}$, Ar sat.'d (pH 7) with a potential scan rate of 2 mV s^{-1} . The charge transferred during deposition and stripping is very similar (here: $Q_{\text{dep}} = -1200 \mu\text{C}$ and $Q_{\text{strip}} = +1280 \mu\text{C}$, respectively), showing that almost no copper is lost during the electrolyte exchange process.

After deposition, the electrolyte is exchanged to the actual 'working electrolyte' by a process developed in a previous work [Mai17]. During the electrolyte exchange, the electrode potential is controlled and a continuous flow of Ar gas into the cell is realized. The latter is done to minimize oxygen present in the system, which may oxidize the copper layer and alter its electrocatalytic properties. The 'working electrolyte', which is used to determine and compare the HER activities here, is a buffered neutral electrolyte consisting of 0.18 M NaOH + 0.12 M H_3PO_4 /Ar sat.'d with pH 7. We chose a neutral electrolyte instead of the alkaline electrolyte used before, to avoid corrosion of the Cu surface during the experiment.

After performing the HER activity measurements in the 'working electrolyte', the Cu is subsequently stripped. The stripping is done by scanning the potential with a rate 2 mV s^{-1} in positive direction from a potential slightly below the actual OCP, which is dominated by the Cu/Cu^{2+} equilibrium, towards a rather positive potential below the onset of the Au oxidation. The upper potential needs to be at least above $+1 \text{ V}_{\text{RHE}}$ to make sure that the whole Cu layer is stripped. An exemplary stripping experiment is shown in Figure 6.9(b). The charge transferred during the stripping experiment turned out to be very similar compared to the charge transferred during the deposition. Exemplary for the 1400 nm electrode (shown in Figure 6.9), the charge transferred is measured with $Q_{\text{dep}} = -1200 \mu\text{C}$ during deposition and $Q_{\text{strip}} = +1280 \mu\text{C}$ during stripping. Since the transferred charge is very similar, we can conclude that there is almost no loss of Cu-ions

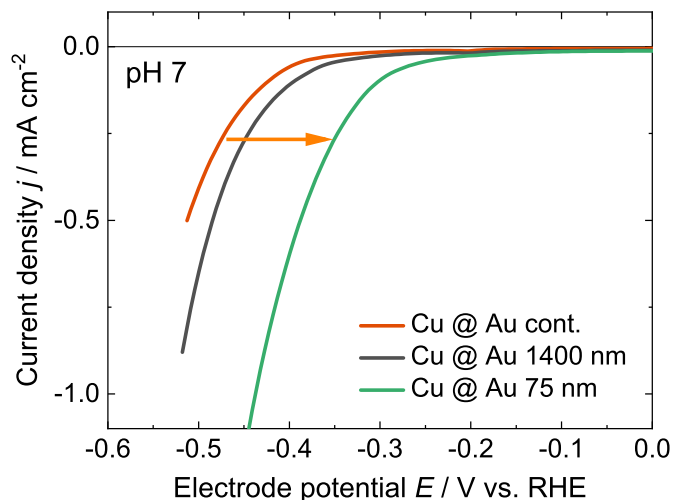


Figure 6.10: LSVs in the HER region of various Cu covered nanostructured electrodes. The electrolyte used here is 0.18 M NaOH, 0.12 M $\text{H}_2\text{PO}_4^-/\text{HPO}_4^{2-}$, Ar sat.'d with pH 7. Scan rate: 50 mV s^{-1} . The Cu layer of approx. 30 ML was deposited onto Au nanostructures before performing the HER measurements. It is visible that the overpotential necessary for HER decreases with decreasing structure size (orange arrow). The same behavior was also observed for pure Au-based as well as Pt-based nanostructured electrodes, see previous sections.

from the surface during the electrolyte exchange procedure. Thus, we can conclude that the LSVs performed to determine the HER activity is really conducted on a Cu-covered surface.

Figure 6.10 shows the LSVs in the HER region of three different electrode systems: A continuous layer electrode (brown), and nanostructured electrodes with either 1400 nm structure size (black) or 75 nm structure size (green) in the mentioned neutral working electrolyte consisting of 0.18 M NaOH + 0.12 M $\text{H}_2\text{PO}_4^-/\text{HPO}_4^{2-}$, Ar sat.'d with pH 7. As described above, prior to conducting the LSVs experiments, the Au surface of each electrode has been covered by a copper layer of approx. 30 ML.

It is visible in the data that the overpotential necessary to draw a certain HER current density decreases with decreasing structure size (see orange arrow). In the previous sections we could observe the same trend for pure Au-based, cf. Figure 5.2(b), as well as Pt-based, cf. Figure 6.7(a), nanostructured electrodes in alkaline electrolyte. As already mentioned above, we conducted the measurements of the Cu-covered electrodes in neutral medium. However, it is likely that in neutral medium HER occurs mostly via the reduction of water, as the concentration of protons is in the range of 10^{-7} M, and, consequently, comparatively small. Thus, it is likely that the HER current measured here at pH 7 is determined by water reduction rather than proton reduction. We will see at a later point that nanostructured electrodes with Au structures exhibit also an increased HER activity in neutral medium, cf. section 6.3.1. To assure a rather constant pH value in front of the electrode surface during the potential scan at low to moderate HER current densities, we use a comparatively strong phosphate buffer system (0.12 M $\text{H}_2\text{PO}_4^-/\text{HPO}_4^{2-}$). However, using a buffer system gives rise to further transport restrictions. Consequently, we refrain from conducting any kinetic analysis in this system and we remain with the qualitative consideration of the HER activity at this point. A detailed discussion of measurements conducted in a buffered neutral medium is given in section 6.3.1.

Discussion: Enhanced HER kinetics on Pt- and Cu-based nanostructured electrodes

Although we did not perform a substantial kinetic analysis for Pt- and Cu-based nanostructured electrodes due to the reasons mentioned above, we can clearly see that both metal catalysts exhibit an increased HER rate when using our nanostructured electrodes. Thus, we conclude that the structuring of the electrode surface alters the HER behavior significantly and independently of the metal catalyst material used. This is observable in acidic (for Pt) and clearly present in neutral (Cu) and alkaline (Pt) medium. Moreover, the HER activity of Cu- and Pt-based nanostructured electrodes, respectively, seems to depend on the structure size in neutral and alkaline medium, respectively: Smaller metal structures exhibit an increased HER activity compared to larger structures. This behavior is (at least qualitatively) similar to the behavior observed for Au nanostructures. The analysis of the Pt-based electrodes in alkaline medium further showed that the alkaline HER on the nanostructured electrodes and on the continuous layer electrode appears to have the same RDS. Thus, we conclude that the enhancement is clearly of kinetic nature.

From these observations we can further confirm: The increased HER activity of structured electrodes does not depend on the adsorption energetics of hydrogen atoms. The Free Energy of adsorption of hydrogen atoms is significantly different between gold and platinum. The Free Energy of adsorption on gold is rather large with a value around +0.4 eV, while the value of copper is smaller (value around +0.2 eV) and the value of platinum it is supposed to be much closer to the optimum value of zero (cf. section 2.4.2). Consequently, we can conclude that the presence of the improved HER kinetics on nanostructured electrodes compared to bare metal surfaces is caused by a fundamental mechanism occurring at the metal/oxide interface, which is independent of the adsorption energetics of hydrogen atoms on the catalyst surface.

6.2 Passivation layer

We have seen in the previous section that the improvement of the HER kinetics on structured electrodes is present independent of the surface morphology and for various catalyst materials. Further we showed that the close presence of the metal catalyst and an adjacent insulator (silicon oxide) itself leads to the enhanced HER kinetics. Thus, in this section we investigate the influence of the passivation layer (insulator) on the HER enhancement. We analyze the impact of covering the silicon oxide surface adjacent to the Au nanostructures (section 6.2.1) and of altering the passivation layer material to silicon nitride (section 6.2.2), which is much more practical passivation layer material of silicon-based nanostructured electrodes operating in alkaline media.

6.2.1 Covering the silicon oxide surface

Here, we address the question if the surface state of the passivation layer, in this case silicon oxide, influences the HER activity on nanostructured electrodes exhibiting an Au/oxide interface. To do so, we slightly modify the fabrication method of the electrodes. We reduce the time and intensity of the oxygen plasma (O-plasma) step after the second reactive ion etching (RIE) step, which etches through the oxide layer (cf. section 3.1.2 for details on the fabrication steps). Without the subsequent O-plasma step, the protective layer consisting of $[\text{CF}_2]_n$ groups, which covers the side walls of the etched hole after the RIE step, does not get etched away. Since also part of the top surface close to the emerging hole is exposed to the RIE plasma due to the undercut below the imprint resist coating, residues of the deposited $[\text{CF}_2]_n$ -based layer also remain partly on the top SiO_x surface. In this way, we can produce nanostructured electrodes with metal structures, whose silicon oxide surface adjacent to the metal structures is partly covered by residues of a polymer layer stemming from the RIE step. A scheme of this system is given in Figure 6.11.

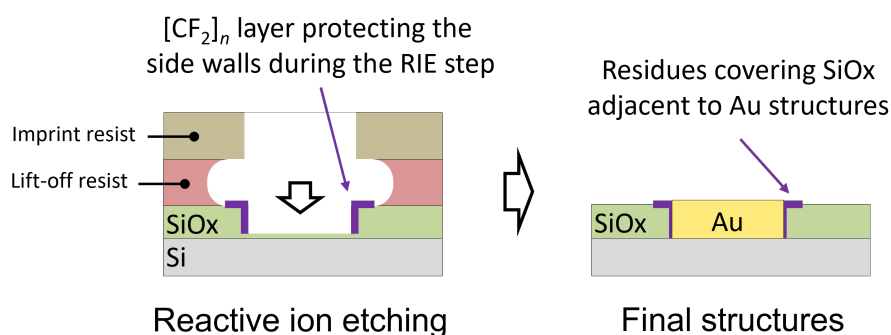


Figure 6.11: Scheme of the process of covering the silicon oxide layer adjacent to the Au structures partly. Without applying an O-plasma step after the reactive ion etching step, residues of the $[\text{CF}_2]_n$ -based layer, which protected the sidewalls during the etching, remains on the top surface of the silicon oxide layer. This layer covers the oxide surface adjacent to the gold structures on the later nanostructured electrodes.

These residues can be seen in Figure 6.12(a) in the left image as the dark halos surrounding the metal structures (see red arrows). These residues can be also removed after the final lift-off step by applying an O-plasma step. An SEM image of an electrode after applying

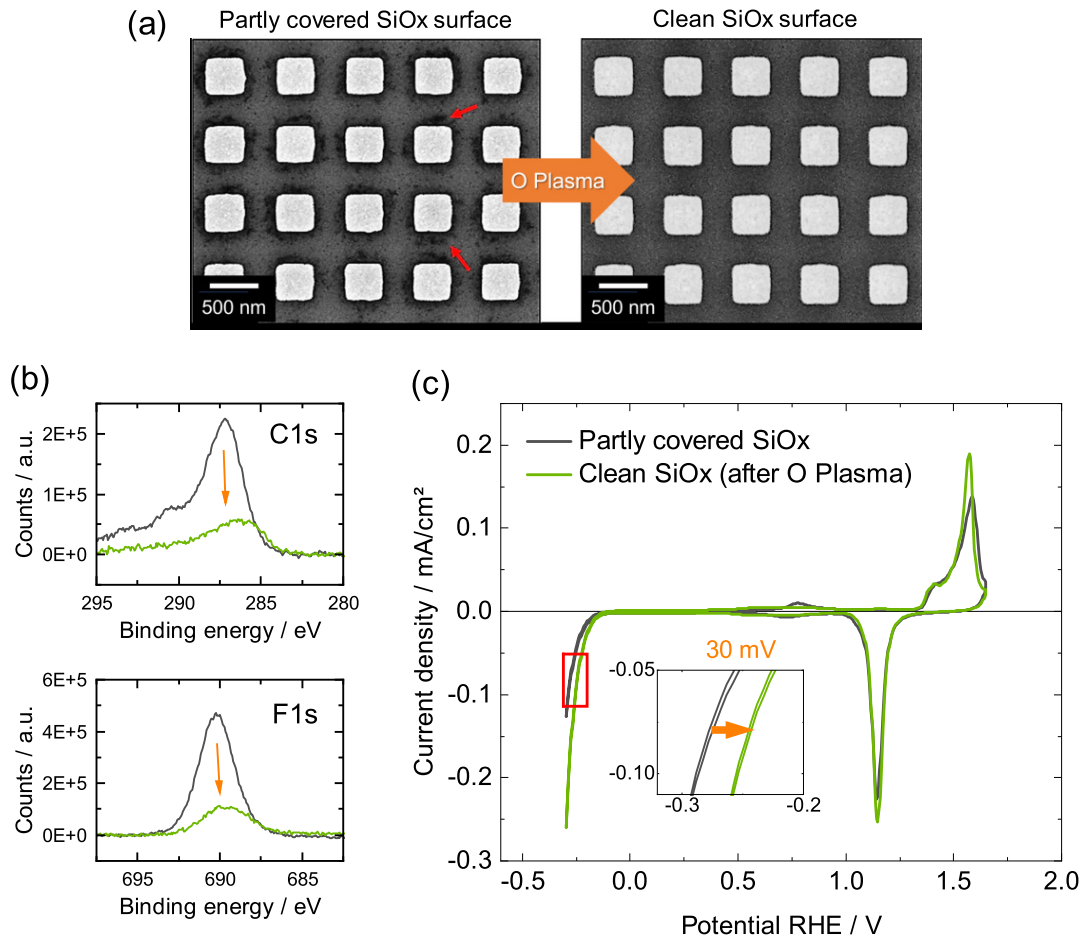


Figure 6.12: (a) SEM image of a structured electrode (here 350 nm structure size) without applying the O-plasma step in the second RIE step (left image). The dark halos surrounding the structures (red arrows) are residues of the protective layer deposited during the reactive ion etching onto the silicon oxide layer. A subsequent O-plasma after the lift-off can remove the residues, which can be seen by the 'clean' oxide surface (right image). (b) XPS spectra of the electrode before and after the subsequent O-plasma step showing that the coverage of F and C containing compounds on the surface decreases. (c) CVs of a structured electrode (1400 nm structure size) in 0.1 M H₂SO₄ before and after the O-plasma step, i.e. with a partly covered and a clean SiOx surface, respectively. The plasma step clearly enhances the HER activity by approx. 30 mV (see inset, orange arrow) which clearly shows, that the presence of the silicon oxide surface increases the HER activity of metal structures. Figures (a) and (b) are taken with modifications from [Ang21].

the O-plasma is shown in Figure 6.12(a) in the right image. Here, no dark halos around the structures are visible and the SiOx surface appears to be rather 'clean'. Further evidence for the removal of the prior present [CF₂]_n residues is visible in the XPS spectra of a covered structured electrode taken before and after an O-plasma step, cf. Figure 6.12(b). As already mentioned above, the protective layer of the side walls consists of fluorocarbon compounds. In the XPS spectra huge peaks appear at approx. 287 eV and 690 eV before applying the plasma step (black lines). These peaks can be assigned to the C1s and the F1s signal, respectively. After applying the O-plasma (green lines), these peaks decrease significantly in height (cf. orange arrows). Thus, a large part of the present protective layer residues on the SiOx surface is removed during the plasma step.

Figure 6.12(c) shows CVs in 0.1 M H_2SO_4 of a nanostructured electrode with 1400 nm Au structure size before (black) and after (green) the O-plasma step. The plasma step alters the electrochemical behavior significantly. First, the Au oxidation peak ensemble (anodic current around $+1.5 \text{ V}_{\text{RHE}}$) changes. The peak at $+1.58 \text{ V}_{\text{RHE}}$ becomes sharper. This can be a hint towards a changed Au surface (bulk surface) due to the exposure to the plasma. A sharper peak at the mentioned potential is indicative of a larger contribution of the Au(111) facet on the electrochemical behavior of the surface, cf. section 6.1. Second, the HER activity changes. The electrode having the 'clean' SiOx surface exhibits a higher HER activity than the electrode with the partly covered SiOx surface. The overpotential to draw a current of -0.1 mA cm^{-2} decreases by approx. 30 mV (see orange arrow).

This behavior is quite remarkable. Although the (overall) Au surface changes and becomes more dominated by Au(111) sites, the HER activity of the electrode increases. It is expected that an increased contribution of Au(111) sites leads to the opposite behavior, i.e. to a decreased HER activity, see section 6.1. The most obvious explanation for the observed result is that the presence of the SiOx surface adjacent to the Au structures increases the HER activity at this interface (and consequently of the whole electrode). The partial passivation of the SiOx close to the structures with fluorocarbon compounds would then decrease its activity, which is the behavior observed. This result presents further evidence that the Au/SiOx interface is the origin of the observed enhancement. The presence of SiOx surface itself appears to influence the HER activity of the metal structures at the interface. It seems that the reaction rate at the border of the structures is determined by a 'bifunctional mechanism'. However, so far it still remains unclear, if the SiOx surface is just a 'spectator species' in the reaction and varies the local HER rate indirectly by changing e.g. the electrochemical environment (i.e. the double layer configuration), or if it is somehow directly involved in the reaction mechanism.

6.2.2 Nanostructured electrodes with silicon nitride as passivation layer

We have seen that the presence of the silicon oxide surface enhances the HER activity of a metal surface. However, this leads to the question, if silicon oxide is the only passivation layer material, which exhibits the mentioned effect. To address this question, we consider another passivation layer material: silicon nitride. The usage of silicon nitride has two advantages: First, we may further pinpoint the bifunctional reaction mechanism present at the metal/insulator interface, and, second, it is much more stable in alkaline environment than thermal silicon oxide, cf. Figure 6.13. The latter property makes it an even more practical candidate for the passivation layer material of a future final solar-to-hydrogen device.

We use a commercial low-pressure-chemical-vapor-deposited (LPCVD) silicon nitride film. More information regarding the silicon nitride film used is given in section 3.1.2. In the further course of this work we abbreviate the silicon nitride film/surface by SiN without the intention to determine any stoichiometric composition. The production of nanostructured electrodes consisting of a silicon nitride-based passivation layer on a silicon surface is straight forward. In the fabrication process, we just need to alter the substrate used from a thermal silicon oxide covered wafer to a silicon nitride covered wafer of the desired layer thickness. In addition, the parameters of the second RIE etching step need to be slightly modified [Ang21] due to the different etching properties of nitride compared to oxide.

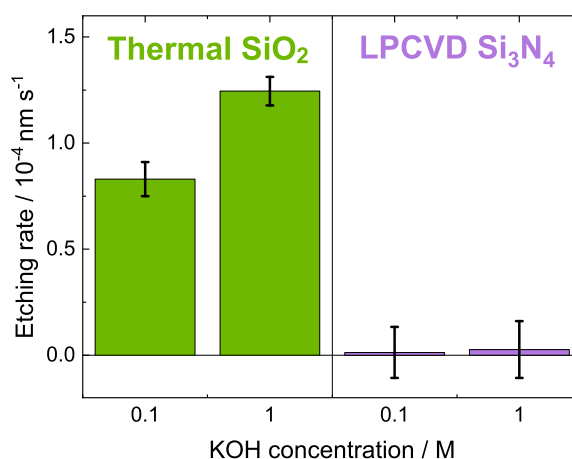


Figure 6.13: Etching rates of thermal silicon oxide and LPCVD silicon nitride exposed to an electrolyte containing 0.1 or 1 M KOH at room temperature. The rates were measured after at least 48 hours of exposure time. The etching rate of silicon nitride is about two orders of magnitude smaller compared to silicon oxide. Thus, it is expected to be a much more stable passivation layer material when working under alkaline conditions.

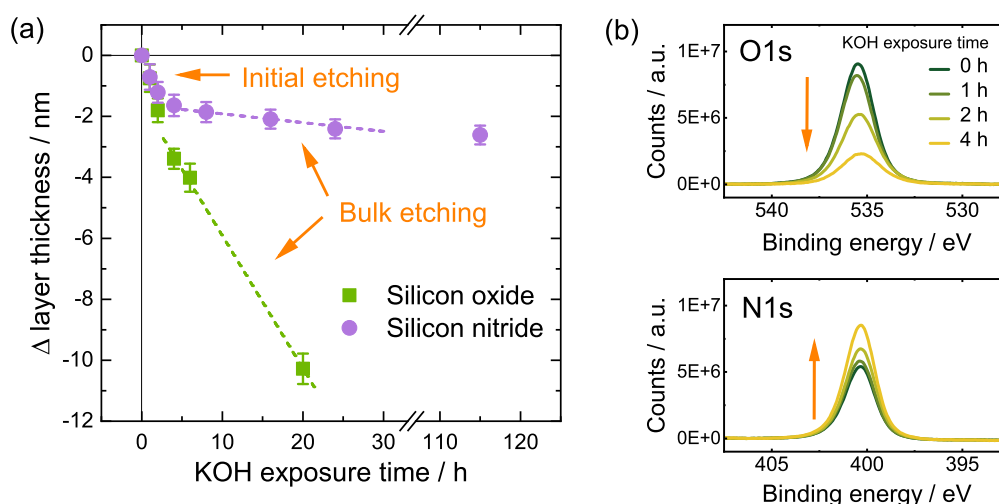


Figure 6.14: (a) Change of the thickness of a LPCVD silicon nitride (purple) and a thermal silicon oxide (green) layer plotted over the exposure time to an alkaline electrolyte containing 0.1 M KOH (pH 13). Note that both surfaces have been treated by O-plasma before exposure to the electrolyte. After approx. 3 hours, the etching rate of the silicon nitride layer becomes much smaller than the etching rate of the silicon oxide layer (bulk etching). (b) XPS spectra of the O1s and the N1s signal of a silicon nitride layer after several selected etching times during the initial etching phase. The signal of O1s decreases, while the signal of N1s increases (orange arrows). The images are taken with modifications from [Ang21].

Although the production process is adapted rather simply, maintaining a 'pure' silicon nitride surface exposed to the electrolyte during the electrochemical measurements of nanostructured electrodes is difficult to establish, as, already at ambient conditions, the surface of silicon nitride is known to oxidize quite fast (see section 2.1.3). An oxide covered silicon nitride layer would not give any additional information about the bifunctional mechanism at the Au/insulator interface. However, T. Angerer [Ang21] showed that the oxidized atomic layers on top of the silicon nitride film can get etched away, when exposing

the oxidized surface to alkaline electrolyte. This is visible in Figure 6.14(a), in which the change of the thickness of a thermal silicon oxide layer and a LPCVD silicon nitride layer exposed to an electrolyte containing 0.1 M KOH is plotted over the exposure time. Note that both surfaces have been exposed to an O-plasma before the experiment. This is done in order to maintain a similar surface composition compared to the structured electrodes. The structured electrodes are treated by a subsequent O-plasma step to guarantee that no residues of the second RIE step remain on the insulator surface (see previous section). In Figure 6.14(a), it can be seen that at the beginning of the etching process (initial etching) the decrease in height of the layers is quite similar for both surfaces, until approx. 3 hours of exposure. Afterwards, the etching rate of the silicon nitride samples becomes much lower than the rate determined for silicon oxide samples. This is visible in the less steep slope (bulk etching, dashed lines). It can be concluded that, within the first hours of exposure, most of the oxygen containing compounds on the silicon nitride surface get removed. Further evidence for the removal of oxygen compounds on the surface is given by XPS measurements of the silicon nitride layer, performed at several times during the initial etching phase shown in Figure 6.14(b). The O1s signal decreases with increasing exposure time, while the signal of N1s increases (see orange arrows). This further confirms the hypothesis that oxygen compounds present on the initial silicon nitride surface get etched away during the initial etching phase. An assumption made here is that the XPS O1s signal in the silicon nitride system is rather dominated by surface oxygen. This assumption can be confirmed by conducting angle resolved XPS measurements. Measurement of the initial nitride surface at different angles show that the O1s is indeed dominated by surface oxygen compounds, cf. appendix A.11.

Coming back to nanostructured electrodes: As already mentioned above, in order to gain new insights in the role of the passivation layer on the HER enhancement mechanism, we need to maintain a surface with the least possible oxygen content. As it can be concluded from the data shown above, this can be achieved by exposing the electrodes to an alkaline electrolyte prior to conducting the actual electrochemical measurements. Consequently, all electrochemical data of silicon nitride based nanostructured electrodes shown in the following is determined after at least 3 hours of exposure time to a 0.1 M OH⁻ containing electrolyte.

We now consider the nanostructured electrodes consisting of a SiN based passivation layer surrounding the Au structures in acidic and alkaline electrolyte. Figure 6.15 shows LSV curves of differently sized gold nanostructures (a) in 0.1 M H₂SO₄ and (b) in 0.1 M NaOH containing electrolyte. It is visible that in both electrolytes the necessary overpotential, which needs to be applied for drawing a certain HER current density, decreases with decreasing structure size. The absolute potential difference at -0.1 mA cm⁻² is approx. 55 mV in 0.1 M H₂SO₄ and approx. 150 mV in 0.1 M NaOH. This behavior is quite remarkable, as it gives the same trend as observed for electrodes with the same geometric design, but utilizing a silicon oxide based passivation layer (cf. Figure 5.2).

Figure 6.16(a) shows the Tafel plot of the data in 0.1 M H₂SO₄. The data is further corrected by the non-faradaic current measured at 0 V_{RHE} before logarithmizing. All curves exhibit two different slopes, one at potentials larger than approx. -0.15 V_{RHE}, one at potential smaller than approx. -0.2 V_{RHE}. These two different slopes are most visible for the 75 nm electrode and indicated by the dashed lines in Figure 6.16(a). The parameters of the linear fittings of the data in these two potential ranges is given in

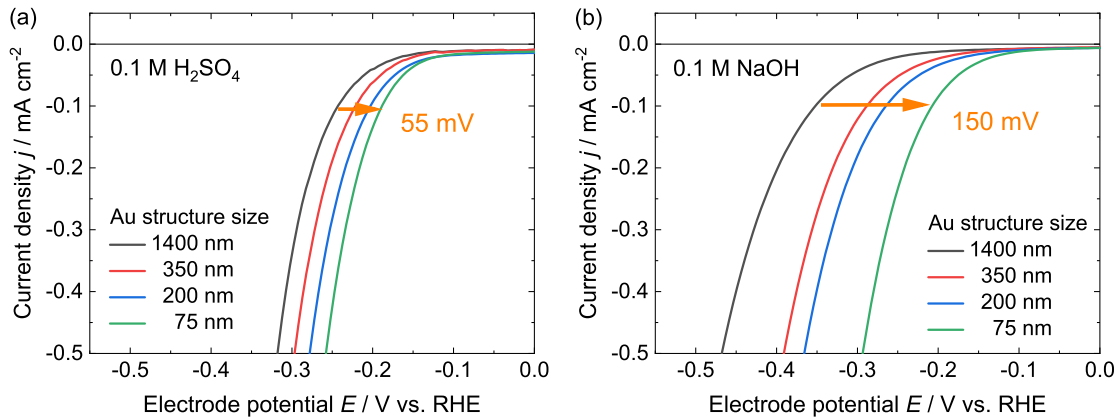


Figure 6.15: LSVs of nanostructured electrodes composed of Au structures and a silicon nitride passivation layer in (a) 0.1 M H_2SO_4 at pH 1 and (b) 0.1 M NaOH at pH 13. Smaller Au structures show an increased activity for HER in both electrolytes. The same trend was seen for structurally identical electrodes consisting of silicon oxide passivation layer (cf. Figure 5.2). The images are taken with modifications from [Ang21].

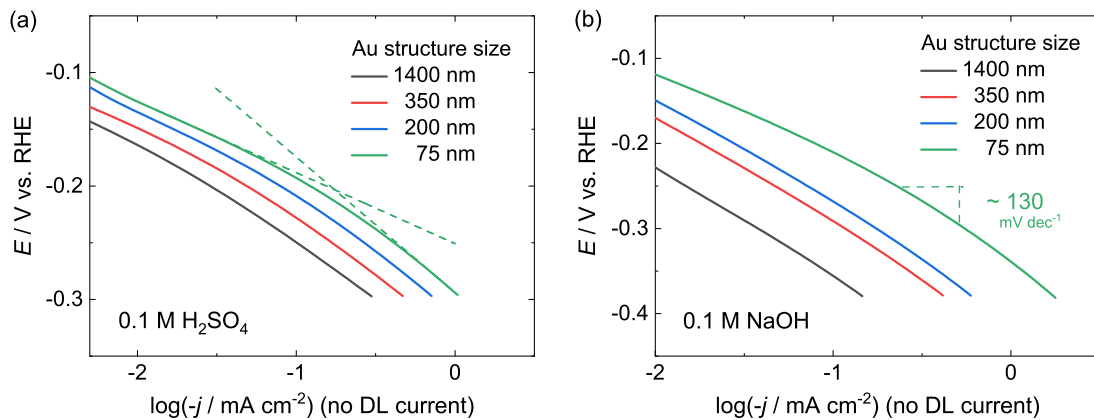


Figure 6.16: Tafel plots of the LSVs shown in Figure 6.15. (a) in 0.1 M H_2SO_4 at pH 1, (b) in 0.1 M NaOH at pH 13. The non-faradaic contribution to the current (determined at 0 V_{RHE}) has been subtracted prior to logarithmizing.

Table 6.1. Again, similar to the case with silicon oxide as the passivation layer, there are two potential ranges which show slopes around 60 mV dec^{-1} at small overpotentials and around 110 mV dec^{-1} (102 to 120 mV dec^{-1}) at larger overpotentials. When interpreting these slopes as Tafel slopes, this may indicate that there is the same mechanistic change of the reaction during the potential scan as found for the SiO_x based electrodes and extensively discussed in section 5.1.2. The intercepts, which are interpreted as exchange current densities, increase with decreasing structure size. This is valid for both of the potential ranges with different fittings. The plot of the determined exchange current densities at high overpotentials over the inverse of the structure size $1/d$, given in Figure 6.17(a), shows a linear behavior, which is, again, similar to the case where SiO_x passivation layers were used. The determined exchange current densities at low overpotentials are not shown. Note that the data shown in this Figure is the data from one individual electrode per size and not averaged over multiple electrodes.

Structure size d	Fitted slope [mV dec ⁻¹]		j_0 (from intercept) [10^{-4} mA cm ⁻²]	
	$E > -0.15$ V	$E < -0.2$ V	$E > -0.15$ V	$E < -0.2$ V
1400 nm	67	102	-	(4 ± 3)
350 nm	65	108	-	(8 ± 3)
200 nm	67	114	-	(17 ± 5)
75 nm	63	120	-	(35 ± 7)

Table 6.1: Tafel fitting parameters of the LSV curves in 0.1 M H₂SO₄ shown in Figure 6.16(a). j_0 values in the low overpotential range are not given due to the large fitting error. The electrode potentials E are given in RHE scale, i.e. in V_{RHE} .

Structure size d	Fitted slope [mV dec ⁻¹]	j_0 (from intercept) [10^{-4} mA cm ⁻²]
1400 nm	122	(1.4 ± 1.2)
350 nm	127	(5 ± 2)
200 nm	130	(9 ± 3)
75 nm	130	(28 ± 4)

Table 6.2: Tafel fitting parameters of the LSV curves in 0.1 M NaOH shown in Figure 6.16(b). The fits are evaluated at $-0.3 V_{\text{RHE}}$.

Figure 6.16(b) shows the Tafel plot the LSV curves in 0.1 M NaOH. At sufficiently large overpotential ($E \approx -0.3 V_{\text{RHE}}$), all curves proceed parallel with a rather constant slope of approx. 130 mV dec^{-1} (122 to 130 mV dec^{-1}). At higher overpotentials ($E < -0.35 V_{\text{RHE}}$), the slopes tend to get even larger. This effect is more dominant for smaller sizes. Thus, it may be caused by a nascent diffusion domination of the measured current, which is higher for smaller structures at this potential. At rather small overpotentials ($E \approx -0.15 V_{\text{RHE}}$), the slope tends to be smaller for smaller structure sizes. This is well visible for the 75 nm sized structures, for which the curve (green) does not proceed parallel to the others. However, since at these potentials the current for larger structures is quite small and mostly dominated by the charging current of the double layer, it is not possible to resolve this effect for the other sizes. The linear fitting parameters of the logarithmic current at $-0.3 V_{\text{RHE}}$ is given in Table 6.2. We interpret the intercepts of the fittings as the exchange current densities j_0 . The absolute values of j_0 for the respective structure sizes found for silicon nitride based electrodes appear to be very similar to the values determined for silicon oxide based electrodes (cf. Table 5.1). When plotting the determined j_0 over the inverse of the structure size $1/d$, which is done in Figure 6.17(b), it is clearly visible that the exchange current density of the nanostructured electrodes scales linearly with the inverse of the structure size. Similar to the case for electrodes utilizing a silicon oxide based passivation layer, this indicates an enhanced reactivity at the nanostructure border (see discussion in section 5.1).

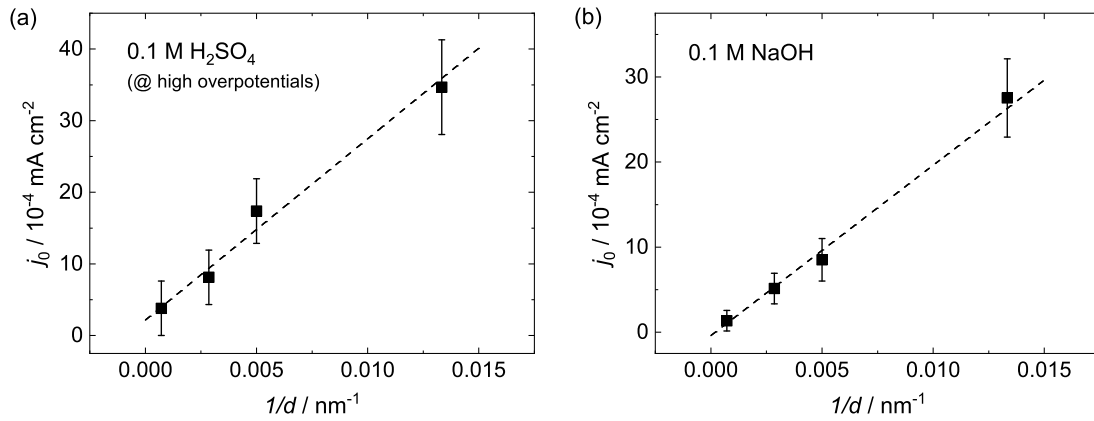


Figure 6.17: Determined exchange current densities j_0 of HER on Au nanostructured electrodes utilizing a silicon nitride based passivation layer material plotted over $1/d$. (a) in 0.1 M H_2SO_4 at pH 1 and (b) in 0.1 M NaOH at pH 13. The linear scaling (dashed line) is similar to the one observed for nanostructured electrodes consisting of silicon oxide based passivation layers (cf. Figures 5.8 and 5.4). Thus, we can conclude that HER activity at the Au/SiN interface is increased compared to the Au structure bulk.

In summary, nanostructured electrodes utilizing silicon nitride as the passivation layer material adjacent to the Au nanostructures show the very same enhancement of the HER as nanostructured electrodes using silicon oxide based passivation layer presented in section 5.1. The observed improved HER kinetics with decreasing structure size is qualitatively as well as quantitatively similar for both kinds of passivation layers, which suggests the conclusion that HER at the metal/insulator interface gets enhanced by the same bifunctional mechanism, i.e. it appears to be occur at both interfaces, the Au/SiN interface as well as at the Au/SiO_x interface.

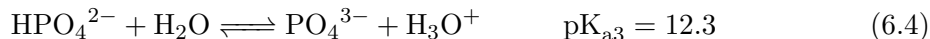
6.3 Electrochemical environment

So far, we just systematically altered the properties of the electrodes, such as the size of the metal structures, the surface and the material of the catalyst, and the surface and the material of the passivation layer. In this section, we vary several properties of the electrolyte and analyze the influence on the HER enhancement at the metal/insulator interface. From the dependence of the HER activity of nanostructured electrodes on the properties of the electrolyte we can further elaborate the actual mechanism behind the bifunctional improvement present at the interface. In particular, we analyze in this section the dependence of the HER rate on the pH value of the electrolyte (section 6.3.1), on the concentration of cations present in solution (section 6.3.2), and on the cationic species present in solution (section 6.3.3).

6.3.1 pH value of the electrolyte

When varying the pH value of the electrolyte, the concentration of protons in the bulk is changed. The pH value can have major impact on the composition of the surface (as already mentioned in section 2.1.3, the bulk pH value determines the surface charge present on the silicon oxide or nitride surface in contact with the electrolyte), or on the reaction by changing its mechanism (cf. section 2.4.1). Thus, in this section, we investigate the HER activity of nanostructured electrodes in neutral medium and compare it to alkaline medium.

In neutral medium at sufficiently high overpotentials, the HER reaction rate is expected to be determined by transport of species rather than by kinetics, since the concentration of ions involved in the reaction (H^+ or OH^-) is several orders of magnitude smaller compared to the acidic or alkaline electrolytes considered in the previous sections with pH 1 or 13, respectively. In order to maintain a comparably large current window, in which the current is dominated by kinetics rather than by transport, we use a buffered electrolyte. The buffer we use is the phosphate buffer system, as it can be well adjusted in the neutral range. The three dissociation steps of phosphoric acid and their respective pK_a values are given by:



In principle, a large buffer capacity lowers the dependence of the current on the transport properties at a given current density and, thus, increases the current window for determining the kinetics of the reaction. However, a larger buffer capacity is, in the case of phosphate, tantamount to a higher concentration of anionic species ($\text{H}_2\text{PO}_4^-/\text{HPO}_4^{2-}$), which, in turn, gives a larger amount of cationic species present in the electrolyte in order to assure charge neutrality. We will see later that the concentration of cationic species in the electrolyte will also affect the HER activity (cf. section 6.3.2). Consequently, we restrict the buffer capacity to the same range as the ionic concentration of the alkaline/acidic reference electrolytes, i.e. containing 0.2 M of ionic species. A good compromise between comparatively low buffer capacity and still a minor transport effect at low current densities turned out to be 0.12 M $\text{H}_2\text{PO}_4^-/\text{HPO}_4^{2-}$. Since the pK_{a2} value is very close to 7,

adjusting the pH value of the electrolyte to 7 results in an approximate similar concentration of both ionic species. However, we will just give the sum of the concentrations of both present species ($\text{H}_2\text{PO}_4^-/\text{HPO}_4^{2-}$) in the following, since there may also be local deviations in the concentrations at the electrode surface due to the buffering capability of the species at current flow condition. The cationic species present in the electrolyte is chosen to be K^+ here. We will see later that the cationic species influences the HER activity as well (cf. section 6.3.3). The concentration of cations in the electrolyte in order to maintain pH 7 was around 0.18 M.

In this section, we investigate three different electrode configurations:

- A continuous Au layer (Au cont.). This layer behaves as a typical poly-crystalline gold electrode, as shown in the beginning of chapter 5. This electrode further works as a benchmark system for comparison with the literature.
- 1400 nm sized Au structures.
- 75 nm sized Au structures.

The passivation layer surrounding the structures of the latter two electrodes is silicon nitride. Silicon nitride is preferred over silicon oxide, as it showed to be more stable in alkaline electrolyte (see previous section 6.2.2). Thus, the degradation of the electrodes is significantly reduced compared to the case of using silicon oxide. Moreover, electrodes based on silicon nitride show a similar HER enhancement with decreasing structure size (see section 6.2.2) compared to the electrodes consisting of silicon oxide passivation layer.

Figure 6.18 shows LSVs of the three different electrode systems in two different electrolytes: The neutral buffered electrolyte based on phosphate with a pH value of 7 (solid lines), and an alkaline electrolyte based on KOH with a pH value of 13 (dashed lines). The gray dashed line indicates the approximate current density at which the current becomes dominated by transport effects rather than kinetics in the neutral medium used here. This value is estimated from a Tafel analysis of the data in neutral medium, which is shown in the appendix A.12. Since the transport of species may influence the current already at lower current densities, a Tafel analysis in this neutral electrolyte is omitted in this section completely.

We first consider the behavior of each electrode individually: For Au cont. (yellow), the necessary overpotential at a certain current density (e.g. -0.2 mA cm^{-2} , see orange arrow) is significantly smaller in an alkaline electrolyte, than in a neutral electrolyte. Note that in this system no Au/SiN interface is present. An increased HER activity of Au(pc) at pH 13 compared to neutral or mildly alkaline electrolytes is known from the literature [GK21a]. The reason for the enhanced HER rate at pH 13 compared to pH 7 is likely caused by a larger concentration of cationic species present in the vicinity of the electrode surface in the previous case. Note that the potential axis of the graph is given in RHE scale. It is known that the point-of-zero-charge (PZC) of a given Au surface is almost constant in the absolute potential scale (i.e. in SHE scale) or shifts positively with increasing pH in RHE scale [GK21a]. Consequently, the electrochemical interface is polarized more strongly in a pH 13 than it is in a pH 7 electrolyte at the same potential in RHE scale, which is tantamount to an increased concentration of cations present in the electrochemical double layer. A higher concentration of cations at the interface influences the properties of the double layer and is known to influence HER reaction rate significantly, although the actual

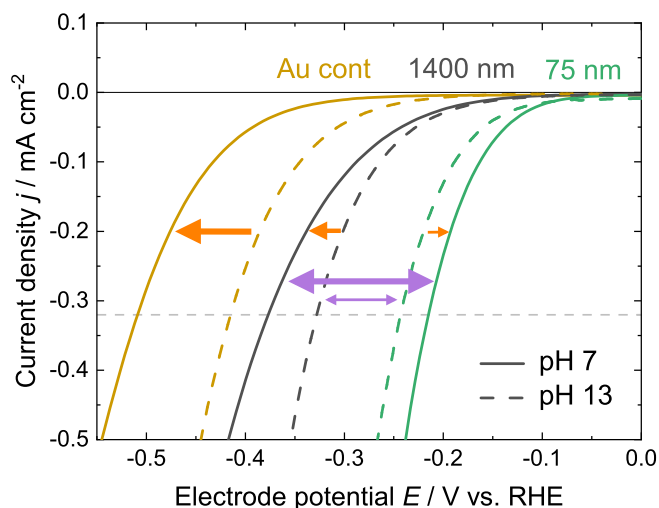


Figure 6.18: LSVs of a continuous Au layer (yellow), 1400 nm Au structures (black), and 75 nm Au structures (green) in an electrolyte with either pH 7 (solid lines) or pH 13 (dashed lines) in RHE scale. Scan rate: 50 mV s^{-1} . The alkaline electrolyte consists of 0.1 M KOH, the neutral electrolyte consists of 0.18 M K^+ and 0.12 M $\text{H}_2\text{PO}_4^-/\text{HPO}_4^{2-}$. The orange arrows indicate the difference of overpotential of each individual electrode in the distinct electrolyte, the purple arrows indicate the difference between the largest (1400 nm) and smallest (75 nm) structure size in the either neutral or alkaline electrolyte.

mechanism is still under debate. Possible explanations given in the literature are: The presence of cations stabilizes the adsorbed hydrogen atoms due to an increased electric field at the interface [Xue+18]. The cations interact with the transition state of the water splitting reaction [GK21a], or the presence of cations may help in the water dissociation step [Sub+11]. However, independent of the actual mechanism, a higher concentration of cations present at the interface is known to increase the HER activity on Au(pc) in alkaline media.

The LSVs of the 1400 nm Au structured electrode show a similar behavior: The HER activity in pH 7 is worse than in pH 13, although the absolute overpotential difference (see orange arrow) is much smaller compared to the Au cont. system. Contrary, for the 75 nm Au structures the dependence is inverted: In pH 7, the activity is slightly better, at least not worse, than it is in pH 13.

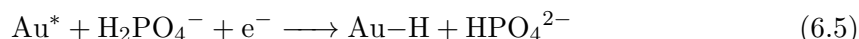
We now consider the complete set of data. The results suggest that the trend of increasing HER activity in more alkaline electrolyte observed for the continuous layer (benchmark system) appears to decrease when increasing the border contribution of Au/SiN (smaller orange arrows). The situation seems to become even slightly inverted for the smallest structure size (75 nm). Assuming that the PZC is similar for all electrodes and quite constant in SHE scale, it appears that higher polarization of the electrode slightly lowers the HER efficiency for nanostructured electrodes. Or in other words: Decreasing the electrode polarization (or cation concentration in front of the electrode) at a given potential in RHE scale seems not to decrease the HER activity in the nanostructured case as strongly as for the continuous Au layer. We will consider the explicit dependence of the HER activity on the actual cation concentration in the next section.

As a consequence of the previously mentioned observation, the overpotential difference between the largest and the smallest structure size (i.e. between 1400 nm and 75 nm)

at a given current density is larger in pH 7 than it is in pH 13 medium (see purple arrows). This coincides very well with the data of Filser et al. [Fil+18]. They investigated HER (and CO₂RR) on nanostructured electrodes in an electrolyte containing dissolved CO₂ (75 mM K₂CO₃ + 100 mM H₃PO₄/CO₂ sat'd.), so the pH value of the solution was around 6.8. The absolute potential difference in their system between the largest and the smallest nanostructured electrode is 170 mV, which is bigger than the difference of the data presented in section 5.1 at pH 13 with a value of 120 mV. Furthermore, the activity seems to depend on the cationic species present in the electrolyte, which will be investigated in the next section.

Influence of the anionic species

The question remains if the presence of (di-)hydrogen phosphate in the neutral electrolytes investigated here only leads to the desired local pH buffering during the reaction, or if the presence itself can influence the reaction speed and/or the mechanism of HER. A direct influence of the H₂PO₄⁻/HPO₄²⁻ species on the reaction needs to be considered in order to conduct a reliable comparison between buffered neutral and alkaline electrolyte in RHE scale. A possible direct influence on the reaction may be that (di-)hydrogen phosphate molecules may work as additional proton sources in the hydrogen adsorption step via hydrogen phosphate reduction:



A similar observation has been made when using bicarbonate as a buffer [Res+18; MBK22]. However, in neutral electrolyte and at negative HER overpotential, the electrode is polarized negatively, since the PZC is at approx. +0.2 V_{SHE} (cf. section 7.2.3). Consequently, the charge on the electrolyte side of the double layer is positive in sign and, thus, the concentration of the cationic species close to the electrode surface is supposed to be much larger than the concentration of anionic species, which makes a 'direct' dissociation of di-hydrogen phosphate at the electrode surface rather unlikely. However, it can be that the di-hydrogen phosphate dissociation is mediated by an OH⁻/H₂O redox reaction at the surface, which finally leads to a similar additional pathway for the Volmer step, as mentioned in the reaction equation above.

To prove if the presence of hydrogen phosphate influences the HER rate, we compare two different systems: A system containing only sulfate ions (SO₄²⁻) as the anionic species and a system containing only hydrogen phosphate (HPO₄²⁻) as the anionic species. The concentration of both ions is similar and chosen to be 50 mM. The cationic species present in both electrolytes is K⁺. Since we want to avoid any effect of buffering caused by the third phosphate dissociation, we choose a pH value of 10, which is well between the two relevant pK_a values. In addition, at this pH the sulfate ion is completely deprotonated (and it is far away from the second dissociation level, which is at pK_a ≈ 1.9), and HER is likely to be dominated rather by water splitting than by proton reduction.

Figure 6.19(a) shows LSV curves of a continuous Au layer in the two mentioned electrolytes. It is clearly visible that the HER activity of the electrode is different in the two electrolytes. Taking the SO₄²⁻ electrolyte as the reference, the HER activity in HPO₄²⁻ electrolyte is slightly higher. The difference in overpotential is around 20 mV at -0.03 mA cm⁻² (see orange arrows). It needs to be mentioned that both electrolytes are

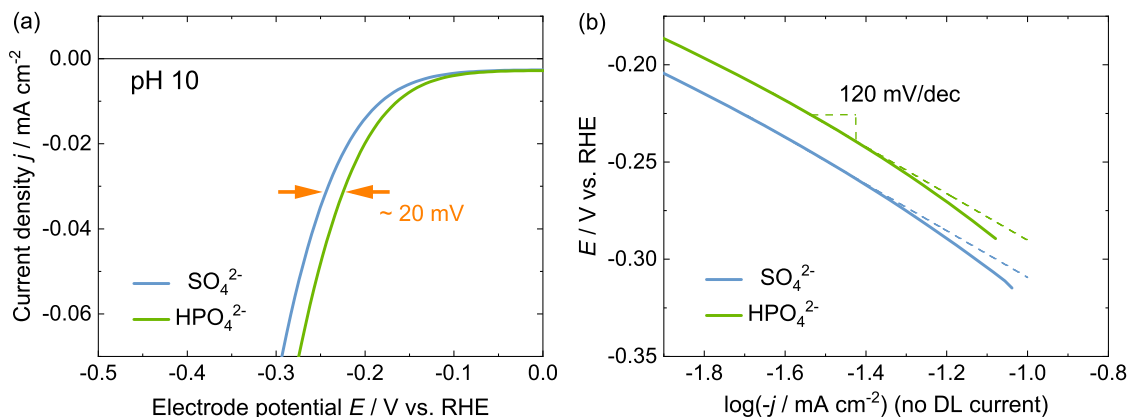


Figure 6.19: HER on a continuous Au layer with various anionic species. (a) LSVs in electrolytes containing 50 mM of either SO_4^{2-} (blue) or HPO_4^{2-} (green). Both electrolytes have pH 10 and are not buffered. The cationic species present in both media is K^+ . Scan rate: 50 mV s^{-1} . (b) Tafel plots of the respective LSV curves after subtraction of the non-faradaic current at $E = 0 \text{ V}_{\text{RHE}}$ (DL current).

not buffered. Thus, the pH value may change in front of the electrode during the scan and/or the reaction rate may be determined by the transport at comparably low current densities. However, it is still very likely that the difference in the LSV scans at these small current densities considered here is rather caused by a difference in the reaction kinetics than by transport effects. This becomes clear when considering the logarithmic current density, cf. Figure 6.19(b). The RDS of HER on Au(pc) at pH 10 and at low overpotential is likely the Volmer step. Consequently, we can infer that the slope of the logarithmic current is supposed to be around 120 mV dec^{-1} , if the reaction is determined by kinetics. And indeed, below $\log |j| < -1.4$ both curves decrease linearly with the mentioned slope. Above this value the curves deviate from the linear dependence (see dashed lines). Thus, we can conclude that the potential difference observed in Figure 6.19(a) is really of kinetic nature and not caused by any transport domination present at these rather low current densities.

The data clearly shows that the present anionic species can influence HER. The presence of HPO_4^{2-} slightly enhances HER compared to the presence of SO_4^{2-} , either directly by changing the proton adsorption mechanism or indirectly by altering the electrochemical environment in front of the electrode surface in a favorable way. A similar effect can also be observed indirectly in the data of other groups [Res+18]. However, the overpotential difference between the two investigated systems observed here is rather small compared to the overpotential difference between the structured electrodes and the continuous layer electrode, cf. yellow and green curves in Figure 6.18. Considering that the HER activities at pH 7 (i.e. in a (di-)hydrogen phosphate containing electrolyte) may also be increased due to an additional contribution stemming from the specific anionic species present in the solution, the interpretation of the data given previously would not change. In case of the continuous Au layer the overpotential difference between the curves of pH 13 and pH 7 values is rather big. A shift of approx. 20 mV of the pH 7 curve towards more negative potentials (i.e. subtracting a potential influence of the (di-)hydrogen phosphate species on HER activity) would even increase the overpotential difference between the pH 13 and the pH 7 curve. Contrary, in case of the 75 nm electrode, a shift of approx. 20 mV of the pH 7 curve towards more negative potential would decrease the overpotential

difference between the curves of the two pH values. However, a smaller difference would also not change the qualitative statement made previously. A smaller difference for the 75 nm electrode may indicate that the activity in pH 7 electrolyte is not necessarily larger, but can also be similar to the activity in pH 13 electrolyte. However, it is definitely not considerably lower, as observed for the continuous Au system.

6.3.2 Cation concentration

As already mentioned above, at negative polarization of the electrode, the dominating species present in front of the electrode surface are cations. The next question we address in this section is, how the (bulk) concentration of cations influence the HER rate on structured electrodes. We investigate the electrodes in neutral electrolyte, as here the concentration of cations can be easily varied by several orders of magnitude, while keeping the pH value constant.

The investigated electrolytes are mixed from KOH, H₃PO₄ and K₂SO₄ with a suitable amount to achieve the desired concentration of K⁺ ions. The goal is to assure the desired cation concentration while maintaining a similar pH value of 7 for all electrolytes investigated. A similar pH value of the electrolytes makes it possible to assign the observed differences to the difference in the (surface) cation concentration, as the effective polarization of the electrode in RHE scale is similar. If the pH value is not kept constant and the data is plotted in RHE scale, the surface concentration of cations would not necessarily scale with the given bulk concentration of cations. The buffer capacity is chosen to be similar for all electrolytes with a constant value of 12 mM H₂PO₄⁻/HPO₄²⁻, except for the lowest concentrated electrolyte, which has a buffer capacity of 6.7 mM H₂PO₄⁻/HPO₄²⁻. More information regarding the composition of the electrolytes is given in Table 6.3.

K ⁺ Electrolyte	Approx. ion concentrations [mM]			Approx. ionic strength [mM]
	[K ⁺]	[SO ₄ ²⁻]	[H ₂ PO ₄ ⁻ /HPO ₄ ²⁻]	
10 mM	10	0	6.7	13
30 mM	30	6	12	42
100 mM	100	41	12	147
300 mM	300	141	12	447
1000 mM	1000	491	12	1497

Table 6.3: Overview of the composition (approximate ion concentrations) and the resulting ionic strengths of the respective electrolytes used in this section. All electrolytes have a pH value of 7.

Figure 6.20 shows LSV curves of the (a) 1400 nm structured electrode and the (b) 75 nm structured electrode in the mentioned neutral electrolytes with various cation (bulk) concentrations. Note that the cathodic current is plotted in logarithmic scale and that the double layer charging current present at 0 V_{RHE} has been subtracted from the data. Due to the comparatively small buffer capacity of the electrolytes, the current is expected to be transport dominated at the investigated current densities. This is likely the reason for the deviation from the linear behavior (flattening of the curves) at comparatively small current densities $\log |j_c| > -1$. However, at current densities below that value, the data can be assumed to be dominated by kinetics, as the slope is approximately linear for all concentrations.

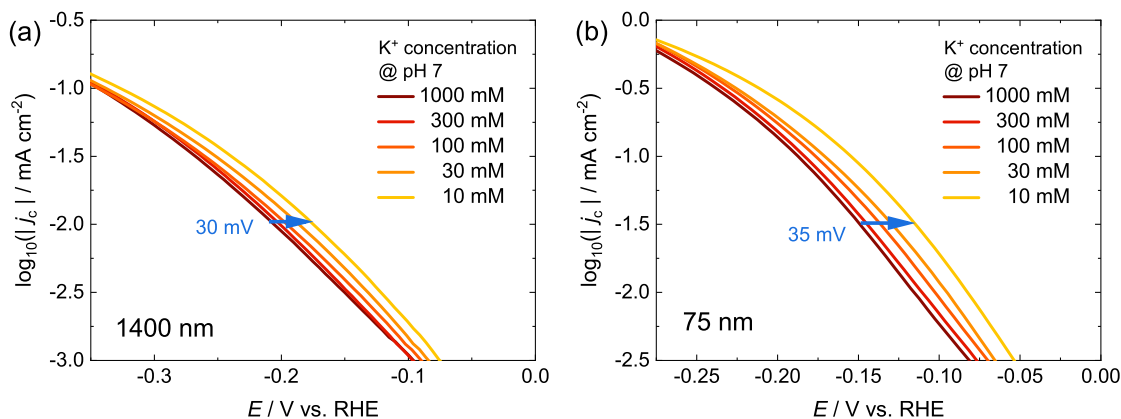


Figure 6.20: Linear sweep voltammograms of a nanostructured electrode with (a) 1400 nm and (b) 75 nm sized Au structures in electrolytes with various K^+ concentration at pH 7. The composition of the electrolytes is given in Table 6.3. Scan rate: 50 mV s^{-1} .

There are two important observations:

- With decreasing cation concentration the necessary overpotential decreases, i.e. the LSV curve shifts systematically towards more positive potentials (see blue arrows).
- This trend is qualitatively and even quantitatively similar for the larger structures (1400 nm) and the smaller structures (75 nm).

Discussion: HER promotion at the metal/insulator interface for low cation concentration

This trend of increasing HER activity with decreasing cation concentration is not expected. A reverse trend, i.e. decreasing HER activity with decreasing cation concentration, has been observed by Goyal et al. [GK21a] on poly-crystalline Au electrodes in mildly alkaline electrolyte at pH 11 and using Na^+ as the cationic species. The authors explained this behavior by a promotional effect of the presence of cations for HER, as they interact with the transition state of the water splitting reaction [GK21a] at mildly alkaline conditions. This dependence changed, when they further increased the electrolyte pH. At pH 13 they found a trend similar to ours, i.e. an increasing HER activity with decreasing cation concentration. The authors explained the trend at pH 13 by the comparatively high concentration of cations at the electrode surface in this case, which leads to the "blockage of the surface" [GK21a]. A similar 'site-blocking mechanism', which can inhibit HER due to a higher near-surface cation concentration for weakly hydrated cations, has also been proposed by Monteiro et al. [Mon+21]. However, in our system the pH value is rather low (pH 7), which leads to less polarized electrode in the potential range evaluated here (when assuming the same PZC) compared to the systems presented above. Following the explanation given by Goyal et al. and Monteiro et al., our system should be in the 'promotional regime' [Mon+21] of HER, in which a higher concentration of cations in front of the electrode surface is supposed to increase the HER rate. However, a contrary behavior is observed here for HER on structured electrodes.

Consequently, we may need to consider a different explanation for the increased HER rate with decreasing cation concentration at pH 7 in our system. According to the mechanism presented by Ledezma-Yanez et al. [Led+17] the electric field in the double layer is a crucial parameter affecting the activity of HER from water splitting. The authors proposed

that the transport of OH^- ions from the surface towards the electrolyte bulk is the rate determining mechanism. Since this ionic transport necessitates a reorganization of the double layer, a stronger polarized double layer necessitates a higher reorganization energy of the rigid layer to assure the same transport rate. A decreased cation concentration in front of the electrode surface would reduce the electric field in the double layer at a given electrode potential and, thus, would reduce the necessary reorganization energy of the double layer, which would, in turn, result in a higher reactivity. This mechanism may appear in parallel to the promotional effect of HER from water splitting for a higher cation concentration, as proposed by Monteiro et al. and Goyal et al. [Mon+21; GK21a].

Considering this explanation, we can conclude that the transport of charged ions (which can be either OH^- ions or HPO_4^{2-} ions due to the buffering capability in the electrolyte) away from the electrode surface is the rate dominating mechanism for structured electrodes in neutral pH 7 electrolyte, as a reduced cation concentration in front of the electrode surface (i.e. low electric field in the double layer) appears to be beneficial for HER on structured electrodes. As the behavior of structured electrodes is contrary to the behavior expected for continuous Au layer electrodes at these conditions (cf. Goyal et al. [GK21a]), we recognize that the presence of the metal/insulator interface somehow significantly changes the dependence of the HER rate on the local cation concentration. As we expect a promotional effect of HER from water reduction with increasing cation concentration at these conditions, we may conclude that the reaction mechanism itself is changed drastically at this interface. However, at this point, i.e. on the basis of the results shown so far, a further interpretation of the results is rather speculative. The final mechanism is proposed in chapter 8.

6.3.3 Cationic species

We have seen in the previous section that the concentration of cations affects the HER reaction rate. Apart from altering the cation concentration, the cationic species itself can be altered, which is supposed to influence the HER activity, although cations do not participate directly in the reaction but work as a spectator species. The dependence of the HER rate on the cationic species has been investigated in many studies [Xue+18; Liu+19; GK21a; Mon+21]. In this section, we compare four different alkali metals as the cationic species present in the electrolyte: Li, Na, K, and Cs. First, we consider the effect in alkaline electrolyte, later in neutral electrolyte.

Alkaline medium

The electrolytes investigated in the first step are consisting of 0.1 M $AM\text{OH}$, where AM can be one of the alkali metals mentioned above. The pH is similar for all solutions and has a value of 13. We compare, again, the three different electrode systems, namely: A continuous Au layer (Au cont.), an electrode with 1400 nm sized Au structures (1400 nm) and an electrode with 75 nm sized Au structures (75 nm). Figure 6.21(a) shows linear sweep voltammograms of the three electrodes in the various electrolytes. As the comparison of the data is rather complex, we again start the discussion by describing the behavior of the electrodes individually:

We start with discussing the data of the continuous Au layer (Figure 6.21(a), top), as this system works as the benchmark. It becomes evident in the data that the HER activity

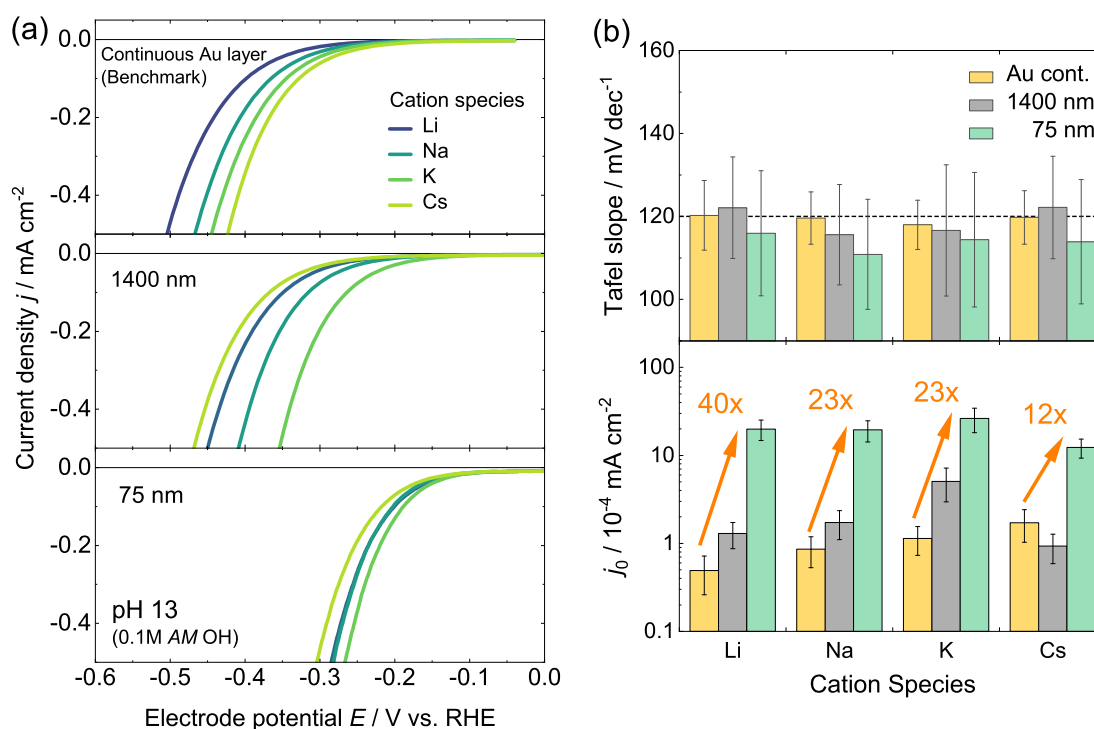


Figure 6.21: (a) Linear sweep voltamograms of a continuous Au layer (top), 1400 nm Au structures (middle), and 75 nm Au structures (bottom) in alkaline electrolyte 0.1 M AMOH (pH 13) for various cationic species ($AM = \text{Li, Na, K, Cs}$). Scan rate: 50 mV s^{-1} . A detailed explanation of the visible trends is given in the text. (b) Tafel analysis: Tafel slope (top) and exchange current densities (bottom) of the electrodes for various cationic species. Within the errors the Tafel slopes are well around 120 mV dec^{-1} for all electrodes and cationic species, indicating that there is no difference in the reaction mechanism. The exchange current density increases with decreasing structure size.

of the electrode changes when altering the cationic species present in the electrolyte. The necessary overpotential for drawing a certain current density decreases, i.e. the HER activity *increases*, in the following order: $\text{Li} < \text{Na} < \text{K} < \text{Cs}$. Thus, the HER activity systematically increases down the periodic table, i.e. with decreasing degree of solvation of the ions [GK21b]. The overpotential difference between the two most separated curves is $\approx 80 \text{ mV}$ at -0.5 mA cm^{-2} .

This data is well in accordance with the literature. Many groups have observed the same trend of the alkaline HER activity with the cationic species on gold electrodes [Xue+18; GK21b]. However, the actual mechanism, i.e. how the cation as a spectator species influences the reaction activity, is still under discussion. Bandarenka et al. [Xue+18] proposed that the cationic species present at the electrode surface changes the binding energy between the adsorbed hydrogen atom and the metal active site, likely due to the distance of the cation from the surface. This would directly influence the adsorption energetics of the adsorption process and consequently change the reactivity. Koper et al. [GK21b] proposed that the HER enhancement with decreasing degree of solvation of cations is due to the increase in effective concentration of cations near the electrode surface. They propose that the cation enhance HER on Au by interacting with the transition state of the Volmer reaction [GK21a; GK21b]. Interestingly, a reverse trend with the cation

identity, i.e. the alkaline HER activity *decreases* when going from Li to K, is found in the literature when using Pt as the catalyst material [Xue+18; WJO19; Liu+19].

Next, let us consider the data of the electrodes with 1400 nm structures (Figure 6.21(a), middle image). Again, the activity of the electrode appears to depend significantly on the cationic species present in the electrolyte. The HER activity increases now in the order $\text{Cs} < \text{Li} < \text{Na} < \text{K}$, which is a different order compared to the continuous Au layer presented above. The overpotential difference between the two most separated curves is $\approx 110 \text{ mV}$ at -0.5 mA cm^{-2} and, thus, a bit larger compared to the value found for the continuous Au layer. The comparison of the activities found for a certain cationic species on various electrode systems is given below.

Last, let us consider the data of the electrodes with 75 nm sized Au structures (Figure 6.21(a), bottom). Again, the HER activity is depending on the cationic species present. It increases in the order $\text{Cs} < \text{Na} \approx \text{Li} < \text{K}$. The overpotential difference between the two most separated curves is $\approx 45 \text{ mV}$ at -0.5 mA cm^{-2} and, thus, considerably smaller compared to the other two systems.

Tafel analysis

To further quantify the observed changes of HER activity with the cationic species, we further perform a Tafel analysis of the LSV data. The fitted slope as a function of the respective electrode (color) and cationic species (y -axis) is shown in Figure 6.21(b), top image. The respective exchange current density j_0 determined from the intersect of the Tafel fitting is shown in Figure 6.21(b), bottom image.

The Tafel slope appears to be quite similar for all cationic species and all electrodes investigated within the range of the error. Its value is approx. 120 mV dec^{-1} . This indicates that there is an identical reaction mechanism for all systems considered here. Moreover, the Tafel slope of 120 mV dec^{-1} indicates that the first electron transfer step is the RDS, which is likely to be the Volmer step in this case. The same slope is found in the literature [GK21a; GK21b] for Au-based electrodes.

The determined exchange current densities clearly show that there is a huge influence of HER activity on both parameters, the cation identity and the structure size. There are possibly two distinct effects overlaying on structured electrodes, which both may depend differently on the cation identity:

1. The cation-specific variation of the HER rate due to the 'intrinsic' properties of the systems when changing the cationic species. This dependence is evident when considering the data of the continuous Au layer electrode.
2. The variation of the HER rate caused by the appearance of the metal/insulator interface, i.e. the border of the structures, which may show a different dependence on the cation identity as the effect previously mentioned.

To analyze the dependence of j_0 of structured electrodes on the cationic species more in detail, we define the scaling factor of the exchange current densities F_{AM} for a certain cationic species AM by:

$$F_{AM} = \frac{j_{0,AM,75}}{j_{0,AM,\text{cont}}} \quad (6.6)$$

Here $j_{0,i,75}/j_{0,i,\text{cont}}$ is the exchange current density of the 75 nm electrode for cation i normalized to the respective exchange current density of the continuous layer electrode.

We choose this quantity to be a descriptor for the latter effect, as the determined j_0 of the electrodes still have an intrinsic dependence on the cation identity ('first' effect). This influence can be minimized by normalizing the data to the data of the continuous layer. We explicitly consider the data of the 75 nm electrode in the numerator, as this system shows the largest contribution stemming from the metal/insulator interface. We determine the following scaling factors $F_{\text{Li}} \approx 40$, $F_{\text{Na}} \approx F_{\text{K}} \approx 23$, and $F_{\text{Cs}} \approx 12$. Thus, the scaling factor increases when going up the periodic table, i.e. it systematically increases with increasing degree of solvation:

$$F_{\text{Cs}} < F_{\text{K}} \approx F_{\text{Na}} < F_{\text{Li}}$$

We assign this systematic increase of the HER activity with the cation identity to the mentioned alteration of the reaction mechanism at the metal/insulator interface. An explanation/discussion of the observed trend is given in chapter 8, in which the possible bifunctional reaction mechanism at the metal/insulator interface is evaluated. At this point, we sum up the two most important observations made in this section: (1) It is evident that the metal/insulator interface exhibits an increased HER activity in alkaline medium, this is visible for all cationic species investigated here. (2) The actual enhancement of the HER activity at the border of the structures depends on the cationic species present in the electrolyte. The largest increase is seen for Li (40x larger), the smallest for Cs (12x larger).

Neutral medium

A similar comparison can be performed in neutral medium. As already explained in the previous section, the point of zero charge is almost constant in SHE scale. Consequently, the polarization of the electrode at a given potential in RHE scale in neutral electrolyte is smaller compared to the same potential in RHE scale in alkaline electrolyte. Again, we look at the LSVs of the three mentioned electrode systems in a buffered neutral electrolyte with pH 7 consisting of 0.18 M AM^+ ($AM = \text{Li, Na, K, Cs}$) and 0.12 M $\text{H}_2\text{PO}_4^-/\text{HPO}_4^{2-}$. A systematic analysis of the HER kinetics is, again, omitted, as the current measured in this electrolyte may be influenced by transport already at rather small current densities.

Figure 6.22 shows the LSVs of the mentioned systems. The continuous layer electrode (top) clearly shows a dependence of the HER activity on the cationic species. The activity increases systematically from Li to Cs. Thus, this trend with the cationic species is qualitatively similar to the trend found for alkaline electrolyte (cf. Figure 6.21(a), top). The difference in overpotential for the two most separated curves is found to be ≈ 70 mV at -0.1 mA cm^{-2} , and thus it is slightly smaller than in the previous case. However, for 1400 nm and 75 nm the situation appears to be different. Again, less overpotential needs to be applied for the 1400 nm electrode compared to Au cont., and even less for 75 nm. This effect appears to be clear, as it was already discussed before and it is known from the data shown in Figure 6.18. However, we do not observe a significant spreading of the curves of the structured electrodes when varying the cationic species. This observation differs from the behavior seen in alkaline electrolyte. In the current density range considered here, the curves lie approx. on top of each other and tend to separate only at larger negative currents. In alkaline electrolyte, the separation of the curves (at least for the 1400 nm electrode) has been observed already at small negative current densities.

The major conjectures from these observations are: Without metal/insulator interfaces (continuous Au layer electrode), the trend of the HER activity alternation with the cationic

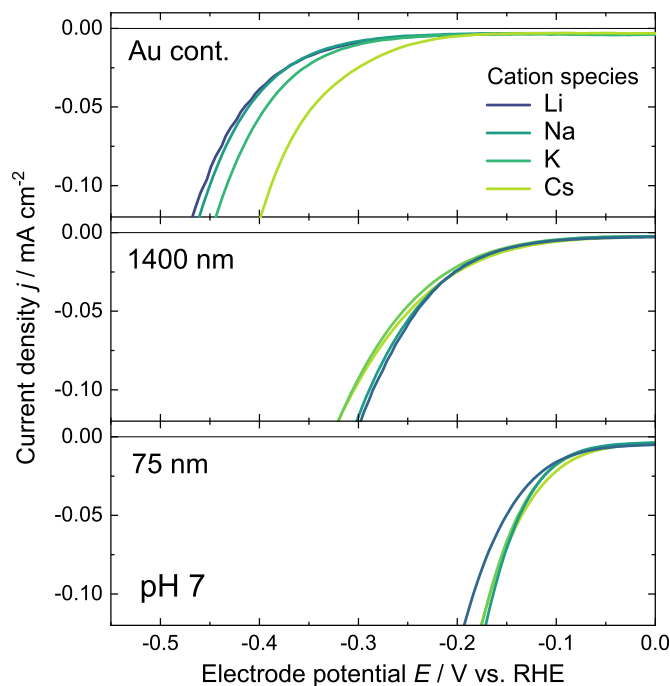


Figure 6.22: Linear sweep voltamograms of a continuous Au layer (top), 1400 nm Au structures (middle), and 75 nm Au structures (bottom) in neutral electrolyte (pH 7) for various cationic species. The electrolyte consists of 0.18 M X^+ ($X = \text{Li}, \text{Na}, \text{K}, \text{Cs}$) and 0.12 M $\text{H}_2\text{PO}_4^-/\text{HPO}_4^{2-}$ (pH 7). Scan rate: 50 mV s^{-1} .

species is similar in neutral and in alkaline media. This behavior can also be anticipated from the measurements shown by Goyal et al. [GK21b]. Thus, it appears that the cationic trend observed in this system (Au cont.) is, to some extent, not so much dependent on the polarization of the electrode. Note, the electrode polarization at pH 7 is supposed to be much smaller compared to the polarization at pH 13.

For nanostructured electrodes the HER rate enhancement in neutral electrolyte (at low electrode polarization) is nearly independent of the cationic species present. Thus, the mechanism at the metal/insulator interface appears to repeal the intrinsic cationic trend. Consequently, we can conclude that for low polarization of the electrode, the mechanism appearing at the metal/insulator interface is rather independent of the actual cationic species.

6.4 Summary

Let us summarize the main observations and conclusions made in this chapter, as they work as the basis for the elaboration of the bifunctional mechanism:

Electrocatalytic surface and catalyst material

We compared nanostructured electrodes with the same structure size, but different dominating Au-facets. In acidic environment, the observed HER improvement can be partly explained by a variation of the Au-facets for smaller structure sizes. However, this effect appears to be too small to explain the full improvement of HER kinetics observed for smaller structures in acidic medium.

Investigations of silicon oxide nanostructure arrays on a Au(pc) surface further showed the same trend of HER enhancement on electrodes with smaller structures. This further supports the hypothesis, that the enhanced HER rate on gold nanostructures is not caused by an alteration of the catalyst surface configuration/topography, but stems from the close presence between the oxide and the catalyst surface.

By changing the electrocatalytic active material, we noted, that the HER enhancement is also qualitatively present for Pt-based structures (shown in acidic and alkaline electrolyte), and for Cu-based structures (shown in neutral electrolyte). As both materials have very different proton adsorption energetics, we concluded that the observed HER improvement is almost independent of the hydrogen adsorption energetics on the electrode surface, but is due to an alteration of another mechanism involved in the rate determining Volmer step.

Passivation layer

The HER activity of structured electrode could be considerably decreased by covering part of the oxide surface, which is in close contact with the Au catalyst, by a polymeric compound. Thus, we concluded that the composition of the SiO_x surface influences the HER activity at the Au/SiO_x interface. However, we could not conclude from the measurements, if the oxide is necessary for the actual reaction mechanism, or if by covering the oxide we changed the electrochemical environment (i.e. the local double layer structure) in an unfavorable way.

In addition, we investigated nanostructured electrodes utilizing silicon nitride (SiN) as the passivation layer material adjacent to the Au nanostructures. We could observe very similar results compared to the silicon oxide based electrodes, i.e. the improvement of HER activity with decreasing structure size is quantitatively very similar for both different passivation layer materials. Thus, we concluded that the effect is either intrinsically caused by the geometry of the system, or dependent on the composition of the SiN/Electrolyte or SiO_x/Electrolyte interface, which appears to be chemically similar for both kinds of materials.

Electrochemical environment

The electrochemical environment itself can have a huge influence on the activity of HER from the reduction of water (present in neutral to alkaline medium), for continuous as well as for nanostructured electrodes. However, the actual HER improvement at the metal/insulator interface (nanostructured electrodes) appears to have a very different de-

pendence on the electrochemical environment compared to HER at the bare metal surface (continuous Au electrode). To sum up the main observations, we consider the two systems separately:

Considering an electrode *without* an metal/insulator interface (continuous Au layer), the largest HER improvement is found, if:

- there is a considerably high, but not too high ('surface blocking', c.f. Goyal et al. [GK21a]), (bulk) concentration of cations.
- using Cs^+ as the cationic species (lowest degree of solvation)
- the electrode is strongly polarized (activity in pH 13 is higher than in pH 7)

The presence of a significant concentration of cations in front of the electrode surface appears to 'support' HER. However, even in the best case considered here, the activity of HER is considerably lower compared to the activity of structured electrodes. The lowest overpotential is found for 0.1 M CsOH, pH 13.

Considering an electrode *with a comparatively high share* of a metal/insulator interface (75 nm electrode), the largest HER improvement is found:

- for the lowest (bulk) concentration of cations.
- using Li^+ as the cationic species (which has the highest degree of solvation, i.e. farthest distance of the ion from surface)
- for a weakly polarized electrode (activity in pH 7 slightly higher than in pH 13)

It appears that a smaller concentration of cations in front of the electrode surface, which can be achieved either directly by changing the electrode polarization or the (bulk) cation concentration, or indirectly by changing the cationic species, helps in accelerating HER at the metal/insulator interface. However, we can conclude that the actual electrochemical environment has only minor importance for the HER activity at this interface, as the spreading of the individual measurements for a variation in the electrochemical environment is found to be small for the 75 nm electrode compared to the spreading observed for a continuous Au layer. Consequently, we have seen that the HER promoting properties of the metal/insulator interface outperforms most of the effects tunable by the electrochemical environment by strength.

Chapter 7

Increasing the double layer capacitance by electrode nanostructuring

In this chapter, the influence of nanostructuring on the double layer capacitance of the metal/silicon electrodes is investigated. In the first section 7.1 we analyze the capacitance determined via cyclic voltammetry. In the second section 7.2 we analyze the capacitance determined via impedance spectroscopy.

7.1 Differential capacitance determined via cyclic voltammetry

First, we determine the capacitance of the electrodes via cyclic voltammetric experiments. We conduct a potential scan in the double layer region with various defined scan rates ν and record the non-faradaic current, i.e. the double layer charging current I_{DL} . From the plot of I_{DL} over the scan rate ν we can calculate the differential capacitance C_{DL} according to [BF01]:

$$C_{\text{DL}} \equiv \left(\frac{\partial Q_{\text{DL}}}{\partial E} \right) = \frac{\partial Q_{\text{DL}}}{\partial t} \frac{\partial t}{\partial E} = I_{\text{DL}} \nu^{-1} \quad \Rightarrow \quad \frac{\partial I_{\text{DL}}}{\partial \nu} = C_{\text{DL}} \quad (7.1)$$

Figure 7.1(a) shows a typical cyclic voltammetric experiment in the double layer region for various scan rates. Figure (b) shows the double layer charging current (averaged from the upward and the downward scan) determined at $0.35 \text{ V}_{\text{SHE}}$ plotted over the scan rate. In principle, the determination of C_{DL} can be performed at any electrode potential. However, the current needs to be determined by the double layer charging current only, i.e. no faradaic reactions or adsorption should occur. In this section we will show the values determined at $0.35 \text{ V}_{\text{SHE}}$. We did choose this potential for the calculation of the electrode capacitances, because at this potential the interference of the current signal with other faradaic reactions (sulfate ad-/desorption and reduction of traces of oxygen present in the system) could be avoided quite well.

It needs to be mentioned at this point that the electrodes investigated here consist of a metal/electrolyte interface connected in series to a MIS interface. With this method it is not possible to separate the two contributions and analyze the double layer capacitance individually. However, this will be part of the next section.

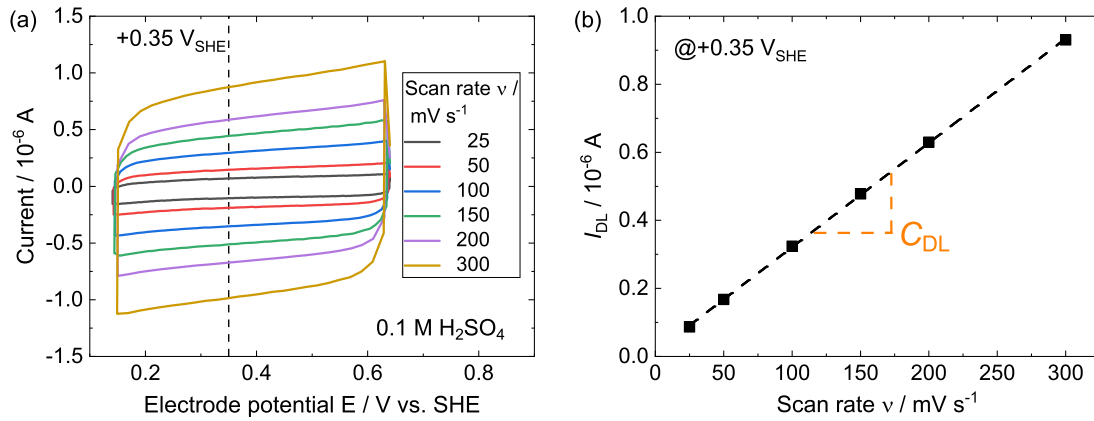


Figure 7.1: Exemplary determination of the double layer capacitance via cyclic voltammetry. (a) CVs in the double layer region at various scan rates. Electrolyte: 0.1 M H₂SO₄. (b) Plot of the double layer charging current determined at +0.35 V_{SHE} over the scan rate. The slope of the linear fitting gives the double layer capacitance C_{DL} . Electrode: nanostructured with 75 nm Au structure size (without passivation layer).

7.1.1 Comparison of protruding and embedded structures

The determination of the specific capacitance necessitates the normalization of the determined absolute capacitance to a certain area. Usually, the geometric surface area (here: gold covered surface area) is used for normalization. However, in case of a nanostructured surface area, this normalization can not be performed straight forwardly, as for nanostructured electrodes also the oxide covered area beside the gold structures may contribute to the measured capacitance significantly. The influence of the oxide surface is expected to be significant for protruding structures, as the oxide layer thickness in this case is in the order of 1.5 nm and, thus, comparatively small compared to electrodes with embedded structures, which consist of an oxide layer thickness is in the order of 10 nm. We will analyze the capacitance of both kinds of nanostructured electrodes in the following. The measured capacitance C_{DL} is assumed to be given by the two mentioned contributions, a contribution stemming from the Au covered and from the Ox covered surface:

$$C_{DL} = A_{Au}c'_{Au} + A_{Ox}c'_{Ox} \quad (7.2)$$

Here, $A_{Au/Ox}$ is the area of gold and oxide exposed to the electrolyte, respectively, and $c'_{Au/Ox}$ is the specific capacitance of the respective surface. If the second term is not negligible, it becomes clear that a normalization of the capacitance to the gold area A_{Au} is not meaningful. First, we normalize the determined capacitance to the total (geometric) electrode area A_{El} in order to calculate the specific electrode capacitance c'_{El} :

$$c'_{El} = \frac{C_{DL}}{A_{El}} \quad (7.3)$$

Here, A_{El} is the macroscopic electrode area, i.e. the gold covered area plus the remaining (un)covered silicon area exposed to the electrolyte. When normalizing the measured capacitance to the macroscopic electrode area, it is possible to compare electrodes with embedded and protruding structures, without misinterpreting the absolute value. A_{El} is determined by the macroscopic dimension of the electrode exposed to the electrolyte, i.e. by the area determined by the O-ring sealing used. In the present case it is 0.567 cm².

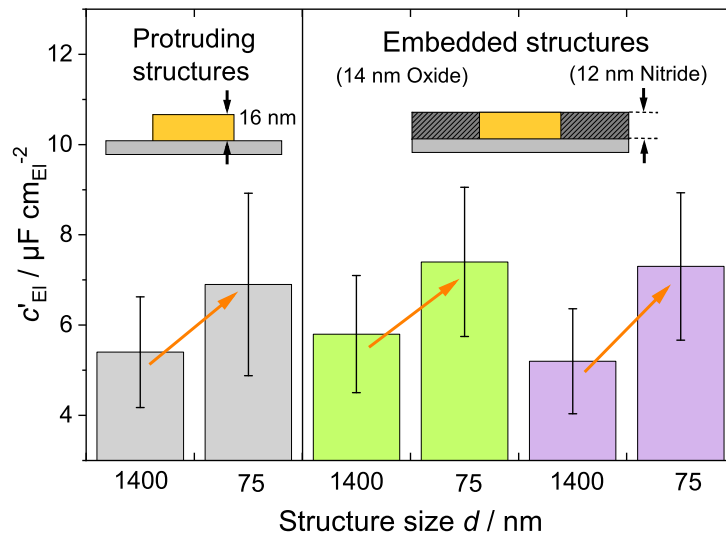


Figure 7.2: Specific capacitance of nanostructured electrodes with two different structure sizes (1400 nm and 75 nm) for three electrode types: Protruding structures (grey), structures embedded in silicon oxide (green), and structures embedded in silicon nitride (purple) passivation layer. The measurement has been performed in 0.1 M H_2SO_4 and the capacitance determined at $0.35 V_{SHE}$. Note that the capacitance is normalized to the total geometric electrode area (gold covered surface plus exposed silicon surface). For all three electrode types, the electrodes with small structures show a larger capacitance than the electrodes with larger structures.

Figure 7.2 shows the determined specific electrode capacitances of nanostructured electrodes with 1400 nm and 75 nm Au structure size in three different configurations: Without passivation layer (protruding structures) in gray, with 14 nm oxide passivation layer in green and with 12 nm nitride passivation layer in purple (embedded structures).

Let us first consider the data of the electrodes with protruding structures. The electrodes with 75 nm sized Au structures show a larger specific capacitance c'_{EI} compared to the 1400 nm electrode. Since the filling factor of the gold arrays is quite similar in both cases, the higher capacitance cannot come from a higher gold coverage. However, both electrodes consist of structures of the same height. Thus, the 75 nm electrode is supposed to have a larger total gold area, due to the lateral surface of the structures (cf. Table 5.4). This hypothesis is quite meaningful, since the actual areas of the differently sized electrodes measured indicate a larger active surface area for the smaller structures. As the gold/electrolyte interface is supposed to have a larger specific capacitance than the silicon/oxide/electrolyte interface, we expect a larger capacitance for smaller structures.

We now further investigate, whether the larger capacitance measured for smaller protruding structures is only caused by the larger area. Therefore, we calculate the specific capacitance of the geometric gold surface c'_{Au} from the experimental data of the structured electrodes. If just the larger area causes the larger capacitance, this value determined from experimental data would be similar to the actual measured value of a bulk gold electrode. We calculate the geometric gold area of the individual electrodes $A_{geo,i}$ by assuming cuboid (1400 nm) or cylindrical (75 nm) shape of the protruding structures and calculate c'_{Au} from equation (7.2), considering that A_{Ox} and c'_{Ox} is similar on both electrodes with different

structure sizes. We determine:

$$c'_{\text{Au,geo}} = \frac{C_{\text{DL},75} - C_{\text{DL},1400}}{A_{\text{geo},75} - A_{\text{geo},1400}} \approx 50 \mu\text{F cm}_{\text{geo}}^{-2} \quad (\text{calculated from structured electrodes}) \quad (7.4)$$

Let us compare this value to the value of a continuous gold layer electrode. Here, there is no contribution of any oxide surface, as the sample surface is completely covered by gold. The (geometric) specific capacitance is determined as:

$$c'_{\text{Au,geo}} = (44 \pm 9) \mu\text{F cm}_{\text{geo}}^{-2} \quad (\text{measured from continuous film}) \quad (7.5)$$

This value is a bit smaller than the value calculated from the structured electrodes. However, within the error, both values are well in accordance. Thus we can conclude that the larger capacitance of the electrode with 75 nm sized protruding structures stems only from the larger Au surface due to the larger lateral gold surface.

By normalizing the measured capacitance of the continuous gold layer not to the geometric, but to the actual measured gold area (cf. section 3.2.7), we can determine the specific capacitance of our gold film. We obtain a value of $c'_{\text{Au,meas}} = (29 \pm 8) \mu\text{F cm}_{\text{meas}}^{-2}$. Within the error, this value is quite similar to values reported in the literature for poly-crystalline gold in sulfuric acid based electrolytes [CH72].

Now, let us look closer at the data of the embedded structures (with passivation layer) in Figure 7.2 (green and purple). One can recognize that the electrodes with smaller structures (75 nm), again, show a higher capacitance compared the electrodes with larger structures (1400 nm). This is visible independent of the actual passivation layer material. This is quite remarkable. Since these structures do not have a lateral surface the electrodes should exhibit an almost similar gold area, which could be further verified by explicit measurements of the respective Au areas giving very similar values for both structure sizes. We further analyze this observation in the next section.

7.1.2 Dependence of the differential capacitance on the size of the nanostructures

In order to investigate the structure size dependence of the capacitance of the MIS electrodes further, we normalize the measured capacitance now to the actual measured gold area. For embedded structures, the contribution of the area covered by the passivation layer to the total electrode capacitance is supposed to be much smaller than the contribution of the gold surface. Thus, the measured capacitance is largely dominated by the contribution of the gold/electrolyte interface and normalizing to the gold area does not give a large error. We can determine the specific capacitance of gold in our system by rearranging equation (7.2):

$$c'_{\text{Au,meas}} = \frac{C_{\text{DL}} - A_{\text{ox}}c'_{\text{ox}}}{A_{\text{Au,meas}}} \quad (7.6)$$

Here, c'_{ox} is the specific capacitance of the oxide surface. We determine the capacitance of the oxide film explicitly by measuring an silicon-based electrode completely covered by an oxide film with similar properties as the one used for the nanostructured electrodes, i.e. 12 nm oxide thickness and similar fabrication parameters. The differential capacitance of the film turned out to be slightly potential dependent. We determined values between $0.45 \mu\text{F cm}_{\text{ox}}^{-2}$ at 0 V_{SHE} and $0.25 \mu\text{F cm}_{\text{ox}}^{-2}$ at $0.35 \text{ V}_{\text{SHE}}$.

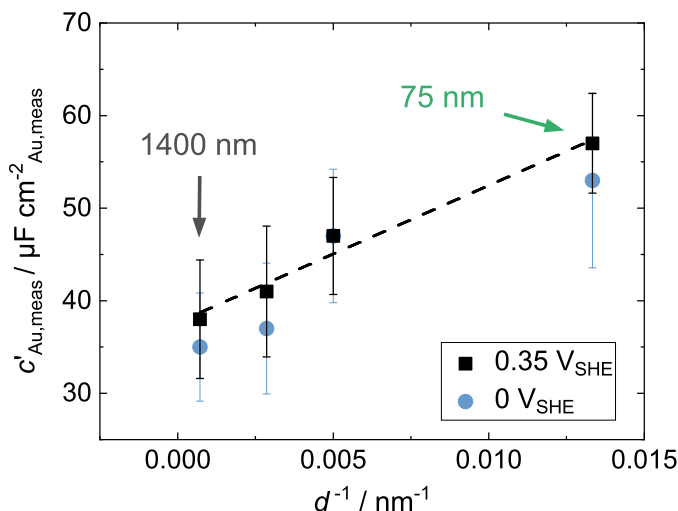


Figure 7.3: Specific capacitances of structured electrodes determined by potential scans plotted over the inverse of the respective structure size d^{-1} . The data was collected in 0.1 M H_2SO_4 and determined at either $0.35 V_{\text{SHE}}$ (black) or $0 V_{\text{SHE}}$ (blue). The capacitance data is normalized to the measured gold area.

Figure 7.3 shows the determined specific capacitances of the structured electrodes for different Au structure sizes plotted over the inverse of the respective structure diameter, i.e. over $1/d$. Note that electrodes with both kinds of passivation layers (nitride and oxide) showed a very similar behavior. Thus, we do not differentiate between the passivation layer materials in the following.

We recognize that the capacitance of the nanostructured electrodes increase with decreasing structure size. This could be already conjectured from the data shown in the last section. The increase of the capacitance with decreasing structure size is visible on a wide potential range throughout the double layer range. We indicated this by plotting two data sets collected at $0 V_{\text{SHE}}$ (blue) and $0.35 V_{\text{SHE}}$ (black). The capacitance of the electrode with smallest structures (75 nm) is about 50% larger than the electrode with the largest structures (1400 nm). In addition, the capacitance seems to scale linearly with $1/d$, which is indicated in the graph by the black dashed line as a guide to the eye.

Discussion: Increased border capacitance due to geometry?

Applying the same argumentation and geometric considerations as made in section 5, in which we analyzed the increased HER rate on nanostructured electrodes, a linear scaling of the capacitance with the inverse of the structure size d would implicate an increased capacitance at the border of the structures. However, contrary to the previous case, here this 'border effect' may be solely caused by geometric reasons, which we will discuss in this section.

Let us deduce an analytical expression for the specific capacitance c' of the structured electrodes. We first parameterize the structure geometry. This geometric parametrization is shown in Figure 7.4. We assume a protrusion height h , an edge radius r_{in} (curvature of edges) and the structure diameter d . This results in three contributing gold areas: A_{lateral} , A_{top} , and A_{edge} . Further, we assume the Helmholtz-model for the double layer. This leads to a fixed charge position in the electrolyte phase at a distance δ from the mentioned

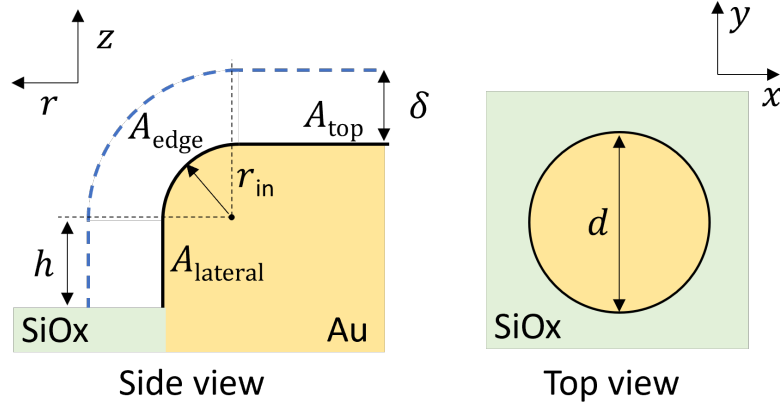


Figure 7.4: Scheme of the geometric parametrization of the circular structure. This geometric parametrization is used to derive an analytical expression for the capacitance of structured electrodes.

surfaces. This is indicated by the blue dashed line in the scheme.

We model this configuration by a parallel connection of three individual parallel plate capacitors, the capacitance of which can be expressed analytically. The capacitance of the top and the lateral parts are given by:

$$C_{\text{top}} = \varepsilon \frac{A_{\text{top}}}{\delta} = \varepsilon \frac{\pi(d/2)^2}{\delta} = \frac{\varepsilon \pi d^2}{4\delta} \quad (7.7)$$

$$C_{\text{lateral}} = \varepsilon \frac{A_{\text{lateral}}}{\delta} = \varepsilon \frac{2\pi d/2 h}{\delta} = \frac{\varepsilon \pi d h}{\delta} \quad (7.8)$$

here $\varepsilon = \varepsilon_0 \varepsilon_r$ is the absolute permittivity inside the double layer. The capacitance of the edge part can be derived from Gauß' law. First, we consider an 1D-area element de of the edge area with radius r :

$$de(r) = r d\phi \quad \Rightarrow \quad e(r) = \int_0^{\pi/2} r d\phi = \frac{\pi}{2} r \quad (7.9)$$

and calculate the contribution of the corresponding 1D spherical capacitor:

$$d \frac{1}{C} = \frac{1}{\varepsilon e(r)} \quad \Rightarrow \quad \frac{1}{C} = \frac{2}{\varepsilon \pi} \int_{r_{\text{in}}}^{r_{\text{in}}+\delta} \frac{dr}{r} = \frac{2}{\varepsilon \pi} \ln \left(\frac{r_{\text{in}} + \delta}{r_{\text{in}}} \right) \quad (7.10)$$

which then can be multiplied by the perimeter of the structures to get an expression of total capacitive contribution of the edge:

$$C_{\text{edge}} = \frac{\varepsilon \pi}{2} \frac{1}{\ln \left(1 + \frac{\delta}{r_{\text{in}}} \right)} \cdot 2\pi \frac{d}{2} = \frac{\varepsilon \pi^2}{2} \frac{d}{\ln \left(1 + \frac{\delta}{r_{\text{in}}} \right)} \quad (7.11)$$

The total capacitance C of the structure is the sum of these three contributions:

$$C = C_{\text{top}} + C_{\text{lateral}} + C_{\text{edge}} \quad (7.12)$$

We now consider the following assumptions:

- (a) $r_{\text{in}} \approx \delta$ (i.e. same order of magnitude)
- (b) $d \gg r_{\text{in}}$ (large structures compared to the curvature at the edge)
- (c) $4h < d$ (small structure heights compared to structure diameter, i.e. 'embedded' structures)

Considering these assumptions we see that the total gold area A_{tot} is dominated by the top area:

$$A_{\text{tot}} = A_{\text{top}} + A_{\text{lateral}} + A_{\text{edge}} = \frac{\pi}{4}d^2 + \pi h d + \frac{\pi}{2}r_{\text{in}} \cdot \pi d \quad (7.13)$$

$$\underbrace{\frac{\pi d^2}{4}}_{(b)} \left(1 + \frac{4h}{d}\right) \underbrace{\approx}_{(c)} \frac{\pi d^2}{4} = A_{\text{top}} \quad (7.14)$$

We then get an analytical expression for the specific capacitance c' of the gold surface of the structures:

$$c' = \frac{C}{A_{\text{tot}}} = \frac{C_{\text{top}} + C_{\text{lateral}} + C_{\text{edge}}}{A_{\text{top}}} = \frac{\varepsilon}{\delta} + \frac{\varepsilon 4h}{\delta d} + \frac{2\varepsilon\pi}{\ln\left(1 + \frac{\delta}{r_{\text{in}}}\right)} \frac{1}{d} \quad (7.15)$$

$$= \frac{\varepsilon}{\delta} + \left(\frac{\varepsilon 4h}{\delta} + \frac{2\varepsilon\pi}{\ln\left(1 + \frac{\delta}{r_{\text{in}}}\right)} \right) \cdot \frac{1}{d} \quad (7.16)$$

From this analytical expression it becomes clear that

$$c' \propto 1/d \quad (7.17)$$

which stems only from the geometric considerations made here for the system, i.e. it is due to the curvature present at either the cylindrical lateral area (first term in the big bracket) or at the edges of the structures (second term in the bracket). It becomes evident that the latter term increases in magnitude when further decreasing the curvature of the edges r_{in} while keeping δ constant.

Assuming values for the relevant quantities in equation (7.16) in the right order of magnitude: $\varepsilon \approx 20\varepsilon_0$, $h \approx 3$ nm, $\delta \approx 0.5$ nm, and $r_{\text{in}} \approx 1$ nm leads to the prediction that the measured capacitance of the 75 nm electrode should be approx. $10 \mu\text{F cm}^{-2}$ larger than the one measured for the 1400 nm electrode. Comparing this predicted difference with the actual experimentally measured difference between the two electrodes, cf. Figure 7.3, gives a quite good accordance, although the model is rather simple and the experimental data exhibit comparatively large errors. As a consequence of the latter, the interpretation of the experimentally observed linear dependence of the capacitance with the inverse of the structure size needs to be made very carefully. However, it is clearly shown here that the capacitance of the electrodes increases with decreasing structure size (this will be further investigated in the next section), and that this increase can be explained quite well by the changing geometry of the investigated systems.

7.2 Capacitance determined via impedance spectroscopy

In this section, we analyze the capacitive behavior of reference systems and nanostructured electrodes determined from electrochemical impedance spectroscopy (EIS). In section 7.2.1, we analyze a silicon-based electrode covered by a continuous silicon oxide layer of finite thickness as a reference system. In section 7.2.2, we consider the behavior of a continuous Au film on a silicon substrate. In section 7.2.3, we determine the theoretical behavior of the capacitance with the electrode potential by simulating the modified Poisson-Boltzmann equation in 1D, in order to compare and discuss the experimental data of the continuous layer electrode. In the last section 7.2.4 of this chapter, we further determine the capacitive behavior of nanostructured electrodes and compare it to the continuous Au layer electrode.

7.2.1 Capacitive behavior of the silicon/oxide/electrolyte interface

Nanostructured electrodes consist partly of silicon/metal/electrolyte as well as silicon/oxide/electrolyte interfaces. In this section, we look closer at the capacitance of a silicon/oxide/electrolyte interface.

The capacitive response of the oxide covered semiconductor substrate in contact with the electrolyte is determined by two contributions: A contribution stemming from the oxide film C_{ox} , and a contribution stemming from the space charge layer present in the semiconductor C_{SC} [SBB95]. Since the Helmholtz capacitance C_{H} present at the insulator/electrolyte interface is supposed to be much larger (in the order of $20 \mu\text{F cm}^{-2}$ [HEB96]) than both other contributions, we can neglect it at this point [SBB95]. Both mentioned contributions add inversely to the total capacitive behavior of the interface C_{eff} , as they are connected in series [SBB95]:

$$\frac{1}{C_{\text{eff}}} = \frac{1}{C_{\text{ox}}} + \frac{1}{C_{\text{SC}}} \quad (7.18)$$

In the equivalent circuit used for fitting the impedance data of this system, both contributions can be combined in one CPE||R element representing the complete interfacial behavior [SBB95]. Consequently, the equivalent circuit consists of a serial resistance R_{s} connected in series to only one CPE||R element. The serial resistance accounts for the finite resistance of the semiconductor as well as the resistance of the electrolyte, while the CPE||R accounts for the semiconductor/insulator/electrolyte interface. The equivalent circuit is further shown as an inset in Figure 7.5(a). We assume that this system provides a normal distribution of time constants (serial connection of time constants, i.e. 'stack') due to its composition. The effective capacitance of the system C_{eff} can then be calculated from the fitted parameters by the Hsu and Mansfeld formula [HM01; Hir+10]:

$$C_{\text{eff}} = Q^{1/n} R_{\text{f}}^{(1-n)/n} \quad (7.19)$$

Here Q and n are the fitting parameters of the CPE and R_{f} is the determined value of the resistance located in parallel to the CPE. The fitted values of n have always been above 0.98 in the experiments conducted here for the oxide covered silicon electrodes, which indicates a very linear capacitive response of the system.

We now determine the effective capacitance of an n-doped silicon substrate (1-10 Ohm cm) covered by a thermal silicon oxide layer with 12 nm thickness in contact with an

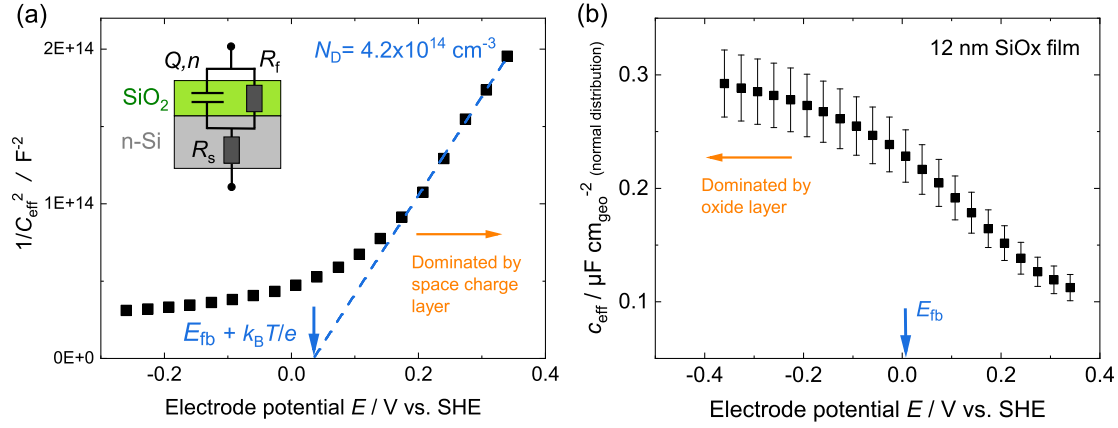


Figure 7.5: Capacitance of a silicon/oxide/electrolyte interface (thermal silicon oxide with 12 nm thickness) as a function of the applied electrode potential. (a) Mott-Schottky plot (b) Effective capacitance. Electrolyte: 0.1 M H_2SO_4 (pH 1). The equivalent circuit fitted to the raw impedance data is given as the inset. Equation (7.19) is used for calculating the effective capacitance from the fitting values of the impedance data.

electrolyte containing 0.1 M H_2SO_4 (pH 1). Figure 7.5(b) shows the determined effective specific capacitance calculated from the fittings of the impedance data via equation (7.19) plotted over the electrode potential E . Figure 7.5(a) shows the inverse of the squared effective capacitance (absolute value) plotted over the electrode potential. This plot is also known as Mott-Schottky plot.

Now let us consider the two limiting cases, at 'rather positive' and at 'rather negative' potentials. At *rather positive potentials*, the potential independent oxide contribution C_{ox} is supposed to be sufficiently larger than the contribution of the space charge layer C_{SC} , as the majority charge carriers (here electrons as we use an n-doped silicon substrate) become depleted from the interface, which results in a decrease of the capacitance. As a consequence the oxide contribution can be omitted and we obtain:

$$\frac{1}{C_{\text{eff}}} \approx \frac{1}{C_{\text{SC}}} \quad (7.20)$$

For depletion condition the inverse of the square of C_{SC} scales linearly with the electrode potential according to the Mott-Schottky equation [SBB95; Li19]:

$$\frac{1}{C_{\text{SC}}^2} = \frac{2}{\varepsilon_{\text{Si}}\varepsilon_0 A^2 e N_D} \left(E - E_{\text{fb}} - \frac{k_B T}{e} \right) \quad (7.21)$$

Here, A is the electrode area, ε_{Si} is the relative permittivity of silicon ($\varepsilon_{\text{Si}} \approx 11.9$ [Zha04b]), N_D is the donor doping density and E_{fb} is the flatband potential. Thus, a linear dependence of the inverse of the squared capacitance over the applied electrode potential would indicate a domination of the space charge layer. We find this linear dependence for potential above approx. $0.2 \text{ V}_{\text{SHE}}$, see blue dashed line in Figure 7.5(a).

To further verify that the observed linear dependence stems from the dominating contribution of the space charge layer in this potential range, we determine several properties of the silicon substrate used from the fitting by considering equation (7.21). First, we determine the doping density of the silicon substrate from the slope of the fitting according

to

$$N_D = 2 \left(\varepsilon_{\text{Si}} \varepsilon_0 A^2 e \frac{\partial(1/C_{\text{eff}}^2)}{\partial E} \right)^{-1} \quad (7.22)$$

and the flatband potential from the x -intercept E_0 of the fitting by:

$$\frac{1}{C_{\text{eff}}^2} \Big|_{E=E_0} = 0 \quad \Rightarrow \quad E_{\text{fb}} = E_0 - \frac{k_B T}{e} \quad (7.23)$$

The last term is approx. 25 mV at room temperature. We calculate the following values from the fitting:

$$N_D \approx 4.2 \cdot 10^{14} \text{ cm}^{-3} \quad (7.24)$$

$$E_{\text{fb}} = +7 \text{ mV}_{\text{SHE}} \quad (7.25)$$

The flatband potential is in good accordance with values given in the literature for H-terminated silicon/electrolyte systems, usually reported at similar potentials in this electrolyte [Li19]. The presence of the oxide layer itself between the silicon substrate and the electrolyte is not expected to alter the flatband potential significantly compared to the case without oxide layer. Considering the oxide as an ideal dielectric medium, we expect that only the scaling of the band bending with the applied electrode potential changes due to the potential drop in the dielectric medium, but no intrinsic change of the flatband potential, which is rather determined by surface states. The doping density is in good accordance with the value given by the supplier for the silicon wafers used. The resistivity is given by 1-10 Ω cm, which is tantamount to approx. $4 \cdot 10^{14} - 4 \cdot 10^{15} \text{ cm}^{-3}$ for n-doped silicon according to Sze [Sze07], p. 32. This confirms that the linear behavior observed in this system for potentials above $0.2 \text{ V}_{\text{SHE}}$ is indeed determined by the space charge layer present at the silicon/dielectric interface.

At *rather negative potentials* (referred to the flatband potential), the capacitive response of the system is likely dominated by the oxide contribution, since the capacitive contribution of the space charge layer appears to become very large due to the accumulation condition of the majority charge carriers in the space charge layer. We consider the Poisson-Boltzmann approximation of the space charge capacitance for accumulation conditions (here $E < E_{\text{fb}}$) [Li19]:

$$C_{\text{SC}} = \sqrt{\frac{e^2 \varepsilon_{\text{Si}} \varepsilon_0 N_D}{2k_B T}} \exp\left(-\frac{e(E - E_{\text{fb}})}{2k_B T}\right) \quad (7.26)$$

$(E - E_{\text{fb}})$ is the electrode potential relative to the flatband potential. From the equation it becomes evident that the space charge capacitance increases exponentially with decreasing electrode potential. Contrary, the capacitance of the oxide can be modeled by a standard parallel plate capacitor:

$$C_{\text{ox}} = \varepsilon_{\text{ox}} \varepsilon_0 \frac{A}{d} \quad (7.27)$$

Here, ε_{ox} is the relative permittivity of the oxide layer ($\varepsilon_{\text{ox}} \approx 3.9$ [Zha04b]), A is the area and d is the thickness of the oxide film. Hence, the oxide capacitance is rather potential independent. Consequently, at sufficiently negative potentials (i.e. far away from the flatband potential) the measured effective capacitance is supposed to saturate, as now the measured capacitance is dominated by the potential independent oxide contribution:

$$\frac{1}{C_{\text{eff}}} \approx \frac{1}{C_{\text{ox}}} \quad (7.28)$$

This behavior is observed in Figure 7.5(b) at potentials below $-0.2 V_{\text{SHE}}$. From the plot we determine a saturation value of approx. $c_{\text{eff}} \approx 0.3 \mu\text{F cm}_{\text{geo}}^{-2}$ at rather negative potentials. Note, that this value is very similar to the value determined in the previous section from the potential scan experiments of the same system. From equation (7.27) we can now calculate the thickness d_{ox} of the oxide film. We calculate $d_{\text{ox}} \approx 11.5 \text{ nm}$, which is very well in accordance with its nominal thickness of 12 nm determined at dry conditions. This further proves that it is possible to separate the two distinct contributions correctly.

7.2.2 Capacitive behavior of the continuous Au layer electrode

Next, we analyze the behavior of the other reference system, a continuous Au layer electrode. The equivalent circuit model applied to the impedance data of the continuous metal layer electrodes (and also applied later to nanostructured electrodes) is shown in Figure 7.6. Both interfaces, the electrolyte/metal and the metal/silicon interface, are modeled by a parallel connection of resistances R_i and constant phase elements Q_i and n_i . R_s considers the serial resistance of the system (electrolyte resistance, contact resistance, etc.).

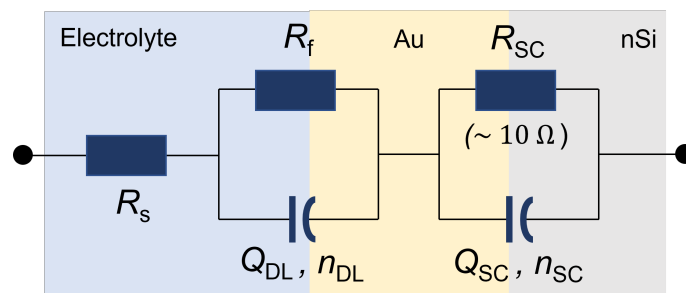


Figure 7.6: Equivalent circuit model applied to the impedance data of the continuous metal layer and nanostructured electrodes.

Here, contrary to the previous system, the impedance data at low to intermediate perturbation frequencies is rather determined by the electrolyte/metal interface, as the metal/silicon interface of the investigated electrodes has a comparatively small finite resistance (in the order of 10Ω). When working in the double layer region or at low faradaic current densities (i.e. large charge transfer resistance at the El/M interface), the current feedback of the El/M/Si stack showed to be rather determined by the capacitive behavior of the El/M interface than by the capacitance of the M/Si interface.

In our model, we fit the data to the two mentioned CPE||R elements. Thus, we can further separate any appearing contribution of the M/Si interface, although the collected data of our electrodes show that this is not necessary for most of the measurements performed. The more 'simple' model R-(CPE||R) consisting of only one CPE||R element often gives the same results for the CPE. However, especially for the nanostructured electrodes at potentials rather close to the PZC (cf. section 7.2.3), the 'extended' equivalent circuit model consisting of two CPEs turned out to be necessary to separate the two contributions and to fit the experimental behavior satisfactory. Thus, we apply the extended model to all data shown in this section. The comparison of an exemplary data set fitted to either the 'simple' or the 'extended' model is shown in the appendix A.13.

From the fitted parameters we calculate the effective capacitance of the metal/electrolyte interface of the electrodes by assuming a surface distribution of time constants (surf. dist.)

via the Brug formula [Bru+84a; Hir+10]:

$$C_{\text{eff}} = Q_{\text{DL}}^{1/n} \left(\frac{1}{R_f} + \frac{1}{R_s + R_{\text{SC}}} \right)^{(n-1)/n} \approx Q_{\text{DL}}^{1/n} (R_s + R_{\text{SC}})^{(1-n)/n} \quad (7.29)$$

We prefer this formula over the Hsu formula (7.19) for calculating the effective capacitance, as the nanostructuring of the electrode surface is likely to show a surface distribution of time constants and we further separate the normal contribution by fitting the data sets to two serial CPE||R elements. Note, that one needs to consider R_{SC} as part of the serial resistance R_s for the calculation of the effective capacitance as implicated in equation (7.29), when applying the extended model consisting of two CPE||R elements instead of one to the impedance data. The specific values of the capacitances c_{eff} are determined from C_{eff} by dividing C_{eff} by the measured gold surface area.

We first consider the specific capacitance of a continuous Au layer (Au cont.), as this is the benchmark system for the nanostructured electrodes. Figure 7.7 shows the effective capacitance of the Au cont. system as a function of the electrode potential (a) in the standard acidic electrolyte used throughout this work based on 0.1 M H_2SO_4 with pH 1, and (b) in a neutral electrolyte containing 0.18 M NaOH + 0.12 M $\text{H}_2\text{PO}_4^-/\text{HPO}_4^{2-}$ with pH 7. The data shown is averaged over measurements with three different electrodes. An analysis of the impedance data at potentials $> 0.4 \text{ V}_{\text{SHE}}$ is not performed in H_2SO_4 based electrolyte due to the adsorption of sulfate, which gives a huge contribution to the determined value of the capacitance.

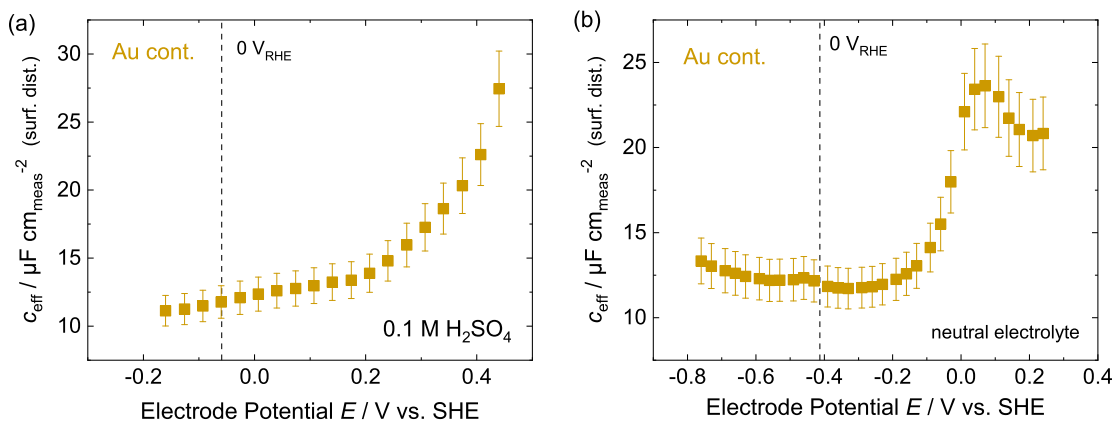


Figure 7.7: Effective capacitance of a continuous Au layer electrode (Au cont.) as a function of the electrode potential in (a) *acidic* (0.1 M H_2SO_4 , pH 1) and (b) *neutral* (0.18 M NaOH + 0.12 M $\text{H}_2\text{PO}_4^-/\text{HPO}_4^{2-}$, pH 7) electrolyte. The EIS data is fitted to the equivalent circuit shown in Figure 7.6. The effective capacitance is calculated from the fitting parameters by the Brug formula (7.29). The capacitance is normalized to the measured Au area.

In both electrolytes, the overall trend with the electrode potential observed is quite similar: Coming from positive potentials, the capacitance decreases steeply (between $0.45 \text{ V}_{\text{SHE}}$ and $0.2 \text{ V}_{\text{SHE}}$ in acidic and between $0.05 \text{ V}_{\text{SHE}}$ and $-0.2 \text{ V}_{\text{SHE}}$ in neutral electrolyte) and reaches a rather constant value of $13 \mu\text{F cm}_{\text{meas}}^{-2}$ at more negative potentials (below $0.2 \text{ V}_{\text{SHE}}$ in acidic and below $-0.2 \text{ V}_{\text{SHE}}$ in neutral electrolyte). The approach of this constant value is likely caused by the Helmholtz capacitance, which is known being the dominating contribution at potentials far away from the point-of-zero-charge (PZC).

The presence of a local minimum observed at approx. $+0.2 V_{\text{SHE}}$ in neutral electrolyte is likely due to the close presence of the PZC, which is supposed to lie between $+0.15$ and $+0.3 V_{\text{SHE}}$ for a poly-crystalline Au surface according to the literature [Vel+14; HW87; CH72]. That the presence of the PZC can lead to the appearance of a local minimum in the capacitive behavior is expected. This becomes clear when looking at theoretical predicted behavior of the double layer capacitance determined from simulations performed by others [MFL20] or by us (see next section). However, the discussion about the actual shape of the capacitance trend with the electrode potential in this potential range is given much more in detail in the next section.

Before interpreting the actual shape of the curve, we discuss, whether the determined value of the double layer capacitance of Au cont. (i.e. the Au(pc) surface as prepared) in the Helmholtz limit is similar to the value expected from literature. As already mentioned, the measured specific capacitance value in the Helmholtz limit is approx. $13 \mu\text{F cm}_{\text{meas}}^{-2}$ and is very similar in acidic (at approx. $0.10 V_{\text{SHE}}$) and in neutral (at approx. $-0.35 V_{\text{SHE}}$) electrolyte. Let us compare the data in neutral electrolyte (pH 7) containing Na^+ cations. At the same absolute electrode potential Bandarenka et al. determined a specific capacitive value of approx. $21 \mu\text{F cm}^{-2}$ in 0.05 M Na^+ containing electrolyte at pH 6 for Au(111) [Gar+18]. Although both values are in the same range, there is a difference by a factor of 0.5. It is unlikely that the difference stems from the different data treatment. The authors of the mentioned reference did not correct the fitting value, but directly considered the uncorrected CPE fitting value Q as the capacitance. Here, the 'effective' capacitance of the system is calculated from the fitted CPE values by correcting it according to equation (7.29). However, the different treatment can be excluded as a reason for the difference, as the n value of the fitted CPE was very close to 1 (at least always > 0.97) here. This results in only a very small difference between Q and C_{eff} .

The difference may be explained by a different normalization of the data, i.e. a different determination of the area, which is needed to calculate the surface specific capacitance plotted. Unfortunately, it does not become clear in the publication, which surface area the authors considered for normalizing the capacitance. As our gold surfaces exhibit a roughness factor of approx. 1.5, a normalization of our data to the geometric area would result in $\approx 20 \mu\text{F cm}_{\text{geo}}^{-2}$ at approx. $-0.35 V_{\text{SHE}}$ in neutral electrolyte in the Helmholtz limit. This value is very similar to the value obtained by Bandarenka et al. Thus, we can conclude that the capacitance values of the continuous layer electrode determined here experimentally are reliable and are representative for a typical gold electrode, when normalizing to the geometric gold area.

7.2.3 Simulation of the capacitive behavior by the modified Poisson-Boltzmann equation in 1D

The continuous metal layer electrode does not exhibit any lateral surface heterogeneity on the macroscopic level. Thus, the system can be considered as one-dimensional (1D). In order to understand the experimentally observed behavior of the capacitance with the electrode potential, it is meaningful to compare the experimental results with theoretical predicted values obtained by 1D simulations. Thus, we determine the theoretically expected capacitive behavior of the metal/electrolyte interface by performing simulations of a modified Poisson-Boltzmann (mPB) equation [BAO00; Rin+19]. In the mPB model, the physical adsorption of 'large' interfacial solvated ions is explicitly considered.

Cation	Li	Na	K	Cs
$a / \text{Å}$	11.6	10.4	8.2	7.0

Table 7.1: Diameters a of solvated interfacial cations present at the electrode/electrolyte interface at negative electrode polarization used in the mPB model. Data from [Rin+19].

The famous Poisson-Boltzmann equation in one dimension is given by [BF01]:

$$\frac{d^2}{dx^2}\phi = -\frac{F}{\varepsilon_0\varepsilon_r} \sum_i z_i c_i(\phi) \quad (7.30)$$

with ϕ being the (local) electrostatic potential, ε_r the relative permittivity of the solvent medium, z_i the charge number of species i , and c_i the (local) concentration of species i . In the mPB model the local ion concentration is given as a function of the local electrostatic potential by [Rin+19]:

$$c_i(\phi) = c_i^* \frac{\exp(-z_i f \phi)}{1 + \chi_0 (\cosh(z_i f \phi) - 1)} \quad \text{with} \quad \chi_0 = 2c_i^* a^3 N_A \quad (7.31)$$

with c_i^* being the bulk concentration of species i , $f = F/RT$, χ_0 being the ion occupied volume fraction, and a being the diameter of the solvated interfacial ions (here: cations). An overview of diameters of solvated interfacial alkali-metal cations relevant in this work is given in Table 7.1.

From the mPB model the spatial electrostatic potential distribution inside the electrolyte domain can be determined. As boundary conditions we specify the absolute electrostatic potential at the metal (surface) $\phi(x=0) = \phi_M$ and in the electrolyte bulk $\phi(x=n) = \phi_{El}$ (Dirichlet boundary conditions). The difference in these two values can also be interpreted as the difference of the actual electrode potential from the potential of zero charge ($E - E_{pzc}$). In this configuration, zero net charge is stored at the Metal/Electrolyte interface if the potential difference between electrolyte bulk and metal is zero, i.e. if the electrode is at E_{pzc} :

$$E - E_{pzc} = \phi_M - \phi_{El} \quad (7.32)$$

This relabeling makes the later comparison with experimental data easier. From the potential distribution $\phi(x)$ it is possible to calculate the local concentration of ions c_i at each position x via equation (7.31). The total net charge σ^{El} stored in the double layer can then be calculated by integrating over the whole electrolyte domain El:

$$\sigma^{El} = \int_{El} \sum_i z_i c_i(x) dx \quad (7.33)$$

As the system intrinsically fulfills charge neutrality, the counter charge σ^M present in the metal domain has the same magnitude, but is opposite in sign. The actual (differential) capacitance of the system $c'(E)$ at a certain electrode potential E can be calculated from the local derivative of the (σ^M, E) datasets:

$$c'|_E = \left. \frac{\partial \sigma^M(E')}{\partial E'} \right|_E \quad (7.34)$$

We conduct a 1D finite-difference simulation of the mentioned system by a self-written Python code. We simulate a physical x -dimension of 1 μm with a resolution of 0.05 nm.

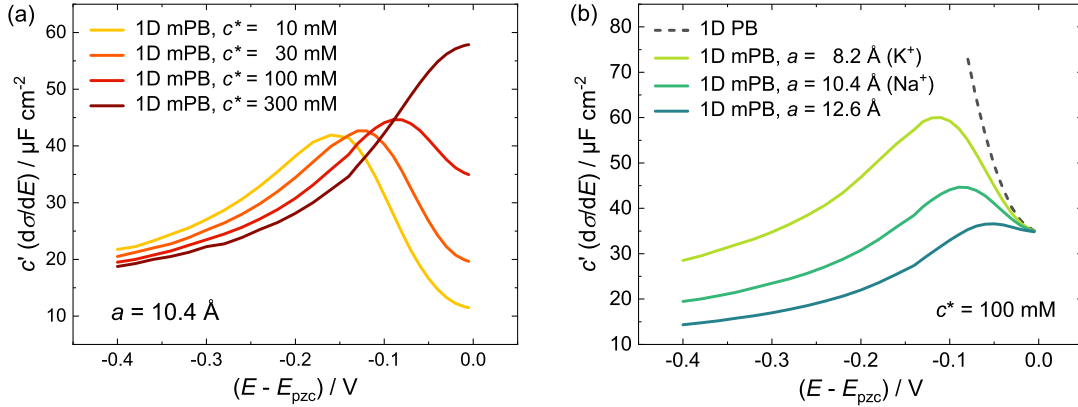


Figure 7.8: Simulated specific capacitance c' as a function of the electrode potential E relative to the potential of zero charge E_{pzc} . (a) Variation in the salt (bulk cation) concentration c^* , determined for an interfacial cation diameter of $a = 10.4 \text{ \AA}$ (Na^+). (b) Variation in the diameter of solvated interfacial cation at $c^* = 100 \text{ mM}$. The dashed line indicates the capacitance according to the standard Poisson-Boltzmann (PB) model (Gouy-Chapman theory).

This results in a total number of $n = 20.000$ elements. Moreover we assume $\varepsilon_r = 20$ [YB99] as the relative permittivity of the solvent present in the interfacial double layer. We consider this rather small value since we assume the presence of a rather strong electric field in the double layer at the evaluated potentials. According to [YB99] the interfacial water layer shows the mentioned ε_r if the electric field strength is in the order of 10^9 V m^{-1} , which is typical order of magnitude expected in the double layer [Ge+17].

Figure 7.8 shows the specific capacitance c' determined from simulation via equation (7.34) as a function of the applied electrode potential E with respect to the potential of zero charge E_{pzc} . Note that we just show negative polarization (potentials negative to the PZC), which is the relevant potential regime in this work. We show two dependencies: In Figure 7.8(a) the dependence of the capacitance on the bulk salt concentration, which is similar to the bulk concentration of the cationic species as we consider a monovalent 1:1 salt here. In Figure 7.8(b) the dependence on the diameter a of the interfacial solvated cationic species.

Let us first consider the dependence on the bulk concentration shown in Figure 7.8(a). Here, the diameter of the solvated interfacial solvated cation is set to value of 10.4 \AA , which is tantamount to Na^+ as the cation species present in the double layer. In the graph we can differentiate between two potential regimes: (1) Potentials close to the PZC. Here, the capacitance is dominated by the diffuse layer (see Gouy-Chapman (GC) model). For low to moderate salt concentration ($< 100 \text{ mM}$ in this case) we see that the behavior can be well approximated by a parabolic function known from the GC theory. For rather high salt concentrations (here visible for 300 mM) the minimum turns to a maximum, which is the expected behavior [MFL20]. (2) At potentials far away from the PZC, the capacitance is supposed to be dominated by the Helmholtz layer. Here the capacitive behavior is supposed to be almost independent of the actual bulk ion concentration, as the electrode is strongly polarized and its surface becomes highly covered by cations. This results in a constant capacitance rather independent of the actual bulk ion concentration. The maxima present between these two regimes (visible for low to intermediate bulk concentrations) is due to the transition between these two regimes.

Now let us consider Figure 7.8(b). It becomes evident that the presence of a local minimum or maximum at the PZC does not depend on the actual diameter a assumed for the interfacial cation. The GC theory assumes infinitely small ions, which can be consequently seen as the limiting case when further decreasing the cation size. This limit is plotted as the dashed line in the Figure. However, the actual value of the capacitance at the PZC is independent of the cation size, since the electrode is not polarized. Here, the capacitance is determined by the diffuse layer, which capacitance is supposed to be independent of the actual ion size present in the electrolyte. Contrary, in the Helmholtz limit we assume a different limiting capacitance when changing the cation size. A different size of the solvated cations results in a different distance of the center of charge from electrode surface in the highly polarized case. Considering the known formula of the specific capacitance of a parallel plate capacitor:

$$c' = \frac{\varepsilon_0 \varepsilon_r}{\delta} \quad (7.35)$$

Decreasing the plate distance δ (expected for smaller solvated cations) results in an increasing capacitance.

Discussion: Comparison of simulated and experimental data of the continuous Au layer

Let us now come back to the experimental data of a continuous Au layer (Au cont.) in neutral electrolyte, which was shown in Figure 7.7(b). We further consider the simulated data of the 100 mM concentration plotted in Figure 7.8(a), which is the simulated concentration being closest to the concentration used in the experiment. The comparison between the experimental data of the continuous layer and the 1D simulated system shows that both systems exhibit qualitatively the very same trend with the electrode potential. Thus, we can conclude that the experimentally investigated system can be well described (at first qualitatively) by the mPB theory and the simulations performed here. However, we note the absolute values do not match completely. The calculated theoretical capacities are systematically larger than the experimentally determined values by a factor of approx. 0.5:

Experimental at $+0.2 V_{\text{SHE}}$ (local minimum, approx. PZC):	$21 \mu\text{F cm}_{\text{meas}}^{-2}$
Theoretical at $(E - E_{\text{pzc}}) = 0 \text{ V}$:	$35 \mu\text{F cm}^{-2}$
Experimental at $-0.2 V_{\text{SHE}}$ (Helmholtz- limit):	$12 \mu\text{F cm}_{\text{meas}}^{-2}$
Theoretical at $(E - E_{\text{pzc}}) = -0.4 \text{ V}$:	$19 \mu\text{F cm}^{-2}$

Similar to the discussion given in the previous section, this systematic difference by a factor 0.5 reminds to originate from the normalization of the measured absolute capacitance to the *measured* electrode surface in the experimental case. It appears to be more meaningful to normalize the actual experimentally determined capacitance to the geometric area. This becomes very present, when plotting the simulated data and the experimentally determined data normalized to the geometric area in the same plot, cf. Figure 7.9. It becomes evident that the experimental data can be very well approximated by the simulation for potentials below -0.1 V , if normalizing the data to the geometric area. Consequently, the measured electrode area determined by adsorption experiments, may not be the right normalization for comparing capacitive data. However, in order to avoid any misinterpretations stemming from a wrong assumptions for the geometric area of nanostructured electrodes, we will keep the normalization of the capacitive data to the measured electrode area in the further course of this work, when comparing nanoelectrodes with each other or with the continuous layer electrodes.

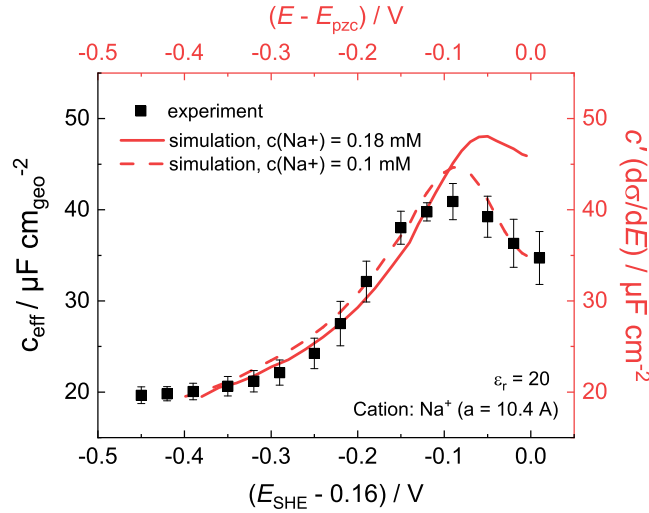


Figure 7.9: Comparison of the experimentally determined (black) and simulated (red) capacitance as a function of the electrode potential. The experimental data shown is the data of a continuous Au layer (Au cont.) and similar to the data shown in Figure 7.7(b), but normalized to the geometric gold area and shifted by 0.16 V to correct for the assumed position of the PZC. The simulation of the capacitance is conducted as described above. We consider $a = 10.4 \text{ \AA}$ (solvated interfacial Na^+ ion, see Table 7.1).

As already mentioned, Figure 7.9 shows the direct comparison between the simulated capacitance (red lines) and experimentally determined capacitance (black squares) of a continuous Au layer electrode, here normalized to the geometric gold area. Besides of normalization, the potential axis of the experimental data is shifted by -0.16 V . This is done to correct for the assumed position of the PZC in the experimental data, which is, according to the comparison, very likely at $+0.16 \text{ V}_{\text{SHE}}$. This estimated position is well in accordance with the literature reporting values between $+0.15$ and $+0.3 \text{ V}_{\text{SHE}}$ for poly-crystalline Au surface [Vel+14; HW87; CH72].

In the graph, we plot the simulated data for two different bulk cation concentrations, 100 mM (red dashed) and 180 mM (red solid). We consider Na^+ as the cationic species, as this species was used in the experiments. Let us first consider the case of 180 mM. Coming from positive potentials, the experimentally measured descending branch when approaching the Helmholtz dominated regime can be very well reproduced by the simulation. However, at potentials close to the PZC, the simulation deviates from the actual measured capacitance. In this regime the experimental data can be much better approximated by the 100 mM Na^+ simulation.

This difference may lie in the simplification made when modeling the system. First, we assume a monovalent 1:1 salt being present in the electrolyte. Since the experimental data is collected in the mentioned neutral electrolyte consisting of a significant concentration of HPO_4^{2-} ions, the interaction of this anionic species with the cationic species may lead to further deviations from the simplified model in this potential range. In addition, in the simulated model we assumed the electrolyte as a continuous dielectric medium with a constant relative permittivity of $\epsilon_r = 20$. However, this assumption may not be correct as it is known that the altered structure of water at the interface [AMV10] as well as the nature of the electrode surface itself [BGN11] can significantly influence the dielectric constant of water in the double layer. Due to the appearing chemical interaction between the electrode surface atoms and the present solvent (water) molecules at low electric

fields, which is tantamount to potentials close to the PZC, we assume deviations from the classic continuum approach made here in the simulation. The chemical interaction between the molecules is supposed to be much more dominating compared to the case when the electrode is highly polarized. In the latter case, the electrostatic interaction is supposed to dominate. However, it appears that these additional interactions could be taken into account indirectly in the simulation by assuming a lower bulk concentration of ions. Since the influence of the bulk concentration on the capacitance in the Helmholtz limit is only minor, the curve considering the smaller bulk concentration appears to reproduce the experimental data better than the actual 'correct' concentration. However, we can see that the descending branch as well as the beginning of the Helmholtz limit of the experimentally determined capacitance can be well approximated by the theoretical prediction of the mPB model using the actual 'correct' cation concentration.

7.2.4 Increased capacitance of nanostructured electrodes

In this section, we investigate the specific effective capacitance of nanostructured electrodes (here Au structure of sizes 1400 nm and 75 nm) as a function of the applied electrode potential. Furthermore, we will discuss the appearing trends as well as compare the data of the nanostructured electrodes to the data of the continuous Au layer electrode (Au cont.) as the reference system.

For fitting the impedance data of nanostructured electrodes we use the same equivalent circuit as used for the continuous layer electrodes, cf. Figure 7.6. The model consists of the serial connection of two CPE||R elements together with a serial resistance R_s . Contrary to the continuous metal layer case, the nanostructured electrodes exhibit a lateral inhomogeneity. However, the contribution of the silicon/insulator/electrolyte interface can be neglected in the model: The thickness of the insulating layer is rather thick (12 nm), which results in a very small capacitance in the order of $0.2 \mu\text{F cm}^{-2}$, cf. section 7.2.1. Since the capacitive behavior of this interface would need to be placed in parallel to the actual metal/electrolyte interface in the equivalent circuit, its value would be additive to the actual capacitance of the metal/electrolyte interface and is therefore negligible. Thus, its contribution to the total capacitance can be omitted. An additional argument for omitting the capacitive contribution of the oxide covered surface is that the fitted spectrum with the equivalent circuit used also for the continuous Au layer electrode is able to fit the experimental data of nanostructured electrodes very well, cf. appendix A.13. The effective capacitance shown in the following is calculated, similar to the continuous electrode, from the fit parameters via the Brug formula given in equation (7.29).

Figure 7.10(a) shows the specific capacitance of the electrode set in *acidic* electrolyte containing 0.1 M H_2SO_4 , pH 1. The data of Au cont. is similar to the data shown already in Figure 7.7(a). The data is averaged over three sets of electrodes. It is not differentiated between silicon oxide and silicon nitride passivation layer in this data, as both passivation layers give very similar results, cf. T. Angerer [Ang21]. Coming from positive potentials, the effective capacitance of the electrodes decreases for all electrodes investigated. The capacitance of the continuous as well as the 1400 nm electrode both saturate around $0.15 V_{\text{SHE}}$ at very similar values of ca. $13 - 14 \mu\text{F cm}_{\text{meas}}^{-2}$. Contrary, the capacitance of the 75 nm electrode does not saturate but passes a minimum around $0 V_{\text{SHE}}$ and increases again at potentials more negative. It is apparent that the capacitance of the electrodes increases in the order Au cont. < 1400 nm < 75 nm, virtually at all potentials in the

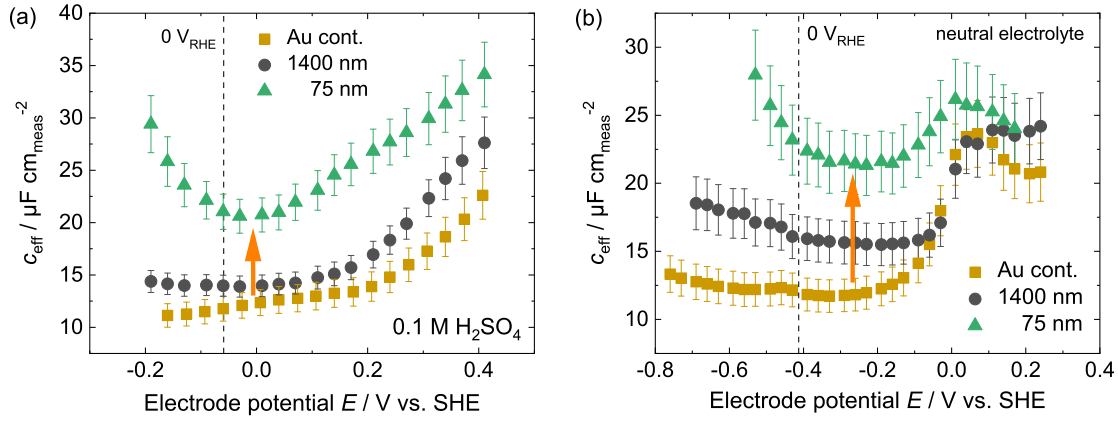


Figure 7.10: Effective capacitance of Au nanostructured electrodes with structures sizes of 1400 nm (black) and 75 nm (green) and the continuous Au layer (Au cont., yellow) plotted over the electrode potential. (a) In *acidic* electrolyte containing 0.1 M H_2SO_4 at pH 1. (b) In *neutral* electrolyte containing 0.18 M $\text{NaOH} + 0.12 \text{ M } \text{H}_2\text{PO}_4^- / \text{HPO}_4^{2-}$ at pH 7. The determined EIS data is fitted to the equivalent circuit shown in Figure 7.6. The effective capacitance plotted is calculated from the fitting parameters via the Brug formula (7.29). The data is normalized to the measured Au area.

investigated range, but explicitly considered here at 0 V_{SHE} , which is indicated by the orange arrow in Figure 7.10(a).

A similar trend is found in buffered *neutral* electrolyte. Figure 7.10(b) shows the effective capacitance of the same electrode set in 0.18 M $\text{NaOH} + 0.12 \text{ M } \text{H}_2\text{PO}_4^- / \text{HPO}_4^{2-}$, at pH 7. Starting from 0 V_{SHE} and going in the negative potential direction, the capacitances decrease and approach a rather constant value. Below 0 V_{RHE} the capacitances start to increase again. This appears for all three different electrode types, although the slope is steepest for the 75 nm electrode. Similar to the acidic electrolyte, in neutral electrolyte the capacitance of the electrodes increases in the order

$$c(\text{Au cont.}) < c(1400 \text{ nm}) < c(75 \text{ nm}),$$

which is best visible at the potential of the minima, at approx. $-0.25 \text{ V}_{\text{SHE}}$, indicated by the orange arrow in Figure 7.10(b). Here the capacitances have the following absolute values: $c(\text{Au cont.}) = 12 \mu\text{F cm}_{\text{meas}}^{-2}$, $c(1400 \text{ nm}) = 16 \mu\text{F cm}_{\text{meas}}^{-2}$, $c(75 \text{ nm}) = 22 \mu\text{F cm}_{\text{meas}}^{-2}$. Thus, the capacitance of the electrode with smallest structures exhibits almost double the value of the continuous Au layer. A detailed discussion of the observed capacitive trend in this potential range follows below. At potentials above 0 V_{SHE} , the capacitance decreases (Au cont., 75 nm) or stays constant (1400 nm). It appears that the capacitance of all electrodes in this potential range becomes similar due to the close presence to the point of zero charge, which appears to be at a rather similar potential for all three electrodes investigated.

A detailed analysis of the capacitance as a function of the cationic species present in the electrolyte is not given at this point. There appears to be a slight dependence of the capacitive behavior of the systems on the cationic species present. A detailed analysis can be found in the Masters Thesis of T. Angerer [Ang21]. However, the trend shown here for Na^+ as an example is similarly present for all alkali metal cations investigated in the mentioned work.

Discussion: Increased capacitance at the metal/insulator interface

We already verified in the previous section that we can reproduce the experimentally observed behavior of the benchmark system (Au cont.) in the intermediate potential range by the 1D mPB model. In the intermediate potential range we observe the transition between the diffusive (close to the PZC) and the Helmholtz dominating regime of the double layer capacitance. We will now discuss the capacitive behavior of the nanostructured electrodes on this basis.

Let us recap the four main qualitative observations when comparing the capacitive data of the nanostructured electrodes and the continuous layer electrode shown in Figure 7.10:

- (1) The behavior around the assumed PZC at approx. $0.2 V_{\text{SHE}}$ in neutral electrolyte is quite similar for all electrodes within their error.
- (2) The descending branch when approaching the Helmholtz regime shifts towards more negative potentials for smaller structure sizes. This is visible in the data determined in acidic and in neutral electrolyte, i.e. Figure 7.10(a) and (b), respectively.
- (3) In the Helmholtz dominated regime, the absolute value of the specific capacitance increases with decreasing structure size. This is, again, visible in acidic and in neutral electrolyte at approx. $0 V_{\text{SHE}}$ and $-0.25 V_{\text{SHE}}$, respectively.
- (4) At potentials below $0 V_{\text{RHE}}$, the capacitance increases with decreasing potential for nanostructured electrodes. The absolute increase is larger for smaller structures (here 75 nm). This is, again, visible in both electrolytes below approx. $-0.3 V_{\text{SHE}}$ in neutral and below approx. $0 V_{\text{SHE}}$ in acidic electrolyte.

Let us start with observation (1): Since the behavior in the range above $\approx 0.1 V_{\text{SHE}}$ is rather similar for all electrodes considered here, it is likely that the PZC is rather at the same potential for all electrodes investigated. Thus, we may conclude that the nanostructuring itself does not lead to a significant change of the position of the PZC.

We continue with observations (2) and (3): The change of the behavior, i.e. a shift of the descending branch towards negative potentials *and* an increased capacitance in the Helmholtz limit, with decreasing structure size shows the same trend as when decreasing the ion size a of the solvated interfacial cation in the 1D mPB simulation, cf. Figure 7.8(b). It appears to be plausible that this behavior is indeed caused by the geometric properties of the nanostructured interface. As we could show in the previous section, the nanostructuring may lead to an inhomogeneous charge distribution in the double layer. As a consequence, the double layer present at the Au/SiO_x border may exhibit an altered electric field compared to the bulk part of the electrode, which would be only caused by the geometry. By performing 3D mPB simulations of the mentioned system, L. Böhrend et al. [Böh23] could show that the observed altered behavior of the capacitance with the electrode potential for nanostructured electrodes can, indeed, be explained considering only the changing geometry.

Let us finally consider observation (4): According to Goyal et al. [GK21a], the capacitance of the gold surface below $0 V_{\text{RHE}}$ is determined rather by adsorption effects on the surface than by the double layer properties. If we consider adsorption, we can apply the Frumkin-Melik-Gaikazyan model [KP02; HL21] and model adsorption effects by an additional capacitive contribution, which is placed in parallel to the double layer constant phase element, i.e. the double layer capacitance C_{DL} in the simple form, in the equivalent circuit.

Note that the term 'adsorption' is kept rather unspecific by intention, as it can consist of quasi-specific adsorption of cations as well as of specific adsorption of reaction intermediates, here explicitly H_{ad} , exhibiting a different potential dependence. Consequently, both terms, the double layer C_{DL} as well as the adsorption capacitance C_{ad} represent changes in the ion adsorption behavior at the interface [GK21a]. In the Frumkin-Meli-Gaikazyan model, this adsorption pseudo-capacitance is additive to the double layer capacitance in the asymptotic limit [HL21]: $C(\omega \rightarrow 0) = C_{DL} + C_{ad}$ and $C(\omega \rightarrow \infty) = C_{DL}$. Although usually $C_{DL} \ll C_{ad}$, we may see partly a superposition of C_{ad} in the data at intermediate frequencies, at which we perform the fitting of the impedance data. Consequently, the increase of the total capacitance observed for smaller structures at potentials below $0 V_{RHE}$ may be caused by a larger adsorption capacitance C_{ad} seen for smaller structures. In this special case, we see that the capacitance increase of the nanostructured electrodes appears to start below $0 V_{RHE}$, in both electrolytes investigated. This suggests the assumption, that we probe the adsorption of protons rather than the quasi-specific adsorption of cations.

A profound statement about the mechanism causing the increased adsorption capacitance for smaller structures is not possible on the basis of the performed experiments. According to the explicit formulation of C_{ad} given by Huang et al. [HL21], an altered adsorption capacitance may stem, among others, from a changed density of adsorption sites, a changed density of ions (cations) in the solution, or from an increased density of adsorbates at a given potential. The later explanation would be contrary to the result obtained in section 5.1.2, in which we could conclude that there is a similar adsorption isotherm for all nanostructured electrodes, independent of the actual structure size.

7.3 Summary

In this chapter, we analyzed the capacitive behavior of Au nanostructured electrodes in acidic and neutral electrolyte. We determined the capacitance via cyclic voltammetry and electrochemical impedance spectroscopy.

We showed that the nanostructuring of electrodes systematically increases their capacitance. The increasing capacitance with decreasing Au structure size was visible in cyclic voltammetric as well as in impedance spectroscopic experiments. We could further exclude that this effect stems from the silicon/metal interface, and we could assign the increased capacitance to be caused by a phenomenon present at the electrode/electrolyte interface, i.e. an altered double layer capacitance.

We could show that the capacitance of nanostructured electrodes determined from cyclic voltammetry increases linearly with the inverse of the size d of the metal structures. The value of the specific capacitance measured for the smallest Au structures investigated (75 nm) is approx. 50% larger than the value of the largest structures investigated (1400 nm). From the linear $1/d$ dependence of the capacitance we concluded that the metal/insulator (Au/SiOx) interface exhibits an increased capacitance compared to the Au bulk surface, which likely is an intrinsic effect due to the varied geometry caused by nanostructuring.

The same qualitative trend could be verified by impedance measurements. 1D simulations of the charge distribution in the electrolyte via the modified Poisson-Boltzmann equation helped in understanding the capacitive trend with the electrode potential in the double layer regime, i.e. in the diffusive as well as the Helmholtz dominated potential regime. The capacitive trend with the potential observed for small structures can be reproduced in the 1D model by reducing the size of the interfacial cations present at the interface. Thus, we concluded that the border of the structures, i.e. the metal/insulator interface, exhibits an increased ion density, or an increased electric field in the double layer. This electrostatic effect is likely caused only by the changing geometry of the electrode surface due to the nanostructuring.

Furthermore, we could observe an increasing capacitance in the HER dominated potential regime for smaller structures. The mechanism causing this increasing capacitance below $0 V_{\text{RHE}}$ present in acidic as well as neutral solution could not be revealed on the basis of the experiments performed in this work and needs to be part of a future study.

Chapter 8

Bifunctional mechanism at the metal/insulator interface

Based on the results and conclusions made in the previous chapters, we will now propose a bifunctional mechanism, which is assumed to be responsible for the enhanced HER kinetics observed at the metal/insulator interface, with metal being either Au, Cu, Pt, and insulator being either silicon oxide or silicon nitride. We will first present the mechanism and later argue that this mechanism is in accordance with all observations made within the scope of this work.

8.1 Bifunctional mechanism

Volmer step at continuous layer electrodes

Let us first consider the HER mechanism for the non-structured, i.e. continuous, gold/electrolyte interface. In alkaline medium the RDS of HER on Au is found to be the Volmer step:



The label (bulk) means that the OH^- species needs to be present in the bulk of the electrolyte solution. For standard metal electrodes, i.e. electrodes with a continuous surface, we can consequently split the Volmer step in two contributions:



A scheme of these reaction processes can be found in Figure 8.1.

The dependence of this reaction mechanism on various systems parameters is rather complex to understand. According to the literature, a high polarization of the electrode is beneficial for the proton adsorption/water dissociation step, as the presence of a high concentration of cations in front of the surface either (i) enhances the local electric field in the double layer and consequently lowers the necessary energy for water dissociation [Sub+11], or (ii) stabilizes the transition state of water dissociation [GK21a], or (iii) lowers locally the hydrogen-gold adsorption Free Energy, which favors the rate of HER [Xue+18]. However, according to Ledezma-Yanez et al. [Led+17], a high polarization of the electrode surface

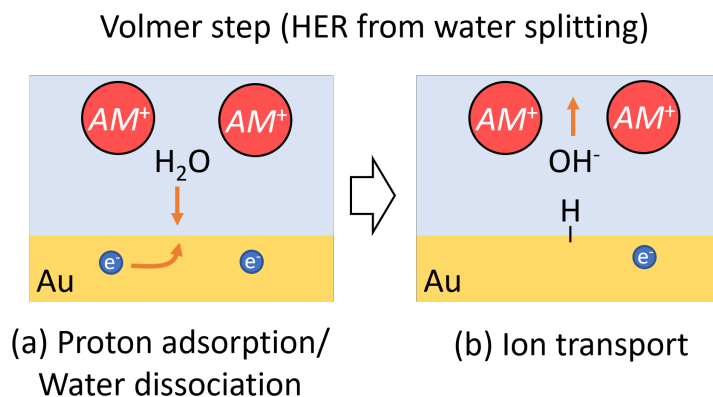
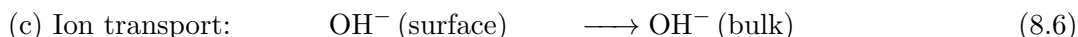


Figure 8.1: Scheme of the processes occurring during the Volmer step during HER from water reduction (in neutral or alkaline electrolyte) at a standard metal/electrolyte interface. The adsorption of protons on the metal (here Au) surface necessitate water dissociation (a), followed by a transport of the produced ionic species through the electrochemical double layer (b).

lowers the rate of the second step (charge transport). The produced OH^- ion needs to be transported from the surface through the double layer into the bulk of the solution. The energy necessary for reorganizing locally the double layer structure, which is needed to maintain the charge transport, increases with increasing cation concentration. Thus, with increasing polarization of the electrode surface, the rate of the second step decreases. Consequently, there proceed two counteracting mechanisms, which may lead to the rather complex dependence of the HER kinetics on various system parameters presented in the literature.

Bifunctional mechanism at nanostructured electrodes

We propose the following HER reaction mechanism (exemplary for the Volmer step) to be present at the metal/insulator (here the Au/SiOx) interface in neutral to alkaline media:



A scheme of the proposed bifunctional mechanism is shown in Figure 8.2. Compared to the 'standard' mechanism (i.e. as present on homogeneous metal surfaces or the bulk part of the structures), the bifunctionality of this proposed mechanism present at the metal/insulator interface yields several advantages for the HER:

1. The insulator/electrolyte interface works locally as a proton source for the proton adsorption step. As the supply of protons is maintained by the interface adjacent to the metal surface ('hydrogen spillover'), there is no need for the dissociation of water molecules in the double layer above the metal surface. As a consequence, the adsorption process of protons may be decoupled to a large extent from the properties of the double layer at the metal/electrolyte interface, such as the electric field present or the concentration of cations.
2. There is no particle (ion) transport necessary across the double layer at the metal/electrolyte interface. Consequently, the ion transport towards the electrolyte bulk

does not necessitate a reorganization of the double layer structure, which is energetically favorable.

The second consequence becomes evident when combining the later two reactions (b) and (c):



This reaction is identical to the dissociation step of the silicon hydroxide species occurring in neutral to alkaline media (see section 2.1.3). As this reaction is supposed to be in equilibrium considering the macroscopic insulator surface, we can consider the forward reaction (water dissociation and ion transport) to be comparatively fast. In addition, the forward reaction rate of reaction (8.7) is supposed to be nearly independent of the polarization of the electrode, as there is almost no additional charging of the dielectric/electrolyte interface when changing the electrode potential/polarization. Most of the further applied overpotential drops across the insulating layer below the dielectric/electrolyte interface [MH19]. Thus, there is no significant further polarization of this interface and, consequently, there is no dependence of the forward reaction rate on the electrode polarization.

Bifunctional Volmer step (HER from water splitting)

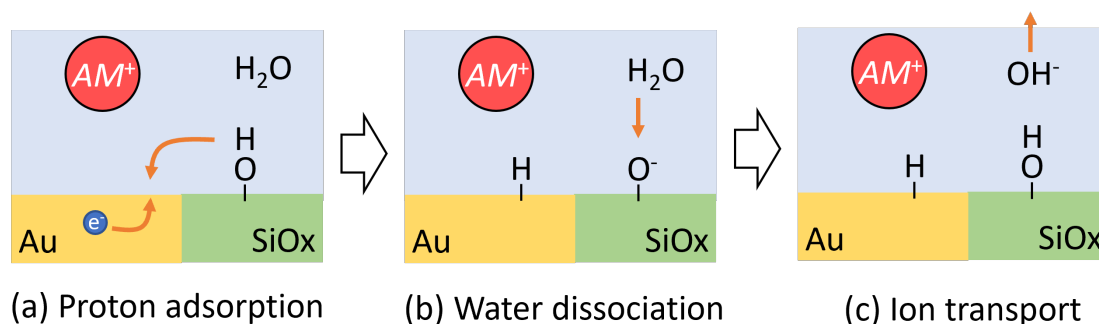


Figure 8.2: Scheme of the proposed bifunctional mechanism, which leads to the increased HER rate at the metal/insulator (here Au/SiOx) interface in neutral to alkaline electrolyte. The local decoupling of the proton adsorption step (a) and the water dissociation/the ion transport step (b)/(c) increases the overall HER rate on nanostructured electrodes.

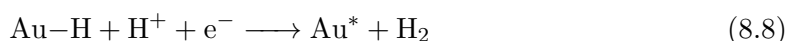
8.2 Discussion of the experimental results on the basis of the proposed bifunctional mechanism

We will now explain and discuss the main observations made in this thesis on the basis of the proposed mechanism. We will see that all obtained results are in accordance with the proposed mechanism.

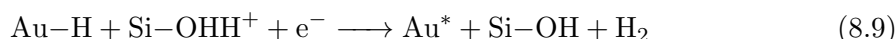
8.2.1 Smaller HER enhancement in acidic medium

In acidic medium, we have seen that the enhancement of the HER rate with decreasing structure size is not as large as observed for alkaline medium or neutral medium (see section 5.1). This is likely to be caused by a different reaction mechanism, as in acidic

electrolyte HER occurs via the reduction of protons and not via the reduction of water. We could show that there is no significant or systematic change in the adsorption energetics of protons, i.e. we did not observe a change of the adsorption isotherm (see Tafel analysis in acidic medium) with decreasing structure size. Thus, the observed (comparatively small) increase of HER activity with decreasing structure size in acidic medium is supposed to be of kinetic nature. The RDS present at relatively large overpotentials, at which we performed the Tafel analysis, cf. section 5.1.2, was determined being the Heyrovsky step:



The insulator/electrolyte interface in close contact with the metal/electrolyte interface may work as an additional proton source, as the insulator surface is partly covered by Si-OHH^+ species at this low pH (cf. section 2.1.3). Consequently, the rate of the Heyrovsky step can be increased by the occurrence of the bifunctional mechanism, as this step also involves a proton transfer:



A scheme of this additional reaction pathway according to the proposed bifunctional mechanism is shown in Figure 8.3. However, the negative polarization of the electrode, which is necessary for conducting HER, also leads to an accumulation of protons in the double layer in front of the metal surface, as protons are the dominating positive ionic species present in the electrolyte. Thus, the Heyrovsky step can occur either via the solvated protons in the double layer, or/and via the protons stemming from the dielectric/electrolyte interface. Consequently, the presence of the metal/insulator interface just increases the local concentration of protons, which may increase the forward reaction rate, but does not change the reaction mechanism at the edges compared to the metal bulk surface. As a consequence, we would see a slightly increased rate at the edges, but not a huge increase in the kinetics, as expected in neutral or alkaline electrolyte, where the mechanism is changed.

Bifunctional Heyrovsky step (HER from proton adsorption)

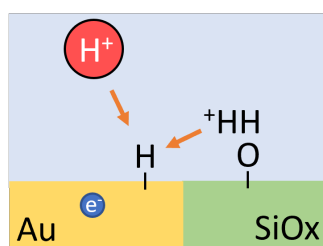


Figure 8.3: Scheme of the proposed bifunctional mechanism in the Heyrovsky step of HER at the Au/SiOx interface in acidic electrolyte. The close proximity of the insulator/electrolyte surface to the metal surface increases the local concentration of protons (reactants) and, consequently, the rate of the Heyrovsky RDS.

8.2.2 Dependence on the electrocatalytic active surface material and structure

We have seen that the enhanced HER kinetics in neutral or alkaline media is not just present for Au based nanostructured electrodes, but is also evident for metal nanostructures based on Cu (here investigated in neutral electrolyte) and Pt (here investigated in

alkaline electrolyte). In addition, we have shown that the enhancement is independent of the nature of the catalyst surface, i.e. the dominating adsorption sites present, cf. section 6.1.

It is evident that the bifunctional mechanism as proposed is independent of the actual catalyst material, and of the nature of catalyst surface. The bifunctional mechanism presented here decouples the 'metal catalyzed mechanism' of the rate determining step (i.e. the proton adsorption for a Volmer RDS, or the hydrogen desorption for the Heyrovsky RDS) from additional necessary atomistic processes of the step, which are supposed to depend particularly on the double layer properties, such as the water dissociation and/or the charge transport towards the electrolyte bulk. As a consequence, the catalytic properties of the metal, i.e. the hydrogen adsorption energy, is expected to become the only descriptor of heterogeneous, bifunctional surfaces. Thus, the appearance of a bifunctional mechanism should increase the HER rate on all electrocatalytic surfaces or materials.

To make this point clearer, let us reconsider the alkaline HER on Pt based nanostructured electrodes. It is known from the literature for alkaline HER on Pt that the rate determining Heyrovsky step is influenced by the double layer properties. In other words, the HER reaction rate is influenced by the presence, the species and the concentration of cations in the double layer [Led+17; Che+17; WJO19; Liu+19]. As the reaction rate of the 'classic' reaction mechanism on homogeneous metal surfaces is likely to be lowered by a contribution stemming from the properties of the double layer (water dissociation or charge transport), the presence of metal/insulator interfaces is supposed to enhance alkaline HER on Pt-based electrodes. This is seen in the data, cf. Figure 6.7.

8.2.3 Dependence on the nature of cations, concentration and pH

We have seen in section 6.3 that the HER enhancement on nanostructured electrodes

1. is largest for the lowest (bulk) concentration of cations,
2. is slightly larger at pH 7 than at pH 13 (in RHE scale),
3. is dependent on the cationic species present in the electrolyte.

By altering the cationic species in the electrolyte, we observed that a huge enhancement is present for all cation identities investigated. In addition, we observed that the quantitative activity enhancement is dependent on the cation species. Remember, we expressed the enhancement quantitatively by the scaling factor of the exchange current densities F_{AM} (see section 6.3.3) in order to exclude the intrinsic influence of the cationic species on the HER reactivity. The scaling factor increases in the following order:

$$F_{Cs} < F_K \approx F_{Na} < F_{Li}$$

It is striking that the enhancement increases systematically from Cs to Li, i.e. from the cation with the lowest degree of solvation to the cation with the highest degree of solvation.

It appears to be plausible that all of those effects have the same origin: According to Goyal et al. [GK21a] the actual cation concentration in front of the electrode surface is a crucial parameter in HER electrocatalysis. The concentration of cations present at the electrode surface can be tuned by:

1. Changing the bulk concentration of cations: Assuming the same PZC, the resulting (surface) concentration of cations at a given potential is then supposed to be larger for higher concentrations (cf. Gouy-Chapman theory).
2. Lowering the electrolyte pH: As the PZC is nearly constant in SHE scale, the electrode is polarized more strongly in alkaline medium compared to neutral medium at the same potential in RHE scale. Thus, the surface concentration of cations is supposed to be higher in alkaline compared to neutral medium at the same potential in RHE scale.
3. Changing the cation identity: If the cationic species has a low degree of solvation, its effective concentration at a given distance from the electrode surface appears to be higher compared to a cation with a higher degree of solvation.

Consequently, the HER enhancement on nanostructured electrodes always increases, when decreasing the local concentration of cations present at the surface. This behavior is in accordance with the proposed bifunctional mechanism. The bifunctional mechanism decouples the proton adsorption, and the water dissociation/the transport of charged ions (OH^- ions in alkaline or HPO_4^{2-} ions in phosphate buffered neutral electrolyte) towards the electrolyte bulk. Considering a sufficiently low electrode potential in RHE scale, i.e. an adequate driving force for proton adsorption at a given surface site, the rate of the Volmer step may be determined by the rate of the ion transport through the double layer above the dielectric/electrolyte interface. As this charge transport through the double layer necessitates the local reorganization of the double layer present at this interface, its rate is increased for a lower effective surface concentration of cations present.

This mechanism further explains, why the activity increase scales differently for the three mentioned variations of the local cation concentration: Let us first consider the comparatively small difference in activity of nanostructured electrodes when comparing pH 7 and pH 13 electrolyte (cf. Figure 6.18, green curves). As already mentioned above, most of the overpotential applied at silicon/insulator/electrolyte interface drops across the insulator layer. Thus, the polarization of the double layer above the insulator is supposed to depend only weakly on the applied electrode potential, which is contrary to the metal part. Here, most of the applied overpotential drops across the electrochemical double layer. Consequently, the rate determining system parameter of HER on nanostructured interfaces becomes the actual driving force of proton adsorption, i.e. potential in RHE scale, which is, indeed, observed in the data of the nanostructured electrode.

Next, we consider the bulk cation concentration: Independent of the actual electrode potential, the surface of the insulator is negatively charged due to chemical dissociation of the hydroxide species in neutral and alkaline medium, cf. section 2.1.3. The negative surface charges interact electrostatically with the positively charged cations present in solution. This electrostatic interaction leads to an accumulation of cations at the insulator/electrolyte interface. As the electrostatic interaction is the dominating contribution, the effective concentration of cations above this interface appears to be only weakly dependent on the actual bulk concentration.

The largest influence on the activity of nanostructured electrodes is supposed to be observed, when varying the cation identity. Due to the above mentioned electrostatic interaction, changing the cationic species will change the effective concentration of cations present at the insulator/electrolyte surface significantly if the cations differ in their degree of solvation (i.e. in their distance from the electrode surface). This alters the effective

cation concentration in front of the insulator surface significantly, independent of the applied electrode potential, and, thus, varies the charge transport rate in the Volmer RDS. Consequently, we expect the largest 'tunability' of alkaline HER activity on nanostructured electrodes by altering the cation identity, which is, indeed, observed.

8.2.4 Higher capacitance as the reason for enhanced HER rate?

In the previous chapter 7, we have seen that nanostructured electrodes exhibit a higher capacitance, which is likely intrinsically present due to the geometry of the system. Since the local capacitance at the borders of the structures is supposed to be higher compared to the bulk metal part, we will achieve a lateral inhomogeneous concentration of cations at the metal/electrolyte interface for a given electrode potential. More precisely, the effective concentration of cations at the borders of the structures is supposed to be higher compared to the effective concentration of cations at the bulk part of the metal structures.

As already described above, a higher local effective concentration of cations can be beneficial for HER from water splitting [GK21a]. Thus, this circumstance may work as an alternative explanation for the enhanced HER activity present at the borders of the structures. However, if a higher concentration of cations may be beneficial for HER in this system, a further increase of the effective cation concentration would further improve the HER activity. Consequently, we would see an increased HER activity on nanostructured electrodes, if (1) increasing the (bulk) concentration of cations, (2) increasing the electrolyte pH, or (3) changing the cation identity from Li^+ to Cs^+ . As explained above we see the opposite trend for all of the experiments listed here. Consequently, we can exclude that the increased capacitance measured for nanostructured electrodes is responsible for the increased HER rate observed for nanostructured electrodes.

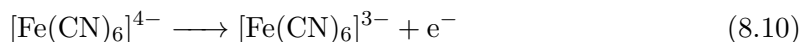
8.3 Implications of the proposed mechanism

8.3.1 No enhancement of other electrocatalytic reactions?

The bifunctional mechanism as presented in the previous sections is selective for a reaction which involves proton transfer. One implication of this hypothetical bifunctional mechanism is that any other reaction, which does not involve proton transfer, should not be influenced by this selective mechanism.

Indeed, we did already observe this conjuncture in chapter 4. We analyzed the competition between HER and CO_2 reduction reaction to CO as the product on nanostructured electrodes. We could observe that HER is selectively enhanced for smaller structure sizes, which hints for a favoring of HER compared to CO₂RR. This further strengthens the hypothesis that the mechanism present at the border enhances HER selectively.

To further prove this hypothesis, we will now analyze an exemplary outer-sphere reaction on nanostructured electrodes. Outer-sphere reactions only involve an electron transfer and do not necessitate adsorption. According to the hypothesis, outer-sphere reactions should not be influenced by this bifunctional mechanism. As a reference outer-sphere reaction we choose the oxidation of hexacyanoferrate(II) (ferrocyanide) to hexacyanidoferrate(III) (ferricyanide):



The redox couple of ferro- and ferricyanide is a standard reversible redox couple in electrochemistry. As a salt present in the electrolyte we choose potassium ferrocyanide ($\text{K}_4\text{Fe}(\text{CN})_6$). The supporting electrolyte we use is a dilute neutral buffer solution based on KOH salt and phosphoric acid, which we already used in the previous chapters. We chose this supporting electrolyte in order to maintain a defined and stable pH, which is set to pH 7, at low salt concentration. Thus, the final electrolyte we use consists of the following ionic concentrations: 10 mM $\text{Fe}(\text{CN})_6^{4-}$ + 50 mM K^+ + 6.6 mM $\text{H}_2\text{PO}_4^-/\text{HPO}_4^{2-}$.

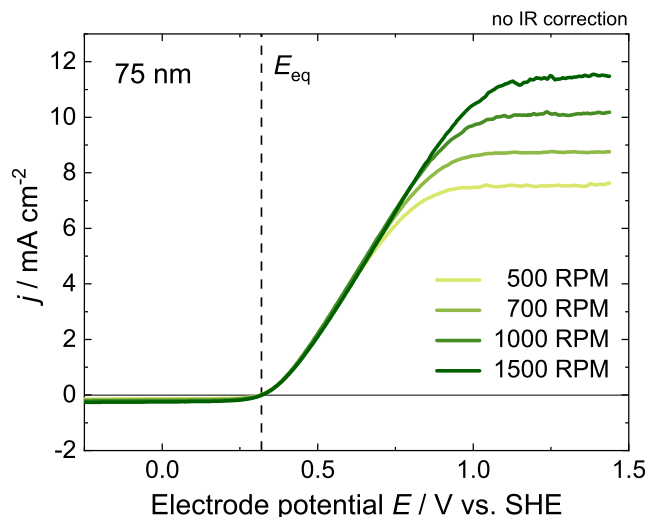


Figure 8.4: Oxidation reaction of $[\text{Fe}(\text{CN})_6]^{4-}$ on a nanostructured electrode with 75 nm sized Au structures conducted at various rotation speeds. The electrolyte is composed of 10 mM $\text{Fe}(\text{CN})_6^{4-}$, 50 mM K^+ , 6.6 mM $\text{H}_2\text{PO}_4^-/\text{HPO}_4^{2-}$ (pH 7). The measurements are conducted in the ReRDE setup at 25 °C. The data is not IR corrected. Scan speed: 50 mV s^{-1} .

Figure 8.4 shows LSV curves of an exemplary nanostructured electrode (Au structures with 75 nm structure size) in the mentioned electrolyte in the relevant potential range at various rotation speeds. The LSV curves are obtained in the ReRDE setup at a set temperature of 25.0 °C and the potential scan goes in positive direction. The anodic current present above 0.32 V_{SHE} is due to the oxidation of ferrocyanide, which appears to become transport limited above approx. 1.0 V_{SHE} . In addition, we observe a small transport-limited cathodic current at potentials below 0.32 V_{SHE} . This cathodic current likely comes from the reverse reaction, i.e. the reduction of ferricyanide. Although we did not explicitly insert ferricyanide salt into the solution, we expect it to be present in minor concentration due to the decomposition of ferrocyanide, when the solution is exposed to light [AD72]. The experiments were not conducted under dark condition. However, its concentration appeared to be stable during the measurement routine and, thus, its presence gives a negligible contribution to the kinetic analysis of the anodic current. In fact, the presence of ferricyanide brings the advantage that we observe a defined equilibrium potential E_{eq} of the redox couple, which can be seen as the OCP of the system (i.e. the zero crossing of the curves with the potential axis, see dashed line in the graph). We determined the equilibrium potential to be 0.32 V_{SHE} for all measurements conducted.

As already mentioned above, the reaction becomes mass transport dominated at rather low overpotentials. Thus, we calculate the kinetic current density from the measured current

via the Koutecký-Levich equation [BF01]:

$$\frac{1}{j_{\text{kin}}} = \frac{1}{j_{\text{meas}}} - \frac{1}{j_{\text{lim}}(\omega)} \quad (8.11)$$

Here j_{kin} is the desired kinetic current density, j_{meas} is the measured current density (including IR drop correction) and j_{lim} is the limiting current density due to the finite rotation speed ω . It is evident that the calculated value of the kinetic current density is just meaningful for current densities which are well below the actual limiting current density.

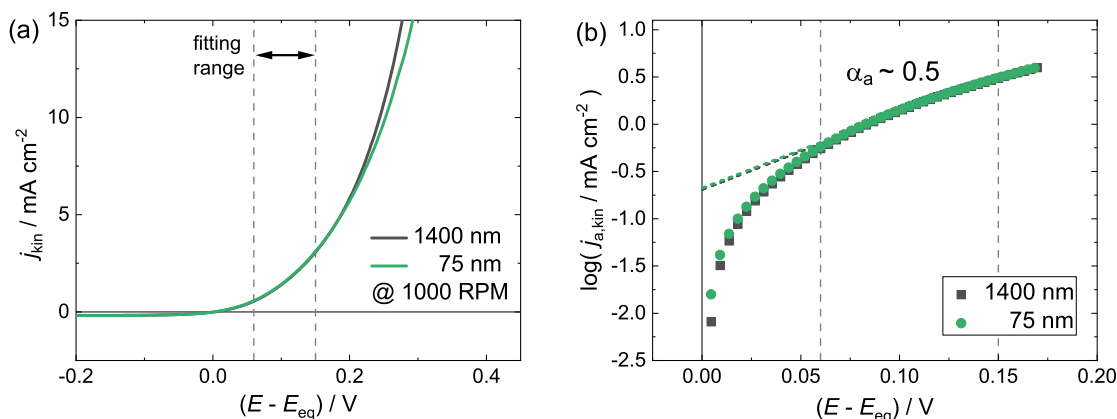


Figure 8.5: Oxidation reaction of $[\text{Fe}(\text{CN})_6]^{4-}$ on a nanostructured electrode with either 1400 nm (black) or 75 nm (green) sized Au structures. (a) Kinetic current density j_{kin} calculated from equation (8.11). (b) Tafel plot of the anodic current density. The electrolyte is composed of 10 mM $\text{Fe}(\text{CN})_6^{4-}$, 50 mM K^+ , 6.6 mM $\text{H}_2\text{PO}_4^-/\text{HPO}_4^{2-}$ (pH 7). Both electrodes show a very similar kinetic behavior of the reaction.

Figure 8.5(a) shows the determined kinetic current density as a function of overpotential ($E - E_{\text{eq}}$) of the oxidation of ferrocyanide on two different electrodes: a nanostructured electrode with 1400 nm Au structure size (black), and a nanostructured electrode with 75 nm Au structure size (green). The response of the latter is supposed to be more determined by the metal/insulator interface, as presented in the previous chapters. It is seen in the graph, that both curves lie approx. on top of each other. Thus, the kinetics of the reaction appears to be similar on both systems. To further analyze this, we conduct a Tafel analysis in the range of intermediate overpotentials, i.e. between 0.06 V and 0.15 V. We chose this range, as for too low overpotentials, there is a contribution stemming from the reduction reaction, and at rather high overpotential we get a contribution from the transport domination of the current. Both effects would limit the kinetic interpretation of the current. Figure 8.5(b) shows the Tafel plot of the two reactions. The fitting parameters of the Tafel analysis are given in Table 8.1.

It becomes evident that both electrodes exhibit very similar values. The anodic transfer coefficient appears to be $\alpha_a \approx 0.5$ at 25 °C. This value is very similar to the value expected from the literature [AD72]. In addition, the calculated exchange current densities are very similar for both electrodes and have values around 0.2 mA cm^{-2} . This determined exchange current density is one order of magnitude lower than we would expect from the literature, in which an exchange current density in the range of $2\text{-}10 \text{ mA cm}^{-2}$ [AD72] is determined. However, a comparison with this source may not be meaningful, as the

Structure size d	Tafel slope [mV dec ⁻¹]	α_a (25 °C)	j_0 [mA cm ⁻²]
1400 nm	124	0.48	0.20
75 nm	123	0.49	0.21

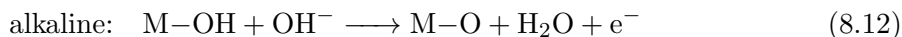
Table 8.1: Tafel fit parameters of the kinetics of the ferrocyanide oxidation on nanostructured electrodes for two various structure sizes. Both electrodes exhibit very similar kinetic parameters.

authors used a different composition of the electrolyte in order to investigate the kinetics. The kinetics of the reaction is likely to be strongly dependent on the composition of the electrolyte. For example, Bockris et al. showed that the kinetics of the $\text{Fe}^{2+}/\text{Fe}^{3+}$ redox couple strongly depends on the composition of the electrolyte. Using Cl^- instead of SO_4^{2-} as the anionic species can alter the kinetics of the reaction by more than one order of magnitude [BMD68]. A similar effect could be observed from Angell et al. for the same reaction as investigated here [AD72].

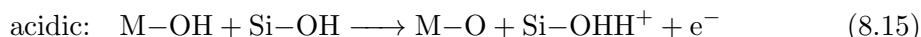
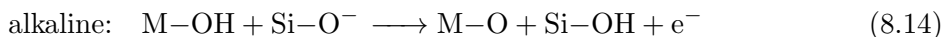
However, it becomes evident that the speed of the reaction appears to be very similar on both kinds of electrodes compared here, i.e. the speed of the reaction appears to be independent of the actual structure size. This further shows that the catalytic activities of other reactions on nanostructured electrodes are not necessarily influenced by the structure size, here explicitly shown for an outer-sphere electron reaction. This further strengthens the hypothesis that the proposed bifunctional mechanism, which we assume to be responsible for the observed HER enhancement on nanostructured electrodes, is really reaction selective. It further implies that there is no effect stemming from altering the double-layer properties (e.g. the local electric field), as this circumstance would also influence the speed of this outer-sphere reaction.

8.3.2 Enhancement of OER?

Although we just analyzed the HER within the scope of this work, the proposed bifunctional mechanism appears to have an intrinsic symmetry, which may help in catalyzing other reactions beside HER. For HER the insulator/electrolyte interface may work as a proton source, which gives a continuous and fast supply of protons. However, the insulator/electrolyte interface may also work as a proton sink. Let us consider the Oxygen Evolution Reaction (OER). The OER is a four-electron-transfer process, which makes the reaction rather complex. However, each reaction step involves the need for a proton sink, in order to continuously remove protons to form finally the oxygen molecule. Let us consider the second step of the OER in alkaline and acidic medium as an example. This step is given by:



If there is a dielectric/electrolyte interface adjacent to the metal adsorption site M, these proceeding steps may be complemented by an additional 'bifunctional' contribution stemming from the scavenging of protons by the dielectric surface:



A scheme of a potential bifunctional mechanism occurring at the interface working as an additional proton sink is shown in Figure 8.6.

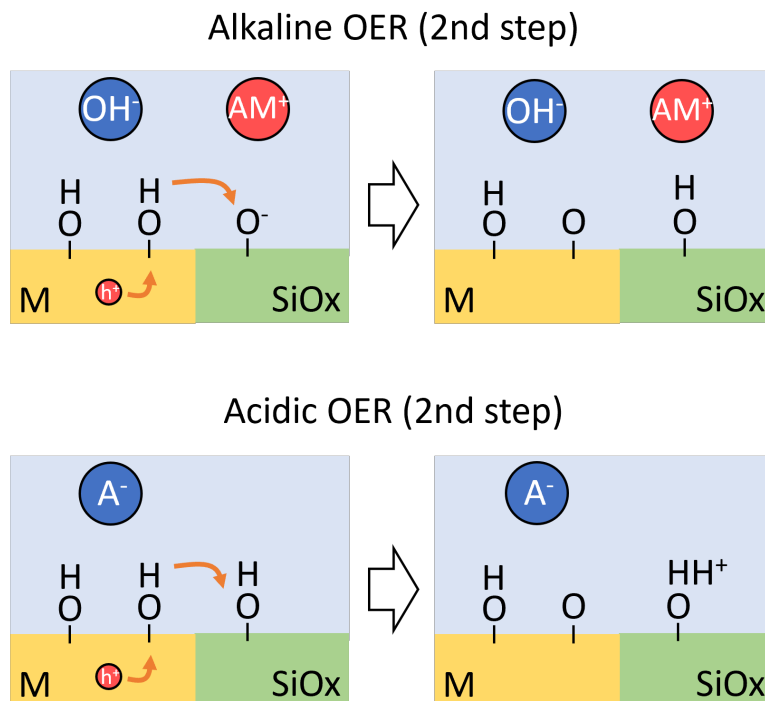


Figure 8.6: Scheme of the bifunctional mechanism at the metal/insulator interface expected for OER. The insulator surface may work as a proton sink, here exemplary shown for the second OER step in alkaline (top) and in acidic medium (bottom).

Consequently, the bifunctional mechanism may also catalyze OER by opening an additional reaction channel for proton capturing from the metal surface. Note that this may not only work for the presented second OER step, but may also be valid for each of the four electron transfer steps in OER. An additional reaction channel for the mentioned reaction would result in an increased activity regarding OER when increasing the area of dielectric/electrolyte interface in contact to the metal/electrolyte interface, i.e. on smaller nanostructures OER would proceed faster (be better catalyzed).

Figure 8.7 shows LSVs in the Au oxidation and the OER region of a continuous Au layer electrode (yellow) and a nanostructured electrode with 75 nm Au structure size (green). The electrolyte consists of 0.1 M KOH/Ar sat.'d. We see that the overpotential necessary for OER is smaller for the nanostructured electrode compared to the continuous Au layer. The overpotential necessary for drawing 0.5 mA cm^{-2} can be decreased by more than 150 mV (orange arrow). Consequently, the OER appears to be catalyzed more strongly on nanostructured electrodes than it is on the continuous layer, which may stem from a bifunctional mechanism occurring at the metal/insulator interface. However, a detailed analysis of this effect is beyond the scope of this work.

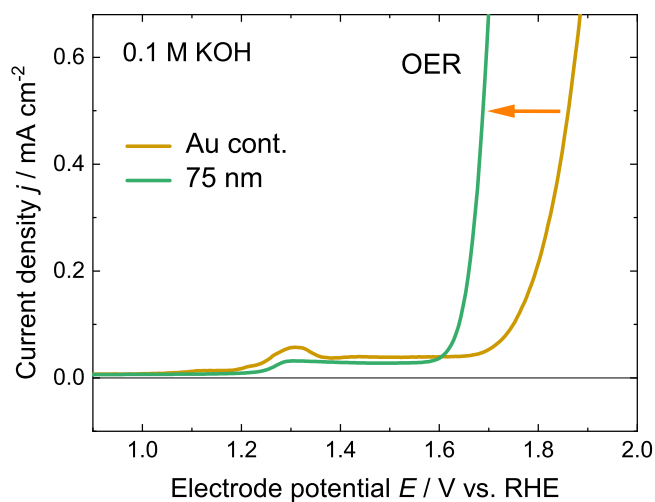


Figure 8.7: LSVs of a continuous Au layer (yellow) and a nanostructured electrode with 75 nm Au structure size (green) in the OER region. The electrolyte contains 0.1 M KOH/Ar sat.'d (pH 13), the scan rate is 50 mV s^{-1} . The necessary overpotential to draw a certain OER current is smaller for the nanostructured electrode compared to the continuous layer electrode (see orange arrow). This may be caused by the proposed bifunctional mechanism occurring at the metal/insulator interface.

Chapter 9

Conclusion and Outlook

In this work, we investigated the electrocatalytic behavior of silicon-based photo-active and photo-inactive electrodes, which are patterned by a metal array, regarding their catalytic activity for hydrogen evolution reaction (HER). Compared to bare metal surfaces, these electrodes exhibit a heterogeneous surface, i.e. a metal/insulator interface on the electrode surface.

When decreasing the size of the metal structures (here Au) on the electrode surface, while keeping the metal coverage constant, we could observe that the catalytic activity regarding HER gets enhanced. This could be observed in acidic, neutral, and alkaline media. The enhancement observed for smaller structures sizes stems from an increasing contact area between the metal part and the insulating part (passivation layer) when decreasing the structure size. We could verify indirectly that the metal/insulator interface exhibits a higher HER activity by showing that the exchange current density j_0 of nanostructured electrodes increases linearly with the inverse of the size d (diameter or side length) of the metal structures. Due to geometric reasons, the dependence of j_0 on $1/d$ is indicative of an increased reaction rate at the border of the metal structures (which is the location of the metal/insulator interface). In addition, we could identify an increased HER rate at the metal/insulator interface directly by local current mapping. SECCM measurements performed in acidic medium showed that the borders of the metal structures exhibit an increased HER reaction rate compared to the metal bulk part. We further showed that the enhancement is caused by a local promoted kinetics of HER and does not stem from different transport properties of reactants towards or products from the surface.

This effect appears to enhance selectively the HER. By investigating the competition between CO₂RR and HER in a CO₂ containing electrolyte, it appears that smaller structures exhibit a higher selectivity for HER [Mai17; Fil+18]. In addition, we could show that the kinetics of the oxidation of ferrocyanide (which is an outer-sphere one-electron transfer reaction) appears to be not dependent on the metal structure size. This further strengthens the hypothesis that the enhancement appears to be selective for the hydrogen reaction. As the outer-sphere reaction rate appears to be not influenced, an explanation on the basis of altered properties in the electrochemical double layer is rather unlikely.

Altered proton adsorption energetics at the border of the metal structures could also be excluded as a reason for the increased enhancement, because: (1) The enhancement is present for electrodes composed of insulator structures on a homogeneous metal (here Au) surface. We observed that HER gets also boosted with decreasing *insulator* structure size. As all of those electrodes are supposed to exhibit an identical surface topography of the

catalyst surface, the enhancement is likely to be caused by the close presence of the insulator/metal interface, rather than by an altered hydrogen adsorption kinetics at the edges of the metal structure. (2) The enhancement is observed for nanostructured electrodes utilizing metal catalysts with very different hydrogen adsorption energies. We observed the effect on electrodes containing Au-based structures, Au structures with electrochemically deposited Cu, and Pt-based structures. This further proves that the hydrogen adsorption energy is not sufficient to explain the observed increase in HER kinetics.

Although we observed an reaction rate increase in a large pH range, we focused on the neutral to alkaline pH range, since in this range HER occurs via the reduction of water and appeared to experience the largest improvement. To finally localize the mechanistic origin of the HER enhancement, we further analyzed its dependence on various electrolyte properties: By changing the salt concentration, the pH of the solution and the cation species present in the electrolyte, we found that the local concentration of cations in front of the electrode surface is a crucial parameter affecting the enhanced HER activity. The largest improvement of the HER reactivity at the metal/insulator interface was found for low local cation concentration. This could be achieved by either (1) low bulk ion concentration, (2) low pH value, or (3) using cations with large solvation energy, e.g. prefer Li^+ rather than Cs^+ ions in solution. This behavior is contrary to the behavior observed for bare metal surfaces.

On the basis of the given results and dependencies, we finally proposed a bifunctional mechanism occurring at the metal/insulator interface, which selectively enhances HER. In acidic medium, the insulator interface works as an additional proton source in the rate determining Heyrovsky step, which increases the local reaction rate. In neutral to alkaline media, i.e. considering HER from the reduction of water, the bifunctional mechanism decouples the proton adsorption from water dissociation and from the ion transport through the double layer. This conjecture can promote the rate determining Volmer or Heyrovsky step significantly, which, in turn, leads to the large enhancement of HER observed on nanostructured electrodes.

Outlook

The proposed bifunctional HER mechanism appears to be a fundamental property of non-homogeneous (i.e. laterally patterned) metal/insulator surfaces. In addition, preliminary results show that the bifunctional mechanism does not only selectively enhance the HER, but also the Oxygen Evolution Reaction (OER) can be enhanced by the presence of the metal(-oxide)/insulator interface. Here, the insulator surface may not work as a proton supply, but as a proton sink. Since the bifunctional mechanism appears to enhance both reactions relevant for water splitting, OER and HER, it may play a crucial role in the design or optimization of future (photo-)electrochemical water splitting devices, which can but not necessarily have to be based on silicon. As it is now known that the reaction rate can be increased significantly by increasing the metal/insulator interface, new design principles of photo-system surfaces can be established. For example surface micro-engineering of the individual catalyst surfaces may now become relevant, as the (often random) deposition of catalyst nanoparticles on an absorber material may not release the full potential of a water splitting device.

However, the relevance of the findings in this work go way beyond the application in photo-electrochemical devices. The appearance of the bifunctional mechanism is not only restricted to systems based on well-defined arrays of metal structures, as the samples in-

vestigated here. It is likely that the mechanism is also present in systems consisting of metal particles deposited onto a putative inactive support material. The large interfacial area between the support and the metal particles is supposed to give an enormous contribution of the bifunctional mechanism to the observed catalytic activity of the whole system, as a large interfacial area promotes the bifunctional mechanism. Consequently, the interpretation of the kinetic data of these kinds of systems and its correlation with intrinsic properties of the metal particles needs to be conducted carefully.

If future studies reveal that the bifunctional mechanism can also improve the rate of the Hydrogen Oxidation Reaction (HOR) or the Oxygen Reduction Reaction (ORR), one may also imagine an application of the bifunctional mechanism in fuel cell devices. The embedding of (cheap) insulator particles in the membrane electrolyte assembly (MEA) in close presence to the catalyst particles may further give a performance boost of the device at low cost, since the large interfacial surface area present in the MEA is also very beneficial for an enhancement of the reactions by the bifunctional mechanism.

Another goal of future studies should be to investigate if the bifunctional mechanism is present for more material combinations (e.g. nickel, titanium oxide, etc.). On the one hand, these fundamental studies would help to further reconcile the proposed mechanism with the results obtained by other groups (e.g. by Markovic et al., Koper et al., and many more) showing an increased HER rate at various heterogenous interfaces and, thus, pointing in the same direction [Sub+11; Dan+12; Led+17; Wu+21]. The comparative studies can help to further develop a fundamental theory of the appearing microscopic processes and to detect relevant system properties, which may help to further optimize the kinetics of the involved reactions. On the other hand, if it can be shown that more material combinations exhibit the bifunctional mechanism and, thus, its appearance is further generalizable, the optimization possibilities for devices in various fields of application via the bifunctional mechanism can be tremendous.

Bibliography

- [Aar+13] Barak D. B. Aaronson et al. “Pseudo-Single-Crystal Electrochemistry on Polycrystalline Electrodes: Visualizing Activity at Grains and Grain Boundaries on Platinum for the $\text{Fe}^{2+}/\text{Fe}^{3+}$ Redox Reaction”. In: *Journal of the American Chemical Society* 135.10 (Feb. 2013), pp. 3873–3880. DOI: 10.1021/ja310632k.
- [Abd+13] Fatwa F. Abdi et al. “Efficient solar water splitting by enhanced charge separation in a bismuth vanadate-silicon tandem photoelectrode”. In: *Nature Communications* 4.1 (July 2013). DOI: 10.1038/ncomms3195.
- [AD72] D.H. Angell and T. Dickinson. “The kinetics of the ferrous/ferric and ferro/ferricyanide reactions at platinum and gold electrodes”. In: *Journal of Electroanalytical Chemistry and Interfacial Electrochemistry* 35.1 (Mar. 1972), pp. 55–72. DOI: 10.1016/s0022-0728(72)80294-8.
- [AMV10] J. L. Aragones, L. G. MacDowell, and C. Vega. “Dielectric Constant of Ices and Water: A Lesson about Water Interactions”. In: *The Journal of Physical Chemistry A* 115.23 (Sept. 2010), pp. 5745–5758. DOI: 10.1021/jp105975c.
- [Ang+87] H. Angerstein-Kozłowska et al. “Elementary steps of electrochemical oxidation of single-crystal planes of Au - Part II. A chemical and structural basis of oxidation of the (111) plane”. In: *Journal of Electroanalytical Chemistry and Interfacial Electrochemistry* 228.1-2 (Aug. 1987), pp. 429–453. DOI: 10.1016/0022-0728(87)80122-5.
- [Ang19] Tina Angerer. “Investigation of the Bifunctional Mechanism of the Hydrogen Evolution Reaction by Changing the Interfacial Geometry of Gold/Silicon Nanoelectrodes”. MA thesis. Technical University of Munich, Department of Physics, 2019.
- [Ang21] Tina Angerer. “Investigation of the Hydrogen Evolution Reaction on Nanostructured Gold/Silicon Nitride Electrodes”. MA thesis. Technical University of Munich, Department of Physics, 2021.
- [AO98] Ken-ichi Ataka and Masatoshi Osawa. “In Situ Infrared Study of Water-Sulfate Coadsorption on Gold(111) in Sulfuric Acid Solutions”. In: *Langmuir* 14.4 (Jan. 1998), pp. 951–959. DOI: 10.1021/1a971110v.
- [BAO00] I. Borukhov, D. Andelman, and H. Orland. “Adsorption of large ions from an electrolyte solution: A modified Poisson–Boltzmann equation”. In: *Electrochimica Acta* 46.2-3 (Nov. 2000), pp. 221–229. DOI: 10.1016/s0013-4686(00)00576-4.
- [BF01] Allen J. Bard and Larry R. Faulkner. *Electrochemical Methods: Fundamentals and Applications*. WILEY, 2001. 864 pp. ISBN: 0471043729.

- [BGN11] Douwe Jan Bonthuis, Stephan Gekle, and Roland R. Netz. “Dielectric Profile of Interfacial Water and its Effect on Double-Layer Capacitance”. In: *Physical Review Letters* 107.16 (Oct. 2011), p. 166102. DOI: 10.1103/physrevlett.107.166102.
- [BGR02] John O’M Bockris, Maria Gamboa-Aldeco, and Amulya K. N. Reddy. *Modern Electrochemistry, Vol 2a - Fundamentals Of Electrodicts*. pp. 1183-1186. Kluwer Academic, 2002.
- [Bir98] D M. Bird. “Effects of coadsorbates in dissociative chemisorption of hydrogen on metallic surfaces”. In: *Faraday Discussions* 110 (1998), pp. 335–346. DOI: 10.1039/a801059e.
- [BMD68] J. O’M. Bockris, R. J. Mannan, and A. Damjanovic. “Dependence of the Rate of Electrode Redox Reactions on the Substrate”. In: *The Journal of Chemical Physics* 48.5 (Mar. 1968), pp. 1898–1904. DOI: 10.1063/1.1668987.
- [Boe+11] Shannon W. Boettcher et al. “Photoelectrochemical Hydrogen Evolution Using Si Microwire Arrays”. In: *Journal of the American Chemical Society* 133.5 (Jan. 2011), pp. 1216–1219. DOI: 10.1021/ja108801m.
- [BP61] I. Bergman and M. S. Paterson. “Silica powders of respirable size. I. Preliminary studies of dissolution rates in dilute sodium hydroxide”. In: *Journal of Applied Chemistry* 11.10 (Oct. 1961), pp. 369–376. DOI: 10.1002/jctb.5010111002.
- [BR05] A. S. Bondarenko and G. A. Ragoisha. “Progress in Chemometrics Research”. In: New York: Nova Science Publishers, 2005. Chap. Chapter 7, pp. 89–102. ISBN: 1594542570.
- [Bru+84a] G.J. Brug et al. “The analysis of electrode impedances complicated by the presence of a constant phase element”. In: *Journal of Electroanalytical Chemistry and Interfacial Electrochemistry* 176.1-2 (Sept. 1984), pp. 275–295. DOI: 10.1016/s0022-0728(84)80324-1.
- [Bru+84b] G.J. Brug et al. “The kinetics of the reduction of protons at polycrystalline and monocrystalline gold electrodes”. In: *Journal of Electroanalytical Chemistry and Interfacial Electrochemistry* 181.1-2 (Dec. 1984), pp. 245–266. DOI: 10.1016/0368-1874(84)83633-3.
- [Büh23] Lukas Bührend. “Finite Element Simulations of the Potential Distributions and Interfacial Capacitances of Nanostructured Semiconductor/Metal/Insulator Electrodes”. MA thesis. Technical University of Munich, Department of Physics, 2023.
- [BW10] Michael Ball and Martin Wietschel, eds. *The Hydrogen Economy: Opportunities and Challenges*. Cambridge University Press, July 2010. 672 pp. ISBN: 0521882168. URL: https://www.ebook.de/de/product/8049064/the_hydrogen_economy.html.
- [CH72] J. P. Carr and N. A. Hampson. “The Differential Capacitance of Polycrystalline Gold in Aqueous Solutions”. In: *Journal of The Electrochemical Society* 119.3 (1972), p. 325. DOI: 10.1149/1.2404196.
- [Che+13] Serhiy Cherevko et al. “Gold dissolution: towards understanding of noble metal corrosion”. In: *RSC Advances* 3.37 (2013), p. 16516. DOI: 10.1039/c3ra42684j.

-
- [Che+15] Yikai Chen et al. “A quantitative analysis of the efficiency of solar-driven water-splitting device designs based on tandem photoabsorbers patterned with islands of metallic electrocatalysts”. In: *Energy & Environmental Science* 8.6 (2015), pp. 1736–1747. DOI: 10.1039/c5ee00311c.
- [Che+16] Leanne D. Chen et al. “Electric Field Effects in Electrochemical CO₂ Reduction”. In: *ACS Catalysis* 6.10 (Sept. 2016), pp. 7133–7139. DOI: 10.1021/acscatal.6b02299.
- [Che+17] Xiaoting Chen et al. “Co-adsorption of Cations as the Cause of the Apparent pH Dependence of Hydrogen Adsorption on a Stepped Platinum Single-Crystal Electrode”. In: *Angewandte Chemie International Edition* 56.47 (Oct. 2017), pp. 15025–15029. DOI: 10.1002/anie.201709455.
- [Che+18] Fanglin Che et al. “Elucidating the Roles of Electric Fields in Catalysis: A Perspective”. In: *ACS Catalysis* 8.6 (Apr. 2018), pp. 5153–5174. DOI: 10.1021/acscatal.7b02899.
- [Coo+10] Timothy R. Cook et al. “Solar Energy Supply and Storage for the Legacy and Nonlegacy Worlds”. In: *Chemical Reviews* 110.11 (Nov. 2010), pp. 6474–6502. DOI: 10.1021/cr100246c.
- [CRK03] Jang H. Chun, Keuk H. Ra, and Nam Y. Kim. “Langmuir Adsorption Isotherms of Overpotentially Deposited Hydrogen at Poly-Au and Rh/H₂SO₄ Aqueous Electrolyte Interfaces”. In: *Journal of The Electrochemical Society* 150.4 (2003), E207. DOI: 10.1149/1.1554919.
- [Dan+12] N. Danilovic et al. “Enhancing the Alkaline Hydrogen Evolution Reaction Activity through the Bifunctionality of Ni(OH)₂/Metal Catalysts”. In: *Angewandte Chemie* 124.50 (Nov. 2012), pp. 12663–12666. DOI: 10.1002/ange.201204842.
- [Dia+13] Oscar Diaz-Morales et al. “Electrochemical water splitting by gold: evidence for an oxide decomposition mechanism”. In: *Chemical Science* 4.6 (2013), p. 2334. DOI: 10.1039/c3sc50301a.
- [DKT06] Todd G. Deutsch, Carl A. Koval, and John A. Turner. “III-V Nitride Epilayers for Photoelectrochemical Water Splitting: GaPN and GaAsPN”. In: *The Journal of Physical Chemistry B* 110.50 (Dec. 2006), pp. 25297–25307. DOI: 10.1021/jp0652805.
- [DML91] T. E. Dinan, M. Matlosz, and D. Landolt. “Experimental Investigation of the Current Distribution on a Recessed Rotating-Disk Electrode”. In: *Journal of the Electrochemical Society* 138.10 (1991), pp. 2947–2951. DOI: 10.1149/1.2085346.
- [ESO18] Kai S. Exner, Iman Sohrabnejad-Eskan, and Herbert Over. “A Universal Approach To Determine the Free Energy Diagram of an Electrocatalytic Reaction”. In: *ACS Catalysis* 8.3 (Jan. 2018), pp. 1864–1879. DOI: 10.1021/acscatal.7b03142.
- [Esp+13] Daniel V. Esposito et al. “H₂ evolution at Si-based metal–insulator–semiconductor photoelectrodes enhanced by inversion channel charge collection and H spillover”. In: *Nature Materials* 12.6 (May 2013), pp. 562–568. DOI: 10.1038/nmat3626.
-

- [Exn19] Kai S. Exner. “Is Thermodynamics a Good Descriptor for the Activity? Re-Investigation of Sabatier’s Principle by the Free Energy Diagram in Electrocatalysis”. In: *ACS Catalysis* 9.6 (Apr. 2019), pp. 5320–5329. DOI: 10.1021/acscatal.9b00732.
- [Fil+18] Simon Filser et al. “Photoelectrochemical reactivity of well-defined mesoscale gold arrays on SiO₂/Si substrates in CO₂-saturated aqueous electrolyte”. In: *Electrochimica Acta* 268 (Apr. 2018), pp. 546–553. DOI: 10.1016/j.electacta.2018.02.018.
- [FK89] Nagakazu Furuya and Shoichiro Koide. “Hydrogen adsorption on platinum single-crystal surfaces”. In: *Surface Science* 220.1 (Oct. 1989), pp. 18–28. DOI: 10.1016/0039-6028(89)90460-3.
- [Fuj+12] Takeshi Fujita et al. “Atomic origins of the high catalytic activity of nanoporous gold”. In: *Nature Materials* 11.9 (Aug. 2012), pp. 775–780. DOI: 10.1038/nmat3391.
- [Gah13] Gerda Gahleitner. “Hydrogen from renewable electricity: An international review of power-to-gas pilot plants for stationary applications”. In: *International Journal of Hydrogen Energy* 38.5 (Feb. 2013), pp. 2039–2061. DOI: 10.1016/j.ijhydene.2012.12.010.
- [Gar+18] Batyr Garlyyev et al. “Influence of the Nature of the Alkali Metal Cations on the Electrical Double-Layer Capacitance of Model Pt(111) and Au(111) Electrodes”. In: *The Journal of Physical Chemistry Letters* 9.8 (Mar. 2018), pp. 1927–1930. DOI: 10.1021/acs.jpcllett.8b00610.
- [Ge+17] Aimin Ge et al. “Interfacial Structure and Electric Field Probed by in Situ Electrochemical Vibrational Stark Effect Spectroscopy and Computational Modeling”. In: *The Journal of Physical Chemistry C* 121.34 (Aug. 2017), pp. 18674–18682. DOI: 10.1021/acs.jpcc.7b05563.
- [Ger60] H. Gerischer. “Über den Ablauf von Redoxreaktionen an Metallen und an Halbleitern”. In: *Zeitschrift für Physikalische Chemie* 26.5 (1960), pp. 325–338. DOI: 10.1524/zpch.1960.26.5_6.325.
- [GK21a] Akansha Goyal and Marc T. M. Koper. “The Interrelated Effect of Cations and Electrolyte pH on the Hydrogen Evolution Reaction on Gold Electrodes in Alkaline Media”. In: *Angewandte Chemie International Edition* 60.24 (May 2021), pp. 13452–13462. DOI: 10.1002/anie.202102803.
- [GK21b] Akansha Goyal and Marc T. M. Koper. “Understanding the role of mass transport in tuning the hydrogen evolution kinetics on gold in alkaline media”. In: *The Journal of Chemical Physics* 155.13 (Oct. 2021), p. 134705. DOI: 10.1063/5.0064330.
- [GL08] Jidong Guo and Ernö Lindner. “Cyclic Voltammograms at Coplanar and Shallow Recessed Microdisk Electrode Arrays: Guidelines for Design and Experiment”. In: *Analytical Chemistry* 81.1 (Nov. 2008), pp. 130–138. DOI: 10.1021/ac801592j.
- [Gol+22] Matthias Golibrzuch et al. “Tuning the feature size of nanoimprinting stamps: A method to enhance the flexibility of nanoimprint lithography”. In: *Journal of Applied Physics* 131.12 (Mar. 2022), p. 124301. DOI: 10.1063/5.0079282.
- [Gol23] Matthias Golibrzuch. “(unpublished)”. PhD thesis. Technical University of Munich, 2023.

-
- [Gui+14] Rolando Guidelli et al. “Defining the transfer coefficient in electrochemistry: An assessment (IUPAC Technical Report)”. In: *Pure and Applied Chemistry* 86.2 (2014), pp. 245–258.
- [Ham+90] Antoinette Hamelin et al. “Cyclic voltammetric characterization of oriented monocrystalline gold surfaces in aqueous alkaline solution”. In: *Journal of Electroanalytical Chemistry and Interfacial Electrochemistry* 295.1-2 (Nov. 1990), pp. 291–300. DOI: 10.1016/0022-0728(90)85023-x.
- [Ham96] A. Hamelin. “Cyclic voltammetry at gold single-crystal surfaces. Part 1. Behaviour at low-index faces”. In: *Journal of Electroanalytical Chemistry* 407.1-2 (May 1996), pp. 1–11. DOI: 10.1016/0022-0728(95)04499-x.
- [HEB96] R.E.G. van Hal, J.C.T. Eijkel, and P. Bergveld. “A general model to describe the electrostatic potential at electrolyte oxide interfaces”. In: *Advances in Colloid and Interface Science* 69.1-3 (Dec. 1996), pp. 31–62. DOI: 10.1016/S0001-8686(96)00307-7.
- [Hen+21] Julian Hengsteler et al. “Bringing Electrochemical Three-Dimensional Printing to the Nanoscale”. In: *Nano Letters* 21.21 (Oct. 2021), pp. 9093–9101. DOI: 10.1021/acs.nanolett.1c02847.
- [HHI91] Toshinori Hachiya, Hidetoshi Honbo, and Kingo Itaya. “Detailed underpotential deposition of copper on gold(111) in aqueous solutions”. In: *Journal of Electroanalytical Chemistry and Interfacial Electrochemistry* 315.1-2 (Oct. 1991), pp. 275–291. DOI: 10.1016/0022-0728(91)80076-3.
- [HHV07] Carl H. Hamann, Andrew Hamnett, and Wolf Vielstich. *Electrochemistry*. 2nd ed. Wiley-VCH GmbH, Feb. 2007. ISBN: 352731069X. URL: https://www.ebook.de/de/product/5453322/carl_h_hamann_andrew_hamnett_wolf_vielstich_electrochemistry.html.
- [Hin+98] R. Hinogami et al. “An Approach to Ideal Semiconductor Electrodes for Efficient Photoelectrochemical Reduction of Carbon Dioxide by Modification with Small Metal Particles”. In: *The Journal of Physical Chemistry B* 102.6 (Jan. 1998), pp. 974–980. DOI: 10.1021/jp972663h.
- [Hir+10] Bryan Hirschorn et al. “Determination of effective capacitance and film thickness from constant-phase-element parameters”. In: *Electrochimica Acta* 55.21 (Aug. 2010), pp. 6218–6227. DOI: 10.1016/j.electacta.2009.10.065.
- [HL21] Jun Huang and Chen-Kun Li. “Impedance response of electrochemical interfaces: part II-chemisorption”. In: *Journal of Physics: Condensed Matter* 33.16 (Apr. 2021), p. 164003. DOI: 10.1088/1361-648x/abef9d.
- [HM01] C.H. Hsu and F. Mansfeld. “Technical Note: Concerning the Conversion of the Constant Phase Element Parameter Y0 into a Capacitance”. In: *Corrosion* 57.09 (Sept. 2001). ISSN: 0010-9312.
- [HN95] B. Hammer and J. K. Nørskov. “Why gold is the noblest of all the metals”. In: *Nature* 376.6537 (July 1995), pp. 238–240. DOI: 10.1038/376238a0.
- [Hoo61] J. G. Hooley. “The Kinetics of the Reaction of Silica with Group I Hydroxides”. In: *Canadian Journal of Chemistry* 39.6 (June 1961), pp. 1221–1230. DOI: 10.1139/v61-155.
-

- [Hor+87] Yoshio Hori et al. “Electrochemical reduction of carbon dioxide to carbon monoxide at a gold electrode in aqueous potassium hydrogen carbonate”. In: *Journal of the Chemical Society, Chemical Communications* 10 (1987), p. 728. DOI: 10.1039/c39870000728.
- [HW87] Antoinette Hamelin and Michael J. Weaver. “Dependence of the kinetics of proton reduction at gold electrodes on the surface crystallographic orientation”. In: *Journal of Electroanalytical Chemistry and Interfacial Electrochemistry* 223.1-2 (May 1987), pp. 171–184. DOI: 10.1016/0022-0728(87)85258-0.
- [Jia+17] Chaoran Jiang et al. “Photoelectrochemical devices for solar water splitting – materials and challenges”. In: *Chemical Society Reviews* 46.15 (2017), pp. 4645–4660. DOI: 10.1039/c6cs00306k.
- [KB71] A.T. Kuhn and M. Byrne. “The hydrogen- and deuterium-evolution reactions on gold in acid solutions”. In: *Electrochimica Acta* 16.3 (Mar. 1971), pp. 391–399. DOI: 10.1016/0013-4686(71)85011-9.
- [KBN17] Aria Kahyarian, Bruce Brown, and Srdjan Nescic. “Mechanism of the Hydrogen Evolution Reaction in Mildly Acidic Environments on Gold”. In: *Journal of The Electrochemical Society* 164.6 (2017), H365–H374. DOI: 10.1149/2.1061706jes.
- [Kem+15] E. Kemppainen et al. “Scalability and feasibility of photoelectrochemical H₂ evolution: the ultimate limit of Pt nanoparticle as an HER catalyst”. In: *Energy & Environmental Science* 8.10 (2015), pp. 2991–2999. DOI: 10.1039/c5ee02188j.
- [Kib+18] Ludwig A. Kibler et al. “New insights on hydrogen evolution at Au single crystal electrodes”. In: *Current Opinion in Electrochemistry* 9 (June 2018), pp. 265–270. DOI: 10.1016/j.coelec.2018.05.013.
- [KK11] Larisa A. Khanova and Lev I. Krishtalik. “Kinetics of the hydrogen evolution reaction on gold electrode. A new case of the barrierless discharge”. In: *Journal of Electroanalytical Chemistry* 660.2 (Sept. 2011), pp. 224–229. DOI: 10.1016/j.jelechem.2011.01.016.
- [KP02] Zsolt Kerner and Tamás Pajkossy. “Measurement of adsorption rates of anions on Au(111) electrodes by impedance spectroscopy”. In: *Electrochimica Acta* 47.13-14 (May 2002), pp. 2055–2063. DOI: 10.1016/s0013-4686(02)00073-7.
- [KS08] Katharina Krischer and Elena R. Savinova. “Handbook of Heterogeneous Catalysis”. In: pp. 1873-1905. Wiley-VCH, 2008. Chap. Electrocatalysis.
- [KS15] Katharina Krischer and Konrad Schönleber. *Physics of Energy Conversion*. de Gruyter, Boston, 2015. ISBN: 150150763X. URL: https://www.ebook.de/de/product/23320952/katharina_krischer_konrad_schoenleber_physics_of_energy_conversion.html.
- [KT98] Oscar Khaselev and John A. Turner. “A Monolithic Photovoltaic-Photoelectrochemical Device for Hydrogen Production via Water Splitting”. In: *Science* 280.5362 (Apr. 1998), pp. 425–427. DOI: 10.1126/science.280.5362.425.
- [Lai87] Keith Laidler. *Chemical Kinetics*. New York: Harper & Row, 1987. ISBN: 0060438622.

-
- [LC61] H. A. Laitinen and M. S. Chao. “The Anodic Surface Oxidation of Gold”. In: *Journal of The Electrochemical Society* 108.8 (1961), p. 726. DOI: 10.1149/1.2428206.
- [Led+17] Isis Ledezma-Yanez et al. “Interfacial water reorganization as a pH-dependent descriptor of the hydrogen evolution rate on platinum electrodes”. In: *Nature Energy* 2.4 (Mar. 2017). DOI: 10.1038/nenergy.2017.31.
- [Li19] Qi Li. “Investigation of silicon electrodes functionalized with pyridine for the electrochemical H₂ evolution and CO₂ reduction reaction”. PhD thesis. Technical University of Munich, Mar. 2019.
- [Lia+18] Yunchang Liang et al. “Electrochemical Scanning Probe Microscopies in Electrocatalysis”. In: *Small Methods* 3.8 (Nov. 2018), p. 1800387. DOI: 10.1002/smt.201800387.
- [Liu+19] Ershuai Liu et al. “Unifying the Hydrogen Evolution and Oxidation Reactions Kinetics in Base by Identifying the Catalytic Roles of Hydroxyl-Water-Cation Adducts”. In: *Journal of the American Chemical Society* 141.7 (Jan. 2019), pp. 3232–3239. DOI: 10.1021/jacs.8b13228.
- [LSC16] M. Łukaszewski, M. Soszko, and A. Czerwinski. “Electrochemical Methods of Real Surface Area Determination of Noble Metal Electrodes – an Overview”. In: *International Journal of Electrochemical Science* (June 2016), pp. 4442–4469. DOI: 10.20964/2016.06.71.
- [Mai+20] Thomas L. Maier et al. “Lateral silicon oxide/gold interfaces enhance the rate of electrochemical hydrogen evolution reaction in alkaline media”. In: *The Journal of Chemical Physics* 152.15 (Apr. 2020), p. 154705. DOI: 10.1063/5.0003295.
- [Mai17] Thomas L. Maier. “Characterization of gold/copper nanostructures on silicon electrodes for applications in photoelectrochemical CO₂ conversion”. MA thesis. Technical University of Munich, Department of Physics, 2017.
- [Mar+96] Nenad M. Markovića et al. “Hydrogen electrochemistry on platinum low-index single-crystal surfaces in alkaline solution”. In: *J. Chem. Soc., Faraday Trans.* 92.20 (1996), pp. 3719–3725. DOI: 10.1039/ft9969203719.
- [Mar56] R. A. Marcus. “On the Theory of Oxidation-Reduction Reactions Involving Electron Transfer. I”. In: *The Journal of Chemical Physics* 24.5 (May 1956), pp. 966–978. DOI: 10.1063/1.1742723.
- [MB96] Stefano Mezzasalma and Danilo Baldovino. “Characterization of Silicon Nitride Surface in Water and Acid Environment: A General Approach to the Colloidal Suspensions”. In: *Journal of Colloid and Interface Science* 180.2 (June 1996), pp. 413–420. DOI: 10.1006/jcis.1996.0320.
- [MBK22] Giulia Marcandalli, Katinka Boterman, and Marc T.M. Koper. “Understanding hydrogen evolution reaction in bicarbonate buffer”. In: *Journal of Catalysis* 405 (Jan. 2022), pp. 346–354. DOI: 10.1016/j.jcat.2021.12.012.
- [McC+15] Charles C. L. McCrory et al. “Benchmarking Hydrogen Evolving Reaction and Oxygen Evolving Reaction Electrocatalysts for Solar Water Splitting Devices”. In: *Journal of the American Chemical Society* 137.13 (Mar. 2015), pp. 4347–4357. DOI: 10.1021/ja510442p.
-

- [McK+11] James R. McKone et al. “Evaluation of Pt, Ni, and Ni–Mo electrocatalysts for hydrogen evolution on crystalline Si electrodes”. In: *Energy & Environmental Science* 4.9 (2011), p. 3573. DOI: 10.1039/c1ee01488a.
- [MFL20] Rüdiger Müller, Jürgen Fuhrmann, and Manuel Landstorfer. “Modeling Polycrystalline Electrode-electrolyte Interfaces: The Differential Capacitance”. In: *Journal of The Electrochemical Society* 167.10 (Jan. 2020), p. 106512. DOI: 10.1149/1945-7111/ab9cca.
- [MH19] Frieder Mugele and Jason Heikenfeld. *Electrowetting*. Wiley VCH Verlag GmbH, Feb. 2019. ISBN: 3527412298. URL: https://www.ebook.de/de/product/33036521/frieder_mugele_jason_heikenfeld_electrowetting.html.
- [ML14] James McKone and Nathan Lewis. “Structured Materials for Photoelectrochemical Water Splitting”. In: *Photoelectrochemical Water Splitting: Materials, Processes and Architectures*. Ed. by Hans-Joachim Lewerenz and Laurie Peter. Royal Society of Chemistry, 2014. Chap. CHAPTER 3. Structured Materials for Photoelectrochemical Water Splitting, pp. 52–82. DOI: 10.1039/9781849737739-00052.
- [Mom+16] Dmitry Momotenko et al. “Simultaneous Interfacial Reactivity and Topography Mapping with Scanning Ion Conductance Microscopy”. In: *Analytical Chemistry* 88.5 (Feb. 2016), pp. 2838–2846. DOI: 10.1021/acs.analchem.5b04566.
- [Mon+21] Mariana C. O. Monteiro et al. “Understanding Cation Trends for Hydrogen Evolution on Platinum and Gold Electrodes in Alkaline Media”. In: *ACS Catalysis* 11.23 (Nov. 2021), pp. 14328–14335. DOI: 10.1021/acscatal.1c04268.
- [Mor+90] M. Morita et al. “Growth of native oxide on a silicon surface”. In: *Journal of Applied Physics* 68.3 (Aug. 1990), pp. 1272–1281. DOI: 10.1063/1.347181.
- [MWA08] K. J. J. Mayrhofer, G. K. H. Wiberg, and M. Arenz. “Impact of Glass Corrosion on the Electrocatalysis on Pt Electrodes in Alkaline Electrolyte”. In: *Journal of The Electrochemical Society* 155.1 (2008), P1. DOI: 10.1149/1.2800752.
- [Nag+17] Robin D. Nagel et al. “Nanoimprint methods for the fabrication of macroscopic plasmonically active metal nanostructures”. In: *Journal of Applied Physics* 121.8 (Feb. 2017), p. 084305. DOI: 10.1063/1.4976860.
- [Nag18] Robin D. Nagel. “Nanoimprint technologies for energy conversion applications”. PhD thesis. Technical University of Munich, Institute of Nanoelectronics, 2018.
- [Nak+02] Masashi Nakamura et al. “Surface X-ray diffraction study of Cu UPD on Au(111) electrode in 0.5 M H₂SO₄ solution: the coadsorption structure of UPD copper, hydration water molecule and bisulfate anion on Au(111)”. In: *Surface Science* 514.1-3 (Aug. 2002), pp. 227–233. DOI: 10.1016/s0039-6028(02)01634-5.
- [NB88] R.J. Nichols and A. Bewick. “Spectroscopic identification of the adsorbed intermediate in hydrogen evolution on platinum”. In: *Journal of Electroanalytical Chemistry and Interfacial Electrochemistry* 243.2 (Mar. 1988), pp. 445–453. DOI: 10.1016/0022-0728(88)80047-0.

- [New66] John Newman. “Current Distribution on a Rotating Disk below the Limiting Current”. In: *Journal of The Electrochemical Society* 113.12 (1966), p. 1235. DOI: 10.1149/1.2423795.
- [Nør+05] J. K. Nørskov et al. “Trends in the Exchange Current for Hydrogen Evolution”. In: *Journal of The Electrochemical Society* 152.3 (2005), J23. DOI: 10.1149/1.1856988.
- [Now+05] J. Nowotny et al. “Solar-hydrogen: Environmentally safe fuel for the future”. In: *International Journal of Hydrogen Energy* 30.5 (Apr. 2005), pp. 521–544. DOI: 10.1016/j.ijhydene.2004.06.012.
- [OE92] T. Ohmori and M. Enyo. “Hydrogen evolution reaction on gold electrode in alkaline solutions”. In: *Electrochimica Acta* 37.11 (Sept. 1992), pp. 2021–2028. DOI: 10.1016/0013-4686(92)87118-j.
- [OW89] Joan M. Ogden and Robert H. Williams. *Solar hydrogen: Moving beyond fossil fuels*. World Resources Inst., 1989. ISBN: 978-0915825387.
- [Pag+16] Ashley Page et al. “Fast Nanoscale Surface Charge Mapping with Pulsed-Potential Scanning Ion Conductance Microscopy”. In: *Analytical Chemistry* 88.22 (Nov. 2016), pp. 10854–10859. DOI: 10.1021/acs.analchem.6b03744.
- [PAI86] C.L. Perdriel, A.J. Arvia, and M. Ipohorski. “Electrochemical faceting of polycrystalline gold in 1 M H₂SO₄”. In: *Journal of Electroanalytical Chemistry and Interfacial Electrochemistry* 215.1-2 (Dec. 1986), pp. 317–329. DOI: 10.1016/0022-0728(86)87025-5.
- [Pal+11] M. Palomar-Pardavé et al. “Influence of the substrate’s surface structure on the mechanism and kinetics of the electrochemical UPD formation of a copper monolayer on gold”. In: *Electrochimica Acta* 56.27 (Nov. 2011), pp. 10083–10092. DOI: 10.1016/j.electacta.2011.08.105.
- [Par+11] Adriana Paracchino et al. “Highly active oxide photocathode for photoelectrochemical water reduction”. In: *Nature Materials* 10.6 (May 2011), pp. 456–461. DOI: 10.1038/nmat3017.
- [Per+15] David Perry et al. “Simultaneous Nanoscale Surface Charge and Topographical Mapping”. In: *ACS Nano* 9.7 (July 2015), pp. 7266–7276. DOI: 10.1021/acsnano.5b02095.
- [PGV98] Joelma Perez, Ernesto R. Gonzalez, and Hebe M. Villullas. “Hydrogen Evolution Reaction on Gold Single-Crystal Electrodes in Acid Solutions”. In: *The Journal of Physical Chemistry B* 102.52 (Dec. 1998), pp. 10931–10935. DOI: 10.1021/jp9831987.
- [Pla+08] Ilia Platzman et al. “Oxidation of Polycrystalline Copper Thin Films at Ambient Conditions”. In: *The Journal of Physical Chemistry C* 112.4 (Jan. 2008), pp. 1101–1108. DOI: 10.1021/jp076981k.
- [PY09] Zhenmeng Peng and Hong Yang. “Designer platinum nanoparticles: Control of shape, composition in alloy, nanostructure and electrocatalytic property”. In: *Nano Today* 4.2 (Apr. 2009), pp. 143–164. DOI: 10.1016/j.nantod.2008.10.010.
- [Qua+14] Paola Quaino et al. “Volcano plots in hydrogen electrocatalysis – uses and abuses”. In: *Beilstein Journal of Nanotechnology* 5 (June 2014), pp. 846–854. DOI: 10.3762/bjnano.5.96.

- [Rai+76] S. I. Raider et al. "Surface Oxidation of Silicon Nitride Films". In: *Journal of The Electrochemical Society* 123.4 (Apr. 1976), pp. 560–565. DOI: 10.1149/1.2132877.
- [Reb+18] Luis Rebollar et al. "Determining the Viability of Hydroxide-Mediated Bi-functional HER/HOR Mechanisms through Single-Crystal Voltammetry and Microkinetic Modeling". In: *Journal of The Electrochemical Society* 165.15 (2018), J3209–J3221. DOI: 10.1149/2.0271815jes.
- [Res+18] Joaquin Resasco et al. "Effects of Anion Identity and Concentration on Electrochemical Reduction of CO₂". In: *ChemElectroChem* 5.7 (Feb. 2018), pp. 1064–1072. DOI: 10.1002/ce1c.201701316.
- [Rhe+14] Philipp J. Rheinländer et al. "Kinetics of the Hydrogen Oxidation/Evolution Reaction on Polycrystalline Platinum in Alkaline Electrolyte Reaction Order with Respect to Hydrogen Pressure". In: *Journal of The Electrochemical Society* 161.14 (2014), F1448–F1457. DOI: 10.1149/2.0501414jes.
- [Rin+19] Stefan Ringe et al. "Understanding cation effects in electrochemical CO₂ reduction". In: *Energy & Environmental Science* 12.10 (2019), pp. 3001–3014. DOI: 10.1039/c9ee01341e.
- [Roo84] Alfred J. van Roosmalen. "Review: Dry etching of silicon oxide". In: *Vacuum* 34.3-4 (Mar. 1984), pp. 429–436. DOI: 10.1016/0042-207x(84)90079-4.
- [Rum17] John Rumble, ed. *CRC handbook of chemistry and physics*. 98th ed. CRC Press, 2017. ISBN: 9781498784542.
- [Sak+13] Daisuke Sakai et al. "Chemical Etching Using KOH Aqueous Solution for Corona-Charge Micropatterning of Soda-Lime Glass". In: *Japanese Journal of Applied Physics* 52.3R (Mar. 2013), p. 036701. DOI: 10.7567/jjap.52.036701.
- [San+09] E. Santos et al. "Model for the electrocatalysis of hydrogen evolution". In: *Physical Review B* 79.23 (June 2009), p. 235436. DOI: 10.1103/physrevb.79.235436.
- [Sar+18] Francisco J. Sarabia et al. "Effect of the Interfacial Water Structure on the Hydrogen Evolution Reaction on Pt(111) Modified with Different Nickel Hydroxide Coverages in Alkaline Media". In: *ACS Applied Materials & Interfaces* 11.1 (Dec. 2018), pp. 613–623. DOI: 10.1021/acsami.8b15003.
- [SBB95] P. Schmuki, H. Böhni, and J. A. Bardwell. "In Situ Characterization of Anodic Silicon Oxide Films by AC Impedance Measurements". In: *Journal of The Electrochemical Society* 142.5 (May 1995), pp. 1705–1712. DOI: 10.1149/1.2048644.
- [Sch+99] G. Schmitt et al. "Passivation and corrosion of microelectrode arrays". In: *Electrochimica Acta* 44.21-22 (June 1999), pp. 3865–3883. DOI: 10.1016/s0013-4686(99)00094-8.
- [SCH20] SCHOTT AG. *Technical Glasses - Physical and Technical Properties*. 2020.
- [SGS10] Wenchao Sheng, Hubert A. Gasteiger, and Yang Shao-Horn. "Hydrogen Oxidation and Evolution Reaction Kinetics on Platinum: Acid vs Alkaline Electrolytes". In: *Journal of The Electrochemical Society* 157.11 (2010), B1529. DOI: 10.1149/1.3483106.

-
- [SGT15] Tatsuya Shinagawa, Angel T. Garcia-Esparza, and Kazuhiro Takanabe. “Insight on Tafel slopes from a microkinetic analysis of aqueous electrocatalysis for energy conversion”. In: *Scientific Reports* 5.1 (Sept. 2015). DOI: 10.1038/srep13801.
- [Shk+20] V. Shkirskiy et al. “Nanoscale Scanning Electrochemical Cell Microscopy and Correlative Surface Structural Analysis to Map Anodic and Cathodic Reactions on Polycrystalline Zn in Acid Media”. In: *Journal of The Electrochemical Society* 167.4 (Jan. 2020), p. 041507. DOI: 10.1149/1945-7111/ab739d.
- [SM82] Takeshi Sasaki and Akiya Matsuda. “Mechanism of hydrogen evolution reaction on gold in aqueous sulfuric acid and sodium hydroxide”. In: *Journal of the research institute for catalysis Hokkaido university* 29.3 (1982), pp. 113–132.
- [SN89] William H. Smyrl and John Newman. “Current Distribution at Electrode Edges at High Current Densities”. In: *Journal of The Electrochemical Society* 136.1 (Jan. 1989), pp. 132–139. DOI: 10.1149/1.2096572.
- [SS10] Wolfgang Schmickler and Elizabeth Santos. *Interfacial Electrochemistry*. Springer Berlin Heidelberg, Sept. 2010. 288 pp. ISBN: 3642049362. URL: https://www.ebook.de/de/product/10044664/wolfgang_schmickler_elizabeth_santos_interfacial_electrochemistry.html.
- [Str+16] Dusan Strmcnik et al. “Design principles for hydrogen evolution reaction catalyst materials”. In: *Nano Energy* 29 (Nov. 2016), pp. 29–36. DOI: 10.1016/j.nanoen.2016.04.017.
- [Sub+11] Ram Subbaraman et al. “Enhancing Hydrogen Evolution Activity in Water Splitting by Tailoring Li⁺-Ni(OH)₂-Pt Interfaces”. In: *Science* 334.6060 (Dec. 2011), pp. 1256–1260. DOI: 10.1126/science.1211934.
- [Sze07] S. M. Sze. *Physics of Semiconductor Devices*. 3rd ed. Hoboken, N.J: Wiley-Interscience, 2007. ISBN: 9780471143239.
- [TP91] S. Trasatti and O. A. Petrii. “Real surface area measurements in electrochemistry”. In: *Pure and Applied Chemistry* 63.5 (Jan. 1991), pp. 711–734. DOI: 10.1351/pac199163050711.
- [Tra72] Sergio Trasatti. “Work function, electronegativity, and electrochemical behaviour of metals”. In: *Journal of Electroanalytical Chemistry and Interfacial Electrochemistry* 39.1 (Sept. 1972), pp. 163–184. DOI: 10.1016/s0022-0728(72)80485-6.
- [Urb+14] F. Urbain et al. “Development of Thin Film Amorphous Silicon Tandem Junction Based Photocathodes Providing High Open-Circuit Voltages for Hydrogen Production”. In: *International Journal of Photoenergy* 2014 (2014), pp. 1–10. DOI: 10.1155/2014/249317.
- [Vel+14] Juan-Jesus Velasco-Velez et al. “The structure of interfacial water on gold electrodes studied by x-ray absorption spectroscopy”. In: *Science* 346.6211 (Nov. 2014), pp. 831–834. DOI: 10.1126/science.1259437.
- [VG09] John C. Vickerman and Ian S. Gilmore, eds. *Surface Analysis – The Principal Techniques*. John Wiley & Sons, Ltd, Apr. 2009. DOI: 10.1002/9780470721582.
- [Wae+19] Matthias M. Waegle et al. “How cations affect the electric double layer and the rates and selectivity of electrocatalytic processes”. In: *The Journal of Chemical Physics* 151.16 (Oct. 2019), p. 160902. DOI: 10.1063/1.5124878.
-

- [Wal+10] Michael G. Walter et al. "Solar Water Splitting Cells". In: *Chemical Reviews* 110.11 (Nov. 2010), pp. 6446–6473. DOI: 10.1021/cr1002326.
- [Wil+09] Cara G. Williams et al. "Scanning Micropipet Contact Method for High-Resolution Imaging of Electrode Surface Redox Activity". In: *Analytical Chemistry* 81.7 (Mar. 2009), pp. 2486–2495. DOI: 10.1021/ac802114r.
- [WJO19] D. J. Weber, M. Janssen, and M. Oezaslan. "Effect of Monovalent Cations on the HOR/HER Activity for Pt in Alkaline Environment". In: *Journal of The Electrochemical Society* 166.2 (2019), F66–F73. DOI: 10.1149/2.0301902jes.
- [WN91] Alan C. West and John Newman. "Current Distributions on Recessed Electrodes". In: *Journal of The Electrochemical Society* 138.6 (June 1991), pp. 1620–1625. DOI: 10.1149/1.2085844.
- [Wu+21] Xuewei Wu et al. "Enhanced H₂ evolution reaction due to H spillover during electrolytic reduction of water on a Au/TiO₂ electrode". In: *Electrochemistry Communications* 129 (Aug. 2021), p. 107085. DOI: 10.1016/j.elecom.2021.107085.
- [Wyc63] Ralph W.G. Wyckoff. *Crystal structures*. 2nd ed. Vol. 1. John Wiley & Sons, New York, London, Sydney, 1963.
- [Xue+18] Song Xue et al. "Influence of Alkali Metal Cations on the Hydrogen Evolution Reaction Activity of Pt, Ir, Au, and Ag Electrodes in Alkaline Electrolytes". In: *ChemElectroChem* 5.17 (June 2018), pp. 2326–2329. DOI: 10.1002/ce1c.201800690.
- [YB99] In-Chul Yeh and Max L. Berkowitz. "Dielectric constant of water at high electric fields: Molecular dynamics study". In: *The Journal of Chemical Physics* 110.16 (Apr. 1999), pp. 7935–7942. DOI: 10.1063/1.478698.
- [Zha04a] Xiaoge Zhang. "Electrochemistry of Silicon and its Oxide". In: New York: Kluwer Academic/Plenum Publishers, 2004. Chap. Chapter 4 - Etching of Oxides, pp. 151–154. ISBN: 0306479214.
- [Zha04b] Xiaoge Zhang. *Electrochemistry of Silicon and its Oxide*. New York: Kluwer Academic/Plenum Publishers, 2004. ISBN: 0306479214.
- [Zhe+18] Yao Zheng et al. "The Hydrogen Evolution Reaction in Alkaline Solution: From Theory, Single Crystal Models, to Practical Electrocatalysts". In: *Angewandte Chemie International Edition* 57.26 (May 2018), pp. 7568–7579. DOI: 10.1002/anie.201710556.
- [Zhu+13] Ulmas Zhumaev et al. "Electro-oxidation of Au(111) in contact with aqueous electrolytes: New insight from in situ vibration spectroscopy". In: *Electrochimica Acta* 112 (Dec. 2013), pp. 853–863. DOI: 10.1016/j.electacta.2013.02.105.

Danksagung

Zuerst möchte ich Frau Prof. Dr. Katharina Krischer danken, die es mir ermöglicht hat, dass ich in ihrer Gruppe promovieren kann. Sie konnte mich während meiner Zeit in ihrer Gruppe nicht nur für dieses spannende Thema begeistern, sondern stand mir auch immer mit Rat und Tat zur Seite. Mit ihrer Hilfe konnten nicht nur fachliche Fragestellungen schnell beantwortet, sondern auch administrative Hürden immer schnell gelöst werden und so war sie mir eine großartige Doktormutter.

Anschließend möchte ich unseren Kooperationspartnern danken: Markus Becherer, Simon Mendisch, und insbesondere Matthias Golibruch, der viel Zeit und Energie investiert hat, um gute Proben herzustellen. Ich habe unsere Zusammenarbeit und die vielen Diskussionen über die kleinen und größeren Tücken des Fabrikationsprozesses sehr genossen. Auch herzlich bedanken möchte ich mich bei Dmitry Momontenko, Julian Hengsteler und Tomaso Zambelli, die mich während meines Forschungsaufenthalts an der ETH Zürich betreut und unterstützt haben und dank denen ich mich dort sehr wohl gefühlt habe.

Dann möchte ich einigen ehemaligen und aktuellen Kollegen danken: Simon Filser, Robin Nagel, Qi Li, Simon Stangelmaier, Pierre-Yves Olu, Manuela Ritter, Juliane Wiehl, Maximilian Patzauer, Anton Tosolini, Thomas Gänsheimer, André Dourado, Seungyae Lee, Simon Stork, Hagen Übele, Malo Duportal und vielen weiteren. Danke für die unzähligen Gespräche, die Hilfe bei Problemen verschiedenster Art und auch die vielen schöne Momente, die ich dank euch hatte.

Ganz herzlich bedanken möchte ich mich bei den von mir betreuten Bachelor-, und Masterstudenten: Johannes Wüllenweber, Haiting Yu, Kilian Vettori, Antonia Pawlowski, Corbinian Grön, Lukas Bührend und Andrea Sterr. Besonders hervorheben möchte ich an dieser Stelle Tina Angerer und Moritz Feil, die mich eine sehr lange Zeit während meiner Doktorandenzeit begleitet haben. Euch allen gilt aber viel Dank für die anregenden Diskussionen und eure vielseitige Mithilfe und Mitwirkung. Ohne eure Beiträge wäre meine Arbeit nicht zu dem geworden, was sie heute ist.

Und last but not least möchte ich meiner Familie danken: Ruth Maier, Lorenz Maier, Lukas Oswald und Andrea Oswald. Ohne eure Unterstützung und Förderung auf vielen Ebenen wäre ich heute sicherlich nicht da, wo ich bin. Vielen Dank!

Appendix A

Supplementary Information

A.1 Etching of borosilicate glass in alkaline electrolyte

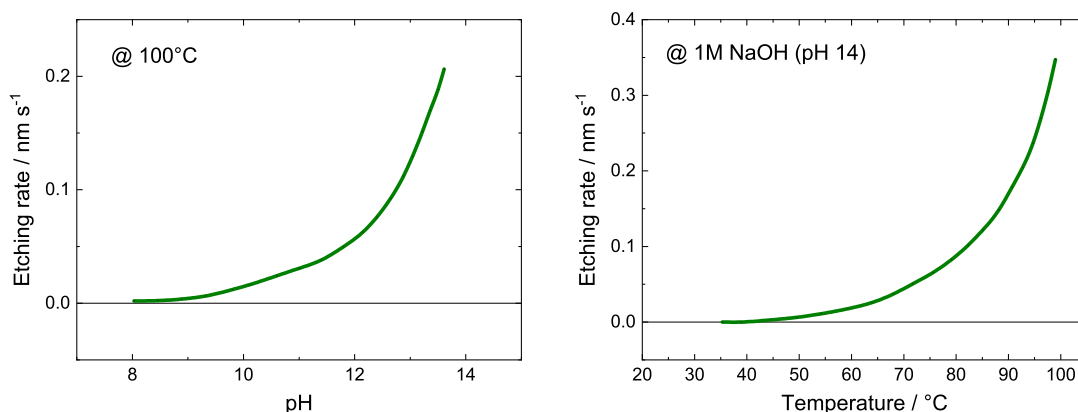


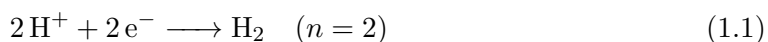
Figure A.1: Etching rate of borosilicate glass (DURAN®[®], SCHOTT AG) in alkaline environment as a function of (a) pH at 100 °C and (b) temperature at 1 M NaOH (pH 14). The etching rate values are self-calculated from the data given in SCHOTT AG report [SCH20], considering a constant density of borosilicate glass of 2.23 g cm⁻³ (25 °C).

A.2 Transfer coefficients for various HER/HOR reaction pathways

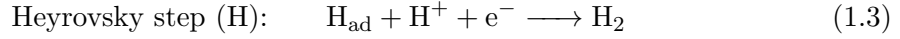
Here, a short overview of the theoretically predicted transfer coefficients of the Hydrogen Evolution Reaction and the Hydrogen Oxidation Reaction for various combinations of reaction pathways/mechanisms and rate determining steps (RDS) is given.

Hydrogen Evolution Reaction ('forward')

Reaction:



Steps:



Possible combinations:

Combination	Step 1	Step 2	ν	n_f	n_r	α_c	n/ν
1f	1·V (RDS)	1·H	1	0	1	β	2
2f	1·V	1·H (RDS)	1	1	1	$1 + \beta$	2
3f	2·V (RDS)	1·T	2	0	1	β	1
4f	2·V	1·T (RDS)	1	2	0	2	2

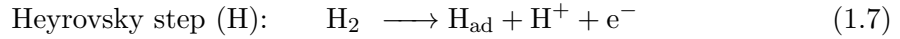
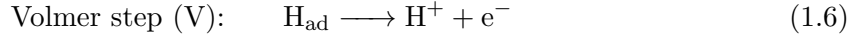
Table A.1: Calculated α_c for HER.

Hydrogen Oxidation Reaction ('backward')

Reaction:



Steps:



Possible combinations:

Combination	Step 1	Step 2	ν	n_b	n_r	α_a	n/ν
1b	1·H	1·V (RDS)	1	1	1	$2 - \beta$	2
2b	1·H (RDS)	1·V	1	0	1	$1 - \beta$	2
3b	1·T	2·V (RDS)	2	0	1	$1 - \beta$	1
4b	1·T (RDS)	2·V	1	0	0	0	2

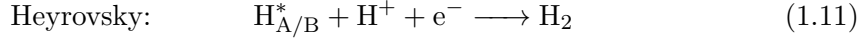
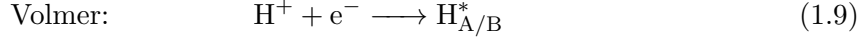
Table A.2: Calculated α_a for HOR.

A.3 HER reaction network on Au(pc) in acidic medium

Here a detailed overview over the HER reaction network on poly-crystalline gold surface in acidic electrolyte is given. This overview is based on the proposed mechanism given by Kahyarian et al. [KBN17].

On poly-crystalline gold surface there are undercoordinated sites (B) present, which show almost no significant activation barrier for the Tafel recombination step. Thus, these sites

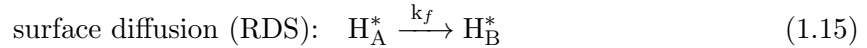
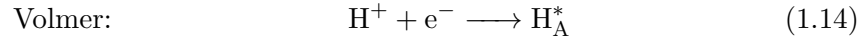
have a much higher activity for the Tafel step, but their surface concentration is just the minority. Consequently, the reaction network at low overpotentials can be modeled as follows:



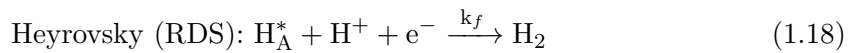
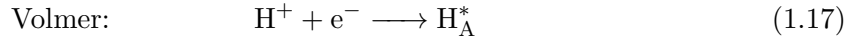
The majority of sites present at the gold surface are labeled A. Thus, the surface concentration of sites A, Γ_{A} , is much larger than the surface concentration of sites B, Γ_{B} . As sites B do not necessarily show an altered adsorption energetics or increased adsorption probability, the coverage θ of both sites is similar. Consequently, the surface concentration of adsorbed protons Γ_{H^*} is dominated by sites A:

$$\Gamma_{\text{H}^*} = \theta(\Gamma_{\text{A}} + \Gamma_{\text{B}}) \approx \theta \cdot \Gamma_{\text{A}} = \Gamma_{\text{H}_{\text{A}}^*} \quad (1.13)$$

At **low coverages**, i.e. at low cathodic overpotentials, the rate is determined by the surface diffusion of protons adsorbed at sites A towards sites B on the surface, where the Tafel reaction occurs fast:



At **high coverages**, i.e. at high cathodic overpotentials, the majority of sites A is occupied. Consequently, the contribution of the minority sites B to the total current can be neglected and the rate of the reaction is determined by the Heyrovsky step on sites A:



A.4 Metal nanostructure array on glassy carbon substrate

We further tried the LO-NIL nanofabrication procedure on commercially available flat and polished glassy carbon (GC) plates (HTW GmbH, Germany) as a substrate material. Figure A.2(top) shows an AFM image of the surface of a black GC substrate before applying the structuring process. An SEM image of an Au nanostructure array (nanostructure size of 75 nm) fabricated onto GC substrate by LO-NIL is shown in Figure A.2(bottom). The rather high roughness of the GC surface leads to a quite inhomogeneous metal array for the structure size investigated, which makes the GC substrate used here a comparatively bad substrate for producing well-defined arrays of metal structures with sizes in the decanometer range.

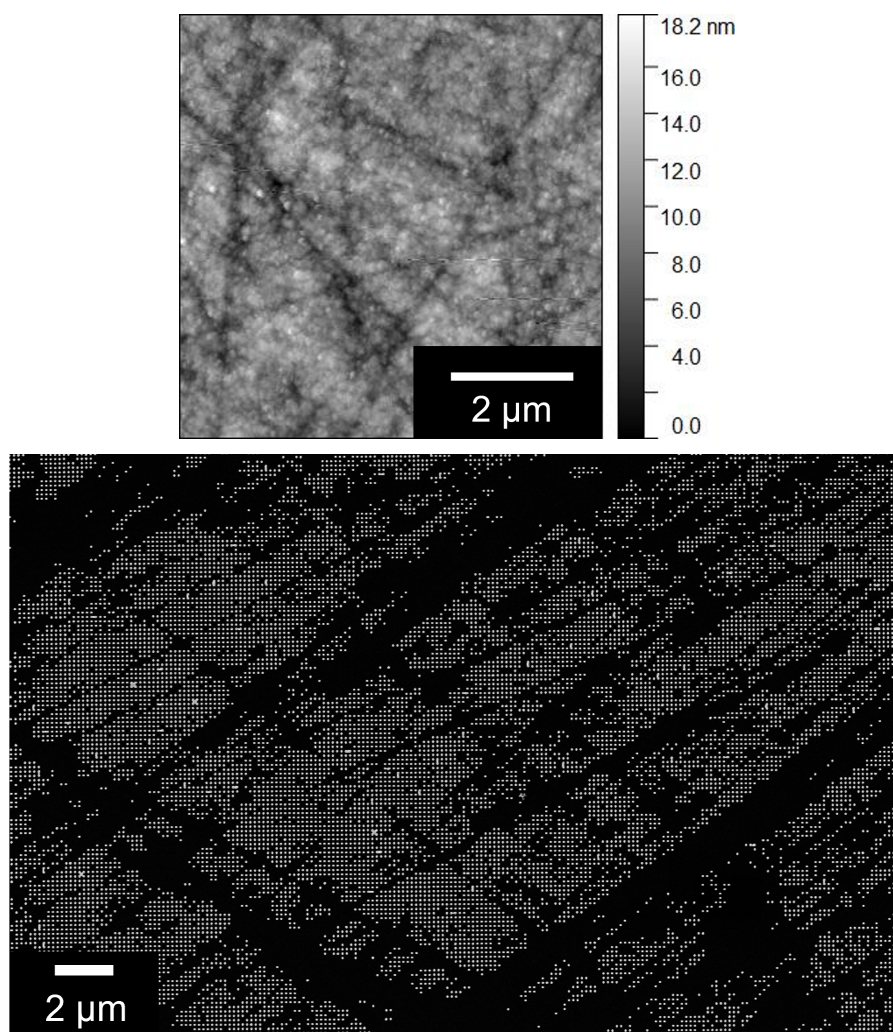


Figure A.2: Metal nanostructures with 75 nm structure size fabricated by Lift-Off Nanoimprint Lithography onto a commercially available flat and polished glassy carbon (GC) substrate. Top: AFM image of the blank GC substrate before nanostructuring. Bottom: SEM image of the Au nanostructure array fabricated onto the GC substrate. Although the fabrication procedure is applicable to the GC substrate and gives metal structures on the surface, the large roughness of the underlying substrate leads to a rather inhomogeneous metal array.

A.5 Presence of protruding edges on metal nanostructures

The shape of the final metal nanostructures is sensitive to the substrate properties and the process parameters of the structuring process. Exemplary, when increasing the thickness (range of 20 nm) of the passivation layer, we could observe that the edges of the final metal structures become protruding [Ang19; Ang21], c.f. Figures A.3 and A.4. The protruding edges are present for all sizes of structures, but are most dominant for the smallest structure size.

This effect is likely caused by the isotropic (lateral) etching properties of the second RIE step with the etching parameters used. This etching step needs to be performed for a longer time, when using a thicker passivation layer, which, in turn, leads to a larger inhomogeneity of the resulting hole. Contrary, when using rather thin passivation layer

thicknesses, the protrusion of the edges could be minimized. In this work we usually use passivation layer thicknesses in the range of 10 nm in order to minimize the presence of the protruding edges.

We could further show in another study, that these edges are rather unstable under electrochemical working conditions and their protrusion height decrease during a usual measurement routine performed with the samples. In addition, we could show that the presence or absence of the protruding edges does not alter the electrochemical response of the electrodes significantly [Ang21].

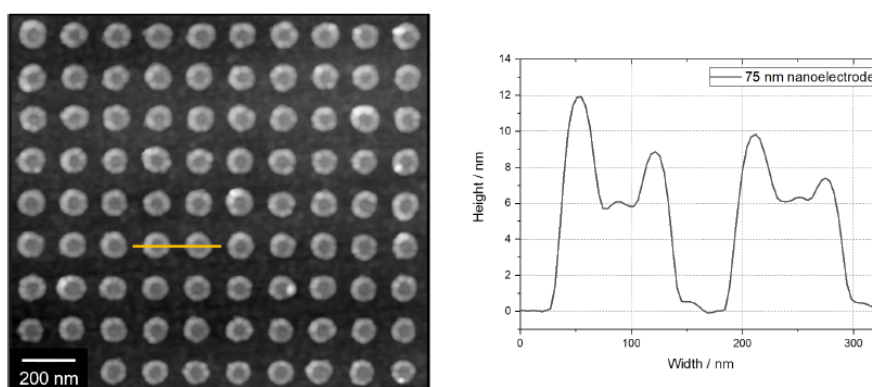


Figure A.3: AFM image of Au structures with 75 nm structure size exhibiting a higher gold layer at the edges surrounding the structures ('protruding edges'). Images are taken from [Ang21].

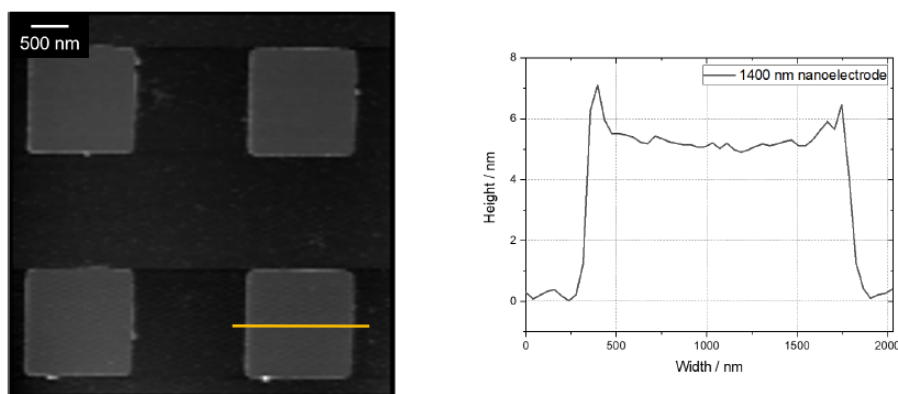


Figure A.4: AFM image of Au structures with 1400 nm structure size exhibiting a higher gold layer at the edges surrounding the structures ('protruding edges'). Images are taken from [Ang21].

A.6 List of chemicals used

Salts

- Lithium hydroxide monohydrate, Alfa Aesar, $\geq 99.995\%$ (metal basis), 44473
- Sodium hydroxide monohydrate, Merck, 99.999 Suprapur Supelco, 1.06466

- Potassium hydroxide monohydrate, Honeywell Chemicals, $\geq 99.995\%$ (metal basis) TraceSelect, 60371
- Cesium hydroxide monohydrate, Arcos Organics, 99.95 %, ACRO189520500
- Potassium sulfate, Merck, 99.999 Suprapur Supelco, 1.05152
- Potassium hexacyanoferrate(II) trihydrate, Merck, Emsure Supelco, 1.04984
- Potassium carbonate sesquihydrate, Merck, 99.999 Suprapur Supelco, 1.04926

Liquids

- Sulfuric acid $\geq 96\%$, Merck, Suprapur Supelco, 1.00714
- Ortho-phosphoric acid $\geq 85\%$, Merck, Suprapur Supelco, 1.00552
- Copper(II)sulfate solution 0.1 mol/l, Merck, Titripur Supelco, 1.02784

A.7 Theoretical curve of HOR in an RDE setup

The following quantities (values at $T = 25^\circ\text{C}$) are used for determining the theory curve of j_{lim} of HOR as a function of \sqrt{w} (according to RDE theory) given in the plot:

Solubility of H_2 in H_2O : 1.55 mg/l [Rum17]

Molar mass of H_2 : $M = 2.02$ g/mol [Rum17]

\Rightarrow Bulk concentration of H_2 gas: $c_{\text{H}_2}^* = 0.77$ mol/m³

Diffusion coefficient of H_2 gas in water: $D_{\text{H}_2} = 4.5 \cdot 10^{-9}$ m²/s [Rum17]

Kinematic viscosity of Water: $\nu_{\text{H}_2\text{O}} = 9.0 \cdot 10^{-7}$ m²/s [Rum17]

A.8 Time dependence of the electrode current with variable electrode potential

Here we give a derivation of the time dependence of the electrode current present at the electrode surface as a function of applied potential *and* time based on the Cottrell approach: We consider that the transport of reactive species towards the electrode is determined by diffusion, i.e. we consider the linear diffusion equation (here for oxidized species):

$$\frac{\partial c_{\text{ox}}(x, t)}{\partial t} = D_{\text{ox}} \frac{\partial^2 c_{\text{ox}}(x, t)}{\partial x^2} \quad (1.19)$$

With the boundary conditions:

$$c_{\text{ox}}(x, t = 0) = c_{\text{ox}}^* \quad (1.20)$$

$$\lim_{x \rightarrow \infty} c_{\text{ox}}(x, t) = c_{\text{ox}}^* \quad (1.21)$$

$$c_{\text{ox}}(0, t) = 0 \quad (\text{for } t > 0) \quad (1.22)$$

Laplace transformation of a partial differential equation in t leads to an ordinary differential equation in x (cf. [BF01] p. 162 and pp. 775). Applying the boundary conditions gives:

$$\bar{c}_{\text{ox}}(x, s) = \frac{c_{\text{ox}}^*}{s} + A(s)e^{-x\sqrt{s/D_{\text{ox}}}} \quad (1.23)$$

$$\text{with } \bar{c}_{\text{ox}}(0, s) = 0 \quad (1.24)$$

After back transformation we get an expression of the time dependence of c_{ox} as a function of space and time:

$$c_{\text{ox}}(x, t) = c_{\text{ox}}^* \operatorname{erf}\left(\frac{x}{2\sqrt{D_{\text{ox}}}\sqrt{t}}\right) \quad (1.25)$$

Assuming the concentration dependent Butler-Volmer equation (see [BF01] p. 99) with $c_{\text{red}}(x) = 0$ we get:

$$j_{\text{el}}(\eta_{\text{el}}) \approx -j_0 \frac{c_{\text{ox}}^S}{c_{\text{ox}}^*} \exp\left(-\frac{\alpha_c F}{RT} \eta_{\text{el}}\right) \quad (1.26)$$

Inserting equation (1.25) into the surface term of the concentration c_{ox}^S and setting the factor $x/2\sqrt{D_{\text{ox}}}$ to a finite constant a gives a dependence of the current on time *and* the applied potential. Thus, the behavior of the current drawn as a function of time t and a variable potential η_{el} can be modeled by:

$$I_{\text{el}}(\eta_{\text{el}}, t) = -I_0 \operatorname{erf}\left(\frac{a}{\sqrt{t}}\right) \exp(-b \eta_{\text{el}}) \quad (1.27)$$

A.9 Tafel analysis of acidic HER at a lower potential scan rate

The Tafel analysis of the data of nanostructured electrodes in 0.1 M H_2SO_4 shown in the main part is conducted at a potential scan rate of 50 mV s^{-1} . Compared to scan rates usually used in Tafel analyses in the literature, this rate is rather high. Figure A.5 shows the Tafel slope dependence on the electrode potential at the rather low scan rate of 10 mV s^{-1} on two selected nanostructured electrodes, Figure A.5(a) without and Figure A.5(b) after subtraction of the non-faradaic (double layer charging) current determined at 0 V_{RHE} . It becomes evident that the behavior of the slope with the electrode potential is rather similar to the case with the larger scan rate of 50 mV s^{-1} shown in the main part of this work. Thus, we can conclude that all qualitative statements made from the Tafel analysis are rather independent of the actual scan rate at which the potential scans are performed in the investigated system.

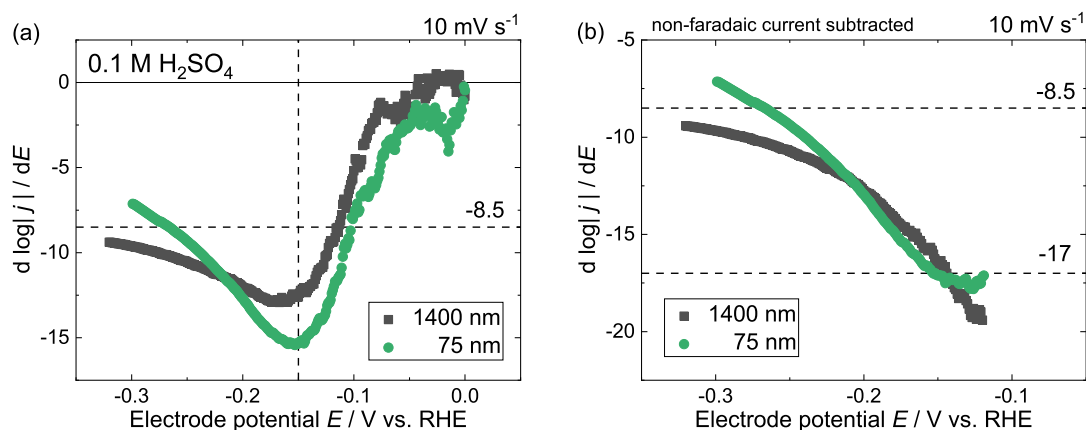


Figure A.5: Derivative of the logarithmic current density over the electrode potential determined from potential scans in $0.1 \text{ M H}_2\text{SO}_4$ with a scan rate of 10 mV s^{-1} . (a) Without subtraction of the non-faradaic (double layer charging) current. (b) After subtraction of the non-faradaic current determined at 0 V_{RHE} . Both graphs show a very similar trends as the curves determined from scans performed with a larger potential scan rate of 50 mV s^{-1} .

A.10 CVs of Pt-based nanostructured electrodes in acidic medium

Full CVs of a continuous Pt layer electrode and nanostructured electrodes with 1400 nm and 75 nm Pt structure size in acidic electrolyte with $0.1 \text{ M H}_2\text{SO}_4/\text{Ar sat.}'d$ (pH 1) are shown in Figure A.6. All typical features of a Pt(pc) surface are well visible in the CVs, which leads to a very similar shape of the CVs for all electrodes considered here.

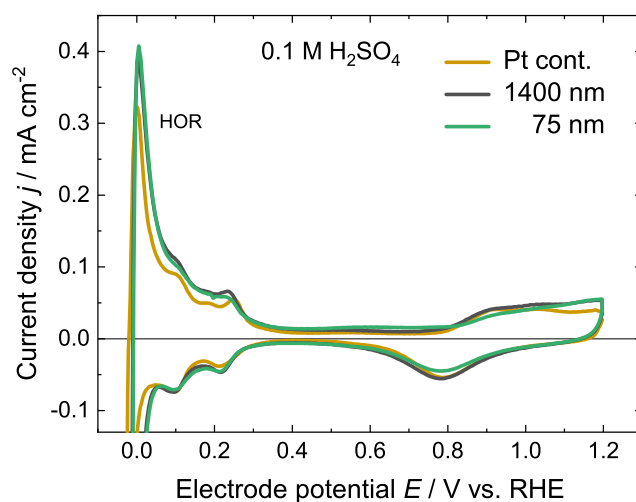


Figure A.6: CVs of a continuous Pt layer, Pt structures with 1400 nm size and Pt structures with 75 nm size in $0.1 \text{ M H}_2\text{SO}_4/\text{Ar sat.}'d$ (pH 1.0). Scan rate: 50 mV s^{-1} .

A.11 XPS spectra of a silicon nitride film at various angles

The silicon nitride (Si_3N_4) based nanostructured electrodes can be analyzed via XPS in various exit angles θ of excited electrons. The decrease of θ makes the technique more

surface sensitive, as the pathlength of electrons excited at certain depth in the sample increases, cf. Figure A.7.

Figure A.8 shows the XPS O1s (left) and the N1s (right) signal of a nanostructured electrode with Au structures of 1400 nm size and silicon nitride as the passivation layer material at (a) $\theta = 90^\circ$ and (b) $\theta = 36^\circ$. Note that the sample has been exposed to an O-plasma before the XPS measurement, which is the usual fabrication procedure for nanostructured electrodes. It becomes evident in the data that the N1s signal decreases, while the O1s signal increases when decreasing the angle θ . Thus, we can conclude that most of the oxygen signal measured here is due to oxygen compounds present on the surface of the silicon nitride film.

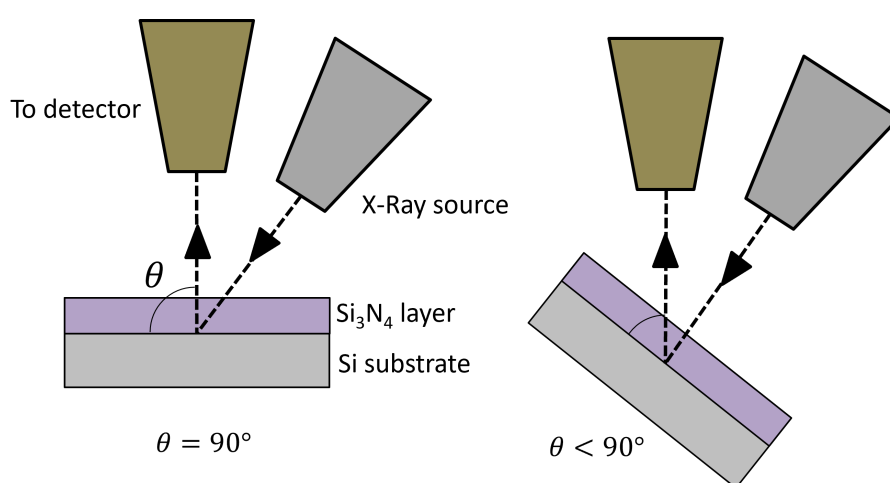


Figure A.7: Scheme of the setup of the XPS measurements. Decreasing the angle θ makes the measurement more surface sensitive, as the pathlength of the electrons excited at a certain depth increases.

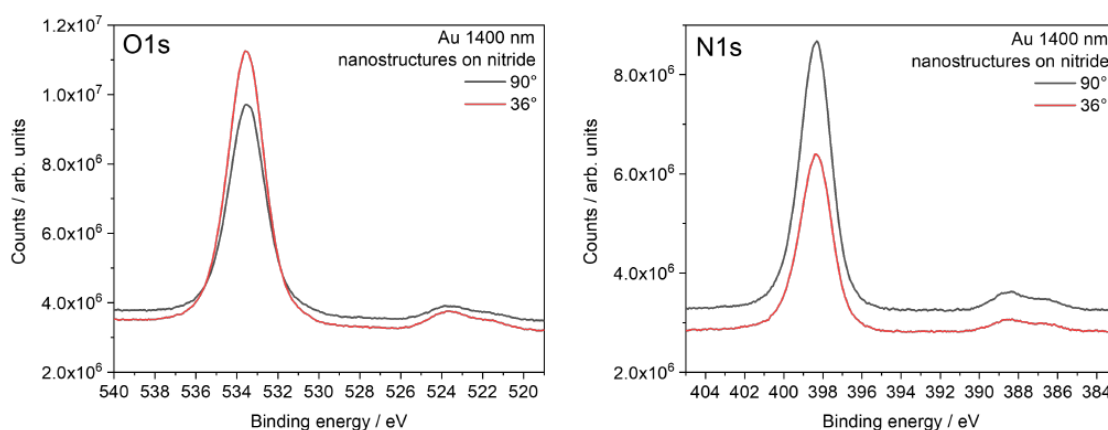


Figure A.8: XPS O1s (left) and the N1s (right) signal of a nanostructured electrode with Au structures of 1400 nm size and silicon nitride as the passivation layer material at $\theta = 90^\circ$ (black) and $\theta = 36^\circ$ (red). The image is taken from [Ang21].

A.12 Tafel plot of LSV curves in neutral electrolyte

Figure A.9 shows the Tafel plot of nanostructured and continuous Au layer electrodes in buffered neutral electrolyte: $0.18 \text{ M K}^+ + 0.12 \text{ M H}_2\text{PO}_4^-/\text{HPO}_4^{2-}$ (pH 7). Scan rate: 50 mV s^{-1} . The double layer charging current present at $E = 0 \text{ V}_{\text{RHE}}$ has been subtracted before building logarithmizing. It is visible, that the slope is approximately linear at low current densities, while it starts to drop from the linear progression at 'high' current densities, here the drop appears at approx. $\log(|j|) \approx -0.5$ (dashed line). It is likely that the current response of the system is kinetically dominated in the potential range, at which the progression of the curve is approximately linear ($\log(|j|) < -0.5$) and becomes transport dominated at higher current densities: $\log(|j|) > -0.5 \Rightarrow j > 0.32 \text{ mA cm}^{-2}$.

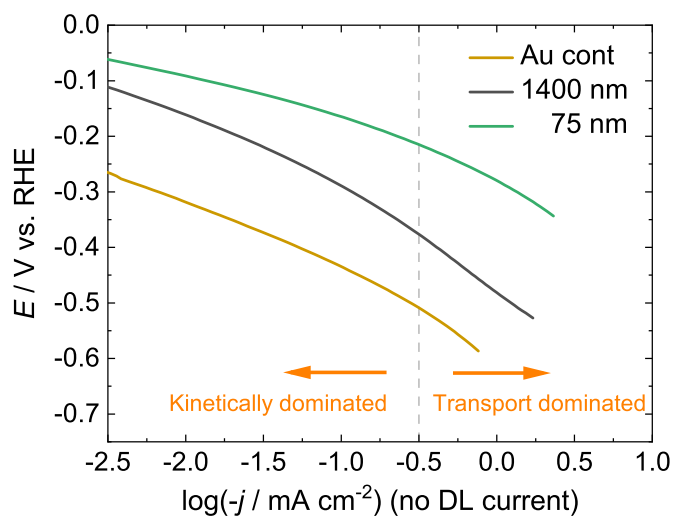


Figure A.9: Tafel plot of the HER current on a continuous Au layer electrode (Au cont.), and nanostructured electrodes with 1400 nm and 75 nm Au structures size in neutral electrolyte: $0.18 \text{ M K}^+ + 0.12 \text{ M H}_2\text{PO}_4^-/\text{HPO}_4^{2-}$ (pH 7). Scan rate: 50 mV s^{-1} .

A.13 Comparison of fitting models of impedance data

The equivalent circuit used for fitting the impedance data of the continuous metal layer system or the metal nanostructures is the 'extended' model consisting of a serial connection of an resistance R_s and *two* $\text{CPE}||\text{R}$ elements. Most of the data could be fitted quite good by a 'simple' model consisting of only *one* $\text{CPE}||\text{R}$ element.

Simple model: $R_s-(\text{CPE}1||\text{R}1)$

Extended model: $R_s-(\text{CPE}1||\text{R}1)-(\text{CPE}2||\text{R}2)$

However, especially for data of the nanostructured electrodes at potentials close and above the determined PCZ ($E > 0.2 \text{ V}_{\text{SHE}}$), the simple model was not sufficient to describe the behavior correctly. This can be seen in Figure A.10. Here, a Bode plot (impedance vs. frequency and phase vs. frequency) of an exemplary dataset of a nanostructured electrode with 75 nm Au structure size at $E = 0.3 \text{ V}_{\text{SHE}}$ and the best respective fits to either the simple or the extended model are shown. The fit values of the fitted parameters are given in Table A.3

It becomes clear that the fit by the simple model is not sufficient to describe the behavior sufficiently. Especially at high frequencies the experimental behavior of the system differs from the corresponding fit to the simple model. However, the extended model is able to describe the behavior quite well in the whole frequency range. Thus, we use the extended model to fit all of the impedance data of the continuous and the nanostructured metal electrodes in this work.

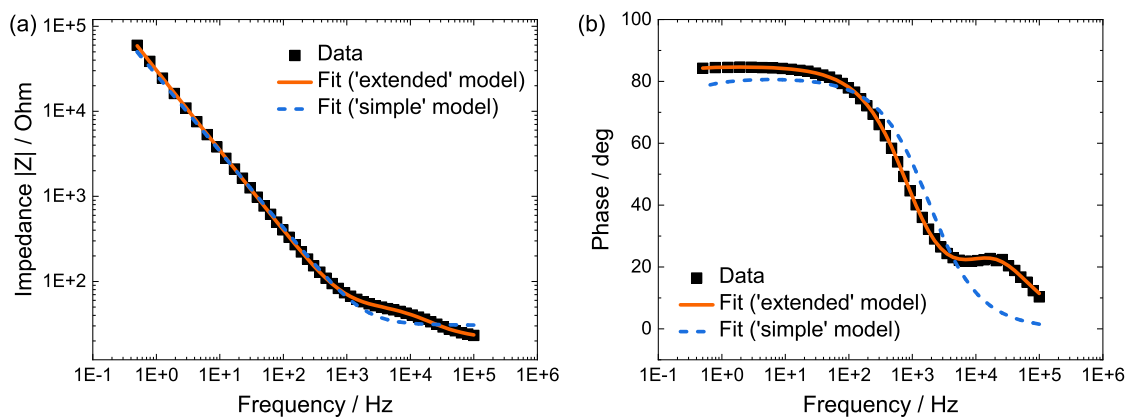


Figure A.10: Bode plot of an exemplary data set (black squares) and the corresponding fit using either the 'simple' (dashed blue line) or the 'extended' (solid orange line) equivalent circuit model for fitting. The respective values of the fit parameters are given in Table A.3. Dataset: Nanostructured electrode with 75 nm Au structure size at $E = +0.3 V_{\text{SHE}}$.

Fit parameter	Simple model		Extended model	
	Value	Error	Value	Error
R_s	30.5	10%	21.4	2%
Q_1	$7.0e-6$	9%	$5.8e-6$	1%
n_1	0.90	2%	0.95	1%
R_1	$1e6$	50%	$5.6e6$	30%
Q_2	-	-	$2.2e-6$	3%
n_2	-	-	0.86	1%
R_2	-	-	27.2	2%

Table A.3: Values of the fit parameter of the simple equivalent circuit and the extended equivalent circuit model with individual errors (calculated by the fit software) determined from the fit of the exemplary dataset presented in Figure A.10.